An Analysis of Proximal Volcanic Ash Emissions

by

Daniel Blair Williams

BSc Geology and Geography, University of Birmingham, 2009

MRes Science of Natural Hazards, University of Bristol, 2011

Submitted to the Graduate Faculty of the

Kenneth P. Dietrich School of Arts and Sciences in partial fulfillment

of the requirements for the degree of

Doctor of Philosophy

University of Pittsburgh

2018

UNIVERSITY OF PITTSBURGH

Dietrich School of Arts and Sciences

This dissertation was presented

by

Daniel Blair Williams

It was defended on

July 19, 2018

And approved by

Committee Chair: Michael Ramsey, Professor, University of Pittsburgh

William Harbert, Professor, University of Pittsburgh

Charles Jones, Senior Lecturer, University of Pittsburgh

Vincent Realmuto, Principal Scientist, NASA Jet Propulsion Laboratory

Brian Stewart, Associate Professor, University of Pittsburgh

An Analysis of Proximal Volcanic Ash Emissions

Daniel Blair Williams, PhD

University of Pittsburgh, 2018

Volcanic ash is a product of explosive volcanic eruptions and refers to those particles < 2 mm in size that are ejected from a volcano. Once erupted into the atmosphere, ash can be transported vast distances. Satellite remote sensing has provided us with the tools to map and monitor these plumes. These methods are restricted in viewing only that portion that is optically transparent, due to the requirement to observe the interaction of ground upwelling radiation with the plume. For this study, methods have been developed to map not only the opaque portion of the plume, but in higher spatial resolution than has been attempted previously. This has been done by using the unique emissivity spectra that are produced by materials in the thermal infrared portion of the electromagnetic spectrum. By using an end-member linear unmixing model with a spectral emissivity library of different volcanic ash types, opaque plume bearing pixels of Advanced Spaceborne Thermal Emission and Reflection Radiometer (ASTER) data have been processed. These end-member results have shown the applicability of this technique, with sampled volcanoes mapped with very low root mean square (RMS) errors. Volcanoes with unknown composition were also mapped with the library with varying degrees of success. Further expansion of the laboratory spectral library will allow more accurate assessment of these volcanoes. The collection of per pixel emissivity spectra of opaque plumes was also attempted using an experimental multispectral FLIR thermal camera apparatus, in order to collect data on the rising volcanic ash column. These data showed that the camera can produce emissivity spectra, however further calibration and correction is required in order to make a volcanological

assessment of the eruptive products. Finally, a method of better tracking disconnected ash plumes is assessed. In cases where a plume is detected disconnected from or distally from the source volcano, the application of geostatistical methods to backward trajectory model data can yield the source location. This could then be used to helped point the ASTER sensor off-axis towards erupting targets, thus providing a greater quantity of data to be analyzed.

TABLE OF CONTENTS

LIST OF TABLES

LIST OF FIGURES

PREFACE

"It's wonderful to know that I could be, something more than what I dreamed, far beyond what I could see" – John Petrucci, Dream Theater, 2005

As my supervisor weaved the lyrics of Rush's Neil Peart through his acknowledgments from his thesis, so I decided to open mine echoing the words of my favorite band, Dream Theater, from the song 'Octavarium'. 6 years at the University of Pittsburgh has required, not just allowed, me to reach beyond what I thought I could do, and become something, someone, who I have never met before. This hasn't just been an academic experience for me. This has been a fight to further who I am, to better myself. I have come up short on many occasions, but I can look back on the last 6 years and have pride in who I am. However, none of this would have happened if it wasn't for the people who have allowed and encouraged me to grow, and whilst this preface is nowhere near enough to express my gratitude, I will make the attempt to demonstrate how thankful I have been for so many people in my time here.

I firstly must thank my supervisor Dr. Michael Ramsey. Mike, you took a punt on a guy that you hadn't met before, and only had the words on some pieces of paper and my former supervisor to go on. Yet, you still brought me here and allowed me to follow through on the work I was so desperate to do. You have been kind, patient, and most important trusting, allowing me to take the lead on projects I felt were important, and accepting my judgement. Without this learning experience I never would have gotten to where I am. I have learned so

much from working with you and I'm looking forward to where this knowledge will take me. Thank you.

I feel lucky to have had the committee that I chose, so I would like to thank Drs. Bill Harbert, Charlie Jones, Vincent Realmuto and Brian Stewart. I have benefitted from your suggestions and learned so much from each of you. It has been a pleasure knowing each of you here, so thank you for being a part of this process. Furthermore, I want to extend this thanks to the faculty at the University of Pittsburgh. I'm glad to have known you all here and thank you for tolerating my excessive talking and my inability to control the volume of my voice. I am also incredibly proud that all of you can hear me simply by being on the same floor of the building. I'd also like to thank all the admin staff who have always let me cause a nuisance around the place, and without whom my time here would have been much less enjoyable, Shannon Granahan, Dolly Chavez, Jessica Caldwell and Annemarie Vranesevic. All of you have done so much to help me, I hope that I was able to put a smile on your faces with my ridiculous conversations.

This work would not have gone the way it did without the help of so many other people around the world. I must first thank Matt Watson at the University of Bristol. Allowing me to come back on three separate Guatemala trips has just been brilliant. You have been kind and thoughtful each time and it was a genuine pleasure. Thank you for encouraging me during my time at Bristol and helping me get this PhD position in the first place. You are one of the reasons I am here right now, and for that I am so grateful. Gustavo and Paco Chigna have also been a great help in the field but also become my friends. The work that you both do for the people of Guatemala is unbelievable, I'm so proud to know you both. I must also thank the MSc Volcanology groups from the University of Bristol from 2015, 2016 and 2018, as well as the

accompanying (former and current) graduate students Emma Liu, Luke Western and Ailsa Naismith. Thank you for welcoming me as part of the group and making the field experiences we had as special as they are. I have so many fond memories to look back on thanks to you all. I also must thank the following (in no particular order) for all the time and effort they have put in to helping me with this work; Leif Jahn, Betsy Clark and Eric Lipsky at Carnegie Mellon University, Peter Webley at University of Alaska Fairbanks, Steve Ruff at Arizona State University, Masato Iguchi and Daisuke Miki from Kyoto University, and David Tratt and Jeff Hall at Aerospace. All of you helped shape this through discussion, laboratory work, or field assistance, and your input was invaluable.

There are, obviously a number of people that I must thank for being good friends and being there when I needed it. I hope I was able to do the same. Rachel, Alison, Bobby – you guys made me welcome here and accepted me into life here. You were the source of so much happiness for me when I arrived – I wish I had known you for longer, so that we could've had crazy adventures together. The difficulties of adjusting to a new place were made so much easier through being able to enjoy myself with you all. Thank you. Sarah – you are one of my best friends, and this last 6 years would have been more difficult had I not had someone who was able to go to concerts with me and support me in my acting endeavors. I'm sorry that we have spent so much time apart and that we don't see each other more regularly. Life gets in the way, but that is no excuse. Chris – I know we don't see each other much, we really should try and rectify that sometime. But I'm so glad for the times we've spent hanging out. You and Sarah have always been great to me, and I've enjoyed just coming over, eating, drinking and just generally talking nonsense. James – I really hope I helped when you arrived, I just wanted to help you get as settled as possible. It's been great to have someone to chat sport to for hours, as well as getting

good scotch together. You're an amazing researcher, and there are many things I envy about you. I hope we can continue to work together and be friends together in the future. Mark – It's been too long since we've seen each other, I always intended to come see you in Cleveland after you graduated, but it's another one of those things I didn't end up doing. I'm sorry about that. But my first year here wouldn't have been the same without you to hang out with, I'm thankful for our beer drinking escapades. Anna – You are someone I'm so proud of for just doing what you do. I'm glad for every long, rambling, meandering conversation that we have ever had, I know we never really hung out outside of Crazy Mocha, but I am so grateful for the time we have spent together, discussing everything and nothing. You are going to be fantastic at whatever you chose to do with your life, and I always hope I can lend a friendly ear when you need it. Rachel – Falling into a friendship with you was just so easy. When things are down, spending time with you and just laughing and being silly is one of the things that really puts a genuine smile on my face. I know I make fun of you a lot, but it really does come from a place of great respect. I will always be there for you, no matter what, wherever in the world I am. Daniel – Having a friend who is completely and utterly nonsense free is not something that happens to most people, but our friendship has been such a simple thing. Thanks for all the great times we have spent together, and the many adventures we have been on through Pittsburgh. Congratulations on getting your PhD, it is richly deserved for a very talented person. Best of luck for your new chapter in Chicago. Ian – I know we've only been friends for a short time, but I'm so glad that we met and clicked. Spending time with you, going on our Friday night bar crawling around Oakland in your first semester is what got me through a very tough period of work. Thank you for being there, for being the fun person that you are. Don't let grad school drag you down – I know you worry about doing well and succeeding with a great project, but you will. I'll always

be there to talk ideas, or just catch up once I'm done here. Ben – Cheers for being fun, for having someone to talk stupid conversation in the office with. I know we don't get to hang out as much as I'd like, what with other commitments and all, but thanks for being a friend in the short time we've known each other. To Frankie and Roy – Roy I am sad that you didn't get to see the end of this. You and Frankie have shown me so much kindness over the course of my time here. Thank you for looking after me and letting me stay with you in Florida. It's appreciated more than you both know. Tyler, Wes, Nick – It's been so great being able to just go grab some beers with you guys and relax. There's never a dull moment and you have all made my last year at Pitt so enjoyable. Nothing beats talking about Nick's experiences with Belgian clowns on a Friday night!

Graduate school has been a strange, transient time. Never in my life have I had so many people come and go, in many cases without ever talking to them again. It hasn't been easy, I have often spent time regretting the lack of time I spent with you. But I would like to take a moment to acknowledge a few people, whom have helped me when I needed it – Dan, Jess, Katherine, Cody, Laura, Mallory, Andrew, and Kathryn. I know I've fallen out of touch with you, some have ended more abruptly than I intended. But all of you impacted my life, and I am thankful for that. There were dark moments that you helped me out of, consciously or unconsciously, which helped me to better move on with my life. I wish nothing but the best for all of you.

One thing that I have ended up doing is becoming a regular somewhere, this time a coffee shop. This is a strange thing for me, I'm not always one for attachments, but one I'm glad I undertook, as I built some great relationships out of it. I'm indebted to everyone that I met there, and I'm proud to say I became friends with many of you. So with that in mind I want to thank

Lala, Alex, Emily, Katie and Jackson (yeah I know you don't work there but it's where we always hung out). I'm so glad to have known each and everyone one of you here, coming over there and just talking nonsense got me through so many days. I wish I had gotten to know some of you better, but to just say I knew you all was a privilege. Thank you.

Of course there are some regrets I have from being here. But many of them are outweighed by the things I undertook, one of which was acting. This has been one of the best outlets I've ever had, and I'm so glad to have gotten to know so many people from doing it. I should come up to Butler more, and I regret not forging closer relationships with you all, but to everyone that I've known through the Butler Little Theater and Hobnob Theater company, thank you all so much for the opportunities you gave me and the welcome I always felt when I got to see you all. It wasn't just about the acting, it was about having fun with some of the finest people I've ever known, and I hope that I've demonstrated my thanks through giving my all for you, and by trying to make it as fun an experience as possible. But especially I must thank the Smith's, Liz and Kenny. You both directed me and I had nothing but fun doing the shows we did. Thank you for thinking of me, for working on getting me into a show whilst fitting it around my schedule. Your kindness and hard work in producing these shows certainly paid off. Louis – you're the funniest person I've ever met. You're so full of life and I'm so glad I could be a part of it (even if you don't always remember your lines!) Phil – you're a fantastic actor and wonderful person. I'm so glad we got to become friends through the shows we have done together. It has been such a tremendous honor knowing you here and I hope you continue to make people's lives happier through the theater into the future.

Finally, I have some of the most important people to thank for helping me through everything, for being there for me and making this experience what it was. Amy, you have been

my best friend and more for 5 and ½ years. Our relationship has taken twists and turns, but no matter what, we always figure it out in the end. Things may not be the same as they were, but I'm more than glad that we still live together and that we still are the best of friends. You have been kind, patient and understanding with me. I know I'm not always easy to deal with. But you have managed it and your loyalty in our friendship has been unwavering. Thank you for everything that you do and everything that you are. Without it, I would have struggled so much more.

Matthew – I'm so lucky to call my brother my best friend. We still talk nearly every day despite the distance between us. You have helped me through so much of this, and I have been so proud to watch where your career has taken you during my time here. Thank you for always being there any time of the day, to help, to laugh and joke. I hope you're able to make it over here so day soon so that I can explore more of the USA with you.

And last of all, to my Mum and Dad. All I ever wanted to do was to make you proud and happy. It was hard going away and I was scared and nervous and I know you were too. But I did it. I finished this, and I got my PhD. This is your achievement too, for everything you did for Matthew and I, for every sacrifice made, for every difficulty that you had to endure for us. I'm lucky to have the parents I have and to be born in to family I was. No matter what I achieve through my career, that is the thing I am proud of most, to be your son. I will continue to do everything I can to stand up for what you taught me, to be the person you know I can be. Thank you for everything.

1.0 INTRODUCTION

Volcanic ash is a mixture of pulverized lithic, mineral and glass fragments that are ejected from a volcano during an eruption (Zimanowski et al., 2003), also referred to as tephra. It is classified as those pyroclastic particles having a grain size of 2 mm diameter or less, with very fine ash being that fraction less than 63 μm in diameter (White and Houghton, 2006). Ash is complex, as its composition and morphology are controlled by the chemistry of the magma beneath a volcano, and the processes occurring within the vent. Ash is formed where magma undergoes fragmentation. During magmatic eruptions, the ascent, decompression and fragmentation of magma is controlled by dissolved volatiles such as CO_2, SO_2 and water vapor, which begin to exsolve and expand as gas bubbles within the magma (Cashman and Sheu, 2015; Cashman and Rust, 2015). This depressurization is more common in dome forming volcanoes, where solidified magma in the vent can collapse due to instabilities, leading to rapid decompression and fragmentation (Alidibirov and Dingwell, 1996). If water is external to the volcano plumbing system (i.e. of glacial or lacustrine origin), then the steam produced provides additional energy for fragmentation, termed a hydromagmatic eruption (Zimanowski et al., 2015). In this case, thermal contraction of the magma occurs, as the water chills the magma at its interface, causing it to shatter and erupt along with a cloud of superheated steam (Langmann et. al., 2012). If the tensile strength of a magma is overcome, the fragments that are created in the resulting gas expansion are lofted into the air, entrained in the volcanic gases, creating an ash

cloud. Fragmentation can be considered primary and secondary. Primary fragmentation is related to those processes occurring in the vent as a result of decompression, expansion, molten fuel-coolant interactions etc. (Mastin et al., 2009), whereas secondary fragmentation refers to the process of further breaking down the already fragmented particles from processes such as abrasion (Durant and Rose, 2009).

The composition of volcanic ash is highly variable and will be a combination of crystal fragments of both those minerals formed within the melting during cooling and ascent, as well as phenocrysts of material that crystallized at depth. What complicates the use of ash as the determiner of the bulk magma composition, is that as minerals crystalize the melt becomes more evolved (SiO_2 rich). If this melt then undergoes quenching, the glass formed will be significantly richer in SiO_2 than that of the bulk magma (Cashman and Rust, 2015). This behavior is determined by the amount of crystallization present. In crystal poor magmas, the glass will be similar in composition to the bulk composition, whereas in crystal rich magmas, the glass will have significantly greater amounts of SiO_2 (except for quartz; Cashman and Rust, 2015).

The plume that is ejected from a volcano is a mixture of ash entrained in a jet of hot gases (Figure 1-1). Plumes can be classified as weak or strong, dependent on the rate of buoyant plume rise. This is controlled by the mass eruption rate and temperature (Bonnadonna and Phillips, 2003). Plumes will rise to a maximum height (H_T) controlled by the momentum of the column. If H_T rises above the level of neutral buoyancy (H_B), the plume will then descend as a gravity current (Bursik et al., 1992). This results in the formation of an umbrella cloud, which will begin to spread laterally. Larger particles (> 100 μm) as well as aggregates formed from finer particles will start to settle out of suspension due to gravity (Taddeucci et al., 2011). The mechanics of this process are becoming better understood (Van Eaton et al., 2015; Mueller et al., 2016).

Smaller particles can remain suspended and travel much further, dependent on downwind advection, gravitational settling and mixing due to atmospheric turbulence (Woods and Kienle, 1994).

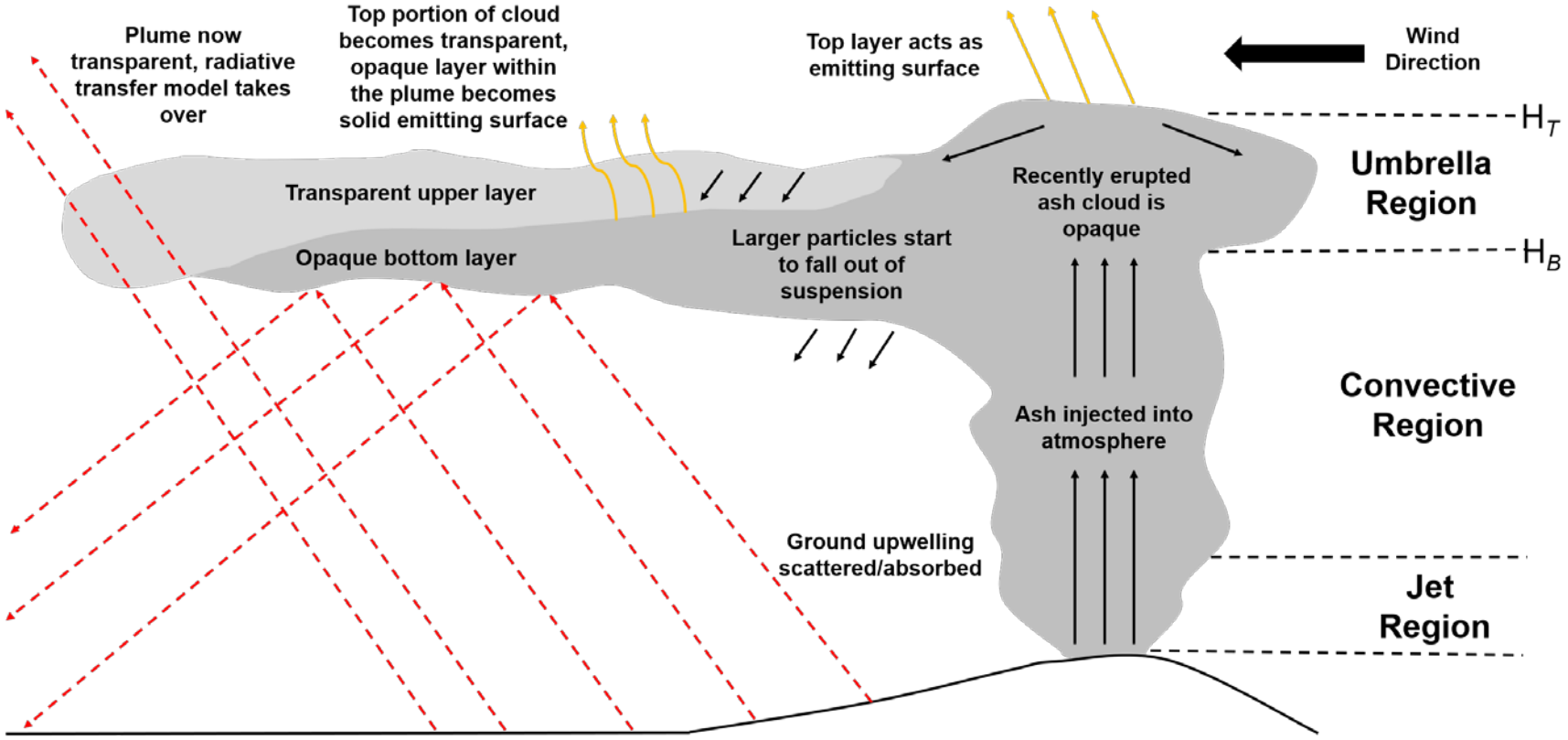

Figure 1-1 Idealized model of a volcanic plume erupting into the Earth's atmosphere, and the pathway of TIR radiance (after Sparks, 1986). The initial momentum is provided in the jet region where the ash and gas mixture is escaping the vent after volatile exsolution and fragmentation. After this, the plume buoyantly rises through convection. Eventually the plume will reach a neutral buoyancy point, where the plume will then spread laterally as a gravity current. The proximal portion of the plume is optically (and by extension thermally) opaque, therefore it will be an emitting source of TIR energy. Volcanic ash begins to fall out of suspension as it drifts further downwind, and a density threshold is reached, at which point ground upwelling TIR radiance is transmitted through the plume.

Volcanic ash presents the most wide-ranging volcanic hazard to both life and property (Folch and Sulpizio, 2010). The health impacts of volcanic ash have only recently been quantified (Horwell et al., 2006), and other studies have demonstrated the effects of ash particle size and chemistry as a health hazard (Horwell et al., 2003). Fine volcanic ash (< 15 μm in size) can enter the respiratory system of humans, with the fraction that is < 4 μm capable of causing chronic lung diseases such as silicosis (Horwell et al., 2006). In particular the potential toxicity caused by cristobalite fragments in volcanic ash is better understood, and it can present a long term hazard for people living proximal to an active volcanic center, particularly in cases where an eruption is quasi-continuous over a number of years (e.g. Soufrière Hills Volcano; Baxter et al., 1999). Owing to its density, significant ashfall can collapse the roofs of buildings, and it also poses a threat to the function of the electrical infrastructure of towns and cities (Wilson et al., 2012). There are also the well-documented hazards to aircraft, which include abrasion of windows and wing tips, damage to the ventilation systems, and possible ingestion, melting and subsequent cooling onto the engine turbine blades, which can cause engines to shut down (Casadevall, 1994).

Thermal infrared (TIR) remote sensing has become a widely used tool in the detection of volcanic ash clouds and the subsequent hazard monitoring. Methods currently employed rely on the interaction of ground upwelling radiance through the TIR transparent portion of the plume to detect the presence of ash and attempt to obtain particle size and density information. This allows clouds to be tracked over large distances, such as during the 2011 eruption of Puyehue Cordón-Caulle, where the drifting ash cloud was detected as far away as Australia and New Zealand (Rose and Durant, 2011). These analyses are routinely performed by Volcanic Ash Advisory Centers (VAAC) around the world with the aim of reducing the hazards posed to aircraft.

However, methods that employ these techniques are not able to retrieve information on a cloud that is optically opaque to TIR upwelling radiation. Therefore, alternative methods of ash quantification need to be determined.

The primary aim of this volume is to answer the question *"Does the nascent volcanic plume behave as a solid emitting surface in the TIR and can these emission be used to quantify the constituents within this portion of the plume?"* This is attempted by combining laboratory, computational and field methods in a unique way to study this region in depth for the first time. The theory presented that led to the development of this work is that an opaque plume will be the source of emitted energy in any pixel in which no ground-upwelling radiance is detected (Ramsey, 2016). If this is the case, then it can be analyzed using similar methods to those employed for ground/solid surfaces, using measurements of that surface's TIR emissivity. By analyzing the unique spectral signature of volcanic ash, a laboratory spectral library of ash types of different compositions was created to act as a series of "end-members", presented in chapter 2. These libraries are applied to data from the Advanced Spaceborne Thermal Emission and Reflection Radiometer (ASTER), due to its moderately high spatial resolution in the TIR portion of the electromagnetic (EM) spectrum, and its multispectral capability. Image data of volcanic ash plumes are analyzed to see if they first contain opaque plume bearing pixels. If so, they are processed using a linear spectral unmixing model (chapter 3; Ramsey and Christensen, 1998). This approach is advanced in chapter 4, which describes the development of a multispectral adaptation for a ground-based thermal camera. The aim is to develop a system that could be easily transported to a field site, and used to collect multispectral image data an erupting volcanic plume. By creating a multispectral dataset, the aim is to determine if emissivity spectra could be successfully derived. These spectra are compared to laboratory spectra of volcanic ash samples

to determine if plume composition is possible. Finally, chapter 5 discusses a model framework to determine the use of a backward trajectory model coupled with methods in geostatistics to constrain the source location of a disconnected volcanic ash plume (i.e., volcanic cloud). The aim is to develop a method that enables targeting of the ASTER sensor to the volcanic source, providing an increased frequency of critical image data of the eruption.

2.0 DEVELOPMENT OF A VOLCANIC ASH THERMAL INFRARED SPECTRAL EMISSIVITY LIBRARY

2.1 INTRODUCTION

Explosive volcanic eruptions produce plumes of ash, a complex mixture of glass, lithic and mineral fragments (Dingwell et al., 2012), ranging in size from < 2 mm to sub-micron scale (Rose and Durant, 2009; Wilson et al., 2012). These plumes are formed by the fragmentation of the parent magma, with higher degrees of fragmentation associated with higher viscosity magmas (Langmann et al., 2012). Coarser particles tend to fall out of suspension first and are deposited close to the volcano, whereas finer particles are capable of travelling a much greater distance from the volcano, and potentially in detectable quantities for remote sensing, as was seen during the 2011 Puyehue-Cordón Caulle eruption in Chile (Klüser et al., 2013). Volcanic ash varies in terms of particle size and composition, depending on the type of volcano, and the style of eruption. Therefore, an accurate assessment of composition is essential in characterizing the eruptive processes occurring.

TIR emission spectroscopy is a tool that is used to evaluate both the composition and particle size of geologic features (Walter and Salisbury, 1989; Rowan et al., 1991; Ramsey and Christensen, 1998). The distinctive vibrational features found within silicate minerals within the thermal infrared (TIR) portion of the electromagnetic spectrum, provide an invaluable analytical

tool. Furthermore, it has been shown that a mixed spectrum is the sum of the areal percentage of the materials comprising the mixture (Ramsey and Christensen, 1998). Therefore, with the correct end-member library and model, compositional determination is possible. Several spectral libraries exist for both reflectance (e.g. Clark et al., 2007; Baldridge et al., 2009) and emission (Christensen et al., 2000) spectroscopy. These are primarily pure mineral suites of differing particle size fractions. Spectral libraries are not restricted for use with laboratory data. They are resolved to the spectral resolution of satellite sensors that operate in the same wavelength region, and used to unmix spectra of image pixels to determine their constituent components. This has allowed the compositional mapping of both terrestrial (e.g. Ramsey, 2002; Zhang et al., 2005) and planetary datasets (e.g. Christensen et al., 2000; Hamilton et a., 2001).

In this chapter, a new spectral emission library for use with the Advanced Spaceborne Thermal Emission and Reflection radiometer (ASTER), the ASTER Volcanic Ash Library (AVAL) spectral library, is presented. The laboratory techniques used to create this library are described, as are the effects of sample composition on the TIR emission spectrum. The compositional variations found within the samples are discussed using both the hyperspectral resolution lab derived emission data, as well as stereoscopic microscope data to determine mineral composition and % glass vs crystals present.

2.2 BACKGROUND

2.2.1 Volcanoes Sampled

Samples of volcanic ash were obtained from selected volcanic centers, listed in Table 2-1. These were chosen because the eruptive material was available shortly after it was deposited and therefore free of weathering products. Furthermore, there are three instances where ash was sampled twice from different eruptions. This was done to observe any changes in compositional characteristics, which may have resulted from changes in the eruption mechanisms. This section also provides a brief background of the eruptive styles and products of these volcanoes. As more samples are collected and processed, they will be added to the library, with the eventual aim of spanning many different lithologies. This library is complimented by a crushed sample of obsidian, obtained from the Mono-Inyo domes complex, California. This sample serves as a proxy for a high silica glass end-member.

Table 2-1. List of ash samples available in the volcanic ash spectral library. Note that several samples were donated, thus the sample coordinates are not known.

Volcano Name	Collected/ Donated	Date of Collection	Coordinates (UTM)/Notes
Volcán De Fuego	Collected	02/24/2015	Trinidad Barranca, Volcán De Fuego, Guatemala (15P, 729744.46m E, 1597125.24m N)
Sakurajima	Donated	07/2013	Collected in July 2013 during IAVCEI meeting field trip, Sakurajima, Japan (coordinates unknown)
Sakurajima	Collected	11/01/2016	Arimura Lava Observatory, Sakurajima, Japan (52R, 659300.00m E, 3492284.00m N)
Santiaguito	Donated (Dr. Jessica Ball, USGS)	02/2011	El Brujo Dome, Santiaguito Volcano, Guatemala (coordinates unknown)
Santiaguito	Collected	03/07/2016	Opposite 2007 lava flow, Santiaguito, Guatemala (15P, 653738.00m E, 1626906.00m N)
Soufrière Hills Volcano	Donated (Dr. Jessica Ball, USGS)	02/2010	Belham Valley, Montserrat (coordinates unknown)
Mono-Inyo Craters	Donated (Dr. Michael Ramsey, Mark Price, U. Pitt)	07/2012	Mono-Inyo Craters complex, California, USA (exact coordinates unknown). Sample is made up of obsidian fragments which were subsequently crushed and sieved.

2.2.1.1 Volcán De Fuego

Volcán De Fuego (also known simply as Fuego) is located in Guatemala, 15 km to the southwest of the town of Antigua (pop. 25,000) and 40 km to the southwest of Guatemala City (pop. 2,200,000). It is a 3700 m high stratovolcano, which was created roughly 17,000 years ago. It forms part of the La Horqueta volcanic complex shown in Figure 2-1. This complex is made of 5 volcanic centers that decrease in age to the south, starting with Ancient Acatenango, followed by Yepocapa, Pico Mayor de Acatenango, La Meseta and Volcán De Fuego (Vallance et al., 2001). Fuego erupts on a frequent basis, making it one of the most active volcanoes in central America. Periods of low level strombolian activity, where eruptions last seconds to minutes can occur for years, which are then punctuated by paroxysmal sustained eruptions of lava and ash, and on occasion vulcanian/sub-Plinian eruptions with no observed concurrent lava effusion also occur (Lyons et al., 2010), such as the 1974 event described by Rose et al. (1978). These intermittent phases of low to high activity followed by periods of quiescence occur throughout historic time (Bonis and Salazar, 1973). The most recent eruption of Fuego occurred in June 2018, and produced an event similar to the large eruption of 1974, with pyroclastic flows deposited ~ 15 km from the volcano.

Eruptive material produced by Volcán De Fuego ranges from pre-historic andesites, to the high Al_2O_3 basalts and basaltic andesites seen today. Assemblages of eruptive material produced in 1974, 1999 and 2003 have shown that the composition is similar (Berlo et al., 2012). The primary mineral assemblages in this material consists of plagioclase feldspars, olivine, clinopyroxene and magnetite (Martin and Rose, 1981; Chesner and Rose, 1984; Buckland et al., 2018).

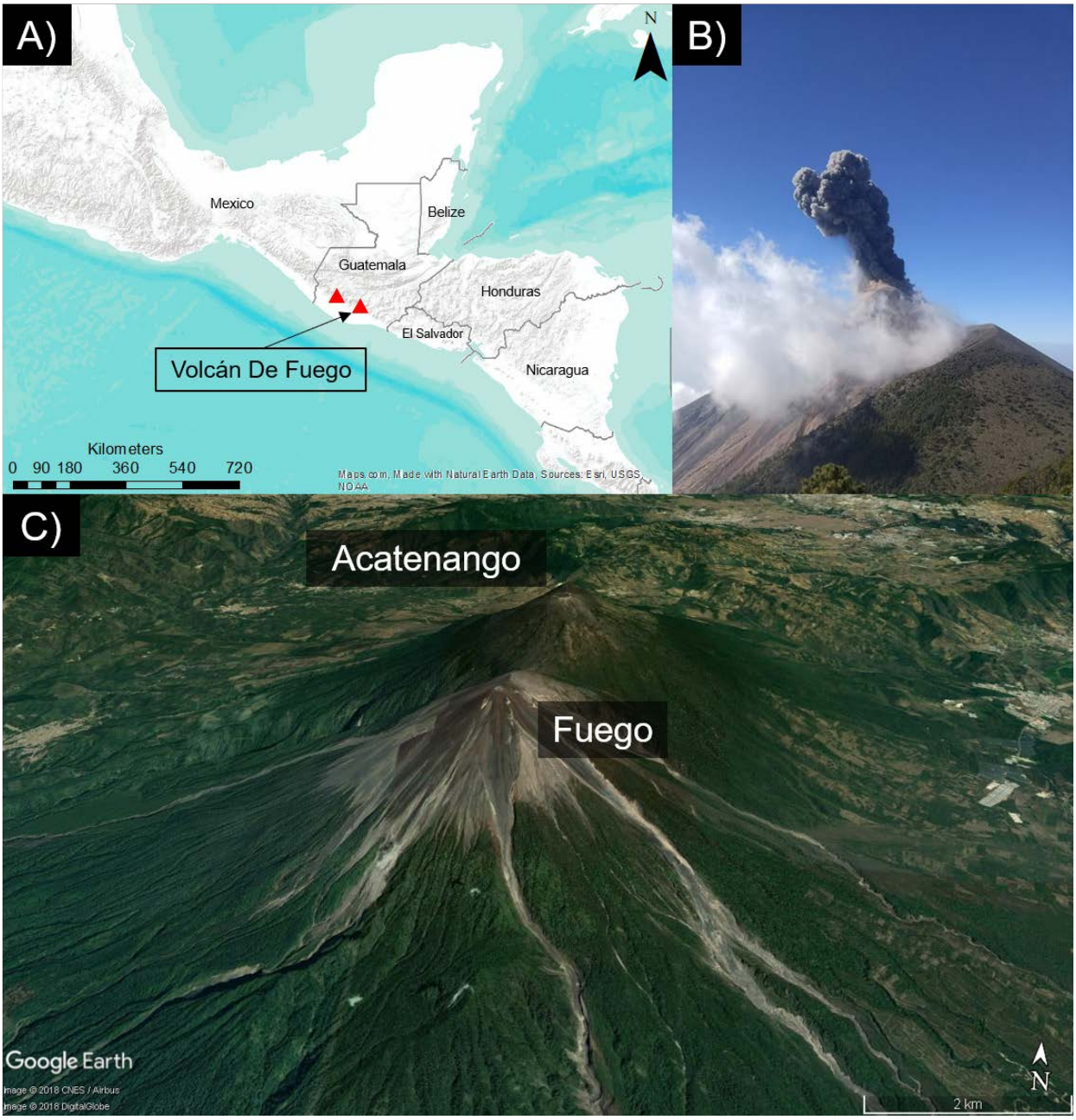

Figure 2-1 Location map and images of Volcán de Fuego, Guatemala. Panel B) shows typical strombolian eruptions that occur at the volcano.

2.2.1.2 Sakurajima

Sakurajima volcano is found in southern Japan on the island of Kyushu, close to the city of Kagoshima (population of ~1,000,000). It formed on the southern rim of the Aira caldera, which collapsed ~29,000 years ago (Biass et al., 2017), with the Sakurajima edifice forming ~13,000 years ago (Smith et al., 2018). This volcano has been through several distinct phases of the current eruption, with pauses ranging from months to years between each. The latest phase of activity began in 2006. Upon reactivation in 1955, Sakurajima produces regular vulcanian explosions and is considered Japan's most active volcano (Hirabayashi et al., 1982). This followed the last Plinian style eruption in 1914 (the Taisho eruption; Oishi et al., 2018). Two distinct summits exist at Sakurajima, Kitadake to the north and the Minamidake crater to the south. An additional vent, the Showa crater is to the south east of Minamidake crater (Figure 2-2).

Activity recorded since 2011 by Oisihi et al. (2018) is defined by frequent dilute plumes of gas and ash, interspersed with more energetic, ash rich eruption clouds. Roughly 80 eruptions per month on average were between May 2009 and April 2017 (Poulidis et al., 2018), However, being of lower energy, these eruptions are significantly lower risk for aviation, as plumes rarely ascend to > 5 km in the atmosphere (Smith et al., 2018).

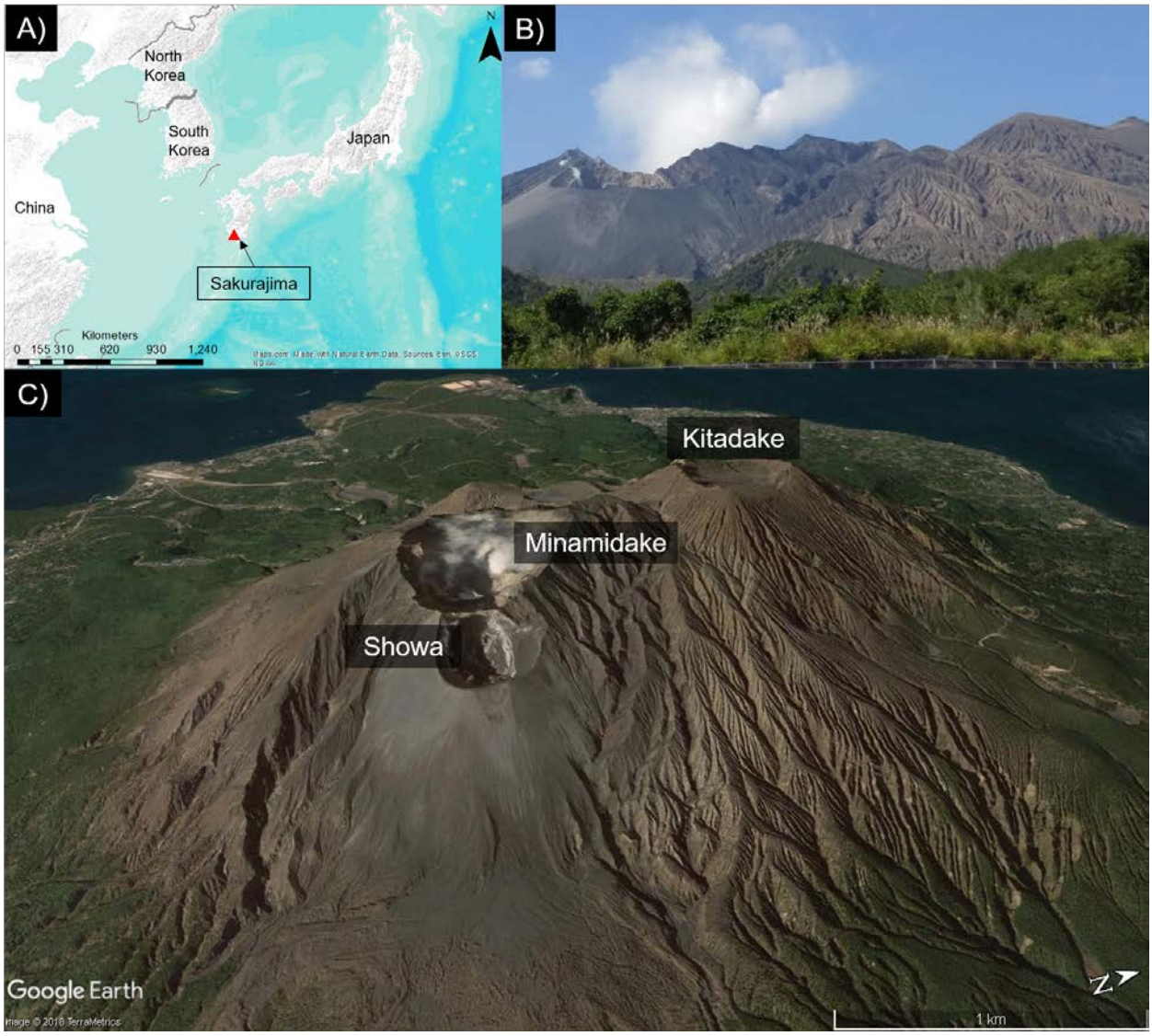

Figure 2-2 Sakurajima volcano. The Showa crater is observed to the left of the image in panel B). The DEM from GoogleEarth™ in panel C) shows both the Showa and Minamidake craters.

The magmatic system beneath Sakurajima is fed by one magma chamber at 10 km depth and located below the Aira caldera, with an additional chamber at 5 km (Iguchi et al., 2013). This chamber second chamber feeds activity at both the Minamidake and Showa craters, with a branched conduit feeding the latter. Compositionally, the erupted material can vary quite dramatically, with Kurniawan et al. (2016) reporting that the glass content ranges from 46.8 – 74.7 %, and plagioclase from 9.6 – 40.9 %. Common minerals found within the tephra are plagioclase feldspar, Ca-rich and Ca-poor clinopyroxene, orthopyroxene, and ilmenite (Miwa et al., 2009).

2.2.1.3 Santiaguito

The Santiaguito dome complex, located ~13 km from Quetzaltenango, a city with an estimated population of ~ 225,000 (Scott, 2013), is a volcanically active series of andesite - dacite lava domes that have formed in the 0.5 km^3 crater caused by the collapse of the south slope of Santa Maria volcano. Santa Maria erupted in October 1902, producing 8.5 km^3 of material (Harris et al., 2003). A period of repose occurred at the volcano until 1922, when lava began to extrude from the crater (Bluth and Rose, 2004) marking a period of continuous activity, consisting of further lava extrusion, passive degassing, small to medium sized eruptions of steam, gas and ash, small pyroclastic flows and rock falls, as well as lahars during the wet season (Scott et al., 2013).

The complex itself consists of four lava domes, El Brujo, La Mitad, El Monje and El Caliente (Figure 2-3). Thus far eight cycles of activity have been recorded since 1922 (Rose, 1972; Harris et al. 2003; Scott et al., 2013), with a new cycle being linked to an increase in extrusion rates. Activity has migrated across the complex, with Caliente dome the first to erupt, followed by Mitad, Monje, Brujo, and back to Caliente, where activity is ongoing. Lava flows

are dominated by a plagioclase feldspar and pyroxene groundmass, with phenocrysts of plagioclase pyroxene, titanomagnetite, and occasional amphibole (Rose, 1972; Scott et al., 2013). Ash samples have shown the presence of crystalline silica in the form of cristobalite as well as plagioclase crystals, together with abundant glass fragments (quantities not given; Jones and Gislason, 2008).

Eruptions at Santiaguito are described as “weak vulcanian” (Sahetapy-Engel et al., 2008). These occur regularly, previously reported on timescales between 30 minutes to 2 hours (Yamamoto et al., 2008), emitting ash for 30 – 60 seconds, followed by several minutes of gas release (Bluth and Rose, 2004; Holland et al., 2011). The top of the Caliente dome is crossed by a fracture system, which allows for degassing during repose periods. This cycle between repose degassing and explosive release of material was modelled by Holland et al (2011) as the ascent of magma experiencing strain on the conduit walls, allowing brittle failure to open a fracture network that provides gas the ability to decompress explosively.

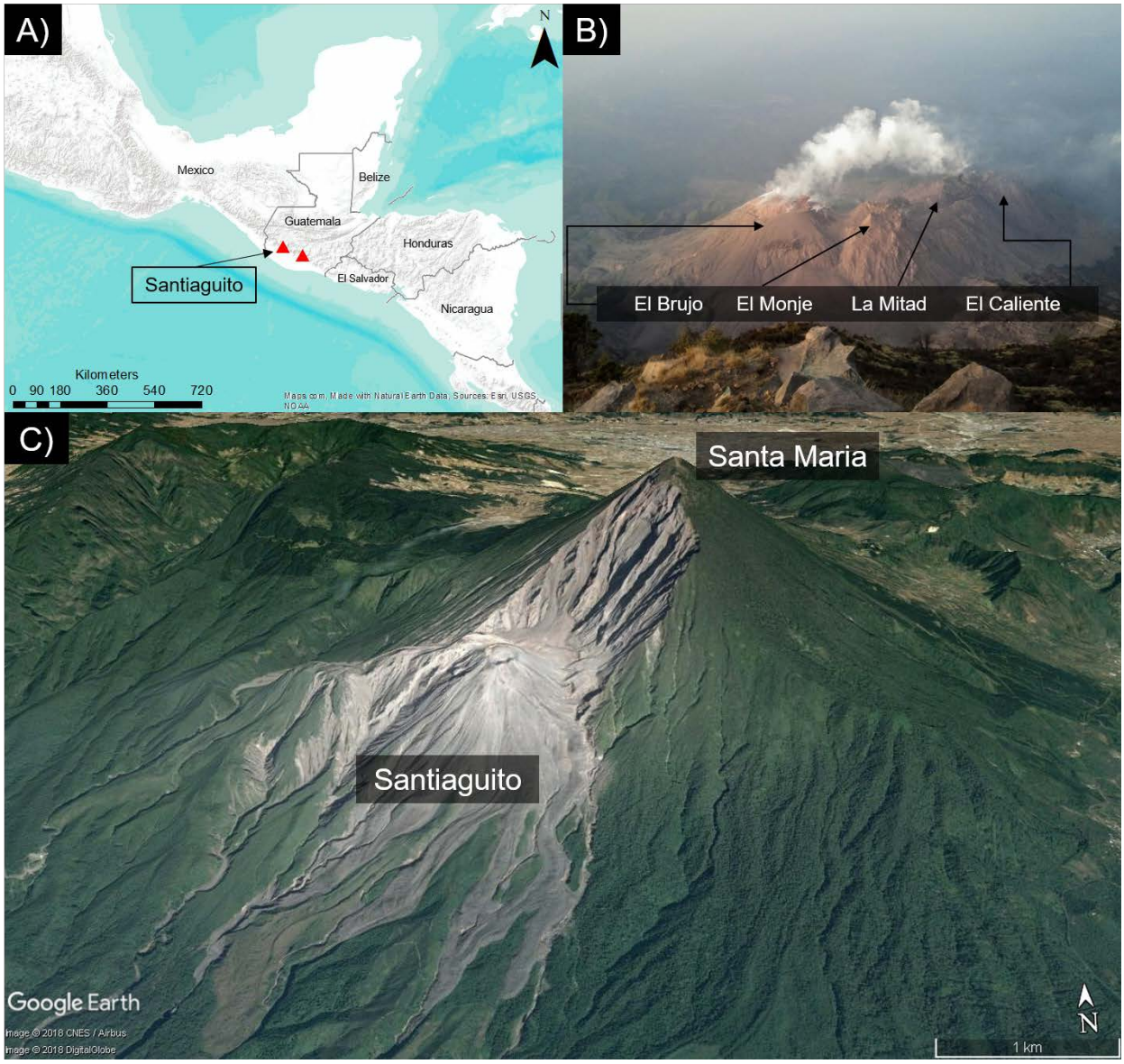

Figure 2-3 Santiaguito volcano as seen from the Santa Maria peak in B), and a GoogleEarth™ DEM in C). The photo in B) was taken on 1 March 2018. The El Caliente dome is to the far left and can be seen passively degassing. From right to left in the photograph, the domes are El Brujo, El Monje, La Mitad and El Caliente. Panel C) shows 1902 collapse scar from Santa Maria more clearly, in which the Santiaguito domes formed.

2.2.1.4 Soufrière Hills Volcano

The Soufrière Hills Volcano (SHV) is located on the island of Montserrat in the Lesser Antilles island Arc in the Caribbean (Murphy et al., 2000). The island has four volcano centers, Silver Hill, Center Hills, the Soufrière Hills and the south Soufrière Hills, which range in age from 4.3 Ma to the present (Sparks and Young, 2002). The SHV volcano was most active between 24 and 16 Ka, with a summit crater that was formed ~ 4,000 Ka (Young et al., 1998). In historical time, an eruption was recorded 323 ± 50 years BP that partially filled this crater with a small ($45 \pm 15 \times 10^6$ m^3) andesitic lava dome (Young et al., 1998). Three years of seismic activity beginning in 1992 foreshadowed the next phases of volcanic activity, as phreatomagmatic events occurred beginning on 18 July 1995, with growth of an andesite lava dome observed around 15 November 1995 (Sparks et al., 1998). This period of dome growth was accompanied by Vulcanian to sub-Plinian eruptive activity, of which there have been over 100 Vulcanian explosions recorded (Voight et al., 1999; Cole et al., 2014). To date there have been five phases of lava extrusion at the volcano (Wadge et al., 2014).

The composition of the material produced from the volcano received considerable coverage in the literature, particularly the rocks produced by Phase 1. Christopher et al., (2014) summarized the work, and provides and overview of the material produced from 1995 – 2010. Bulk rock analysis revealed that the eruptive material is crystal rich (33-63 vol% phenocrysts). This mostly consists of plagioclase feldspar, amphibole, orthopyroxene, with minor Fe-Ti oxides. The groundmass of these lavas is predominantly microcrystalline but can contain ~ 25 % glass that is rhyolitic in composition, from those samples erupted quickly. These samples also contain fragments of more mafic material, leading to the assumption that the andesite magma mingled with more mafic material present at depth (Wadge et al., 2014). Samples of ash

collected from the volcano have shown similar dominance of feldspars as part of the mineral assemblage but have also received particular attention for their concentrations of cristobalite (Baxter et al., 1999; Horwell et al., 2003; Mangan et al., 2017).

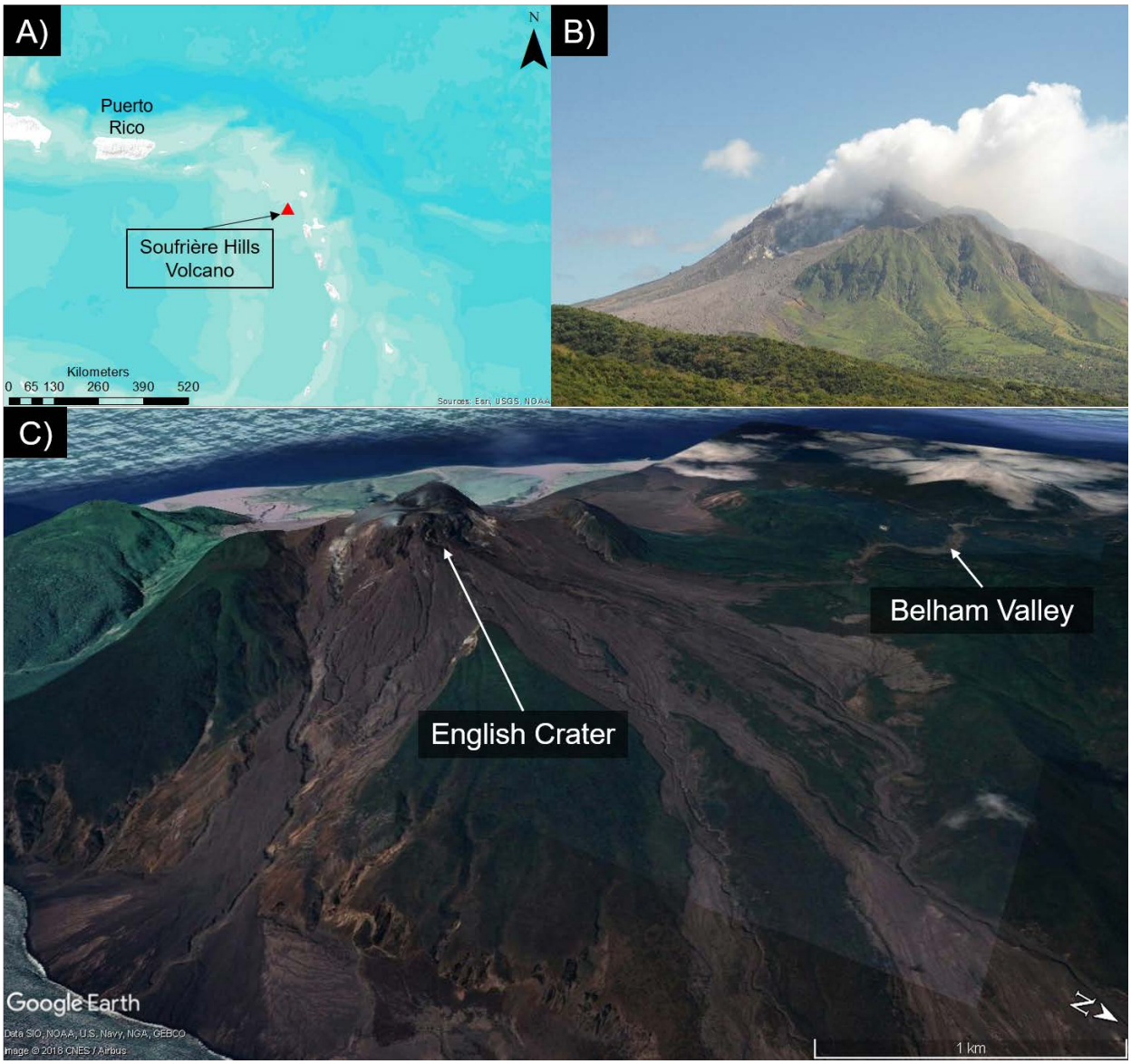

Figure 2-4 SHV Volcano, the photograph in B is the volcano viewed from the Montserrat Volcano Observatory. The collapse scar formed during the 2010 eruption can be seen spreading from the center to the lower left of the image. Multiple collapses of the volcanic dome have occurred during the eruption and the deposits from these can be seen in C).

2.2.1.5 Mono-Inyo Domes and Craters

The Mono-Inyo domes and craters are located to the north of the Long Valley caldera, California. Since the 0.77 Ma eruption of the Bishop Tuff and the formation of the caldera, magmatic activity in the region shifted to the north into the Mono basin (Bray et al., 2017). The Mono domes consist of a series of ~ 30 overlapping domes, coulees and craters, in a 17 km long arcuate feature, whereas the Inyo domes are a 10 km discontinuous line of approximately 6 magmatic and 15 phreatomagmatic eruptive centers (Miller, 1985; Bailey, 1989). This sequence of vents has erupted multiple lithologies, with basalts and andesites in the Mono Basin, between 40 and 13.3. Ka, and high-silica rhyolites at Mono domes between 40 – 0.6 Ka, and low-silica rhyolites between 5 and 0.6 Ka (Bailey and Hill, 1990). The most recent activity in the Inyo chain is estimated at 550 years ago, which formed the three largest of the Inyo domes – Obsidian, South Glass Creek and South Deadman – in addition to the explosion craters at Deer Mountain (Fink, 1985).

The samples in this study are obtained from the North Coulee of the Mono domes. The region is described by Price et al. (2016). The upper surface is unevenly mantled by layers of pyroclastic material. Much of this was poorly sorted, with the majority of clasts and boulders being pumaceous, with obsidian quantities ranging from 10 – 30 % at observed sites.

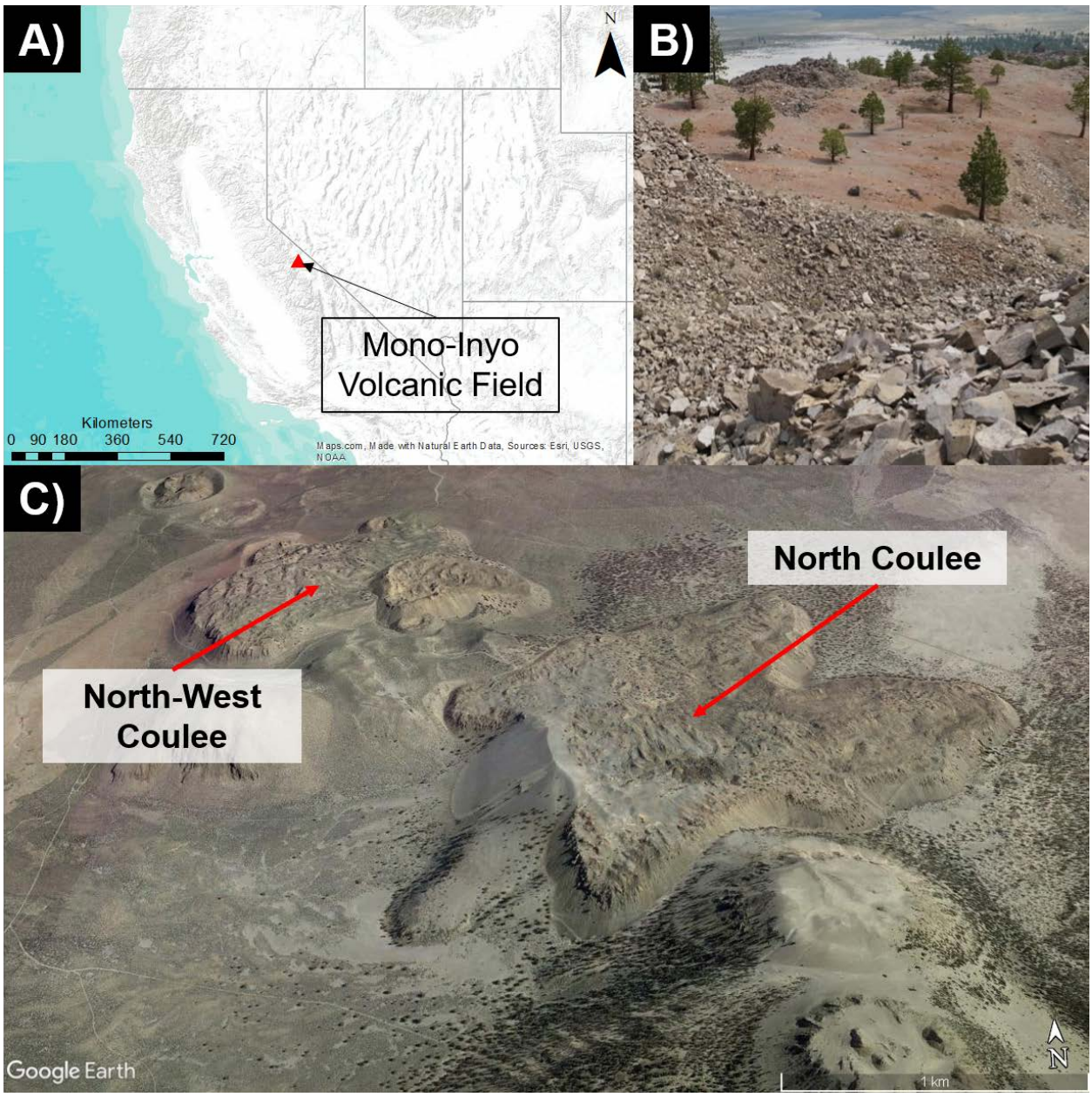

Figure 2-5 Mono-Inyo volcanic chain, located in California, USA. The photograph (http://ivis.eps.pitt.edu/Project6.html) in B is from the North Coulee, which is shown in GoogleEarth image in C). This is the area that was sampled for the crushed obsidian end-member sample.

2.2.2 Principles of emission spectroscopy

Before discussing the acquisition of emission spectra, it is important to understand the fundamental principles. Emissivity is a unitless term that describes the efficiency of radiant energy emitted by a surface, compared to that of a perfect emitter (i.e., a blackbody) at the same temperature. A blackbody is a theoretical reference of an object that is a perfect emitter at all wavelengths. It is the equation of Planck, that can be used to determine the radiant energy at each wavelength for a blackbody at a given temperature, expressed as,

$$L_{(\lambda,T)} = \varepsilon_\lambda B_{(\lambda,T)} = \varepsilon_\lambda \left\{ \frac{C_1 \lambda^{-5}}{\left[\exp\left(\frac{C_2}{\lambda T}\right) - 1\right]} \right\} \quad (2.1)$$

where L is radiance, λ is the wavelength, T is the temperature (in Kelvin), B is the blackbody radiance, ε is the emissivity, C_1 is equal to 3.74 x 10^{-16} W m^2 and C_2 is equal to 0.0144 m K. Radiant energy is derived from integrating equation (1) over all wavelengths and proportional to the fourth power of the absolute temperature (in K). This is known as the Stefan-Boltzmann equation (after Lyon, 1965),

$$L_{BB} = \varepsilon \sigma T^4 \quad (2.2)$$

where L_{BB} is the radiant energy emitted from unit area by a blackbody, σ is the Stefan-Boltzmann constant, 5.67 x 10^{-8} $w^{-1}m^2K^4$. Wien's displacement law is used to determine the temperature at which peak radiance occurs. This is an inverse relationship, described as,

$$\lambda_m = \frac{a}{T} \quad (2.3)$$

where λ_m is the wavelength where radiance maximum occurs, *a* is Wien's constant, 2.898 x 10^{-3} m K, and *T* is the temperature in K.

The relationship between radiant energy, wavelength and temperature is described as follows. For a blackbody, emissivity is constant at 1.0. Terrestrial materials do not generally behave this way, however. They produce emissivity spectra that exhibit features less than 1.0 at discreet and well known wavelengths known as absorption bands (Lyon, 1965). This behavior is governed by the vibrational modes of atoms within crystal lattices as bending and/or stretching of their structures occurs (Salisbury and D'Aria, 1992; Christensen and Harrison, 1993; Wenrich and Christensen, 1996; Hamilton et al., 1997; Ramsey and Christensen, 1998). Of interest to this study are those vibrational features that occur between 5 – 25 μm. This is important particularly for silicate rocks, such as those produced by volcanic processes, as these materials produce fundamental spectral features in this range, allowing it to be used as a diagnostic tool for composition. The primary absorption feature for these materials is termed the Restrahlen band. This occurs just long ward in wavelength from the Christiansen frequency, the wavelength at which the maximum emissivity occurs where the refractive index (n) of the material approaches the refractive index of its surrounding medium. The restrahlen band absorption is caused by a high absorption coefficient (k) for a material, which increases surface scattering, seen in reflectance spectroscopy as a reflectance high at that wavelength (Nash et al., 1993).

This study is concerned with volcanic ash particles, which have a range of sizes, but with many in the < 63 μm diameter range. This is important because as particle size decreases, the grain-photon interactions become more complex, as a result of grain boundary scattering (Wenrich and Christensen, 1996). A decrease in particle size causes a shallowing of the Restrahlen band absorption feature as a result of volume scattering, but additional features can

then arise. These are commonly termed transparency features, which commonly occur in weakly absorbing intraband regions (Ruff and Christensen, 2002). These regions are where the absorption coefficient of a material is very low, and the index of refraction is close but greater than unity. This allows light to interact with more particles, thus producing greater TIR reflectance (or lower emissivity) in these regions (Wald and Salisbury 1995; Hamilton et al., 1997; Ruff and Christensen, 2002). An example of this is shown in Figure 2-6. The exact position of this transparency feature may also be related to the composition of the material observed (Maturilli et al., 2008).

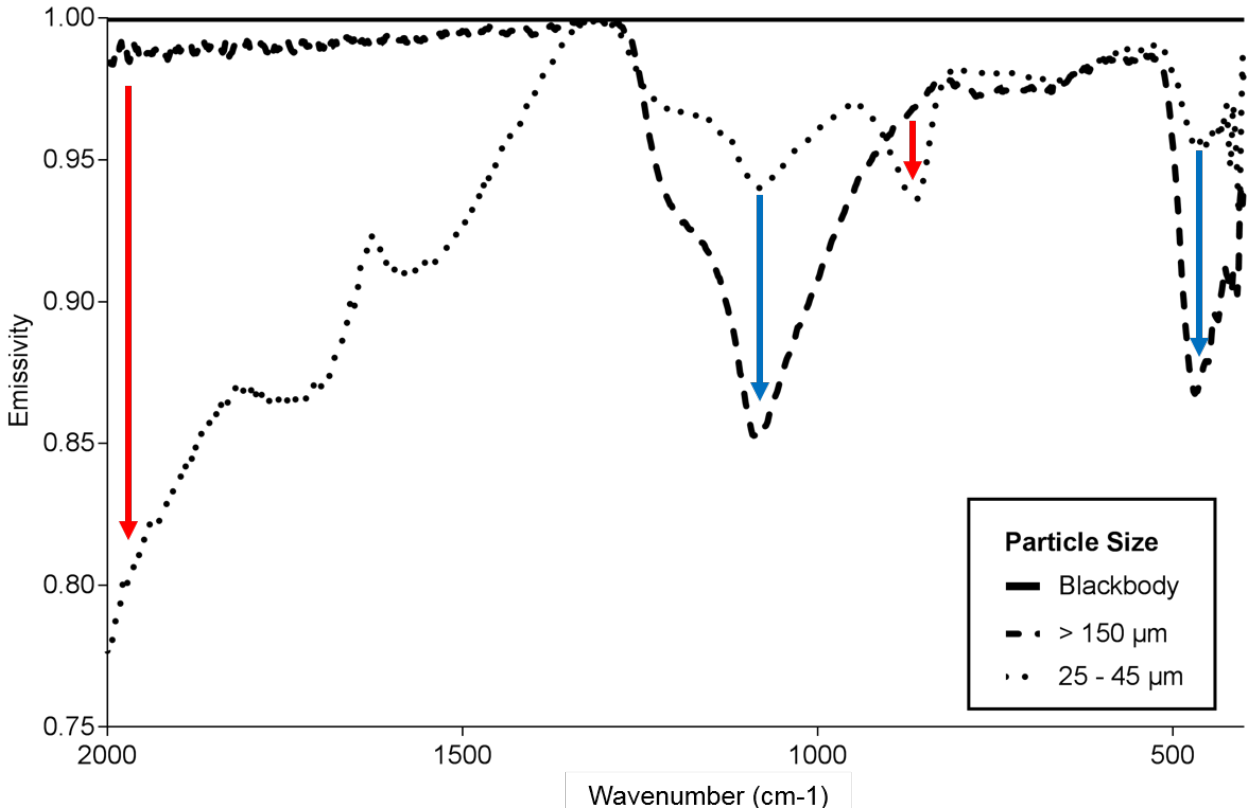

Figure 2-6 Comparison of a perfect blackbody emitter, the largest crushed obsidian fraction, and the 25 – 45 µm fraction. Spectral features in the obsidian are obvious compared to the standard. Additionally, arrows mark the spectral differences between the large and fine fractions. Blue arrows denote absorption features, whereas red arrows represent transparency features.

2.3 METHODS

2.3.1 Sample Preparation and Separation

Ash samples were separated into different size fractions by dry sieving. Samples were left in a drying oven for 12 hours, and then sieved to > 150, 63 – 150, 45 – 63 and < 45 µm. The > 150 µm fraction was washed with acetone to remove any clinging fine-grained particles that would reduce the spectral contrast of the absorption bands due to surface scattering, which will cause transparency features (Salisbury and Wald, 1992). The decrease in spectral contrast of the primary absorption feature (i.e., Restrahlen band) is attributed to an increase in the number of surface reflections. This increases the number of photons scatter away from the detector producing less detected reflectance or higher emissivity (Hays and Mustard, 1997; Ramsey and Christensen, 1998). Below 63 µm is where particle size affects the linearity assumption of spectral mixing (Ramsey and Christensen, 1998). However, analysis of these size fractions is still viable, as linearity remains true provided there is an appropriate end member library at that particle size.

For those particles of ash < 45 µm, a different method of particle separation was needed. This was done using a Microorifice Uniform Deposit Impactor (MOUDI; shown in Figure 2-7), described by Marple et al., (1991) at the Air Quality Laboratory, Carnegie Mellon University. The property which determines the collection of particles is the Stokes number, *St*,

$$St = \frac{\rho_P C V_O D_P^2}{9\mu W} \tag{4}$$

where ρ_P is the particle density, C is the slip correction, V_o is the average air velocity at the nozzle exit, D_P is the particle diameter, μ is the air viscosity and W is the nozzle diameter. This is used to predict whether a particle will hit the impaction plate or remain entrained in the air flow. The MOUDI is a type of inertial impactor, which draws air through the system. The flow rate can be adjusted so that different particle size fractions can be collected on the different stages, thus altering the V_o term in equation 4. The flow rate used for this work was 15 L min $^{-1}$, which allows the ash particles to be subdivided into three size fractions, 25 – 45 µm, 8 – 25 µm and < 8 µm. The sample is placed within a chamber and compressed air introduced, creating a particle suspension that is transported into a dust suspension chamber. A second air pump is used to draw air out of the dust suspension chamber and into the MOUDI system. A series of aluminum foil impaction plates are set on top of each MOUDI stage. These stages are mechanically rotated to allow for a uniform deposition of particles across the substrate once the ash enters the MOUDI inlet. Depending on the aerodynamic radius of the particle and the size of the cut point, finer particles will remain suspended whereas larger particles will impact onto the substrate and later collected. This was performed several times for durations of 15 – 20 minutes. Each sample was collected by mixing it with acetone to remove it from the substrate upon collection.

Figure 2-7 The MOUDI apparatus as used at the Air Quality Laboratory, Carnegie Mellon University. A) Shows how the equipment is set up fully for laboratory separation. Air is supplied and regulated to the appropriate flow rate before entering the beaker (shown in B), where the ash sample is suspended. It is then drawn through in the dust suspension chamber before entering the MOUDI stages shown in C. A pump attached to the base of the final stage is used to draw the air and suspended particles through the stages.

2.3.2 Collection of emission spectra

Emission spectra from each of the samples were collected in the University of Pittsburgh spectroscopy laboratory. Modifications of the existing equipment was performed in 2017, based upon the designs used by Ruff et al. (1997). This is shown in Figure 2-8. To prepare the samples for spectral measurements, they were placed in 3 cm diameter copper sample cups, and the placed in a drying oven at 80^{o}C. The sample itself is not levelled or compressed to avoid a preferential orientation of the grains, which could result in complicating spectral effects.

The emission spectrum of each sample was acquired using a Nicolet Nexus 670 FTIR Spectrometer, following the methods outlined by Ruff et al. (1997). The laboratory glovebox is adjacent to the spectrometer and accommodates two experiments - the standard temperature environmental chamber, and a micro furnace for high temperature experiments. These experiments are on a sliding platform so each can be positioned directly under the collimating mirror, which directs the emitted energy into the spectrometer. The glovebox and spectrometer temperature and humidity are monitored constantly using a hygrometer. If the relative humidity rises above 1%, experiments are halted, and the nitrogen purge used to scrub the air of water vapor. The spectrometer uses and mercury cadmium telluride (MCT-B) detector that is cooled with liquid nitrogen before spectra are acquired to improve the detection threshold. MCT-B detectors have a higher signal to noise ratio compared to uncooled deuterated triglycine sulfate (DTGS) detector (Kempfert et al., 2001). After liquid nitrogen is introduced into the detector dewar, the equipment is left for ~ 20 minutes to allow for complete cooling and thermal equilibration.

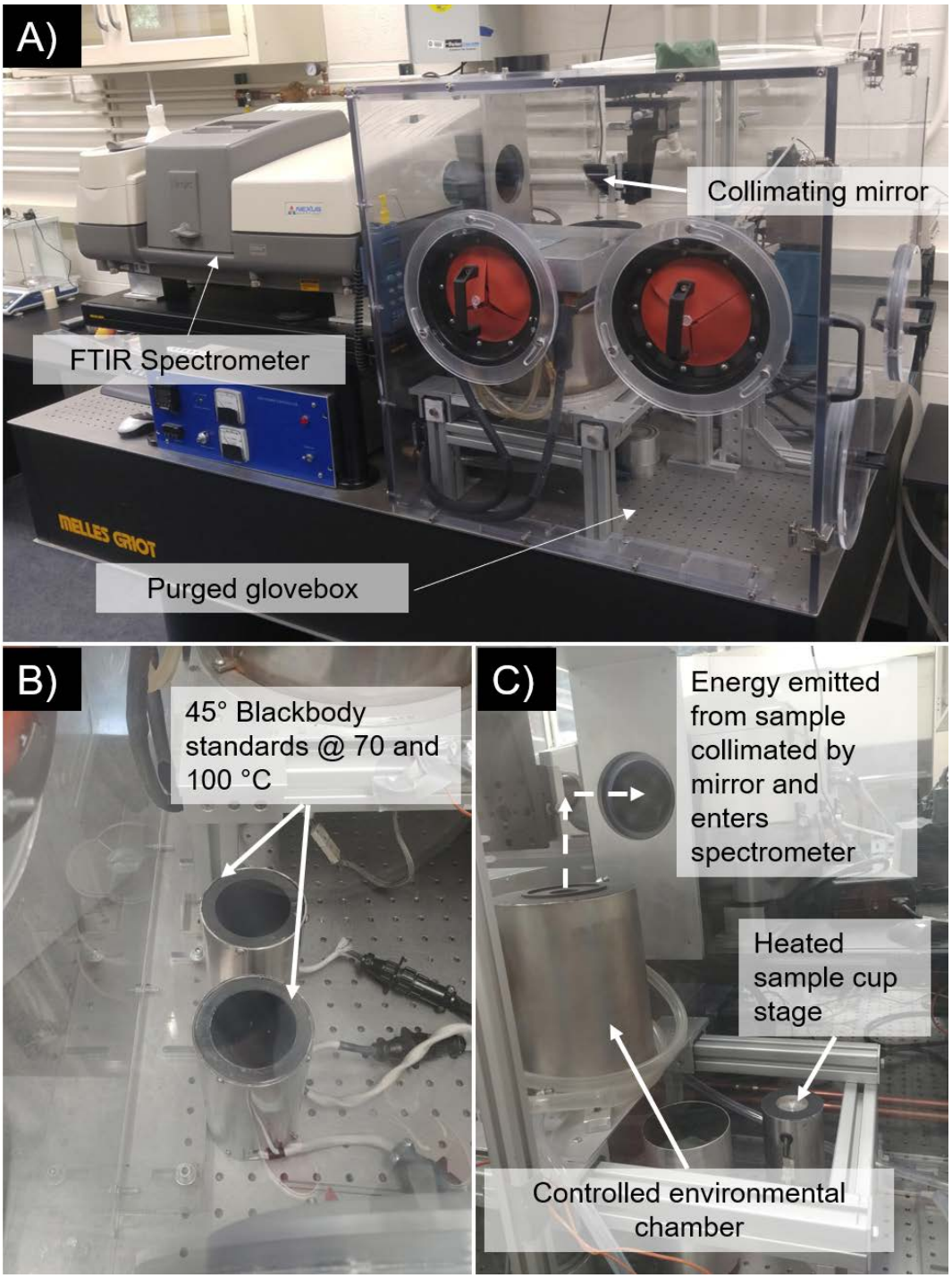

Figure 2-8 Infrared spectroscopy laboratory at the University of Pittsburgh, redesigned and calibrated during the 2016/17 academic year.

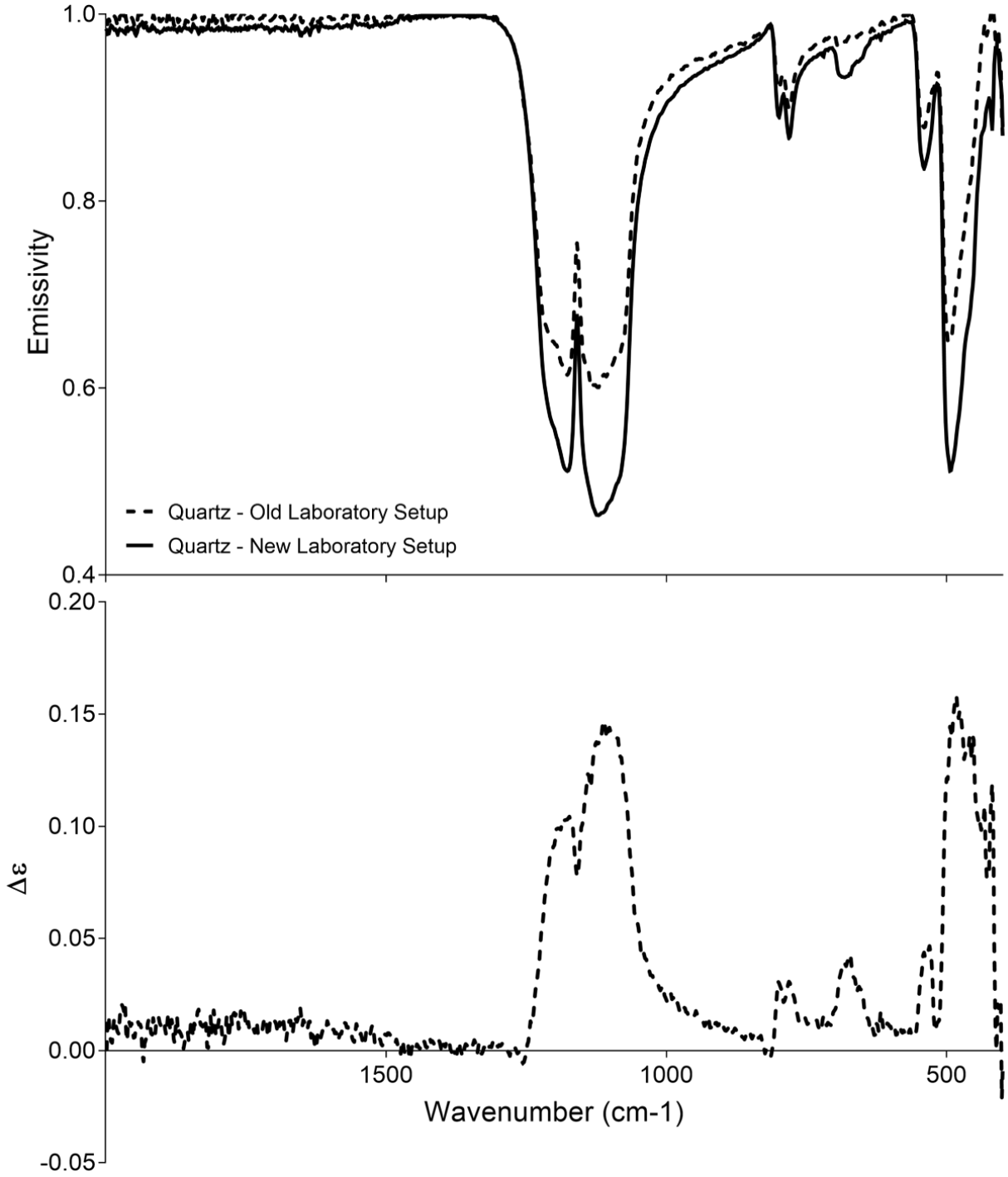

Figure 2-9 Upper panel; comparison between 710 – 1000 µm particle size quartz spectra, and the difference between the two (bottom panel). There is a distinct increase of the restrahlen band absorption depth between the old and new laboratory setup. This is the result of misalignment of the environmental chamber and mirror causing incomplete removal/correction of downwelling blackbody energy from other sources.

This method of spectral acquisition uses the energy from the sample as the source. This is described by Ruff et al. (1997) using the following equation;

$$\varepsilon_{samp} = \frac{\frac{V_{meas}}{F} - B_{env} + B_{inst}}{B_{samp} - B_{env}} \quad (2.5)$$

where, ε_{samp} is the emissivity of the sample, V_{meas} is the measured voltage, F is the calculated response function of the spectrometer, B_{env} is the environmental energy B_{inst} is the instrument energy, and B_{samp} is the sample radiance. The instrument response function is calculated by collecting two blackbody measurements, one at 70 and the other 100 oC. These are custom made 45 ˚ cone blackbodies, which are coated with a high emissivity paint, which closely approximates a perfect blackbody.

The instrument response function (Figure 2-10) can be described as the conversion factor between detector and sample outputs. This varies with wavelength, so a correction must be calculated and applied over the entire spectral range. The blackbody measurements are used for this as well as the voltage measured by the spectrometer for each of the blackbodies. The response function equation is,

$$F = \frac{V_{bb}(T_1) - V_{bb}(T_2)}{B_{bb}(T_1) - B_{bb}(T_2)} \quad (2.6)$$

Both the spectrometer and the attached glovebox are purged in order to remove any atmospheric water vapor and CO_2, both of which have spectral features in the TIR.

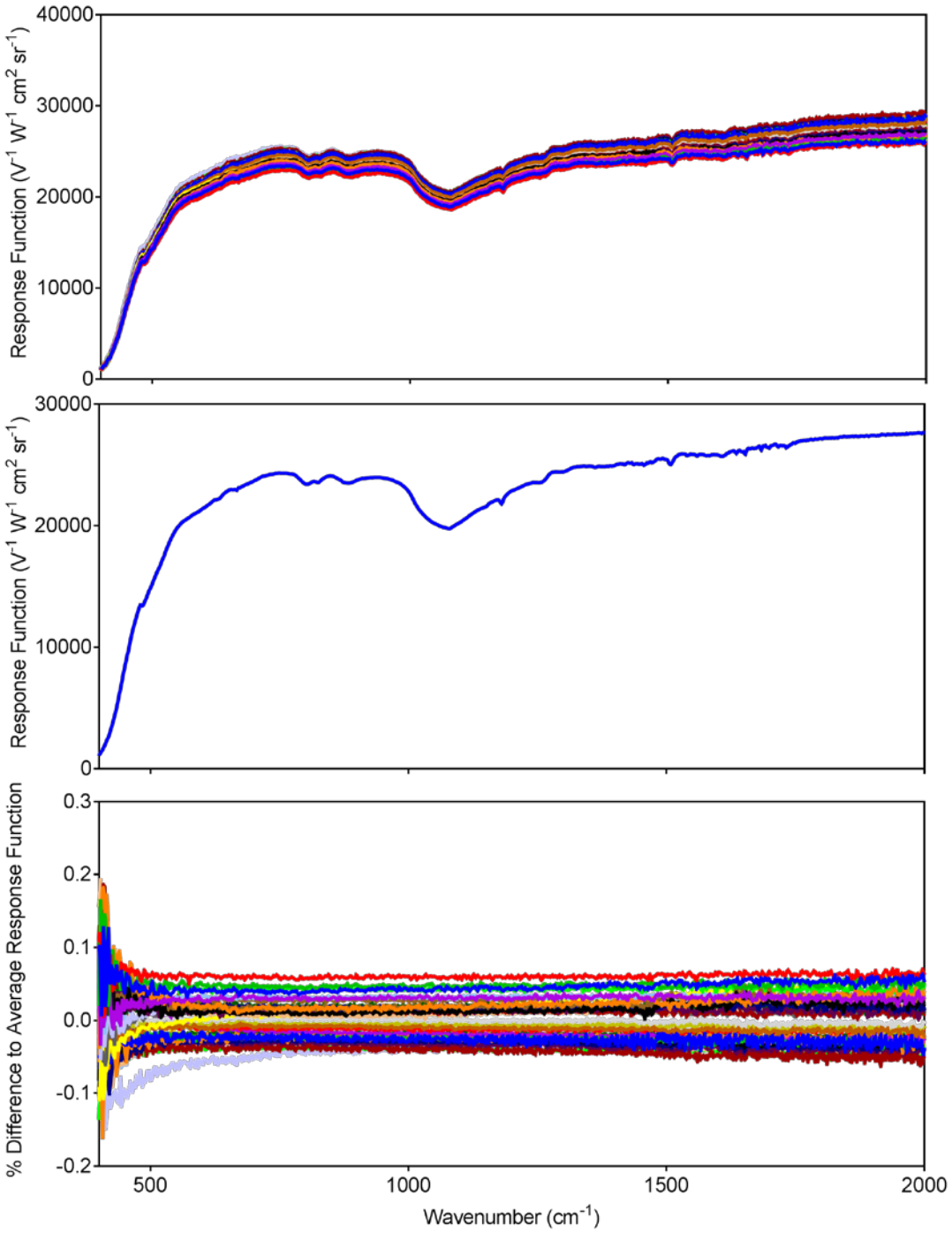

Figure 2-10 (Top) Thirty seven instrument response functions obtained between 21 July and 27 November 2017; (Middle) The mean response function derived from the measurements in the top panel; (Bottom) The difference between each response function and the mean expressed as a percentage. The overall variation is less than 1 %, with the standard deviation of this calculated as 0.174 %.

The sample cup containing the desired ash fraction sample is removed from the oven and placed onto a heated stage, which is left for several minutes to allow the sample to thermally reequilibrate. Furthermore, heating the sample above background temperature increases the signal to noise ratio of the measurement (Christensen et al., 2000). The heated sample is raised up into a thermally-controlled chamber maintained at 25 ^{o}C, which reduces the amount of reflected energy from the surrounding environment. The final spectrum is obtained by averaging 512 individual scans of the sample, and processed using the emcal2 program within the DaVinci software, created by the Mars Space Flight Facility at Arizona State University (Edwards et al., 2011).

Because this was a modified equipment setup, the spectral response function of both these measurements, and also emissivity spectra of two laboratory standards (quartz and obsidian) were taken to determine the variation in spectral measurements between each use. Once each volcanic ash spectrum was obtained, is was reducing to five-points (identical to the ASTER TIR channels) and added to the AVAL spectral library. The error for each emissivity spectrum was also determined, by calculating the noise equivalent delta emissivity (NE$\Delta\varepsilon$). This was approximated by analyzing the 100^{o}C standard blackbody as a sample and subtracting the that sample spectrum from that of a perfect blackbody emitter (Figure 2-11).

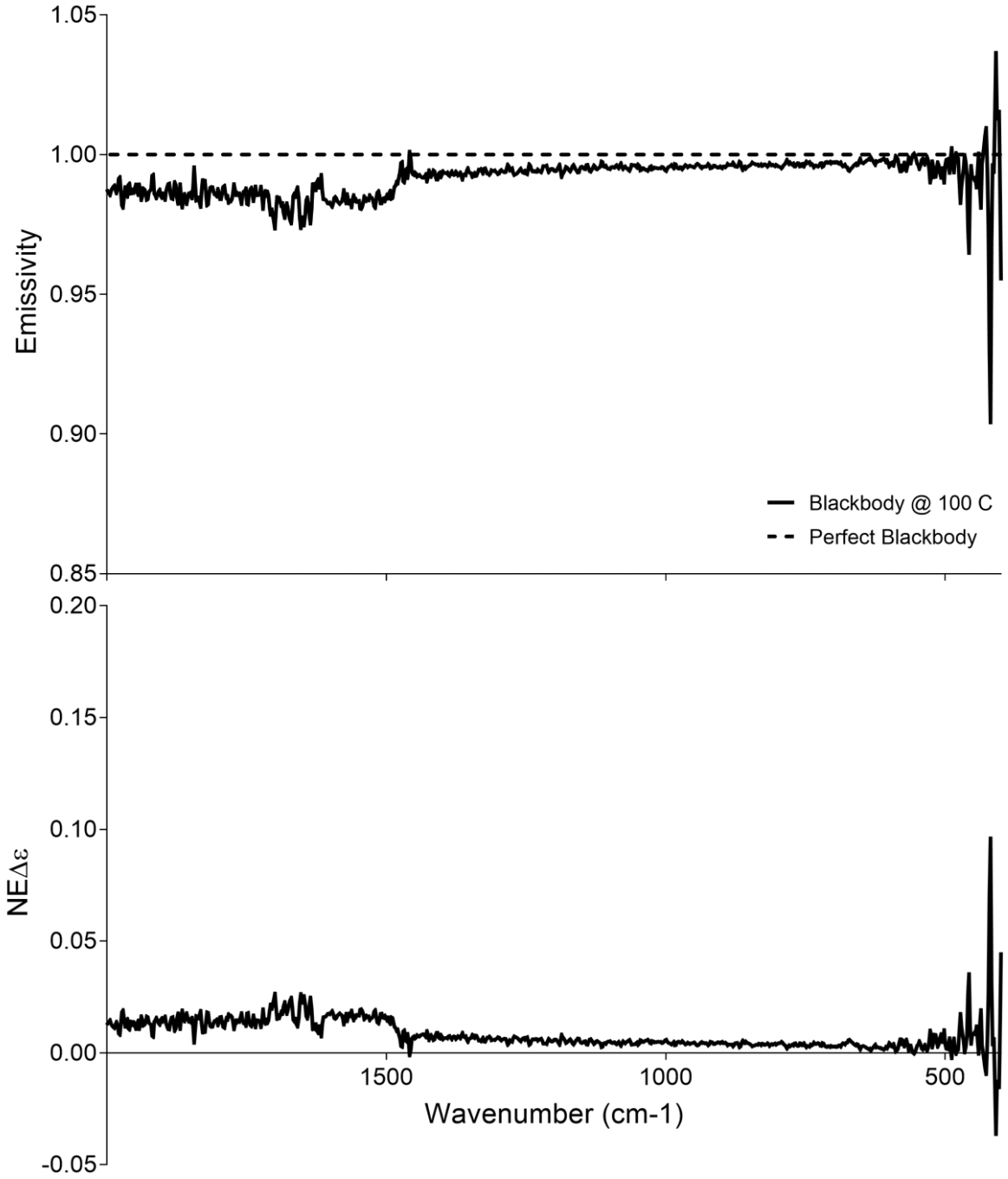

Figure 2-11 Upper panel; Laboratory blackbody run as a sample in the emission spectroscopy laboratory compared with that of a perfect blackbody. Lower Panel; NEΔε estimated by subtracting the laboratory blackbody from a perfect blackbody (ε=1). The overall error is 0.833 %, with a standard deviation of 0.740 %. Of importance to this study is the error found in the ASTER wavenumber region (~ 1250 – 833 cm^{-1}). Here the NEΔε is 0.464 % with a standard deviation of 0.009 %.

2.3.3 Optical Microscopy

An optical mineralogical examination of 2.5 g of each volcanic ash sample was undertaken by RJ Lee group (Monroeville, PA). The sample was analyzed, using both plain and cross polarized light. Each was immersed in an oil with a refractive index of 1.550 and from this, an estimation of the composition was made as well as the % glass versus crystal content. The full report produced can be found in Appendix A.

2.4 LABORATORY DATA

The following plots show both the hyperspectral and AVAL spectra for each ash sample. A brief description of each is provided. Whereas spectra are obtained between 2000 and 400 cm^{-1} and are shown in Figure 2-12, only the region between 1250 and 833 cm^{-1} is given for the remaining spectral plots, to better compare the laboratory measurements to the ASTER TIR resolved AVAL spectra. Furthermore, the NE$\Delta\varepsilon$ value that corresponds to each ASTER channel is shown in the AVAL spectra as error bars. This was calculated by averaging the NE$\Delta\varepsilon$ $\pm$ 100 cm^{-1} either side of the central ASTER band wavenumber. These give an indication of the repeatability of these spectra, and whether any significant overlap exists that would limit their suitability for use with ASTER TIR orbital data.

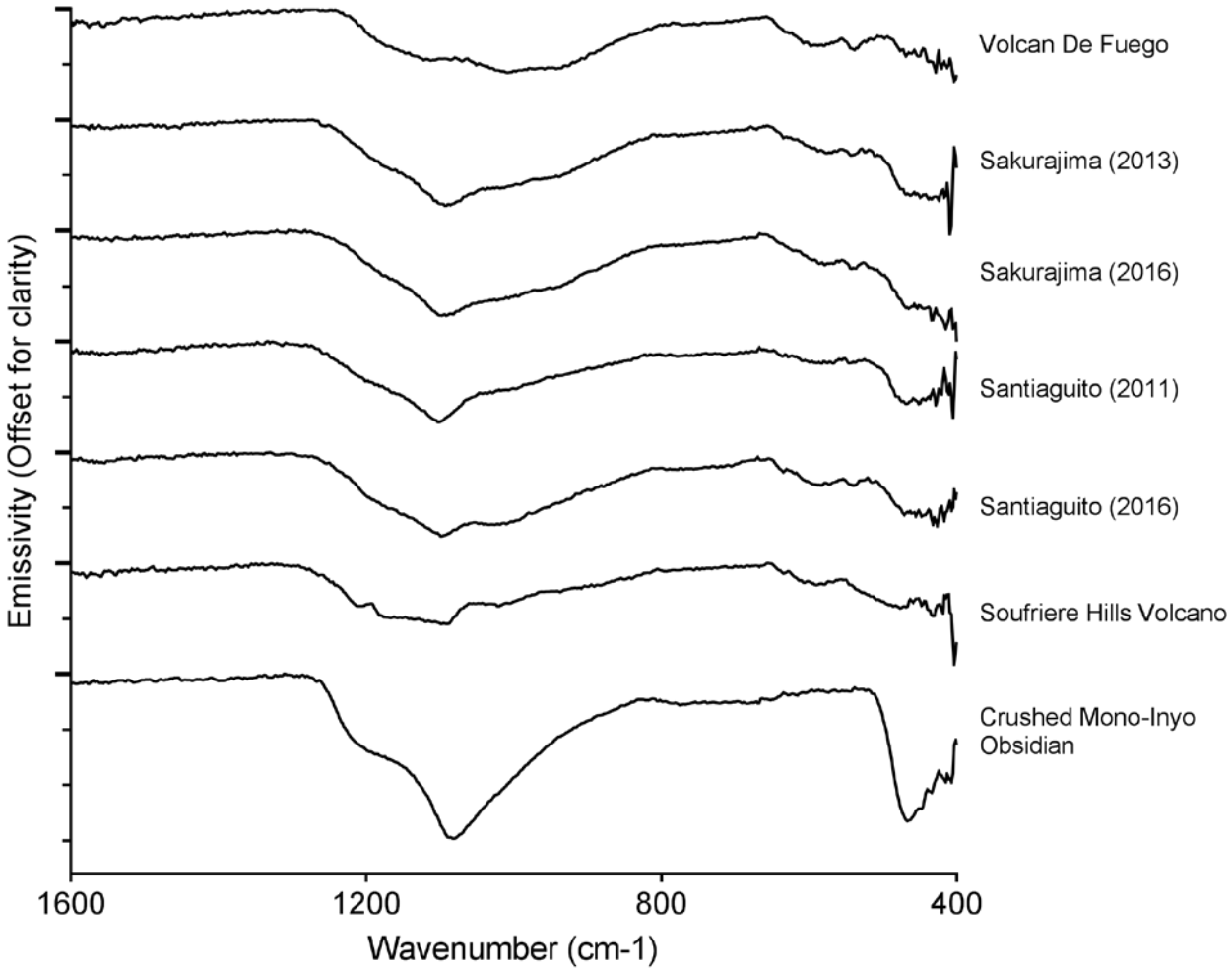

Figure 2-12 > 150 µm fraction TIR emission spectra of the seven samples prepared for this study (to highlight compositional variability). Each y-axis tick mark represents an emissivity of 0.05, with the bold dashes denoting an ε = 1.0. Each sample is distinct, with several different compositions present.

2.4.1 Fuego 2015

This sample of volcanic ash was taken from the Trinidad barranca on February 24, 2015, following a pyroclastic flow from Volcán De Fuego on February 15. There is a broad Restrahlen feature present between 8 and 10 µm (shown in Figure 2-13), which is indicative of the presence of plagioclase feldspar (Millam et al., 2007). At ASTER TIR resolution, this primary absorption feature is still visible, with the emissivity minima occurring in ASTER Band 13 (10.567 µm). Ash fractions at < 63 µm have a second absorption feature that causes the emissivity spectra to cross over between 11 and 12 µm. This is a previously described transparency feature, which is present in both hyperspectral and AVAL. The presence of large quantities of plagioclase feldspar was confirmed in the optical data, with this mineral phase comprising 76 % of the sample. The glass content of the sample was the lowest of the seven samples, at 20 %. Minor amounts (< 2 %) of olivine and amphibole are also present.

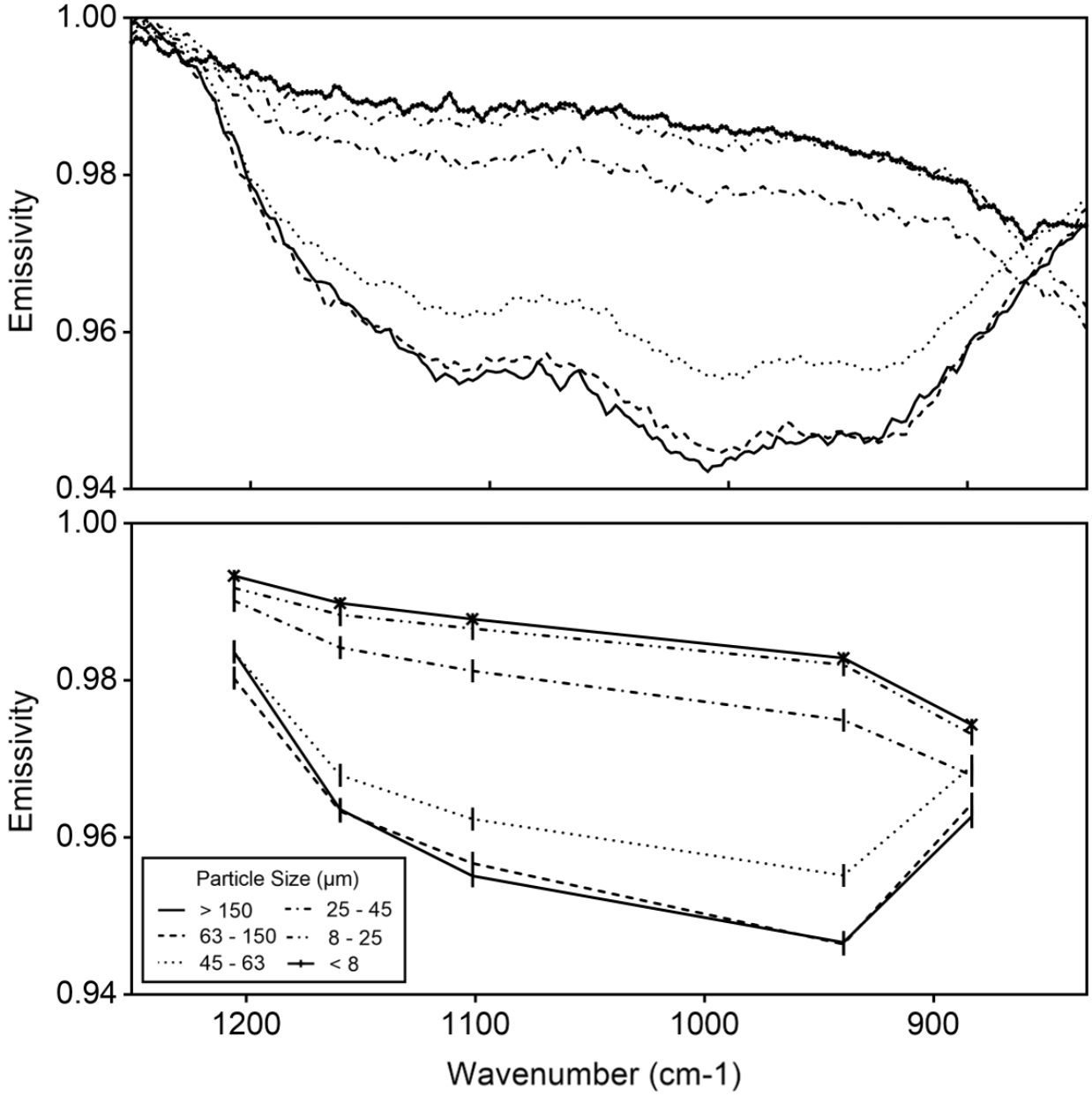

Figure 2-13 Emissivity spectra of the Fuego 2015 sample at (above) hyperspectral, and (below) AVAL spectral resolution. Vertical error bars on AVAL spectra correspond to the NEΔε of the data as measured by the IVIS emission spectrometer.

2.4.2 Sakurajima 2013

Volcanic ash was obtained from eruptions of the Showa crater, Sakurajima volcano during the IAVCEI meeting of 2013. The emission spectrum demonstrates a broad feature between 8 and 12 μm, with a more distinct emissivity minima at ~ 9.1 μm relative to the two samples from Volcán De Fuego (Figure 2-14). Optical analysis determined that 64 % of the sample is volcanic glass, with 20 % plagioclase feldspar. One unusual finding was 15 % of the mass comprising olivine crystals, significantly higher than any of the other samples. Pyroxenes are measured as 1% of the mass. The fine-grained transparency feature is visible in the < 63 μm fractions, with the downward limb visible in AVAL resolution spectra in the ASTER bands 13 and 14 positions.

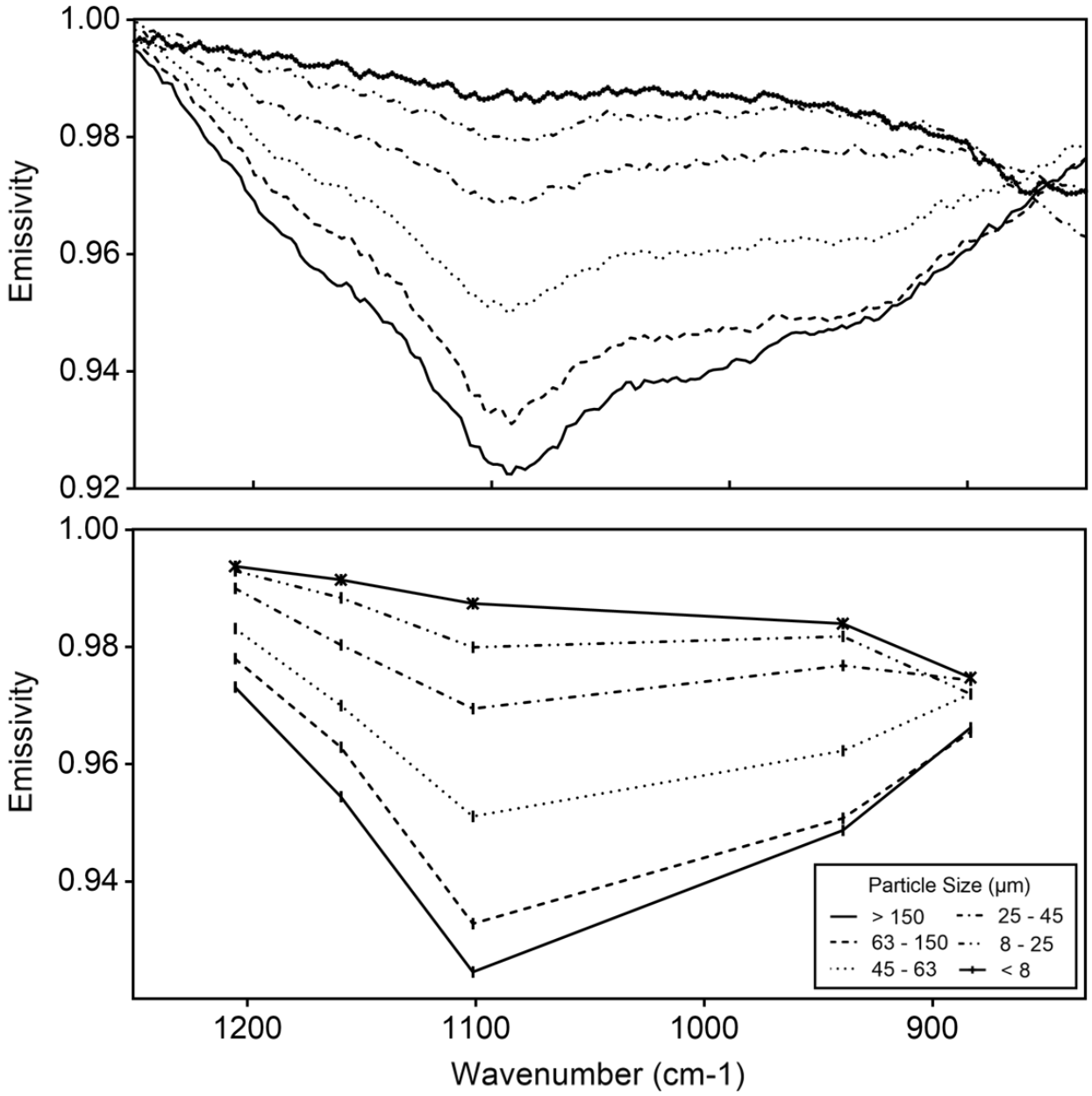

Figure 2-14 Emissivity spectra of the Sakurajima 2013 sample at (above) hyperspectral, and (below) AVAL spectral resolution. Vertical error bars on AVAL spectra correspond to the NEΔε of the data as measured by the IVIS emission spectrometer.

2.4.3 Sakurajima 2016

The second sample from Sakurajima volcano was obtained during fieldwork to the region in November 2016. The sample was collected from ash deposition at the Arimura Lava observatory. The spectral signature is very similar in its shape and position of the main spectral features compared to the 2013 sample (Figure 2-15). It was, however, found to contain more volcanic glass, at 80 % the total mass. The predominant crystalline phase is plagioclase feldspar (18%), with olivine and pyroxene comprising the remainder. At AVAL resolution, both the 2013 and 2016 samples have near identical spectral shapes. As with the previously discussed samples, the fine grained transparency feature at longer wavelengths is also visible at AVAL resolution.

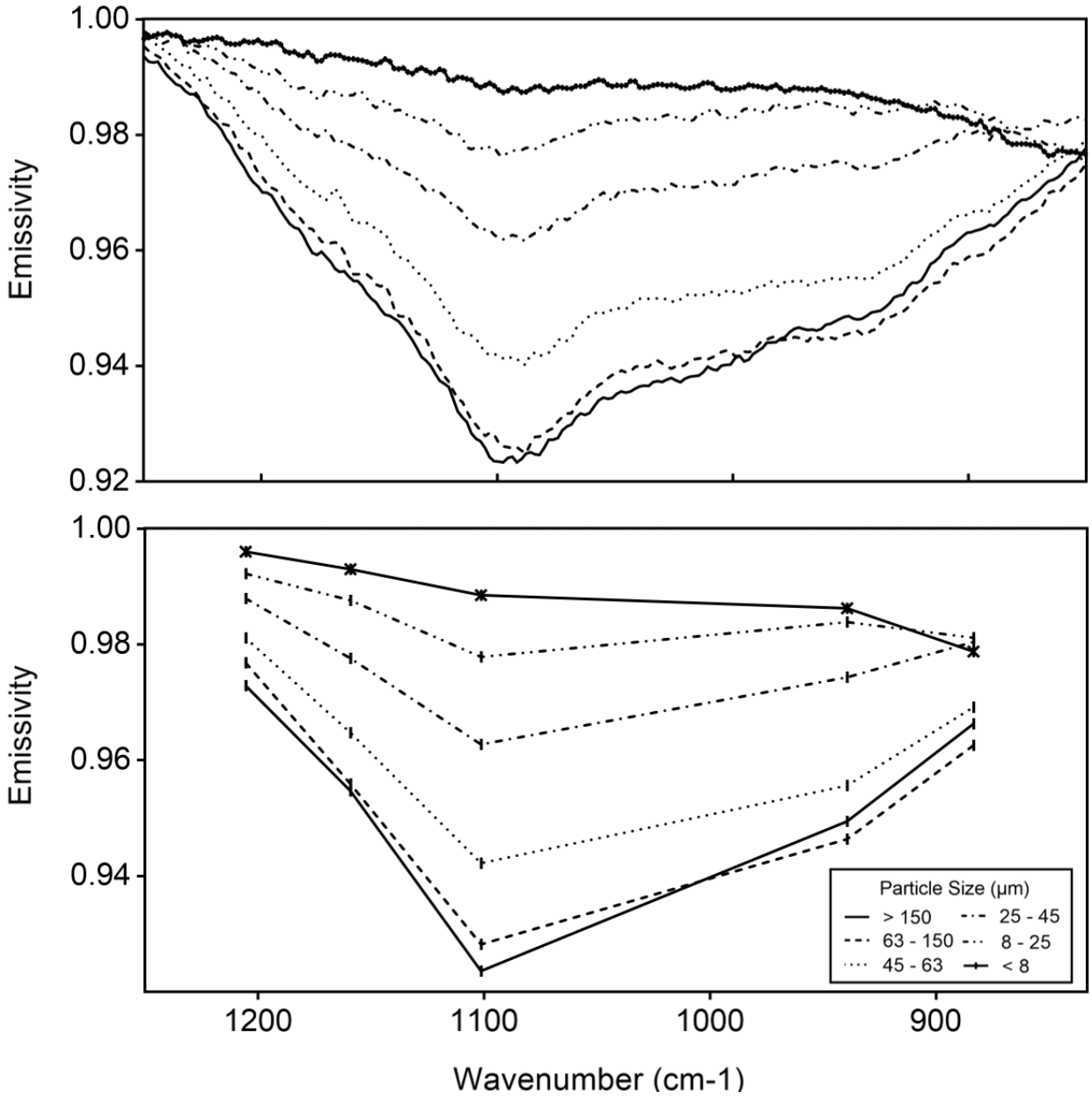

Figure 2-15 Emissivity spectra of the Sakurajima 2016 sample at (above) hyperspectral, and (below) AVAL spectral resolution. Vertical error bars on AVAL spectra correspond to the NEΔε of the data as measured by the IVIS emission spectrometer.

2.4.4 Santiaguito 2011

The Santiaguito 2011 sample was donated to AVAL, collected from El Brujo dome in 2011. The spectral shape is indicative of a silicate glass with a relatively broad spectral feature dominated the AVAL wavelength region (Figure 2-16). Glass dominates the mass of the sample, at 75 % glass. Plagioclase almost entirely comprises the mineral assemblage, 25 %, with minor amounts (< 1 %) of olivine and pyroxene. As with previous samples, the AVAL spectra also contain the fine grained transparency spectral feature.

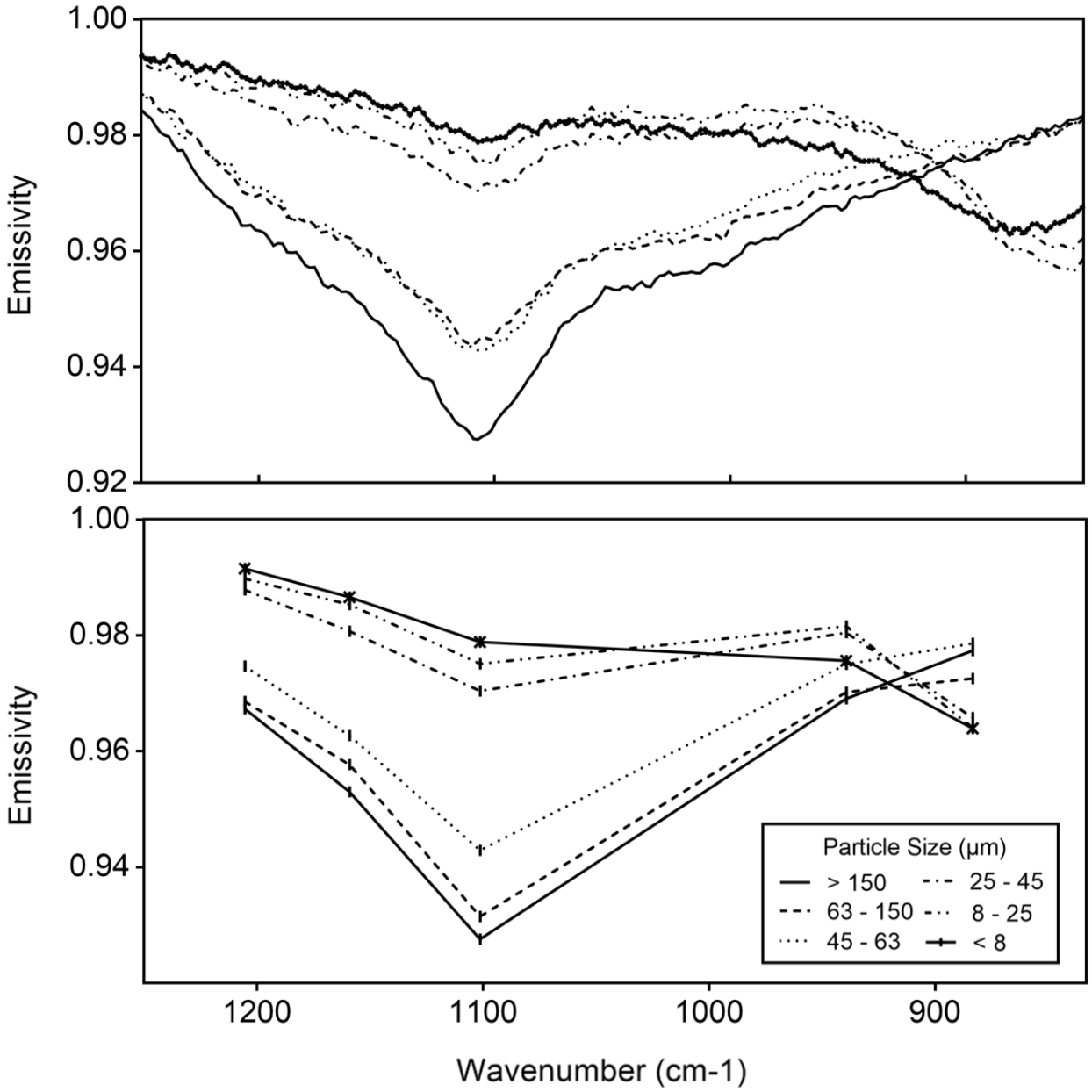

Figure 2-16 Emissivity spectra of the Santiaguito 2011 sample at (above) hyperspectral, and (below) AVAL spectral resolution. Vertical error bars on AVAL spectra correspond to the NEΔε of the data as measured by the IVIS emission spectrometer.

2.4.5 Santiaguito 2016

The second Santiaguito sample from 2016 is similar in composition to the 2011 sample, however, there is a significant reduction in glass fragments (64 %) and an increase in plagioclase (35 %), with olivine and pyroxene once again minor accessory minerals (= < 1 %). The increase in plagioclase feldspar in this sample relative to the 2011 sample may be evident in the TIR spectrum as an emissivity low that causes a doublet between 9.5 and 10 μm (Figure 2-17). At AVAL resolution however, the 2011 and 2016 spectra are similar in their shape, although there are difference seen between ASTER bands 13 (10.657 μm) and 14 (11.318 μm).

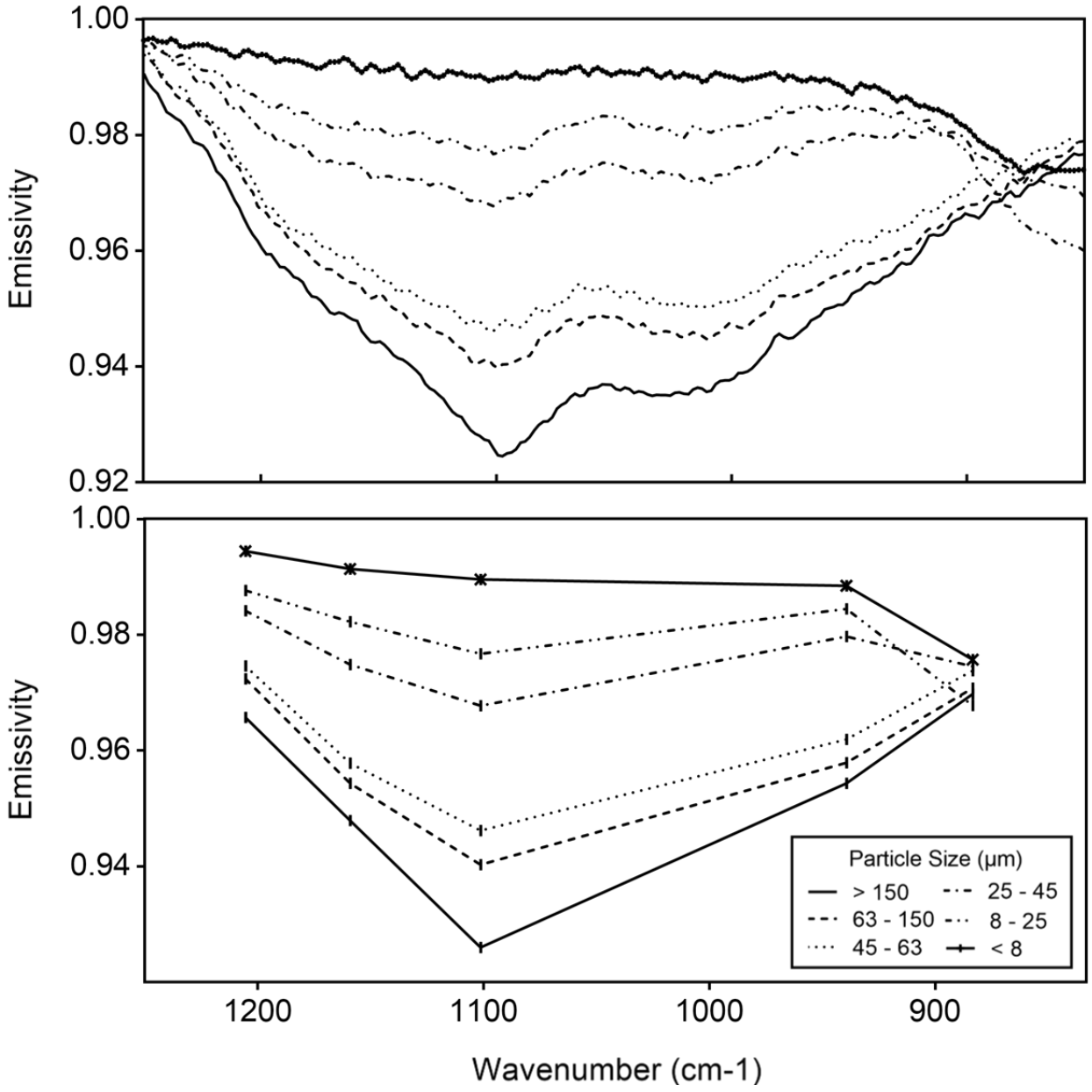

Figure 2-17 Emissivity spectra of the Santiaguito 2016 sample at (above) hyperspectral, and (below) AVAL spectral resolution. Vertical error bars on AVAL spectra correspond to the NEΔε of the data as measured by the IVIS emission spectrometer.

2.4.6 Soufrière Hills Volcano

The Soufrière Hills Volcano (SHV) sample was collected in 2010 from the Belham Valley and donated to this archive. The evidence of a more silicic composition is evident here, as the Christiansen frequency is shifted to shorter wavelengths compared to the other samples (Figure 2-18). The TIR spectrum appears to show evidence of quartz (or a quartz polymorph such as cristobalite, which has been reported in the literature, e.g. Baxter et al., 1999), with the doublet feature superimposed on the spectrum between 8 and 9 μm. Optical analysis did not observe the presence of any crystalline silica, with 76 % of the sample comprised of volcanic glass, with plagioclase feldspar representing 20 %, with 2 % of olivine and monoclinic amphibole. This may be a simple sample bias issue, and does not appear to represent a particle size difference, where different particle size fractions have slightly differing compositions, as this feature is visible across all 6 fractions. Transparency features are once again present in the AVAL spectra at longer wavelengths.

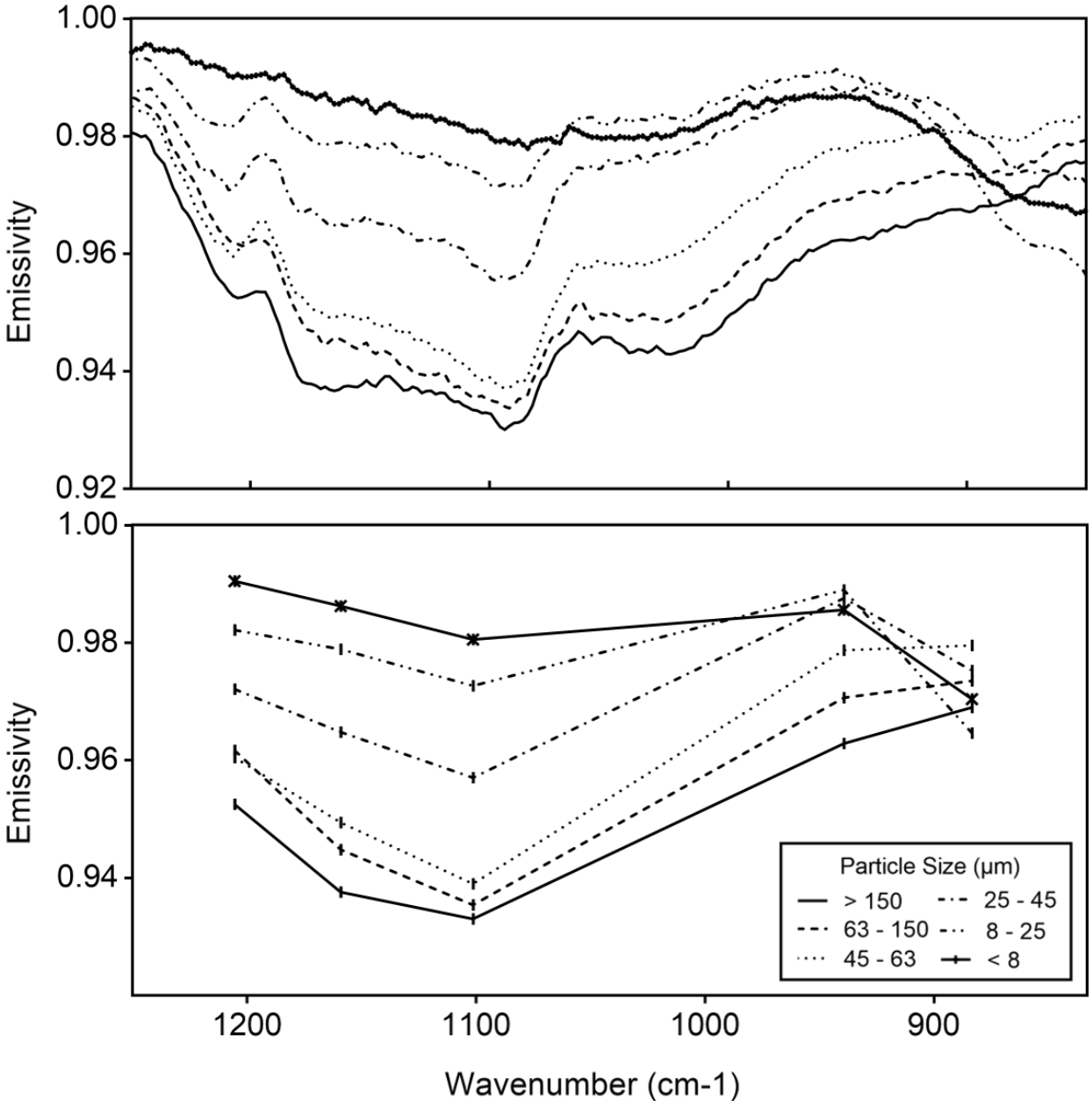

Figure 2-18 Emissivity spectra of the Soufrière Hills Volcano sample at (above) hyperspectral, and (below) AVAL spectral resolution. Vertical error bars on AVAL spectra correspond to the NEΔε of the data as measured by the IVIS emission spectrometer.

2.4.7 Mono-Inyo Domes Obsidian

A sample of crushed Mono-Inyo domes obsidian was used as the high silica end-member. This sample is a pure glass with no mineral component detected. This sample exhibits a typical high silica glass absorption feature described previously in the literature (e.g. Ramsey and Fink, 1999), with an emissivity minimum present at ~ 9.4 μm, and a shoulder found between 8.3 – 8.5 μm (Figure 2-19). The diagnostic features of the sample are present in the AVAL spectra.

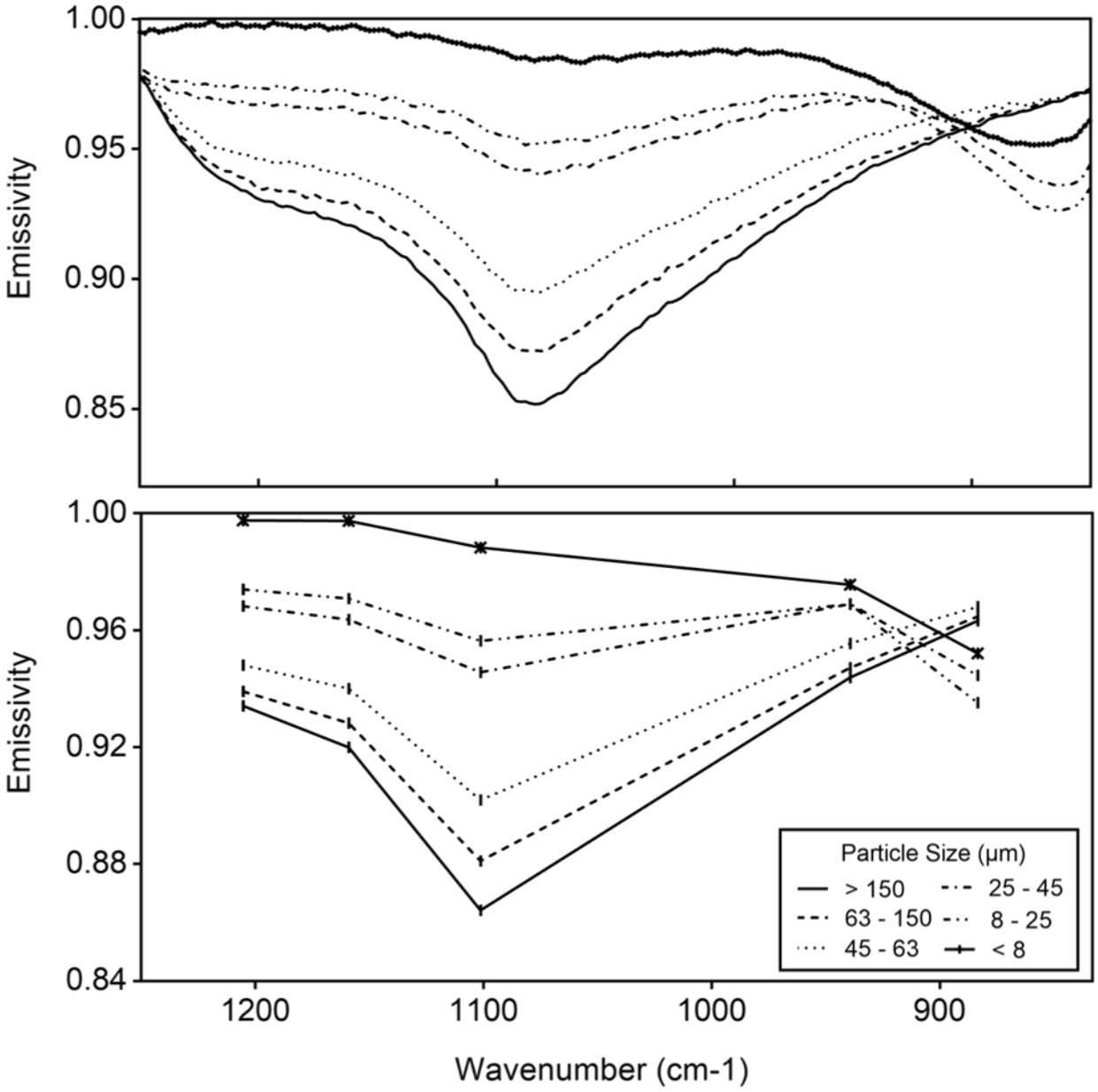

Figure 2-19 Emissivity spectra of the Mono-Inyo Domes crushed Obsidian sample at (above) hyperspectral, and (below) AVAL spectral resolution. Vertical error bars on AVAL spectra correspond to the NEΔε of the data as measured by the IVIS emission spectrometer.

2.5 DISCUSSION

2.5.1 Compositional Variability

The samples presented here represent several different volcanic eruption styles. Whereas there are definite distinctions between each in terms of spectral shape, there are also similarities that should be discussed, so that future samples added to AVAL can be analyzed to determine if new spectral features will add further to the library. All of the samples exhibit their primary absorption feature between 1250 and 1000 cm^{-1}. The exact width and position of that feature are the most diagnostic in terms compositional determination. The results from the optical analysis as well as the TIR spectroscopic methods show that the dominant phase present is volcanic glass, in all cases except for the sample from Fuego, which is dominated by plagioclase feldspar. The composition of the glass present therefore exerts a significant control over the position of the Christiansen frequency and overall spectral shape of each spectrum (Figure 2-20). The movement of the Christiansen frequency emissivity maximum to shorter wavelengths is attributed to an increase in SiO_2 in the sample (Byrnes et al., 2007). This change is also observed within the AVAL spectra as emissivity lows in the shorter wavelength bands for more silicic material, where the Christiansen falls outside the range covered by ASTER.

Table 2-2 Values for the Christiansen frequency for each sample and the emissivity minima in the restrahlen band. Below is a plot showing the movement to shorter wavelengths with increasing SiO_2 content.

	Fuego	Sakurajima (2013)	Sakurajima (2016)	Santiaguito (2011)	Santiaguito (2016)	SHV	Mono-Inyo Obsidian
Christiansen Freq. Position (cm^{-1})	1280.50	1272.79	1282.43	1326.78	1299.78	1338.36	1313.29
ε min Position (cm^{-1})	939.16	1085.73	1091.51	1101.15	1089.58	1093.44	1083.80
Average Composition	Basaltic Andesite	Basaltic Andesite	Basaltic Andesite	Andesite	Andesite	Andesite/ Dacite	Rhyolite

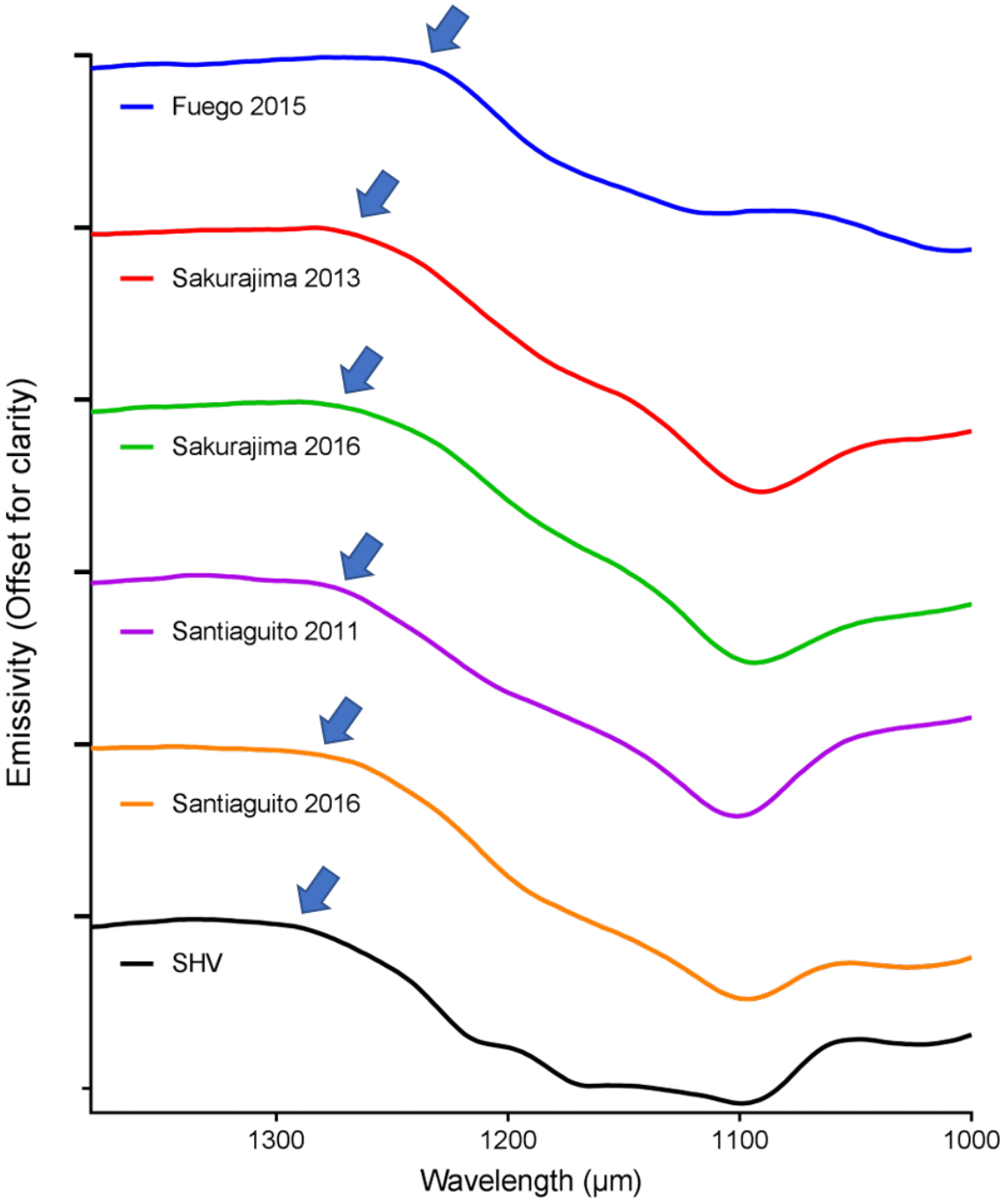

Figure 2-20 Position of the Christiansen frequency of each sample denoted by the blue arrows. These data have been smoothed using a 4th order polynomial to better observe this feature. Data are offset, each tick mark is 0.05 emissivity, and each bold tick is equal to an emissivity of 1. Interestingly, the Santiaguito 2011 sample crosses over the 2016 sample and overlaps the two samples from Sakurajima at ~ 1160 cm^{-1}. This is due to the presence of a pronounced shoulder in the spectrum, caused by the muting of a spectral feature that occurs in more silica rich minerals (Byrnes et al., 2007)

Of the mineral fraction, the dominant phase is plagioclase feldspar, with pyroxene, olivine and amphibole comprising minor amounts. The only exception to this is in the Sakurajima 2013 sample in which optical analysis determined that a significant component was olivine. This does not appear to be consistent with previous analyses and may in fact represent a simple sample bias issue or measurement error by the laboratory conducting the analysis.

2.5.2 Sources of Error

There are potential measurements errors associated with this approach. One initially seen was the effect of clinging fines on the surface of larger particles. Where an aggregate such as this forms, it causes scattering resulting in shallowing of the primary absorption feature. If the particles are fine enough, the transparency effect is also seen. Another consideration is the presence of surface vesicularity. This is particularly important for the larger grains, as particles greater than > 150 μm may still have vesicles present. Vesicles create a different effect to fines, in that they behave as a blackbody (Ramsey and Fink, 1999). This will create an overall shallowing of the TIR spectrum, but without the transparency effects. This may occur in the larger grain sizes of the Fuego 2015 sample, as there is very little distinction between the largest two samples, however this would require further investigation, such as Scanning Electron Microscopy (SEM; Carter et al., 2009).

The optical analysis provided a useful estimation of the composition and allowed percentages to be estimated. It did, however, provide some surprisingly results, particularly in the case of the Sakurajima 2013 sample, where 15 % olivine was recorded. Whereas this may be true for the sample analyzed, it seems unlikely the whole sample would have this much olivine given that previous studies identified only minor amounts or isolated olivine grains (e.g.

Matsumoto. et al., 2013). This would appear to indicate a sample bias in the optically analyzed fraction. This is also the case in the SHV sample, where the TIR spectrum would indicate that there is enough crystalline silica present to produce the feature seen at ~ 1190 cm^{-1}, and this would bring the sample into line with previous work (Baxter et al., 1999). Further geochemical studies are recommended (such as X-Ray Diffraction, or Computer Controlled Scanning Electron Microscopy) to determine the quantity and composition of mineral phases present.

One further aspect is whether or not the particle size range values that were used for this study are accurate. A qualitative measure of successes of the library creation is that as particle size decreases, a progressive shallowing of spectral absorption features is observed, and the increase in depth of transparency features for samples < 63 μm. The spectra do appear to "nest" within one another, which is expected behavior, indicating that some form of decreasing particle size range is present (Ramsey and Christensen, 1997). However, one aspect that makes volcanic ash difficult to separate is the fact that it is commonly very angular. Therefore, using Stokes settling velocity calculations to separate particle size ranges is challenging. The MOUDI uses the aerodynamic diameter where describing the stage cuts (Marple et al., 1991). There is a difference between what is considered the aerodynamic diameter and the mean diameter of an irregular shaped particle, a microscopic analysis to determine modal diameter within each range should be performed.

The NEΔε of the instrument is also a factor in determining the validity if these spectra and whether or not the AVAL library is valid to estimate particle size. As is particularly the case in the spectral suite from the Volcán De Fuego sample, the MOUDI and sieved fractions are distinct from each other, however where compared to other particle size ranges extracted with the same method, are much closer in value. The NEΔε can therefore be used to determine

whether these spectra are distinct enough to be used, particularly to estimate particle size in ASTER data. The NE$\Delta\varepsilon$ values ± 100 cm^{-1} around each ASTER channel were averaged to produce spectral error for AVAL. The average NE$\Delta\varepsilon$ for the ASTER wavenumber range (~ 1250 – 833 cm^{-1}) is 0.005, with a standard deviation of 0.0005. The low errors (< 1 %) associated with the emission spectroscopy techniques show that if repeat measurements are taken of these samples, distinctions between each particle size fraction would still be evident. Only one sample perhaps needs to be analyzed further for its particle size range, that being Volcán de Fuego. For the two finest and two coarsest fractions, the error bars between the spectra imply that crossover between each could occur during repeat measurements, so that the particle size ranges estimated may not be completely exact.

2.6 APPLICATIONS AND CONCLUSIONS

TIR data provide a useful diagnostic tool for earth scientists. The hyperspectral data obtained from hand specimens and powders is a non-destructive and relatively quick way to obtain information on a samples composition. However, it is not possible to apply those measurements directly to satellite or ground based data over large areas, as there is no hyperspectral satellite sensor with a high enough spatial resolution to see small scale variations in composition. Using the data from the ASTER TIR channels, major changes in composition are still evident. Therefore, the spectra in AVAL is significant. These spectra can be used as spectral emission end-members to help determine the composition of materials found in volcanic ash-rich plumes as well as on the surface of the Earth. The analysis techniques are also used on planetary TIR data such as those acquired from Mars (e.g. Hamilton et al., 2001).

The ASTER sensor is chosen for this study because of the availability of data from the world's volcanoes, its multispectral resolution in the TIR, with channels positioned at and around the main absorption features of silicate minerals, and its high spatial resolution (90 m/pixel). These spectra, coupled with an appropriate unmixing model, aid the mapping of different compositions and help to determine particle size distribution on ash-rich surfaces. The results can be used to map temporal changes in the particle size ranges of tephra aprons, as well as determine compositional changes over the course of an eruption. Another application of these data is analysis of volcanic plumes themselves. It is theorized that if a volcanic ash plume is dense enough to be optically opaque, then it would represent the emitting surface within an image pixel. Therefore, the emission spectra found within each pixel of an image could be unmixed linearly similar to the approach for the ground surface. This concept is explored in greater detail in chapter 3.

The spectral library has prepared the ground work for a suite of volcanic ash samples to be used in conjunction with image data. The expansion of the library to include additional samples that have different wt. % glass versus crystals is important and ongoing, as well as adding samples that contain glasses of different compositions. By better understanding how different compositions affect the emission spectra, we can better interpret the resulting images derived from these libraries allowing a more detailed volcanological analysis to be performed.

3.0 HIGH SPATIAL RESOLUTION MAPPING OF VOLCANIC ASH PLUMES USING ADVANCED SPACBOURNE THERMAL EMISSION AND REFLECTION RADIOMETER DATA

3.1 INTRODUCTION

Explosive volcanic eruptions are capable of injecting columns of volcanic glass, mineral particles, and gas several kilometers into the Earth's atmosphere, with potentially little to no warning. These eruptions are constrained by a wide variety of factors, including the vent and conduit diameters, magma composition and the quantity of volatiles present (Wilson et al., 1980; Woods, 1995). Accurate analysis of the physical and chemical parameters of volcanic ash is a vital tool for determining the conditions under which an eruption forms (Heiken and Wohletz, 1991).

Satellite remote sensing provides one practical way to observe volcanic activity and monitor the propagation of the ash through the atmosphere (Rose et al., 2000). One of the most common and well-used approaches for ash detection is the 'split window' or brightness temperature difference (BTD) technique of Prata (1989a,b), which requires two or more thermal infrared (TIR) spectral channels and the transmission of emitted TIR energy from the Earth's surface through the cloud. Volcanic ash clouds are distinguished from meteorological clouds based on the apparent temperature difference that results from the spectrum of the ash. This

technique is further exploited (e.g. Wen and Rose, 1994; Prata and Grant, 2001) in order to retrieve ash densities and effective particle radii. The detection of volcanic ash is primarily undertaken by a suite of high temporal/low spatial resolution satellite sensors, such as the Advanced Very High Resolution Radiometer (AVHRR; (Prata 1989a) and the Moderate Resolution Imaging Spectroradiometer (MODIS; Watson et al., 2004). This low spatial resolution is useful for tracking large volcanic ash clouds over great distances, but with pixel sizes of 1 km or more and few TIR spectral channels, these sensors are limited in performing accurate analysis of a range of particle size distribution. In addition, these techniques are best used to examine a drifting cloud as it moves further from the source. Because the BTD method requires the use of upwelling radiance from the ground, the cloud itself must be optically thin in order to be analyzed, a situation not present where the cloud is proximal to the vent. Given that this proximal portion is one of the most dynamic regions, with particle sizes ranging from < 0.1 to over 100 μm (Piscini et al., 2011), a better understanding is required to provide accurate inputs into plume propagation models and a direct connection to the ongoing vent processes. In addition, plume retrieval models require assumptions of ash composition to make a density estimation. If the assumed ash composition is different to what is presen, then the estimates of effective radii and density are inaccurate up to 17.7 % (Mackie et al., 2014). Furthermore, recent studies demonstrate a large discrepancy between reported distal ash cloud particle sizes from satellite image data techniques (~ 95 % particles at < 17 μm) and reported ash particle sizes from ash fall in these regions (Stevenson et al., 2015).

For geological studies of surface compositions and processes, the use of TIR vibrational spectroscopy is well studied (e.g. Walter and Salisbury, 1989; Rowan et al., 1991). The presence of absorption bands in the emission spectra of silicate minerals allows for the mapping of

surfaces and determining of the rock types present. Provided that emission from the surface is isolated from other effects (e.g. atmospheric downwelling radiation), this is achieved with relative simplicity because of the property of linear addition of each component to the overall emission spectrum based on that component's areal abundance, using an appropriate linear spectral end-member model (e.g. Ramsey and Christensen, 1998). In addition to this, the spectral contrast of these absorption bands decreases as the particle size of the material decreases (Chapter 2; Salisbury and Wald, 1992). This effect is also shown to be linear down through to particle sizes of ~ 10 μm with the appropriate corresponding particle size end-members (Ramsey and Christensen, 1998), allowing for mapping of particle size variations by the same approach. This method allows for mapping and interpretation of geologic processes occurring, not only in the Earth system (e.g. Ramsey et al., 1999), but also to those on other planetary surfaces (e.g. Bandfield et al., 2000). Given that that the proximal portion of a volcanic ash plume is opaque to upwelling radiation from the ground surface, it is therefore theorized that these same methods could be used to map petrological and particle size variations within it by treating the cloud as a solid emitting surface (Ramsey, 2015). Because this region is normally small where compared to the size of a MODIS or AVHRR pixel (~ 1 km^2; Watson et al., 2004), data with smaller spatial resolution than these sensors are required.

The goal of this work is to estimate both the composition and particle size range of opaque proximal plumes, using techniques in emission spectroscopy and TIR image data from the Advanced Spaceborne Thermal Emission and Reflection Radiometer (ASTER; Yamaguchi et al., 1998). The opaque region is modeled as an emitting surface exclusively, and its properties estimated using the linear deconvolution model of Ramsey and Christensen (1998). Three series of tests of the model were performed;

1. Use of ASTER data of volcanoes that are sampled in the AVAL spectral library to determine if the material collected on the ground is representative of “typical” eruption compositions from that volcano
2. Use of volcanoes not sampled in AVAL to determine if composition is estimated using the samples present in AVAL
3. Use of a mixture of different library compositional end-members with the same model to determine if more than one composition should be used to improve accuracy

A total of eight volcanoes were analyzed using this method, chosen for the wide variety of reported compositions erupted. This allows comparison of the model results to the reported compositions.

3.2 BACKGROUND AND DATA

3.2.1 TIR Remote Sensing of Volcanic Ash Plumes

3.2.1.1 History

The TIR portion of the EM spectrum is used extensively to study volcanic ash. After the 1982 El Chichón in Mexico, Matson and Robock (1982) demonstrated the use of Geostationary Operational Environmental Satellite (GOES) TIR data to derive ash cloud top temperatures and associate them with different heights in the atmosphere based upon radiosonde data and assuming the plume was in thermal equilibrium with the surrounding atmosphere. Sawada (1987) provided the first survey for volcanic ash clouds detected from satellite image data using

the Geostationary Meteorological Satellite (GMS) to observe volcanic ash cloud eruption and propagation in the western Pacific. However, the basis for ash cloud discrimination against water vapor clouds was developed by Prata (1989a,b), using AVHRR bands 4 (10.3 – 11.3 μm) and 5 (11.5 – 12.5 μm). The technique uses a radiative transfer model to determine the at-sensor radiance captured by AVHRR from ground upwelling through the atmosphere and through the cloud layer, as well as radiance from the cloud itself. This ash cloud interaction with ground-upwelling radiance is complex and is controlled by the absorption and scattering of ash particles through their extinction cross section, which differs by composition, shape, size and incident wavelength (Pollack et al., 1973). This change over wavelength is seen between AVHRR bands 4 and 5, which is then observed as a brightness temperature difference (BTD), using the inverted form of the Planck equation solving for temperature. Once these are obtained, band 5 is subtracted from band 4 to obtain the BTD of the image data. This calculation is significant, as the transmission of volcanic ash clouds behaves differently between these two bands than water vapor (Figure 3-1). This results in a BTD that is positive for water vapor clouds, but negative for volcanic ash clouds.

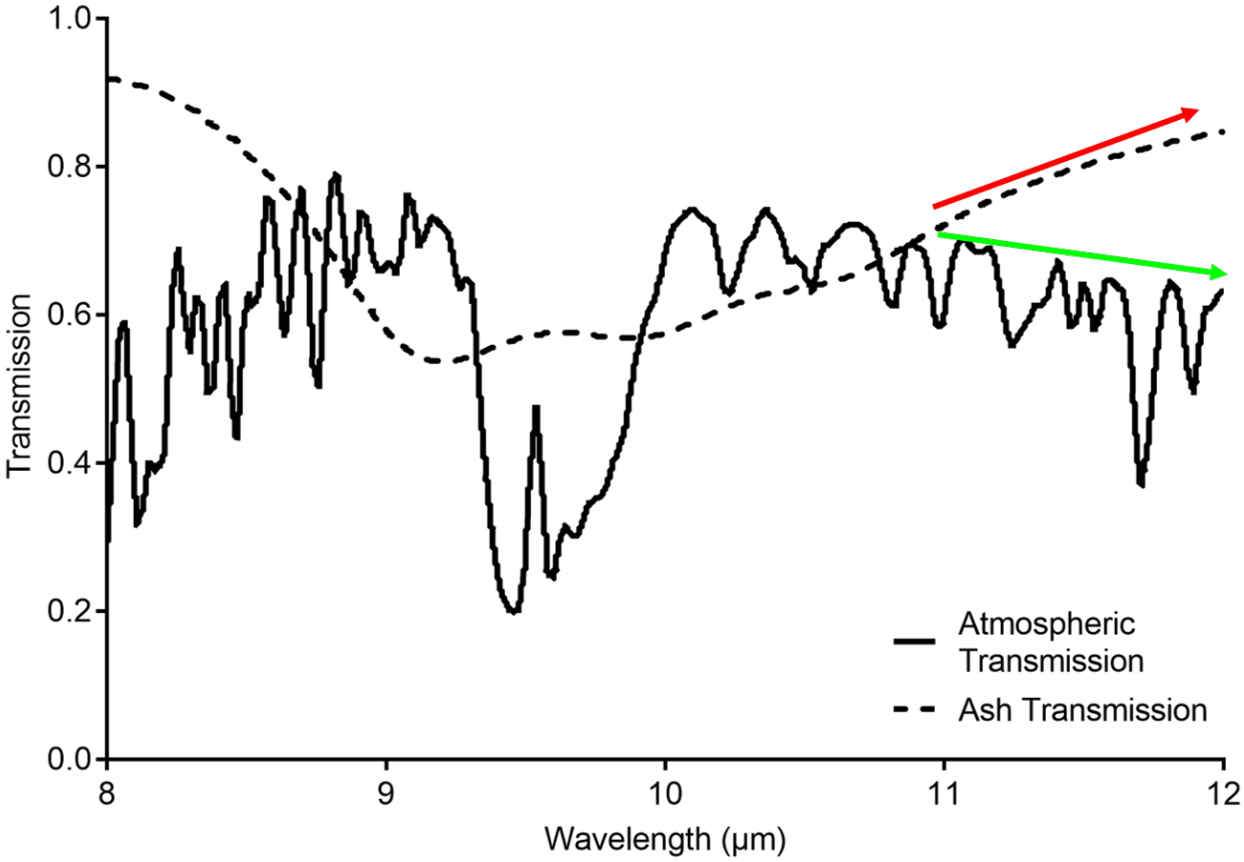

Figure 3-1 (Top) Transmission profiles for andesite ash including the absorbed and scattered component (after Watson et al., 2004), and a typical mid-latitude atmospheric transmission profile (bottom). Where the atmosphere becomes less transmissive at longer wavelengths (green arrow), the reverse is seen in the ash transmission spectrum (red arrow).

That initial work is expanded by Wen and Rose (1994) and Prata and Grant (2001), who demonstrated that a more detailed radiative transfer model, coupled with a microphysical model of volcanic ash particles allows the mean particle effective scattering radius and cloud optical depth to be determined, from which the mass and density is inferred. In the model, particles are assumed to be spherical, which allows the use of Mie theory to extract extinction cross section, asymmetric parameter and the single-scattering albedo, determined for a known refractive index (Pollack et al., 1973). The refractive index (n) is variable with wavelength and composition of the material.

These methods are now regularly in use by Volcano Ash Advisory Centers (VAAC's) worldwide (Prata, 2009) to detect and determine the ash particle size and loading, employing an increasing number of satellite sensors (Table 3-1), including the MODIS (Watson et al., 2004), the Atmospheric Infrared Sounder (AIRS; Prata and Bernardo, 2007), the Infrared Atmospheric Sounding Interferometer (IASI; Clarisse et al., 2008), and the Spin Enhanced Visible and Infrared Instrument (SEVIRI; Prata and Kerkman, 2007). Several of these instruments (GOES, MODIS, AVHRR) are also available on multiple platforms, thus increasing the data availability.

Table 3-1 List of TIR satellite instruments used to detect volcanic ash emissions (adapted from Thomas and Watson, 2010, to include ash observing satellite sensors discussed in the proceeding 8 years)

Instrument	Platform	Altitude	Spatial Resolution (nadir)	Spectral Range (TIR only)	Reference
AHI	Himawari 8-9	22,241 km	2 km	10 Channels: 3.9 – 13.3 μm	Bessho et al., 2016
AIRS	Aqua	705 km	14 km	2378 channels: 3.75 – 15.38	Chahine et al, 2006
AVHRR (1,2,3)	TIROS-N (inactive); NOAA 6-17 (inactive) NOAA 18-19 (currently operational) MetOp-A (currently operational)	870 km	1.1 km	3 channels: 3.55 – 12.50 μm	Bulgin et al., 2018
GOES	GOES (1 – 13 inactive; 14 – 16 currently operational)	35,888 km	GOES 14 – 15: 4 km GOES 16: 2 km	GOES 14 – 15: 4 channels: 3.80 – 12.50 μm; GOES 16 Advanced Bassline Imager (ABI): 10 channels: 3.80 – 13.56 μm	Schmit et al., 2017
IASI	MetOp	817 km	12 km (circular)	8461 channels: 3.62 – 15.50 μm	Clerbaux et al., 2009
MODIS	Terra Aqua	705 km	1 km	16 channels: 3.66 – 14.28 μm	Watson et al., 2004
SEVIRI	MSG	42,000 km	3 km	8 channels – 3.9 – 13.4 μm	Prata and Kerkmann, 2007
VIIRS	S-NPP	824 km	750 m	7 channels: 3.70 – 12.01 μm	Xiong et al., 2013

The methods have also evolved by using additional spectral channels available on many of these platforms, which leads to greater accuracy in ash retrievals. The use of a third channel near 3.9 μm (GOES band 2) for example, was proposed by Ellrod et al., (2001) because of the reflectance of ash particles at this wavelength compared to water and ice (although this relationship is particle size dependent). This translates to a significantly higher brightness temperature (BT). This work is expanded to AVHRR by Pergola et al (2004), who presented a statistical approach to a three-band method, using bands 3 (3.5 μm), 4 and 5 (the original split-window bands). The aim is to more accurately discriminate volcanic ash clouds, by using an Absolutely Local Index of Change of the Environment (ALICE), which provides an estimate of how the signal from each pixel in an image has differed from its "normal" conditions (i.e. image observed at the same place under similar conditions). From this, the Robust AVHRR Technique (RAT) was created to better discern volcanic ash cloud detection thresholds. The use of the reflectance of ash particles is also tested by Corradini et al (2008), who utilized channels analogous to the AVHRR split-window channels on the MODIS sensor (channels 31 and 32) as well as channel 5, centered at 1.24 μm. Pavolonis et al. (2006) included the 0.65 μm visible channel in their algorithm, using the ratio of 0.65 and 3.75 μm to discriminate, as ash has a lower reflectance in the 0.65 μm channels compared to the 3.75 μm (for clouds of the same optical depth). This method is restricted to daytime retrievals, however. More recently Guéhenneux et al (2015) proposed a 3-band method that utilizes the 8.7 μm band found on board the SEVIRI instrument. The original methods of Prata (1989 a,b) are expanded to include a second BTD ratio, subtracting the 11 μm channel from the 8.7 μm channel. In this case, the difference in extinction coefficient of ash particles produces a positive BTD where ash is present. Thus a two statement Boolean test is applied to the data.

3.2.1.2 Sources of Error and Restrictions

There are, unsurprisingly, errors that are associated with all methods for detecting ash clouds, which have been extensively covered in the scientific literature (Simpson et al., 2001; Prata et al., 2001; Simpson et al., 2001). These can lead to over- and underestimations of volcanic ash cloud size. Clouds tend to be underestimated where,

(1) large quantities of moisture are present in the cloud, which can come from a moist humid atmosphere into the which the ash cloud is erupted, or from the eruption itself, derived from the source (Rose et al., 2001). This causes a shift towards a positive BTD values;

(2) the temperature of volcanic clouds is low (< 220 K), which allows for the nucleation of ice around the ash particles. Several mineral species variably promote the nucleation of ice crystals on their surfaces (Murray et al., 2012), which leads to a positive BTD;

(3) for images with a high solar zenith angle, the increased atmospheric column length can create a positive BTD (Guéhenneux et al., 2012);

(4) if the plume is sufficiently optically thick and therefore not transmitting ground radiance through the cloud. This leads to positive BTD determination.

Cloud size can conversely be overestimated if,

(1) the plume is detected in the presence of mineral dusts from other ground sources (Ackerman, 1997);

(2) where the plume is over a quartz rich soil (typically under desert conditions);

(3) for nighttime scenes, thermal relaxation caused as the ground releases heat creates an atmospheric inversion layer;

(4) if the top of a meteorological cloud overshoots the tropopause, a negative BTD arises due to the temperature inversion;

(5) if there is a misalignment between the split-window bands, (particular with AVHRR; Prata et al., 2001).

Additionally, and of importance to the work discussed in this chapter, there are restrictions with the current methods, that this study hopes to resolve. Because of the need for near-real time monitoring of volcanic ash plumes, the works listed above have focused on low spatial, but high temporal resolution satellites exclusively to map the drifting ash plume. This allows analysis of ash clouds that travel a large distance in the atmosphere, but for smaller discrete eruptions that happen on a more frequent timescale (e.g. Sakurajima, Volcán De Fuego), it is much more difficult or not possible to quantify the emissions (Figure 3-2). Furthermore, the use of Mie scattering model of radiance interacting with the plume restricts the maximum detectable particle size that is observed, as Mie scattering is effective where the wavelength of light is near or at the same size as the particles.

For the work outlined here, the ASTER sensor is chosen to map volcanic plumes in significantly higher spatial resolution than is achieved previously, using alternative techniques in spectroscopy that will be discussed.

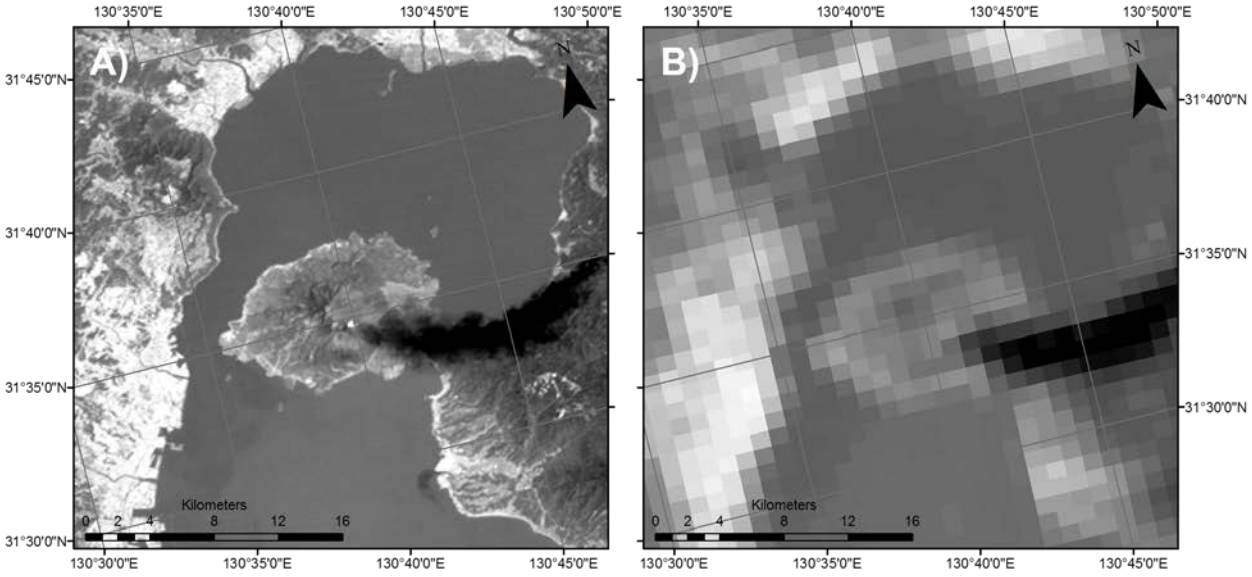

Figure 3-2 Comparison between the ASTER (A) and MODIS (B) sensors. Data are from a relatively small (13 km long, 2.5 km wide) volcanic plume in the TIR. ASTER band 13 and MODIS band 31 are shown in these two images. This size eruption is suited to ASTER sensor and could be analyzed in detail.

3.2.2 The ASTER Sensor

The ASTER sensor was launched on board the Terra satellite in December 1999 (Yamaguchi et al., 1998) and placed into a Sun-synchronous near polar orbit at 705 km altitude. It observes the same position on the Earth every 16 days with a swath width of 60 km. The main goal of the mission is to understand the local and regional scale processes occurring at or near the Earth's surface, and the interactions between the Earth's surface and lower atmosphere (Yamaguchi et al., 1998). The sensor is divided into three distinct subsystems, with three channels in the visible near infrared (VNIR) with a 15 m spatial resolution, six channels in the shortwave infrared (SWIR) with a 30 m spatial resolution, and five TIR channels with a 90 m spatial resolution (Kahle et al., 1991). The SWIR system suffered a failure of the cooling system in 2009; however, the other systems on board the sensor still function, providing an average of 518 scenes per day (Ramsey, 2015). The ASTER sensor is well suited to the study of volcanic eruptions and provides distinct advantages over other satellite sensors. ASTER has a noise equivalent temperature difference (NEΔT) of 0.3 K at 300 K (Gillepsie et al., 1998), resulting in high radiometric accuracy temperature retrievals from the ground (Pieri and Abrams, 2004) The routine collection of multispectral TIR data also allows continual monitoring of thermal anomalies over volcanic regions, and its moderate high spatial resolution is critical in determining volcanic products.

Table 3-2 ASTER system overview (after Pieri and Abrams, 2004)

ASTER Subsystem	Band No.	Spectral Range (μm)	Spatial Resolution	Cross Track Pointing
VNIR	1	0.52-0.60	15 m	24 ˚ 318 km
	2	0.63 – 0.96		
	3N	0.78 – 0.86		
	3B	0.78 – 0.86		
SWIR	4	1.60 – 1.70	30 m	8.55 ˚ 116 km
	5	2.145 – 2.185		
	6	2.185 – 2.225		
	7	2.235 – 2.285		
	8	2.295 – 2.365		
	9	2.360 – 2.430		
TIR	10	8.125 – 8.475	90 m	8.55 ˚ 116 km
	11	8.475 – 8.825		
	12	8.935 – 9.275		
	13	10.25 – 10.95		
	14	10.95 – 11.65		

Furthermore, the sensor can point off nadir at a target (up to 24º off nadir for VNIR and 8.55º for TIR; Pieri and Abrams, 2004). The combination of these capabilities led to the development of the ASTER Urgent Request Protocol (URP; Ramsey, 2015). This program, sponsored by the National Aeronautics and Space Administration (NASA) since 2004, is triggered by observations of thermal anomalies from higher temporal resolution sensors, such as AVHRR and MODIS (Ramsey et al., 2012).

ASTER data are routinely used to calculate the concentration of SO_2. The methods used with ASTER and other TIR sensors are based on those developed for the Thermal Infrared Multispectral Scanner (TIMS; Realmuto et al., 1994). It takes advantage of an SO_2 absorption feature present at 8.6 μm, as well as its transparency between ASTER channels 13 and 14 (10.567 – 11.318 μm; Realmuto and Berk, 2016). The strength of the absorption is dependent on both the temperature contrast between the plume and ground, as well as the SO_2 concentration, as SO_2 burden is a linear function of the temperature difference (Realmuto and Worden, 2000; Henney et al., 2012). This work is applied to ASTER data using the MAP_SO2 program, based upon the MODTRAN atmospheric radiative transfer code (Berk et al., 1989). Since 2016, MAP_SO2 has evolved into the new model Plume Tracker software (Realmuto and Berk, 2016), which has greatly improved computational performance, as well improving the accuracy of the retrieval. The sensitivity of the ASTER sensor to system noise (NEΔT) and its spatial resolution gives it a distinct advantage in being able to detect SO_2 concentrations from passively degassing volcanoes with smaller SO_2 loadings. This method however is also restricted to the transparent portion of the plume. However, a preliminary study by Ramsey (2016) demonstrated that the opaque portion of the plume could be analyzed if it is treated hypothetically as a solid emitting surface. The results from this analysis are shown in Figure 3-3.

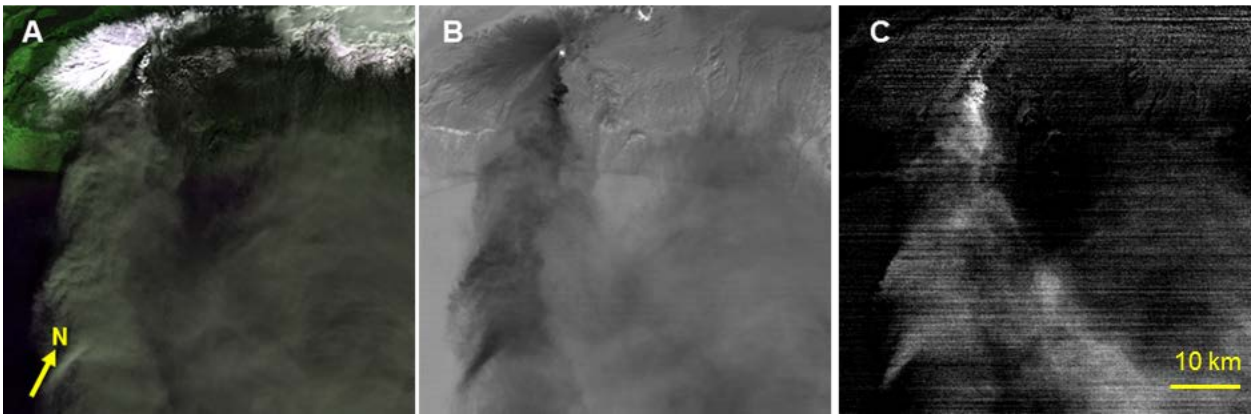

Figure 3-3 19 April 2010 ASTER data of the plume produced by the Eyjafjallajökull eruption in Iceland. A) False color VNIR image of the plume; B) Brightness temperature image from TIR data, which shows variations from 0˚C (black) to 50˚C (white). C) Spectral deconvolution result varying from 0% (black) to ~80% (white) using an andesitic glass end-member and assuming the opaque plume is a solid emitting surface (from preliminary work by M. Ramsey, 2010 for the ASTER science team).

3.2.3 ASTER Data Products

ASTER data are available in a variety of formats, from uncalibrated radiances (Level 1A) to temperature and emissivity corrected image data (Level 2; Abrams, 2000). It was therefore important to determine the appropriate dataset to analyze. ASTER L2 products AST_05 (emissivity) and AST_09T (TIR surface radiance) were initially identified as suitable for this study, given they are corrected atmospherically, geometrically and that the atmospheric correction applied is shown to be accurate to within 5% (Arai and Tonooka, 2005; Iwasaki and Fujisada, 2005; Tonooka and Palluconi, 2005). The AST_05 product is derived from the AST_09T product and undergoes additional processing via the Temperature Emissivity Separation (TES) algorithm to remove the downwelling atmospheric irradiance component of the at sensor radiance (Gillespie et al. 1998). However, as we are dealing exclusively with an atmospheric phenomenon in this work, the standard ASTER L2 emissivity product may be unsuitable. It was decided that a review of the possible data products is warranted.

Table 3-3 ASTER Data Products (after https://asterweb.jpl.nasa.gov/data_products.asp)

Level	Name	Product	Resolution (m)
1A	AST_L1A	Reconstructed Unprocessed Instrument Data	15, 30, 90
1AE	AST_L1AE	Reconstructed Unprocessed Instrument Data - Expedited	15, 30, 90
1B	AST_L1B	Registered Radiance at the Sensor	15, 30, 90
1BE	AST_L1BE	Registered Radiance at the Sensor - Expedited	15, 30, 90
L1T	AST_L1T	Registered Radiance at the Sensor - Precision Terrain Corrected	15, 30, 90
2	AST_07	Surface Reflectance - VNIR & SWIR	15, 30
2	AST_07XT	Surface Reflectance - VNIR & Crosstalk Corrected SWIR	15, 30
2	AST_09	Surface Radiance - VNIR & SWIR	15, 30
2	AST_09XT	Surface Radiance - VNIR & Crosstalk Corrected SWIR	15, 30
2	AST_09T	Surface Radiance TIR	90
2	AST_08	Surface Kinetic Temperature	90
2	AST_05	Surface Emissivity	90
3	AST14OTH	Registered Radiance at the Sensor - Orthorectified	15, 30, 90
3	AST14DMO	Digital Elevation Model & Registered Radiance at the Sensor - Orthorectified	15, 30, 90
3	AST14DEM	Digital Elevation Model	30
3	ASTGTM	ASTER Global Digital Elevation Model	30

Identification of the appropriate data product is performed by examining the emission spectra of plume bearing pixels to determine major changes and Δε between each product. Two images are analyzed of volcanic plumes generated by Chaitén (Chile) and Sakurajima volcanoes. AST_L1B data were processed using the ENVI Thermal Atmospheric Correction algorithm, which is similar to the In-Scene Atmospheric Compensation (ISAC) algorithm, where the atmosphere is assumed to be uniform across a scene, and that a near-blackbody source exists somewhere in the data (Young et al., 2002). This dataset and the AST_09T data were converted to emissivity using the emissivity normalization method (Realmuto, 1990). Because temperature and emissivity for each band is unknown, an assumed emissivity value is used. With this value, the Planck equation is calculated for each band to solve for temperature. Whichever band produces the highest output temperature is assumed to contain the assumed emissivity maximum, and this temperature is then used to solve for emissivity in each of the remaining bands. A pixel from each image was extracted and each spectrum subtracted from the other two to obtain the Δε. Generally, the emissivity spectra appear to have similar spectral shapes, with the primary differences being in absorption band depth. As spectral shape and absorption band depth are an important factor in the linear deconvolution approach used here (Section 3.3.1), demonstrating that the correct data product should be carefully selected.

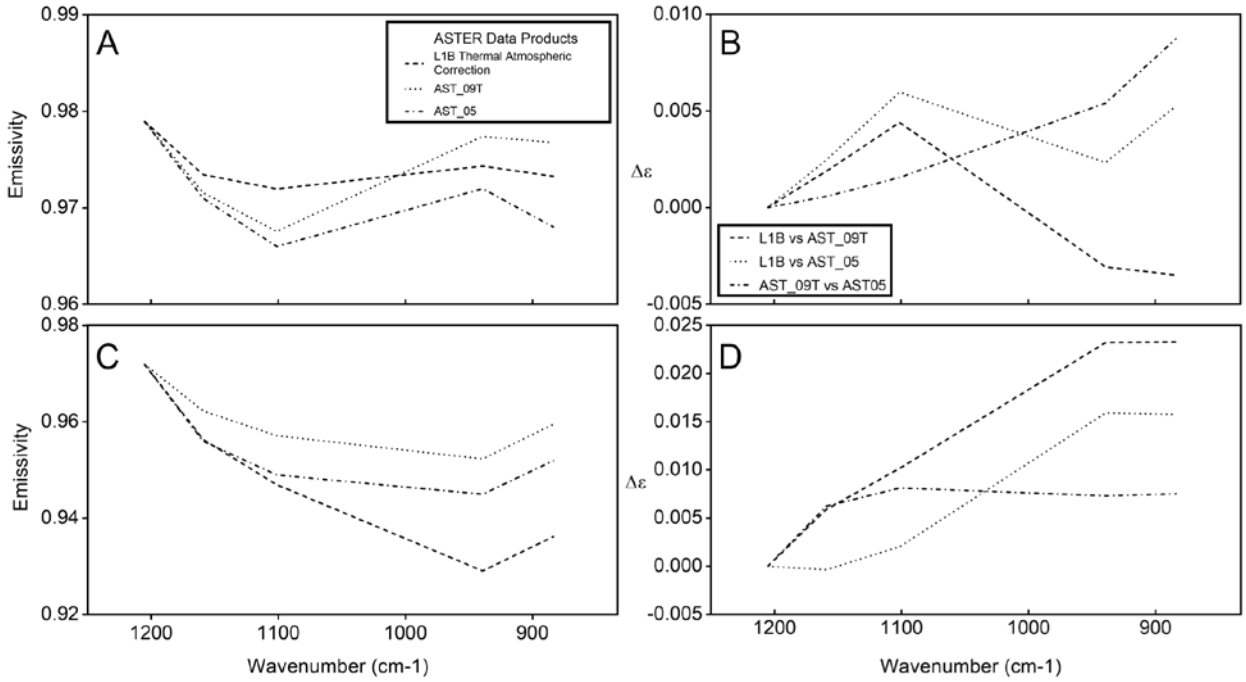

Figure 3-4 Emissivity spectra derived from the same image pixel and difference plots between each data product for Chaitén (A, B) and Sakurajima (C, D). Sakurajima produced greater variation between each spectrum, whereas for Chaitén, those differences are much less (< 1 %). The difference between the AST_09T and AST_05 data products is < 1% in both cases.

3.3 METHODS

3.3.1 Linear Spectral Deconvolution

The model used to map the ash petrology and particle size is the linear spectral deconvolution model described by Ramsey and Christensen (1998). The model is based on the principle that each component contributes in areal proportionality to the overall spectrum. This is expressed mathematically for η isothermal end-members as,

$$\varepsilon(\lambda)_{mix} = \sum_{i=1}^{\eta} \zeta_i \varepsilon(\lambda)_i + \delta(\lambda); \qquad \sum_{i=1}^{\eta} \zeta_i = 1.0 \tag{3.1}$$

where $\varepsilon(\lambda)_{mix}$ is the mixture spectrum, ζ_i is the areal fraction of the ith end member ($\varepsilon(\lambda)_i$) and $\delta(\lambda)$ is the residual error. A root-mean-square error (RMS) analysis provides a method of determining the "goodness of fit" and is expressed as one value for the five ASTER bands. This is determined via the equation,

$$RMS = \sqrt{\frac{\sum_{j=1}^{m} \delta(\lambda)_j^2}{m}} \tag{3.2}$$

where m is the number of instrument bands. This error is a value between 0 and 1.0, where lower numbers correspond to a better fit of the particular model iteration. Where the model is applied to ASTER data, it calculates the percentage of each end member that is present

in each pixel, along with the RMS for each pixel in the form of model output image data. These data can then be used to firstly determine the best fit of each ash sample to the image and then to map the particle size variations along the plume

In order to accurately map the ash component of the opaque plume, an appropriate end-member library is required as input to the model. The library used is the ASTER Volcanic Ash Library, described in Chapter 2. This library contains volcanic ash samples from a variety of different volcanic settings, representing differing wt. % SiO_2. These are further subdivided into size fractions to allow for both petrologic and particle size mapping.

3.3.2 Determining Ash Cloud Opacity

The aim of this study is to map the component of the plume that is opaque, which is assumed to act as an emission source. Therefore, to constrain the purely opaque regions of the plume, it is important to set a series of quality flags that allow discrimination of the opaque regions.

The first of these is the BTD method, as described in in section 3.2.1. In the BTD method, ash plume bearing pixels must be transparent for the algorithm to obtain a negative BTD and thus retrieve ash (Figure 3-5). However, in this method it is possible to isolate plume bearing pixels with a positive BTD. A value of $\geq$ - 0.25 K was recommended for this study, as this accounts for errors with the BTD method (M. Pavalonis, pers. comm). The second test used was to determine the plume top temperature required to isolate plume pixels from those of the ground. Several transects across the plume are taken in order to determine this temperature threshold (Figure 3-6). Where ground upwelling transmission is present in a pixel there is a marked increase in the brightness temperature detected by the sensor. Once the thresholds for the

three parameters are determined, a mask can then be created, applied to each end-member dataset, and the pixels retrieved.

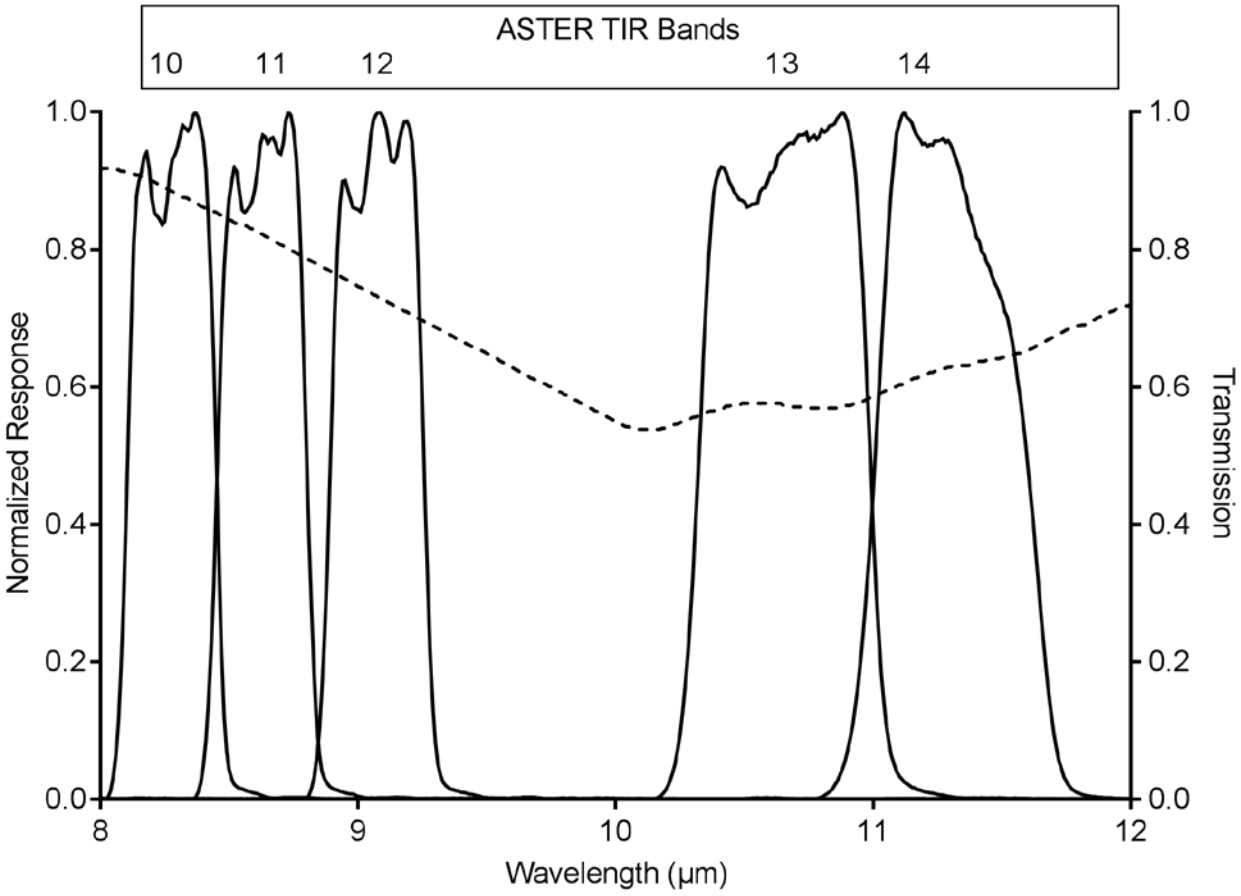

Figure 3-5 ASTER TIR band spectral response (solid lines) compared to the transmission spectrum of an andesitic volcanic ash (dashed line), including both the absorbed and scattered component (after Watson et al., 2004). The increase in transmission between bands 13 and 14 demonstrates that the BTD technique is still a viable method to aid in determining ash plume opacity

3.3.3 Example volcanoes

Several volcanoes were selected for this work and were divided into two categories. The first was to take ASTER data of eruptions occurring at volcanoes where samples listed in chapter 2 (Table 2-1) were obtained. Eruption data from Sakurajima, Volcán De Fuego, Santiaguito and Soufrière Hills Volcano (SHV) were obtained, the presence of an opaque ash plume ascertained, and if present, were processed using the linear deconvolution model. It was important to determine if the laboratory spectra found in the AVAL library were a fit to ASTER TIR spectra from opaque plume bearing pixels. A total of 59 scenes were found using the NASA Earthdata system (https://earthdata.nasa.gov/). For a full list of scenes used in this work, please refer to Appendix B.

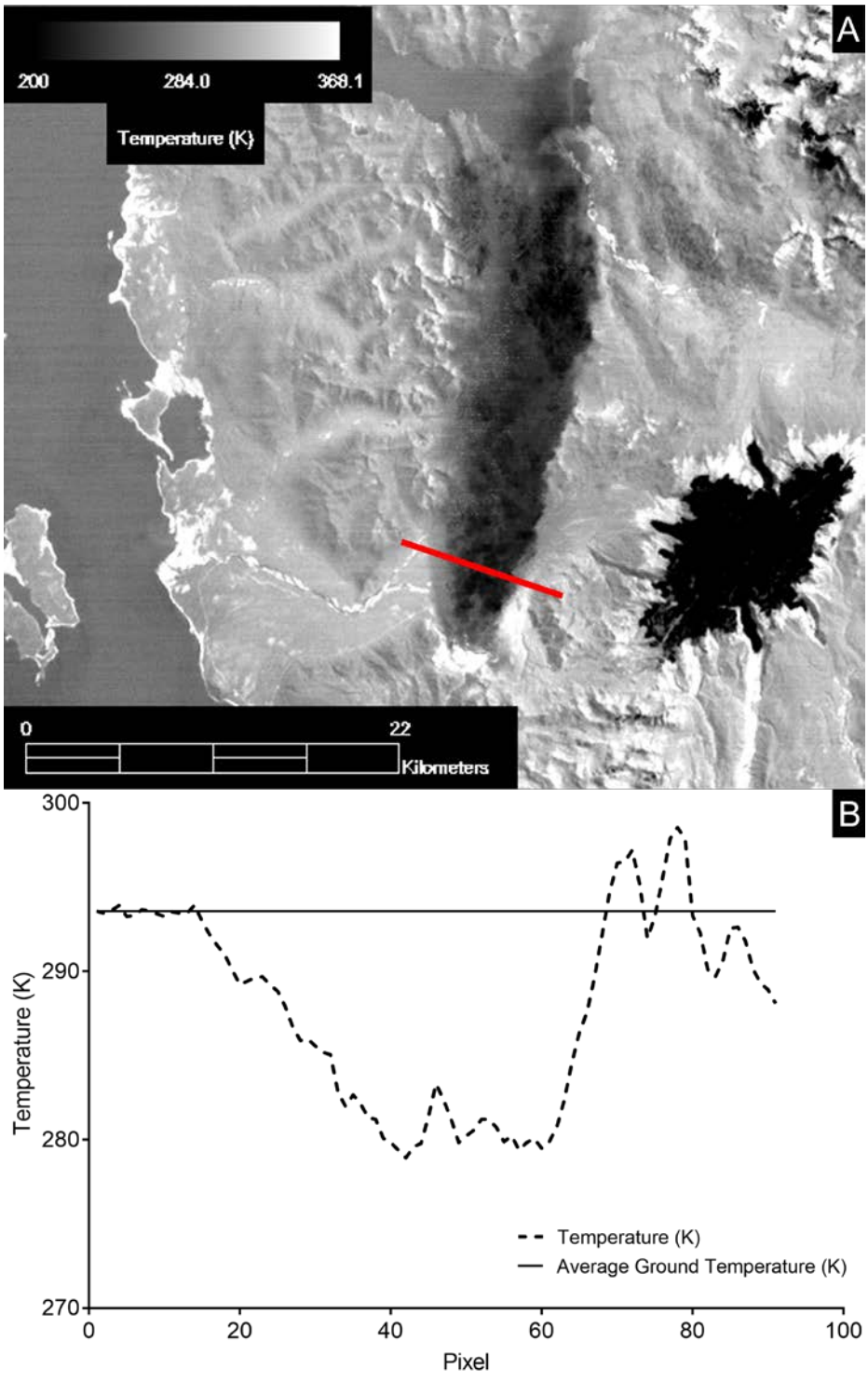

Figure 3-6 Transect taken through an ASTER scene of Chaitén volcano (A; red line). Temperature is lower in plume bearing pixels, demonstrated by the ~ 10 K difference between the plume and the average ground temperature.

Additional image data were also processed from a series of non-sampled volcanoes. This was the second to test, to determine whether or not the ash samples in AVAL were considered appropriate end-members to determine the particle sizes present and an estimation of bulk composition. 11 image data sets were obtained for eruptions from, Calbuco (Chile) and Eyjafjallajökull (Iceland). Furthermore, as a test to see if the high silica glass end-member could be used as an appropriate match for eruptive material from rhyolitic eruptions. Two volcanoes have produced material of this composition in the last 9 years, Chaitén and Puyehue-Cordón Caulle (both Chile). 11 ASTER image data sets contained plume bearing pixels which were analyzed.

3.4 RESULTS

The results obtained from each volcano are presented here. Each of the volcanoes listed is processed using the libraries described in chapter 2. As the Santiaguito and Sakurajima samples collected in different years had very similar spectral features, only one of each is used for this work – Sakurajima 2013 and Santiaguito 2016. Five libraries are used in total. This is to determine if not only particle size but also composition could be determined. For the AVAL sampled volcanoes, only Volcán de Fuego was not analyzed, because no clear ASTER scenes of the plumes were present in the archive. Each image is then processed using the particle size end-members found in libraries of a specific composition. As an addition to this, the final results section focuses on two image datasets, from Sakurajima and Chaitén, where mixtures of different libraries are used as the end-members, to determine if these plumes cover a range of compositions within the same image, as opposed to just one.

3.4.1 AVAL Sampled Volcanoes

3.4.1.1 Sakurajima

Ten ASTER scenes from the Sakurajima volcano, Japan are identified as containing volcanic ash plumes. These were captured between March 2011 and December 2012. Sakurajima regularly produces small vulcanian style eruption plumes rather than those that are sustained and more energetic. Whereas ten images were identified as containing a plume, only six images were actually chosen as appropriate for study with the linear deconvolution method. Three of the end members produced significantly more accurate results, those being the Obsidian, Sakurajima, and Santiaguito libraries. Errors for these three are regularly below 10 %, with the majority of pixels for each being the < 1 – 5 % range. However, the Sakurajima end-member was not always the best fit to the data, with the obsidian end-member providing a much lower average RMS error than the Sakurajima end-member. This may point to the sample that was collected from Sakurajima not necessarily being representative of the material that was airborne at this time. The appropriateness of the obsidian library may also indicate a more silicic glass composition found within these clouds than that collected on the ground. The particle size distribution for these end members was almost bimodal, with finer particles dominated the center of the plume, and larger fractions found towards the edges.

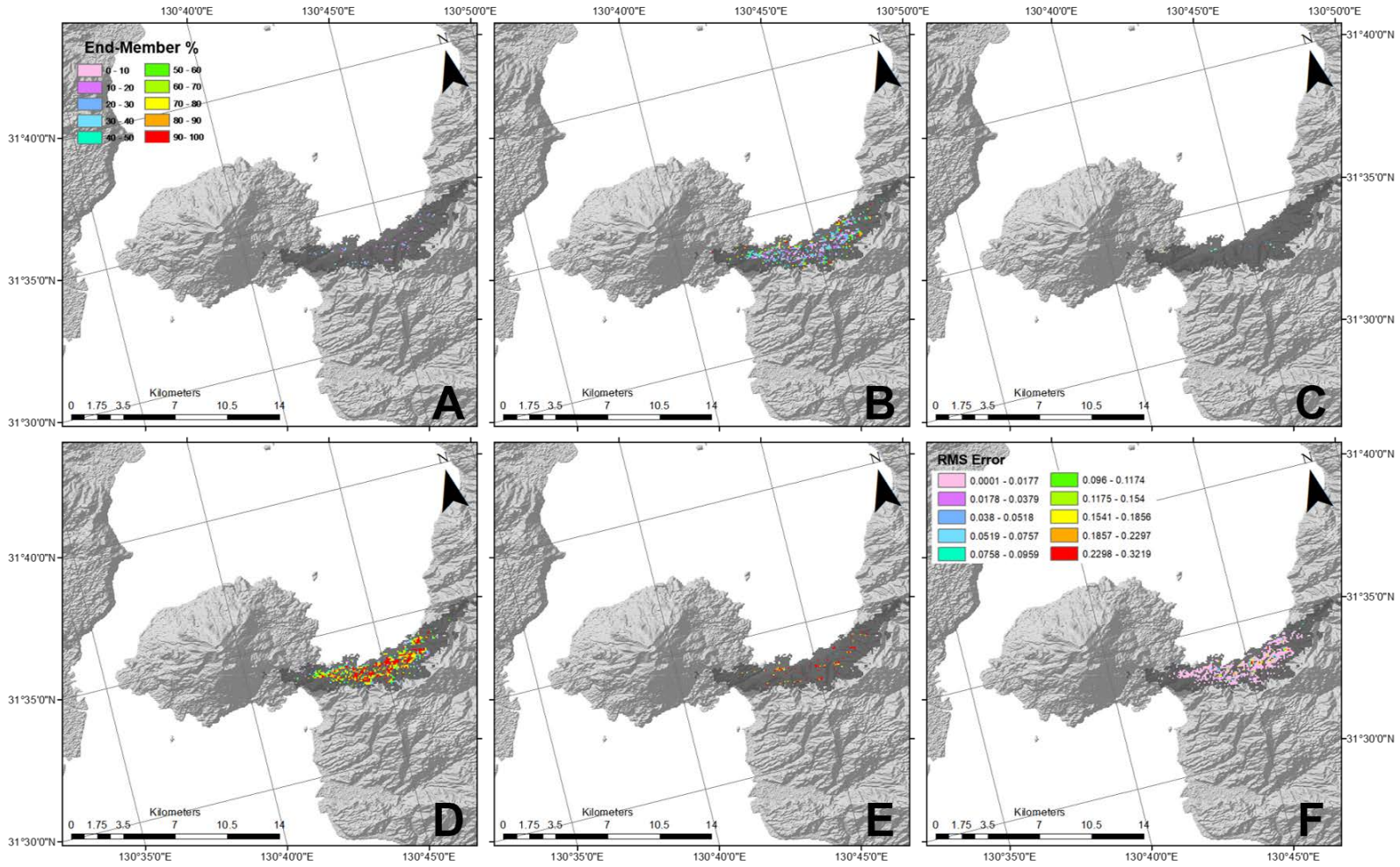

Figure 3-7 Data retrieved from Sakurajima volcano, captured by ASTER on 29 April 2010. These results are from the Sakurajima end-member. The dark area is the approximate area of the plume based upon the temperature and is overlain for retrieved pixel clarity. A) 63 – 150 µm end-member; B) 8 - 25 µm end-member; C) < 8 µm end-member; D) 8 - 25 µm end-member; E) < 8 µm end-member; F) RMS Error. Average error for this retrieval is 2.02 %.

3.4.1.2 Santiaguito

A Santiaguito eruption is captured in an ASTER scene obtained on 17 May 2016, shown in Figure 3-8. However, what is noted is that the plume captured was diffuse, and so contained a large number of BTD negative pixels that therefore not relevant to this study. A small region of opaque pixels was produced from the results, with the Santiaguito library producing a close fit to the data (~ 1 % RMS error), as did the obsidian library. The three other libraries did produce ash retrievals, and the RMS errors in these images are significantly higher than the other two libraries (> 10 %). In this section, a large range of particle sizes is detectable, as the plume is close to vent. Because little settling would have occurred at this point, the mixture of particle sizes present at this location is expected.

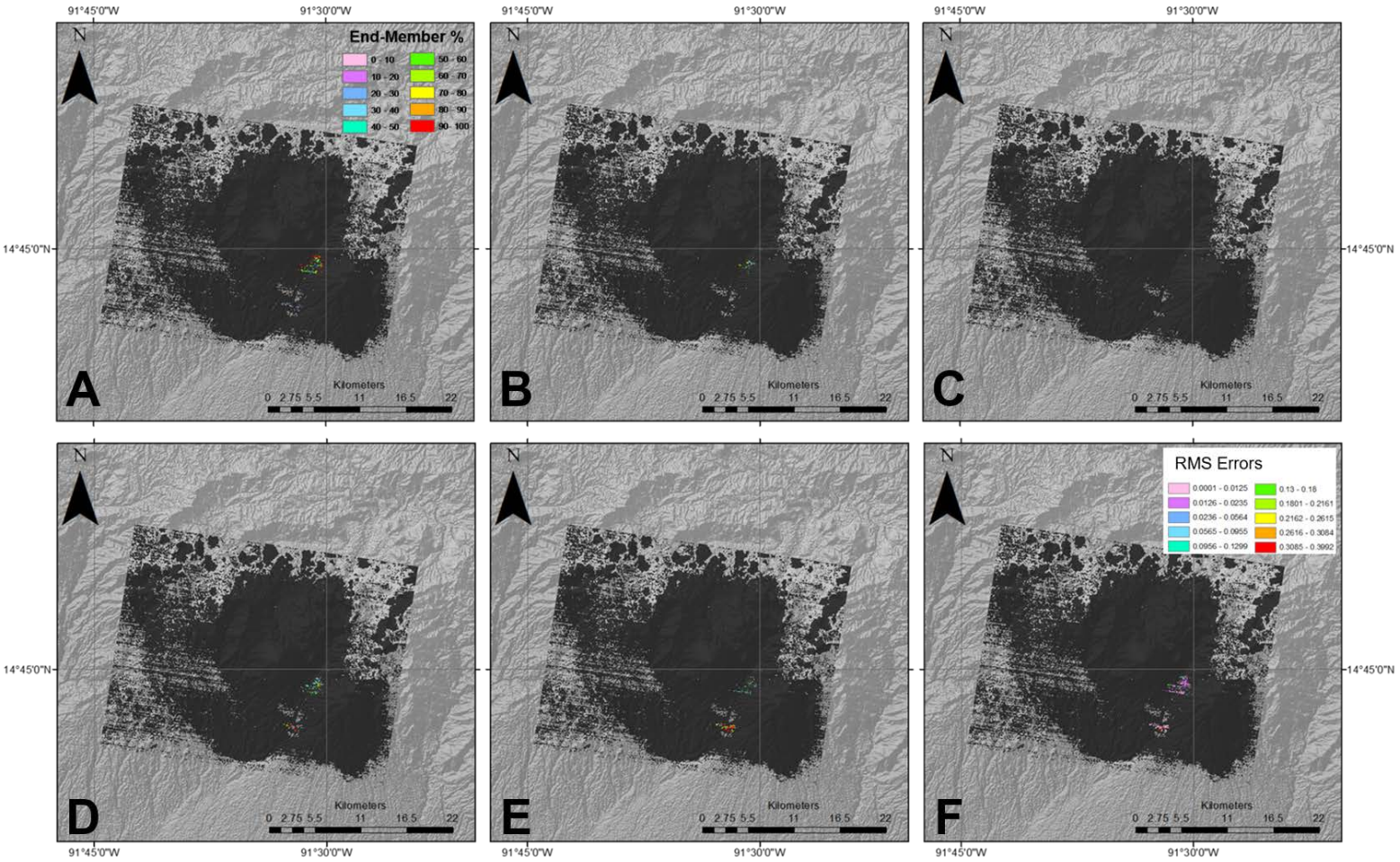

Figure 3-8 Data retrieved from Santiaguito volcano, captured by ASTER on 17 May 2016. These results are from the Santiaguito end-member. The dark area is the approximate area of the plume based upon the temperature and is overlain for retrieved pixel clarity. A) 63 – 150 µm end-member; B) 8 - 25 µm end-member; C) < 8 µm end-member; D) 8 - 25 µm end-member; E) < 8 µm end-member; F) RMS Error. Average error for this retrieval is 6.04 %.

3.4.1.3 Soufrière Hills Volcano

Seven ASTER scenes of the SHV volcano are captured of ash producing eruptions occurring in 2006, 2008 and 2010. One image from 2006 contained only sporadic opaque pixels and therefore is not appropriate for this study. However, the six remaining images contained significant portions of the plume that are optically thick in the TIR. The SHV and obsidian libraries produced the most consistent results, with RMS errors for these libraries being < 10 %. Santiaguito library also produced low-error results, although not as consistently as the other two libraries. No obvious trend in the particle size distribution was observed, although the most abundant size fractions tended to be those that were finer (< 25 μm).

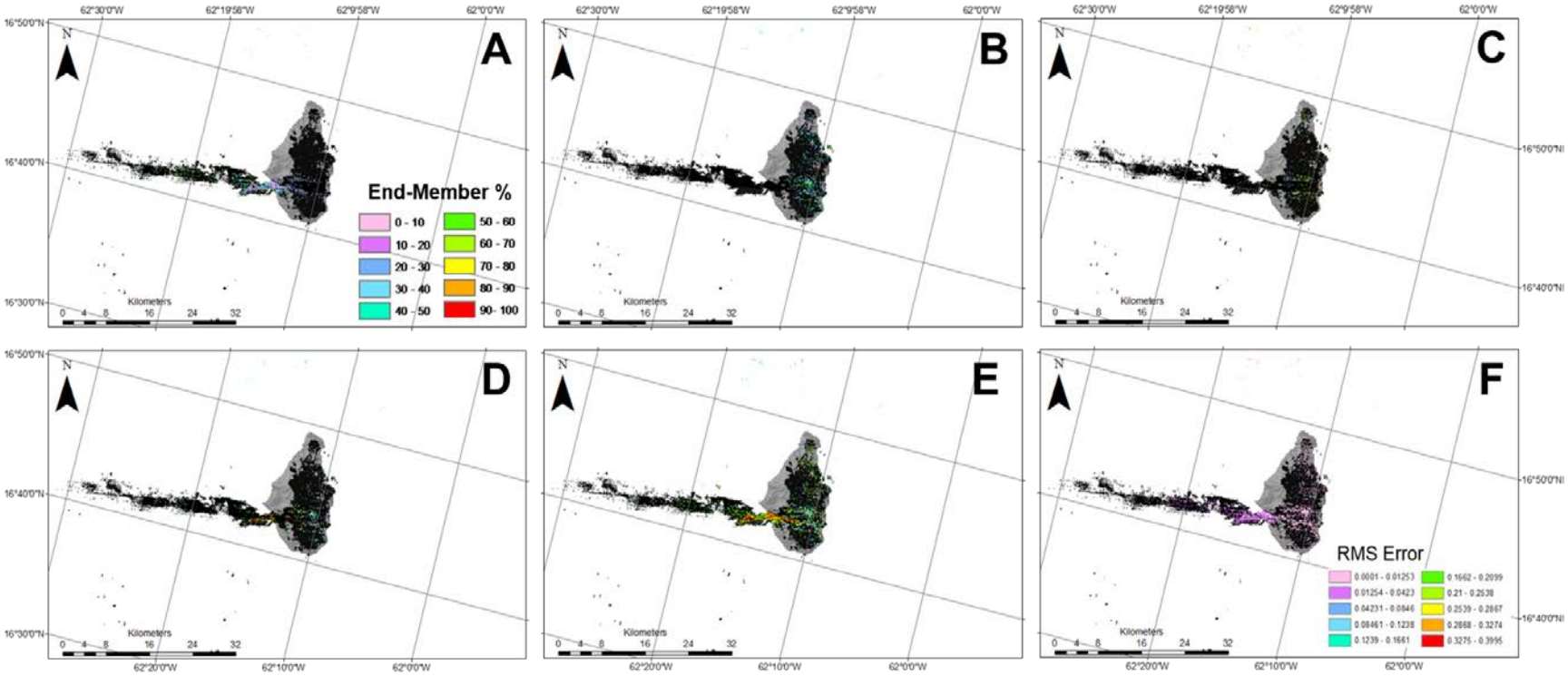

Figure 3-9 Data retrieved from SHV volcano, captured by ASTER on 2 December 2009. These results are from the SHV end-member. The dark area is the approximate area of the plume based upon the temperature and is overlain for retrieved pixel clarity. A) 63 – 150 µm end-member; B) 8 - 25 µm end-member; C) < 8 µm end-member; D) 8 - 25 µm end-member; E) < 8 µm end-member; F) RMS Error. Average error for this retrieval is 1.97 %.

3.4.2 Non-AVAL Sampled Volcanoes

3.4.2.1 Calbuco

One ASTER scene is collected from the April 2015 eruption of Calbuco volcano, Chile. The volcano experienced a sub-plinian style eruption 22 April 2015, with several pulses of activity recorded until the 23 April (Romero et al., 2016). In the subsequent days up until 30 April, activity was marked by brief, vulcanian-style eruptions. The opaque portion of the plume is connected to the vent, with the model failing after ~10 km downwind where the plume became transparent. Romero et al., (2016) and Castruccio et al. (2016) reported that the tephra fallout composition ranged from basaltic-andesite to andesite, with some sample sites also yielding material that was basaltic and dacitic. All five libraries produced low RMS error (< 10 %) retrievals from this cloud. In each the particle size variation does not alter drastically, with a mixture of particles present. No obvious particle size distribution trends are present, with the opaque plume appearing a random mixture of the end-members.

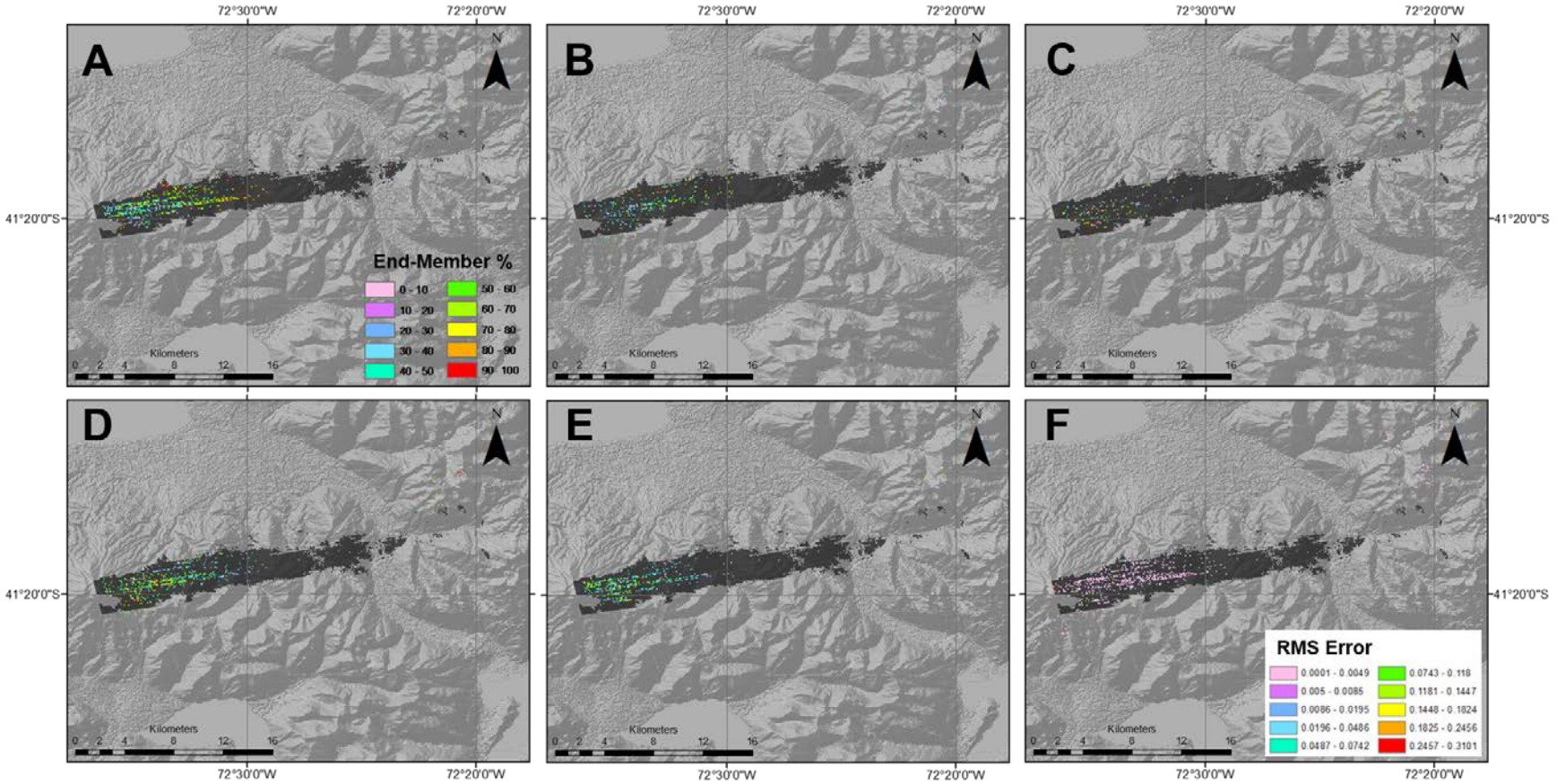

Figure 3-10 Data retrieved from Calbuco volcano, captured by ASTER on 26 April 2015. These results are from the Santiaguito end-member. The dark area is the approximate area of the plume based upon the temperature and is overlain for retrieved pixel clarity. A) 63 – 150 µm end-member; B) 8 - 25 µm end-member; C) < 8 µm end-member; D) 8 - 25 µm end-member; E) < 8 µm end-member; F) RMS Error. Average error for this retrieval is 1.19 %.

3.4.2.2 Chaitén

A total of five ASTER scenes contain eruptions of Chaitén volcano between May 2008 and March 2009. The initial eruptions occurred on 1 May 2008, in an unexpected manner as earthquakes were only felt in the region 24 hours before the onset of the first eruptions (Castro and Dingwell, 2009). The material erupted from this volcano is rhyolitic in composition, and in the five ASTER scenes analyzed for this work, the libraries of more silicic material, in particular Santiaguito, and the Mono Obsidian produced the retrievals with the lowest RMS errors associated. The Sakurajima end member only retrieved ash particle size ranges in 3 of the 5 images, and even then, pixels frequently recorded RMS errors in the 10 – 30 % range. Of the plumes measured, the smallest size fractions dominate the proximal plume region. Of the larger particle sizes detected, the 45 - 63 μm fraction is commonly detected, with particles > 63 μm rarely being detected in large quantities and were confined to the plume edges (Figure 3-11), or in pixels that were adjacent to the vent. Interestingly in the example shown in Figure 3-11, coarser particles are seen almost exclusively around the plume edges.

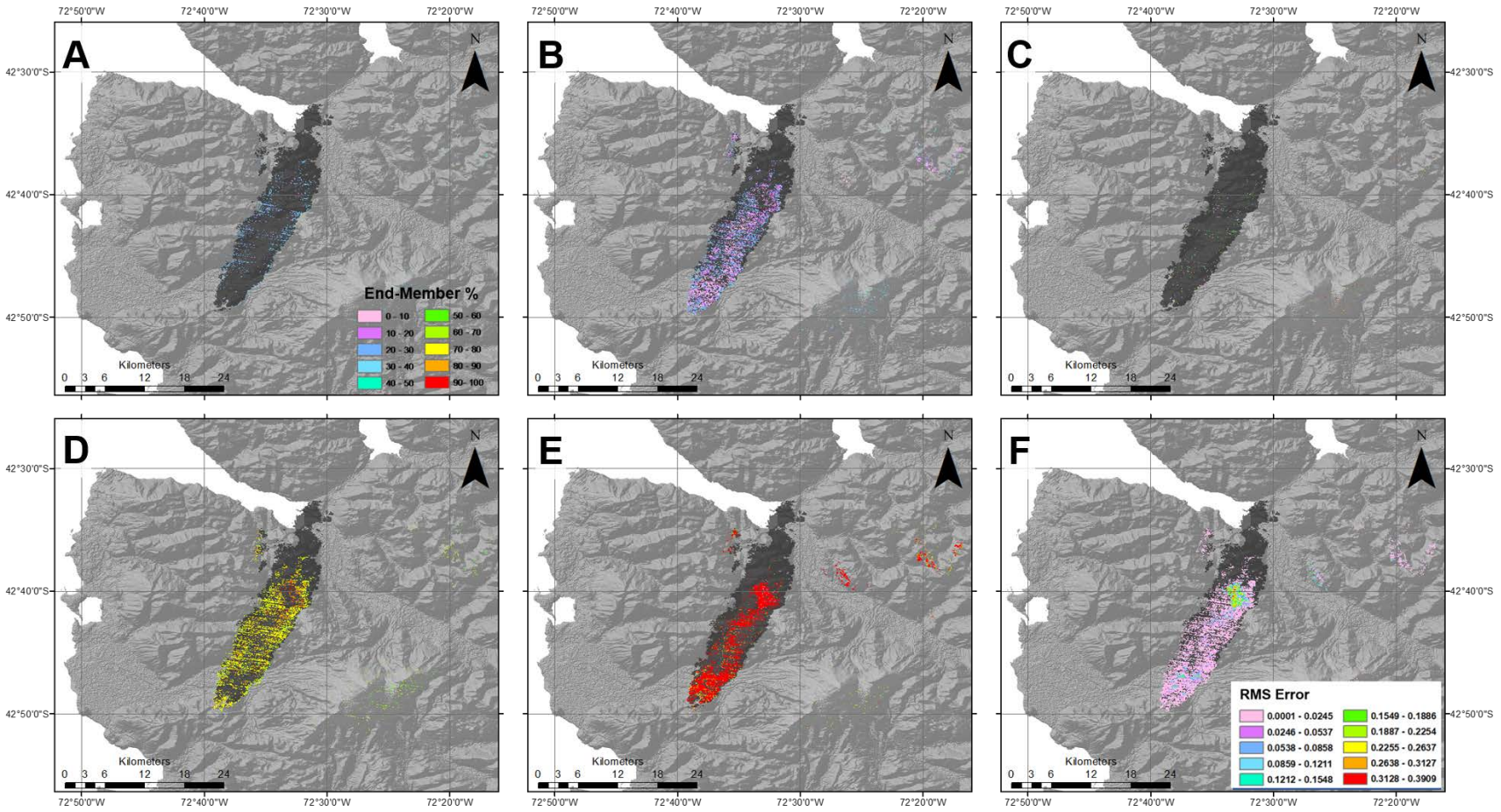

Figure 3-11 Data retrieved from Chaitén volcano, captured by ASTER on 19 January 2009. These results are from the Mono-Inyo Obsidian end-member. The dark area is the approximate area of the plume based upon the temperature and is overlain for retrieved pixel clarity. A) 63 – 150 µm end-member; B) 8 - 25 µm end-member; C) < 8 µm end-member; D) 8 - 25 µm end-member; E) < 8 µm end-member; F) RMS Error. Average error for this retrieval is 2.74 %.

3.4.2.3 Eyjafjallajökull

The 2010 Eyjafjallajökull eruption was the culmination of 18 years of volcanic unrest at the volcano, with an effusive eruption of basaltic lava between 20 March and 12 April preceding explosive events that began on 14 April and lasted until 22 May (Sigmundsson et al., 2010; Stohl et al., 2011). Plumes reached from 3 – 10 km into the atmosphere, derived from an early hydromagmatically driven phase, followed by a magmatically driven phase of the eruption (Gislason et al., 2011). With an extensive threat to air travel caused by this eruption, the ash produced is extensively studied. The first two days of explosive activity is defined by ash samples that had a wide range of compositions (60 - 69 % wt. SiO_2), followed by a lower discharge phase with weaker but sustained explosive plumes with a marked drop in SiO_2 content (58 – 59 %), and then a second explosive phase that saw the eruption of more silicic material again. A final phase was observed with limited ash erupted and typified by the venting of a persistent steam plume over the vent (~ 65 % wt.; Gudmundsson et al., 2012). Twleve ASTER scenes were obtained on 7 days of the eruption with several of these being larger mosaics of the same plume. For this volcano, all but the Sakurajima library provided a significant number of retrieved pixels. The obsidian library provided the best fit (example in Figure 3-12), however RMS errors had a wide range, from < 10 – 30 %, which is likely representative of the varied composition of the material erupted between April and May 2010. The particle size ranges detected tended more towards the finer size fractions (< 45 μm), although a greater number of pixels are retrieved with these particle size fractions for the more explosive phase of the eruption in April, compared to image obtained during May, where the two large size fractions became more evident.

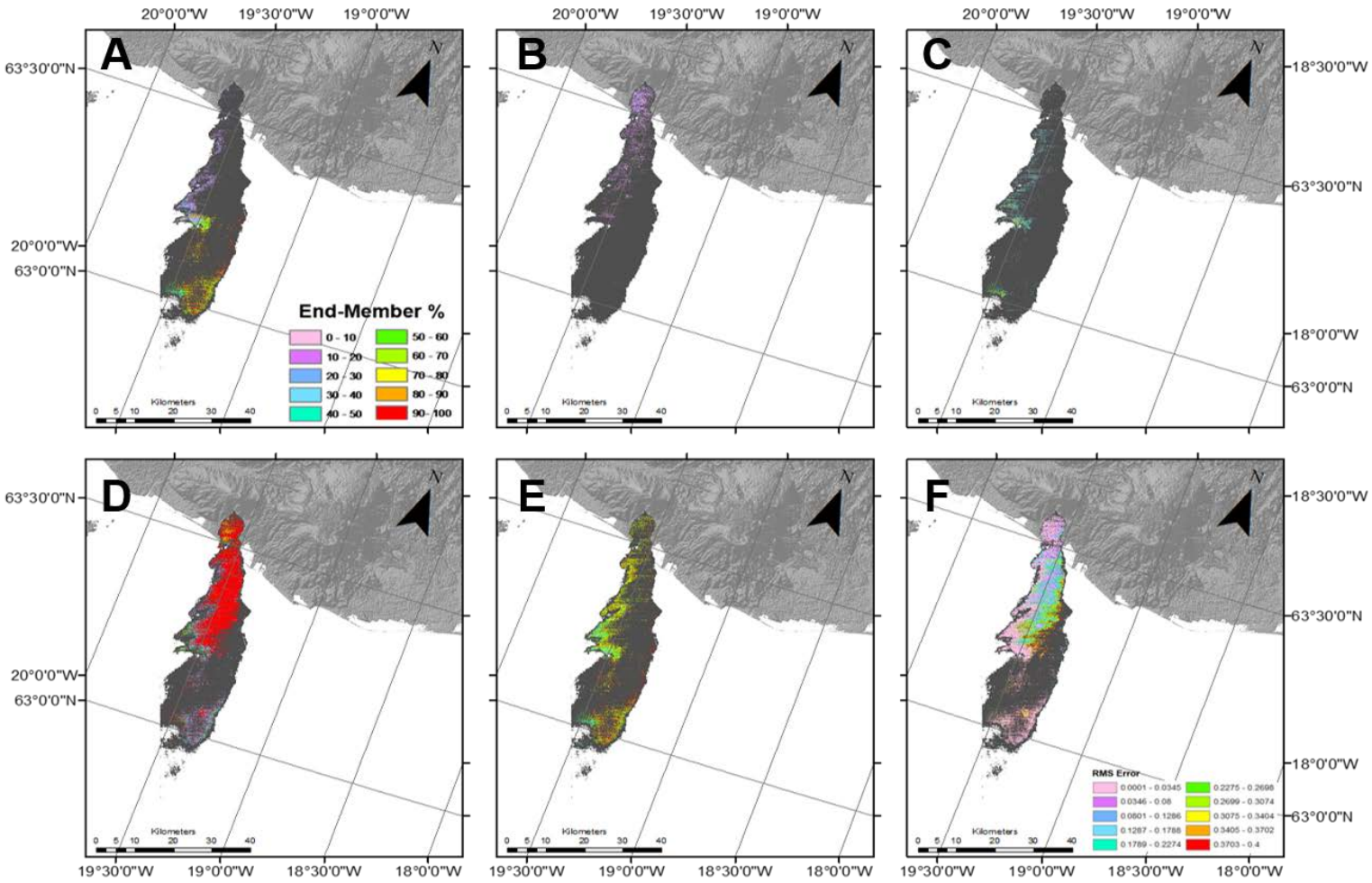

Figure 3-12 Data retrieved from Eyjafjallajökull, captured by ASTER on 17 April 2010. These results are from the Santiaguito end-member. The dark area is the approximate area of the plume based upon the temperature and is overlain for retrieved pixel clarity. A) 63 – 150 µm end-member; B) 8 - 25 µm end-member; C) < 8 µm end-member; D) 8 - 25 µm end-member; E) < 8 µm end-member; F) RMS Error. Average error for this retrieval is 11.34 %.

3.4.2.4 Puyehue-Cordón Caulle

The Puyehue-Cordón Caulle volcano is a large basaltic to rhyolitic volcanic complex in Chile, that began a series of sub-plinian eruptions on 4 June 2011 (Bignami et al., 2014). The eruptions were marked by both effusive and explosive activity, with rhyolitic lava flows being emplaced from the eruptive fissure (Tuffen et al., 2013). Volcanic ash clouds formed by this eruption were captured by satellite remote sensing platforms traversing the southern hemisphere (Klüser et al., 2013). The ASTER sensor collected data from these eruptions in June 2011, and February 2012. 4 of the 6 images obtained provided retrievals of volcanic ash. The obsidian end-member library provides the best retrieval for these images in terms of RMS, with the average error below 10 %, with the other 4 libraries, whereas providing retrievals of particle size variations, had fluctuating errors between < 1 and < 30 %. Particle size ranges are primarily dominated by the < 25 μm fractions, although larger size fractions (45 – 63 μm and in particular 63 – 150 μm) made up a significant portion of the cloud's area. Furthermore, in the example shown in Figure 3-13, particles in the largest size range (63 – 150 μm) are seen in increasing number as distance from the vent increases.

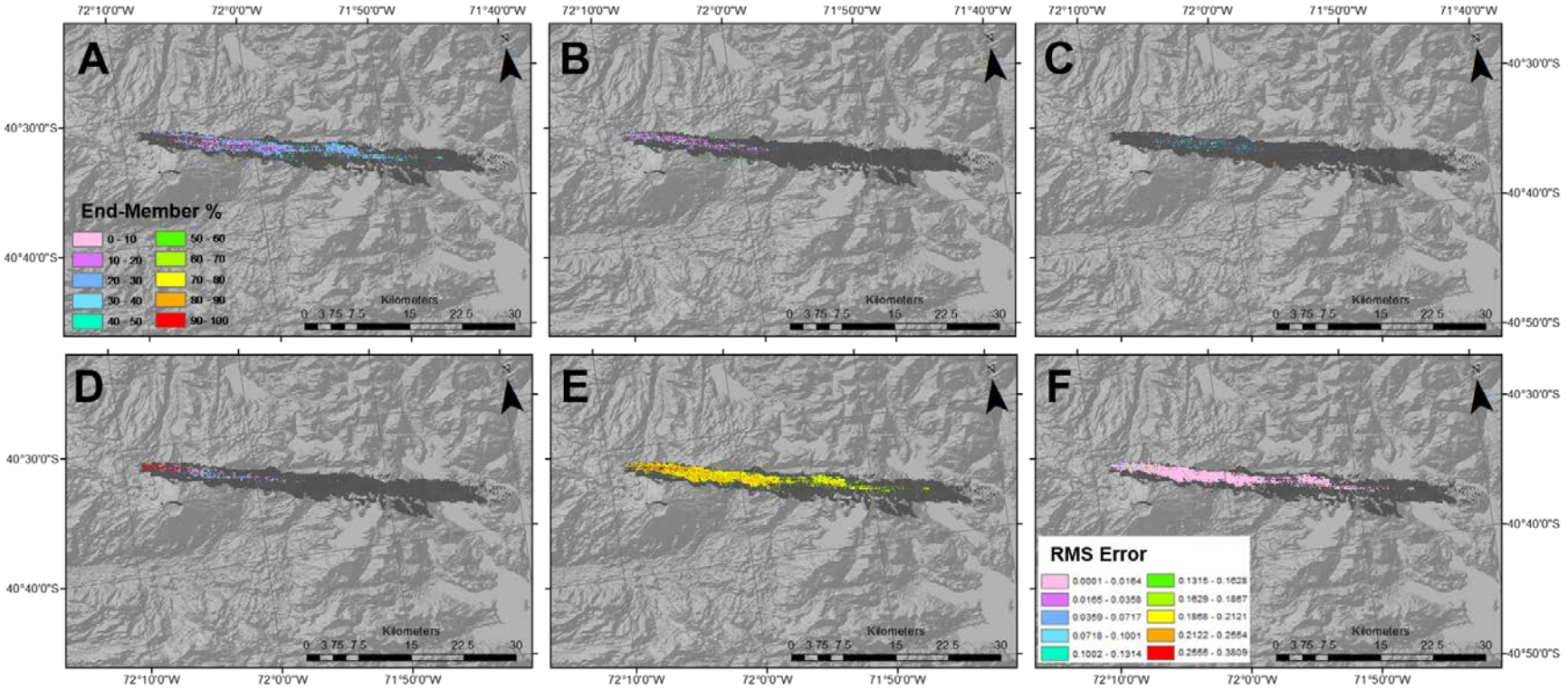

Figure 3-13 Data retrieved from Puyehue-Cordón Caulle, captured by ASTER on 13 February 2012. These results are from the Mono-Inyo Obsidian end-member. The dark area is the approximate area of the plume based upon the temperature and is overlain for retrieved pixel clarity. A) 63 – 150 µm end-member; B) 8 - 25 µm end-member; C) < 8 µm end-member; D) 8 - 25 µm end-member; E) < 8 µm end-member; F) RMS Error. Average error for this retrieval is 1.07 %.

3.4.3 Library Mixture Test

To test these results, an ASTER scene obtained on 29 April 2010 of Sakurajima is analyzed using a mixture of the Sakurajima (2013) and Mono-Inyo Obsidian end-member libraries. These both produced low RMS retrievals, but the analysis of this image in particular is of interest given that the RMS where the Sakurajima library was used was 2.26 %, compared to 0.61 % where the Mono-Inyo Obsidian library was used. The analysis is constructed using combinations of each end-member library in an attempt to see if these mixtures would produce a lower RMS error, meaning that the cloud observed is composed of a mixture of different materials. The model was repeatedly run by adding or subtracting end-members until the lowest RMS was calculated. The results for each iteration are present in Table 3-4. The two most accurate retrievals produced were using four < 45 µm fractions were used, coupled with a 63 - 150 µm end-member. These results demonstrated the predominance of fine grained volcanic ash within the plume, intermixed with ~ 15 % coarser material. Of interest is this intermixing compared to the results discussed previously, as no zoning of larger particles at the edge of the plume is shown. These results are shown in Figure 3-14.

Table 3-4 Results for 10 iterations of the linear deconvolution model performed on an image from Sakurajima volcano obtained 29 April 2010. Black cells indicate that the end-member listed was not used for that iteration of the model. The first two iterations were performed using the pure end-member libraries. Iterations 3 – 10 are listed in order of decreasing RMS.

Iteration	Sakurajima 2013					Mono-Inyo Domes Obsidian					Average RMS
	63 – 150 µm (wt. %)	45 – 63 µm (wt. %)	25 – 45 µm (wt. %)	8 – 25 µm (wt. %)	< 8 µm (wt. %)	63 - 150 µm (wt. %)	45 – 63 µm (wt. %)	25 – 45 µm (wt. %)	8 – 25 µm (wt. %)	< 8 µm (wt. %)	
1	9.121	64.664	0.413	23.879	1.923						0.0226
2						10.386	0.698	3.760	72.633	12.523	0.0061
3	12.819	2.173	84.968			0.040	0.000				0.1689
4	7.488	43.842				0.000	0.000	48.670			0.0188
5	2.906			39.506	25.469		0.000	32.120			0.0183
6		0.780		42.378		5.780	6.56			42.998	0.0080
7			54.237	1.067	16.524				7.018	20.957	0.0071
8				36.748	24.748			18.546	6.235	13.723	0.0065
9	14.041		30.592		26.252			3.050		26.064	0.0051
10				18.815	27.654	13.028			2.813	37.691	0.0048

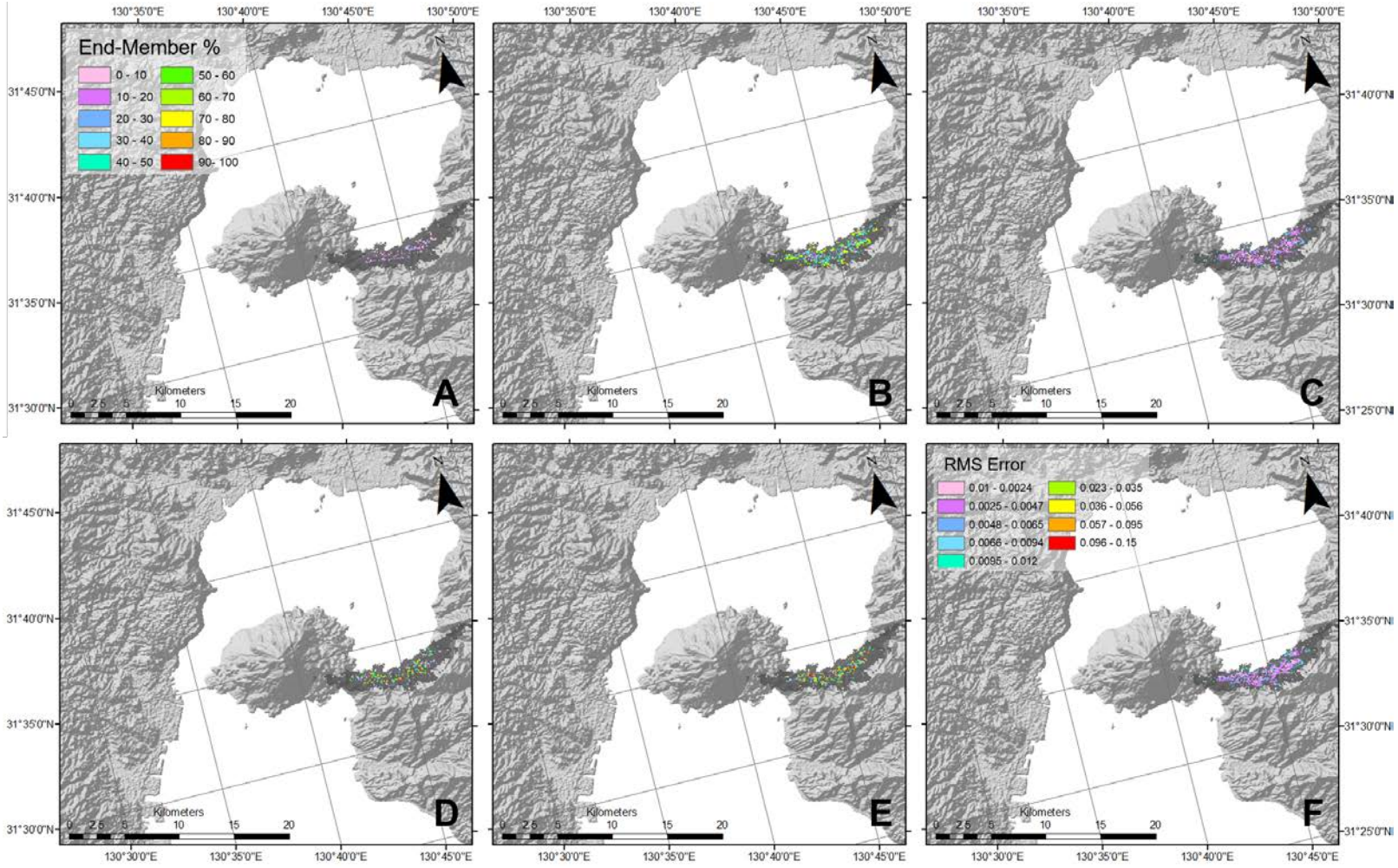

Figure 3-14 The best model iteration of ASTER image data of the 29 April 2010 eruption of Sakurajima volcano. The dark area is the approximate area of the plume based upon the temperature and is overlain for retrieved pixel clarity. A) Obsidian 63 – 150 µm end-member; B) Obsidian 8 - 25 µm end-member; C) Obsidian < 8 µm end-member; D) Sakurajima 8 - 25 µm end-member; E) Sakurajima < 8 µm end-member; F) RMS Error.

3.5 DISCUSSION

The retrieval of composition and particle size of volcanic ash particles from opaque volcanic ash plumes using the TIR provides an important step in being able to understand volcanic ash clouds and the eruptions that formed them. This method has demonstrated promise in being able to routinely observe the opaque portions of plumes. However as with any new method, discussion is needed to determine sources of error and provide direction for improvements.

3.5.1 Model Results

The accuracy of the AVAL library is one of the most important aspects of this work, and it is essential that a wide variety of volcanic ash types are present within it, hence the importance in examining images of sampled and unsampled volcanoes. The accuracy of the laboratory spectral measurements are detailed in Section 2.5.2, and are accurate to within ~ 0.5 %, due to the low NEΔε of the spectrometer. The linear deconvolution model results have, in the majority of cases, showed to have low error associated with them. This was particularly the case for the sampled volcanoes, Santiaguito, SHV and Sakurajima. For the volcanoes with no AVAL samples, the more rhyolitic eruptions (Puyehue and Chaitén) produced results with low errors associated with the Obsidian end-member library. Those with more intermediate compositions produced mixed results, with RMS error for Eyjafjallajökull commonly > 10 %, whereas Calbuco was significantly lower at 1.19 %,

From these observations it may be possible to assume that for samples taken from known volcanoes, the linear deconvolution method coupled with AVAL is valid. However, in many of these cases, not just the library specific to the volcano provided either the best or only fit. This presents somewhat of a conundrum where attempting to determine what the bulk composition of the material is. If this was a phenomenon that was observed in two different parts of the cloud, where one library was best for one region, and another provided the best for a different portion, this may imply that two distinct pulses of material produced from perhaps differing processes. However, the different results commonly cover the same area of pixels. This was seen in the image data from Sakurajima, where both the Sakurajima and Obsidian end-members produced low retrieval errors. Using the linear deconvolution with mixed end-members from two different libraries was considered a possible solution. Where the image data was processed using a mixture of both the Sakurajima and Mono-Inyo Obsidian end-members, greater accuracy was achieved, with 0.48 % the average RMS of the retrieved pixels, with a standard deviation of 0.77 %. The mixture data provides an interesting insight into whether the sample collected on the ground was truly representative of the material present in the cloud at the time of acquisition. Sakurajima presents an interesting case, given the wide range of glass wt. % silica recorded in the glass component (Section 2.2.1.2).

Table 3-5 Details of the linear deconvolution model results for the ASTER scenes discussed in Section 3.4. These data only include the best fit AVAL library where individual compositions are used, as opposed to the mixture test used in section 3.4.3. Average RMS values for the best fit library are given and compared to the reported composition from each volcano. Using Figure 3-15, an estimated SiO_2 enrichment of the ash detected is given. Where the reported composition is in the same range as the AVAL sample used, an average enrichment of the points in Figure 3-15 reported by other investigators is used. In the case of Sakurajima, as the best fit end-member is the Mono-Inyo Obsidian, the enrichment estimate is based on the estimated bulk SiO_2 content compared to the SiO_2 content of the obsidian, which is widely available in the literature (e.g. Varga et al. (1990), who report an SiO_2 value of 71.7 %).

ASTER Scene	Volcano	Best fit AVAL Library	RMS (%)	Reported Composition	Estimated average enrichment (SiO_2)
AST_09T_00304262015034811	Calbuco	Santiaguito	1.19	Andesite	5 %
AST_09T_00301192009145437	Chaitén	Mono-Inyo Obsidian	2.74	Rhyolite	0.5 %
AST_09T_00304172010224304 AST_09T_00304172010224313	Eyjafjallajökull	Santiaguito	11.19	Benmoreite	5 – 7 %
AST_09T_00302132012145257	Puyehue-Cordón Caulle	Mono-Inyo Obsidian	1.07	Rhyolite	0.5 %
AST_09T_00304292010020519	Sakurajima	Mono-Inyo Obsidian	0.61	Andesite	15 %
AST_09T_00301192016164206	Santiaguito	Santiaguito	6.04	Andesite	5 %
AST_09T_00312122009023120	SHV	SHV	1.97	Andesite	5 %

Initially the assumption was that perhaps the cloud examined in the image from 29 April 2010 was simply a much more high-silica glass rich composition, given the low error associated with the retrieval (RMS = 0.8 %). However, through each model iteration it is shown that this error could be reduced further by using end-members from both libraries, provided the appropriate particle size range was chosen. In this instance, 48 wt. % of the cloud was retrieved as Sakurajima ash, with 52 wt. % retrieved as the Mono-Inyo end-member. The mixing of two end-members that have varying wt % glass of different compositions (based upon the Christiansen frequency position discussed in Section 2.5.1) highlights the distinct differences between bulk composition estimated for a volcano based on erupted lithics, the tephra that is deposited proximally to the volcanic, and the composition of the material that remains in the atmosphere (Figure 3-15). Low retrieval errors for the high silica obsidian end-member are common in many of the images discussed here as well, and this may mean that more SiO_2 enriched volcanic material is present in the cloud. It would be prudent for image datasets acquired in the future for them to be unmixed using the obsidian end-member library.

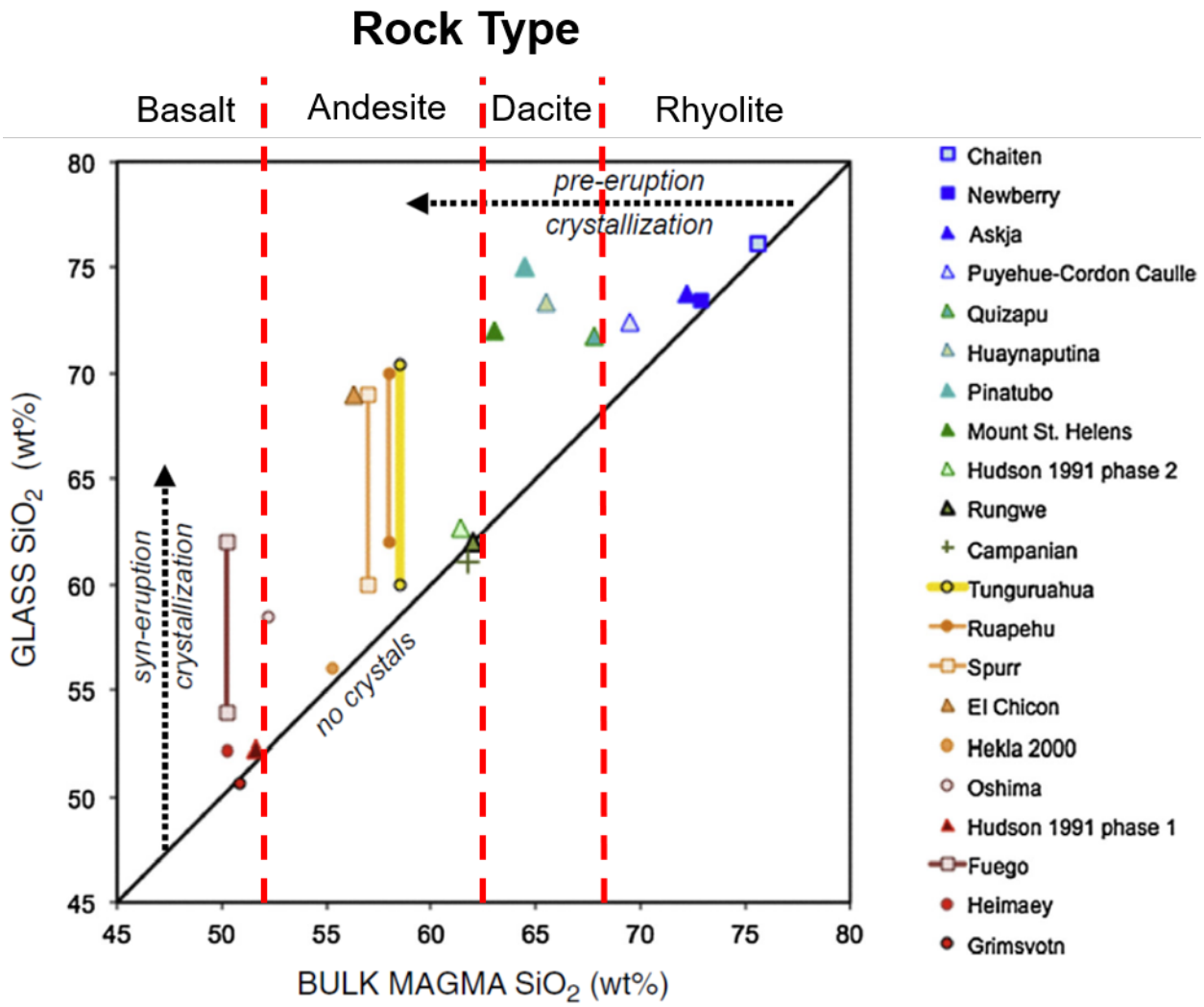

Figure 3-15 Bulk composition SiO_2 concentrations vs those found volcanic glass produced by eruptions from various volcanoes (after Cashman and Rust, 2015). An average glass enrichment of SiO_2 for each rock type was calculated from these points; Basalt 3.2%, Andesite 5%, Dacite 7%, and Rhyolite 0.5%.

A greater number of samples should be added to the library to cover the wide range of material present. What comprises these materials must also be under consideration. Whereas the mineral assemblages present may point to certain compositions, as was shown in Figure 3-15, the glass composition can drastically vary, from having a wt % SiO_2 that is similar to the bulk composition, or one ~ 10 % higher. Given that the samples presented here (Fuego 2015 aside) are predominantly comprise volcanic glass, this composition has exerted a significant control over the spectral shape. This is shown in Figure 3-16, where a mixture of glass and minerals is used to highlight the changes seen in the TIR spectra with changing glass composition, where the mineral assemblage remains constant. It would also appear prudent to complement the AVAL collected samples with a particle size suite of pure glass end-members, to see if an estimated glass SiO_2 enrichment could be obtained from these image data.

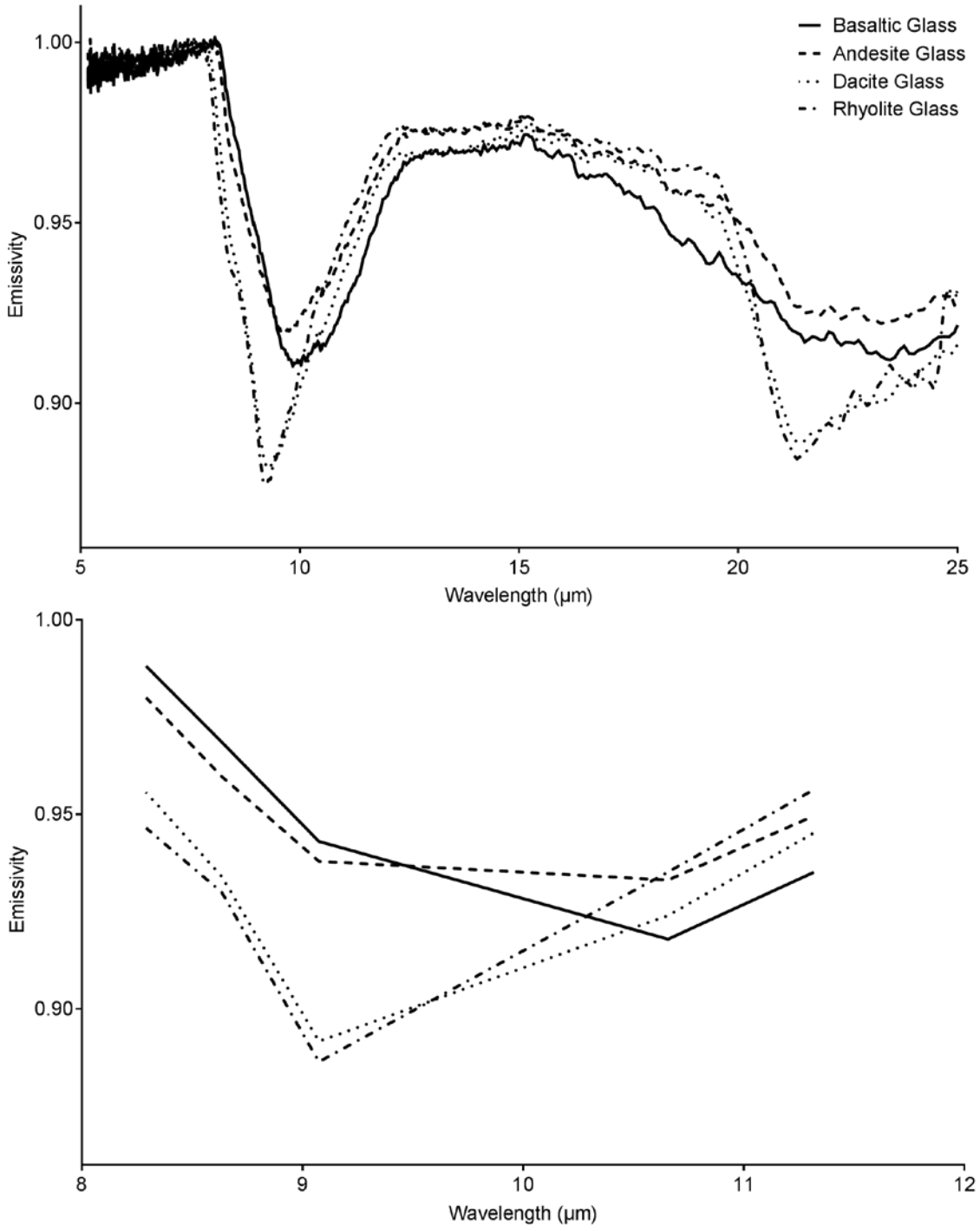

Figure 3-16 Spectra of numerical mixtures of different volcanic glasses (70 %), andesine (25 %), enstatite (2.5 %) and forsterite (2.5 %) at hyperspectral (upper) and AVAL (lower) resolution. The basaltic, andesitic and dacitic glass spectra are taken from Minitti and Hamilton (2010), whereas the rhyolite glass spectrum was the crushed obsidian developed in chapter 3. The mineral end-members were obtained from the ASU TES library (Christensen et al., 2001).

3.5.2 Particle Size Variations

One point of note is that the particle size variations between different end-members stay relatively consistent. Smaller particle sizes tend to be the dominant size fractions detected, particularly for volcanoes that produced larger plumes. These larger plumes are erupted from more explosive volcanoes like Chaitén and Puyehue. For example, the total areal percentage of < 8 μm particles retrieved for the 13 February 2012 eruption of Puyehue Cordón Caulle was 71.9 %. This number does not represent the total percentage of mass of particles in the whole cloud, but the particles found at the uppermost surface. This is also true of the end-member mixture solution, where fine grained fractions from Sakurajima and Mono-Inyo obsidian comprised 87 % of retrieved pixels, and 13 % was made up of the 63 – 150 μm Mono-Inyo end-member.

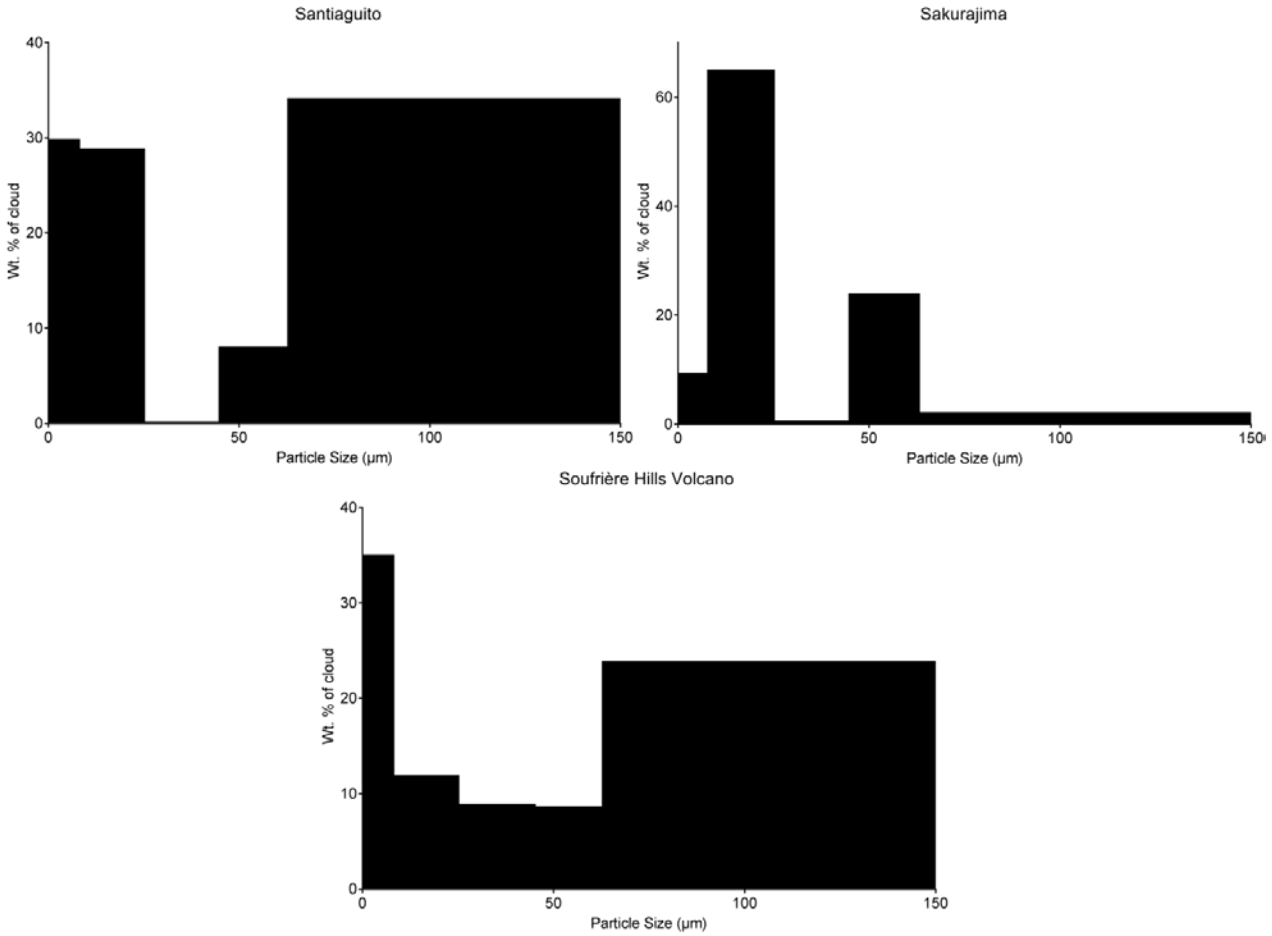

Figure 3-17 Particle size ranges by wt. % of total number of retrieved pixels for the AVAL sampled volcanoes

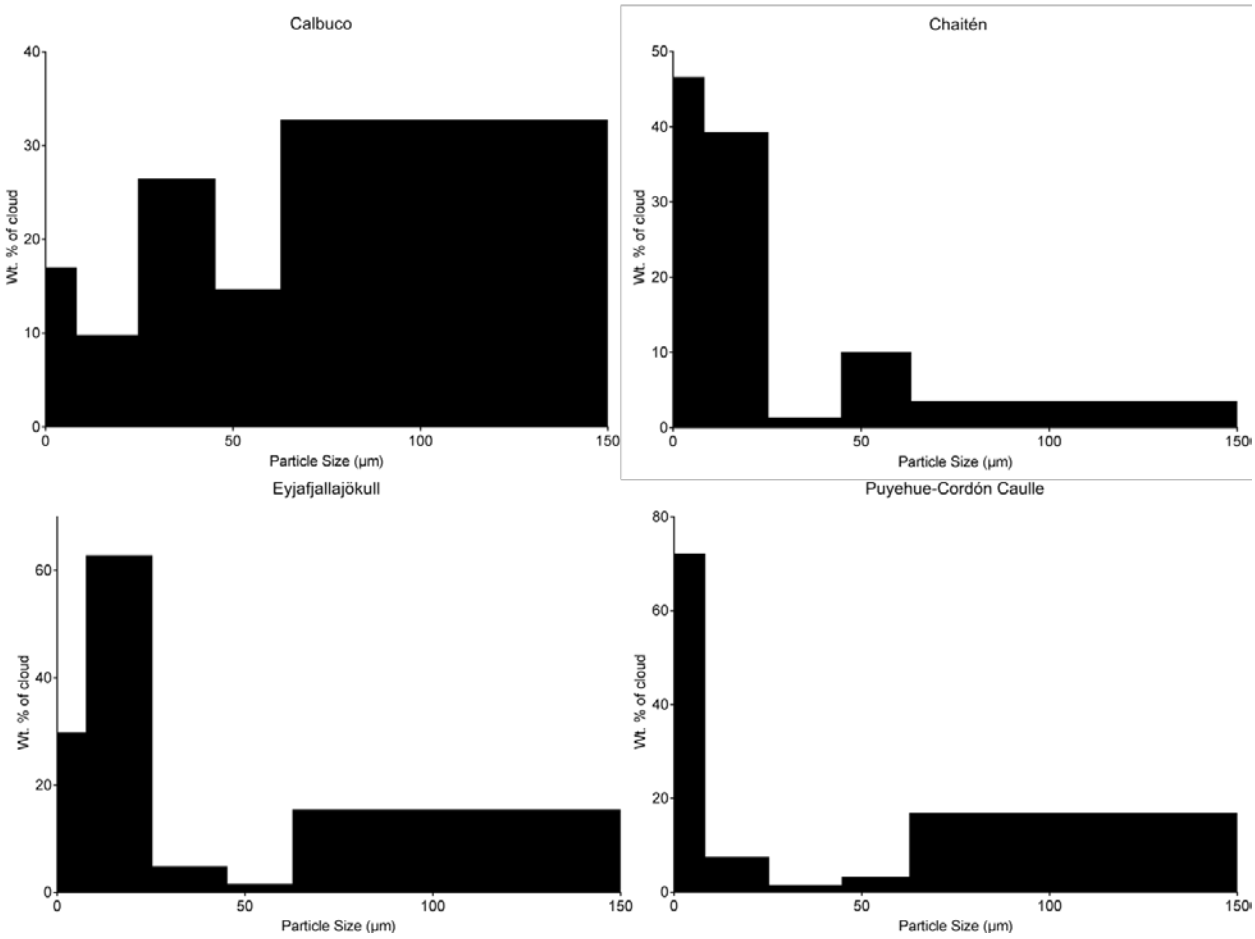

Figure 3-18 Particle size ranges by wt. % of total number of retrieved pixels for the non-sampled volcanoes

Where emission spectroscopy is used, the data detect only the uppermost (~ 100 μm) of the surface. An important assumption made where applying the linear deconvolution model to these data is that the plume top surface is the surface observed. This appeared to be corroborated by ASTER DEMs, in which a new topographic surface is created in the image for an optically-opaque plume. The initial assumption is therefore that a mixture of particles would be evident at the origin of the plume, with decreasing amounts of larger material present as the plume moves downwind and these larger particles settle out preferentially. However, this has tended not to be the case in these results. For smaller plumes from Calbuco, Sakurajima, Santiaguito and SHV the distance travelled is not that great thus, larger and smaller particles are present concurrently. However, for eruptions such as Puyehue and Eyjafjallajökull, larger particles (> 63 μm) are still found to be present in comparable quantities with increasing distance from the vent. Furthermore, for the Chaitén eruptions of 19 January 2009, > 63 μm are almost exclusively found at the plume edges, and not within the central portion. This kind of behavior is also seen in part at the Eyjafjallajökull volcano, with larger particle sizes being found at the edges of the cloud, and fines towards the center, although in this case the trend of observing larger particles much further from the vent is also evident. This zoning of larger particle sizes presents a possible process that may be occurring. But perhaps the more appropriate viewpoint is what the remote sensing instrument is detecting. It may not be the case the plume top is visible exclusively, thus an alternative should be examined.

3.5.3 Volcanic Plume Structure

Given the particle size variations discussed above, it is important to consider the implication that perhaps these TIR are methods are not actually observing the plume top

exclusively. Because larger particles will settle out of the plume more rapidly than smaller particles based on Stokes' settling equation, it therefore is interesting that different modes have been observed. In data from Eyjafjallajökull and Puyehue-Cordón Caulle, larger particles are seen in greater quantities further from the vent. At Chaitén volcano, larger particles are restricted almost exclusively to the plume edges, whereas finer particles are located in the center of the plume.

In order to address this, an experiment is performed using the 19 January 2009 image obtained of the Chaitén volcano, Chile. Upon retrieval of the emissivity data from the AST_09T data product, using the emissivity normalization technique (Realmuto, 1990), a temperature image is also created. These temperature profiles are used during the deconvolution work to provide a method of extracting plume bearing pixels from those that were transparent. It is assumed that the plume is in equilibrium with the atmosphere, and that the plume bearing pixel temperature is correlated with a temperature and altitude profile of the region's atmosphere. Atmospheric temperature for a region is estimated from radiosonde profiles (weather.uwyo.edu/upperair/sounding.html). For Chaitén volcano, the closest radiosonde profile comes from the Puerto Montt station ~ 60 km north of the edifice, which is downwind from the direction of plume travel. Radiosonde data may not always be appropriate if a station is too far away (Oppenheimer, 1998), however in the case outlined here, it was felt that the Puerto Montt station would provide a comparable atmospheric profile to where the plume is located. Furthermore, these image data are taken during the day time in the region, thus the ASTER DEM product is also available. Plume heights are taken from the ASTER DEM and are then compared to radiosonde data, so the assumed atmospheric temperature from DEM plume top height is derived. This is compared to the down track plume temperature taken from AST_09T data. Thus,

it may be possible to determine if the ASTER derived temperature corresponds to the radiosonde temperature at the same height. The results from this are shown below in Figure 3-19.

The discrepancy between the two derived heights does raise questions as to how this occurs. There are two main possibilities that are explored to understand this:

(1) The satellite sensor is not always observing the top of plume but is sampling a thermally opaque layer within the structure with ash gravitationally settling within the plume.

(2) Only plume top pixels are visible and the cloud is still thermally opaque in this region. The height and temperature discrepancy is a result of errors that occur in atmospheric correction. An improved correction scheme is discussed in section 3.5.4.

(3) ASTER DEM and radiosonde derived heights linked to ASTER TIR derived temperature cannot be reliably compared, as the behavior of energy in the VNIR portion of the EM spectrum is different compared to the TIR. Thus the DEM is the representation of this change, with a greater height given as energy is not transmitting from an opaque layer within the plume, so the plume top is viewed as “solid”.

(4) Some combination of the above.

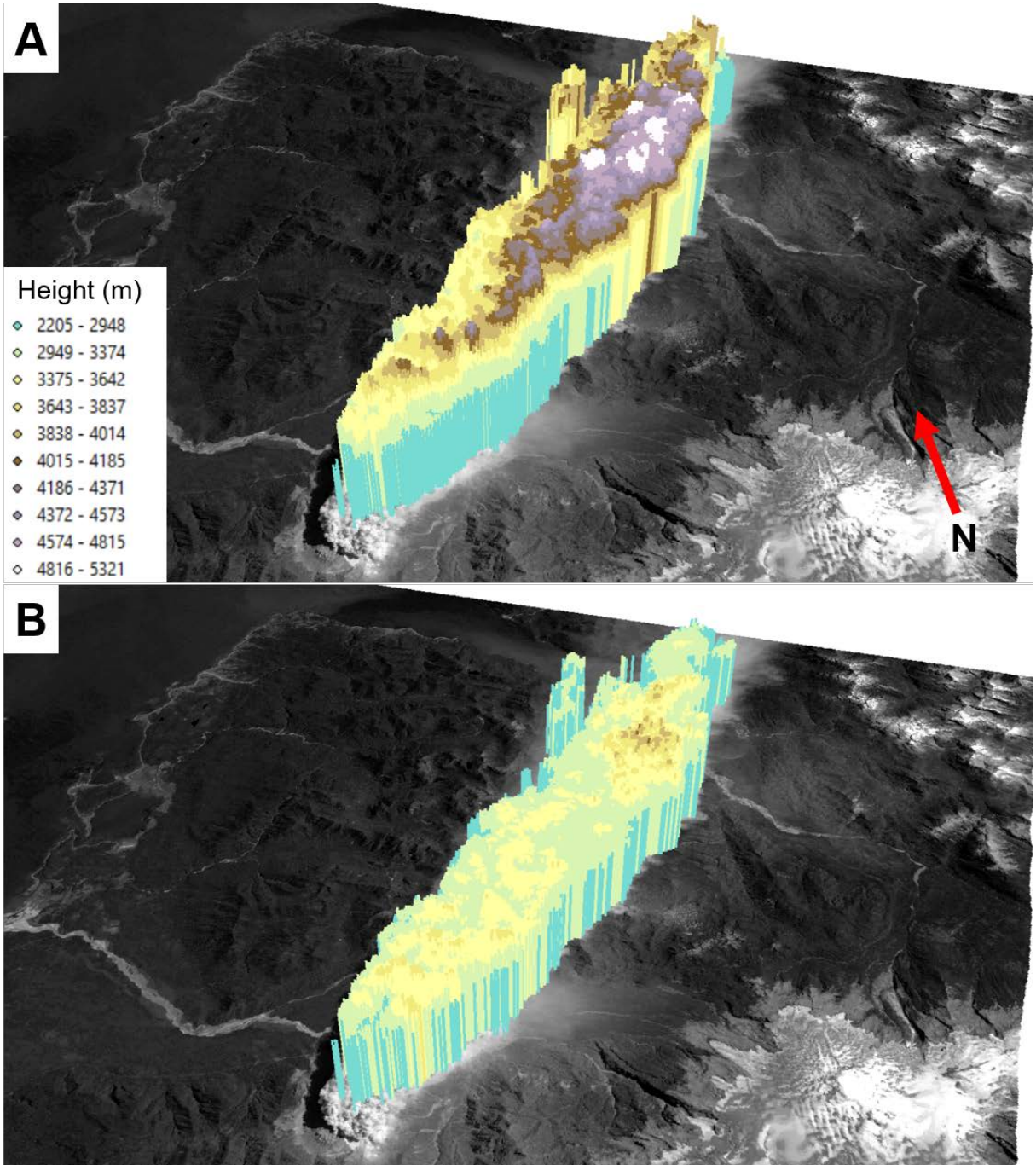

Figure 3-19 Heights derived from A) ASTER DEM and B) AST_09T derived temperature, correlated with radiosonde data. The ASTER DEM was resolved to 90 m in order to provide a better comparison to the temperature data. The temperature of each plume bearing pixel was compared to the radiosonde temperature, and height assigned based on that altitude, assuming the plume is in equilibrium with the atmosphere.

Whereas the exact reason, or combination of reasons for the discrepancy is hard to determine at this point, the particle size evidence from the larger plumes does seem to suggest that there is a difference between opaque plume surface and thermally emitting surface. In the examples shown in the results, there is a tendency for larger particles to be restricted to the fringes of plumes, or to be detected in larger quantities further away. Furthermore, in the example from Chaitén, the finest particle size fraction (< 8 μm) is the dominant, and locally even the only particle size fraction retrieved where the radiosonde derived height is at its maximum. This trend is closely followed downwind of the plume. Coarser particle sizes are much more prevalent where the emitting surface height is lower. However, in addition to these two possibilities there are also other factors that may affect what information the sensor is retrieving. Primarily, this relates to what the plume temperature is relative to the atmosphere. It is possible for a plume to cooler or warmer than the surrounding ambient atmosphere. The maximum plume height may not have yet been achieved, and the plume still has enough thermal energy to lift higher in the atmosphere (Oppenheimer, 1998), or alternatively the plume can overshoot the height at which would reach neutral buoyancy due to momentum, which means the plume will be colder than ambient (Woods and Self, 1992). However, as the plumes distance from the vent increases, these effects will be lessened, and eventually the plume will equilibrate with the surrounding atmosphere.

3.5.4 Effect of Volcanic Gases

One further aspect that requires discussion is the possible effect that volcanic gases may be having on the emissivity spectrum. The effects on transmission of radiant energy by gases produced by volcanoes, such as H_2O, CO_2 and SO_2, are well known, and in the case of SO_2 the

transmission at both 7.3 and 8.6 μm is used to map SO_2 plumes emanating from the source (e.g. Realmuto and Berk, 2016). In the case of SO_2, because the absorption feature of volcanic ash appears at the same wavelength (~ 8.6 μm), one issue is to determine where the SO_2 concentrations are high enough within the plume to have an attenuating effect on emitted radiance. However, the ability to measure these concentrations within an opaque plume would present an enormous challenge, as these methods are normally applied to more diffuse, ash-poor clouds. Whereas this is not trivial to quantify, it is an effect that would require further investigation.

3.6 CONCLUSIONS

A method to analyze opaque volcanic ash plumes, using emission spectroscopy is discussed and tested here. Whereas current methods that use the transmission of energy through a sample to measure the properties of plumes are routine, these are unusable in the opaque portion. The goal of this work is to determine whether particle size and composition can be derived from volcanic ash particles using the described technique. The results presented here covered both samples that were present as end-member spectral in AVAL, and those that were not, to determine if this library is an appropriate suite to use with these data. The results here demonstrate that this method is valid, as plume retrievals of composition were associated with low RMS in nearly all cases (RMS $\leq$ 6.04 %). Of interest is the prevalence of the Mono-Inyo obsidian end-member, which produced low RMS retrievals in all but one of the case studies. This points to a much higher SiO_2 content of the volcanic ash plumes studied. This was further demonstrated by using a mixture of two end-members where analyzing an image of Sakurajima

volcano. Here the obsidian library was coupled with the Sakurajima 2013 library, which after 10 iterations produced a retrieval with RMS errors < 0.5 %. Particle size detection showed the dominance of finer particles, primarily those < 25 μm. This was particularly the case for larger eruptions, such as the plumes produced by Chaitén, Puyehue-Cordon Caulle and Eyjafjallajökull volcano. However, it was also observed that in several instances, larger particles were found exclusively at plume edges and/or distally from the vent. This is assumed to represent the surface that the satellite sensor is detecting, with the plume more diffuse towards the edges, and further from the vent. In this case the top surface may not have a high enough density to act as a solid surface and so a denser layer at lower altitude may be observed.

The estimation of plume composition with ASTER data has the potential to aid in with the traditional methods of plume detection and monitoring. The current methods employed rely on assumptions on plume composition, and these refractive indices are then used to determine mass, density and effective radius using radiative transfer methods. However, this is shown to be inaccurate (e.g. Mackie et al., 2014; Vogel et al., 2017), and if a bad assessment of composition is made, errors of these measurements is as high as 17 %. If composition is defined using ASTER coupled with the AVAL library and the linear deconvolution algorithm, then these data can be used to inform compositional information, leading to more accurate retrievals in higher spatial resolution satellite sensors, such as MODIS, AVHRR and AIRS.

There is however an impending lack of high spatial resolution, multispectral TIR data. Currently there are no planned missions to replace the ASTER sensor, despite the alternatives that have been presented, primarily the Hyperspectral Infrared Imager (HyspIRI) sensor. It is hoped that increasing studies on the usefulness of satellite based, high spatial resolution, multispectral resolution data will trigger the development and launch of new instruments (such

as the ITHEMIS instrument; Ramsey et al., 2017), that will be better equipped for the challenge of quantifying volcanic emissions in the TIR.

4.0 GROUND BASED MULTISPECTRAL IMAGE DATA FROM A THERMAL CAMERA – APPLICATIONS TO VOLCANIC ASH COLUMNS

4.1 INTRODUCTION

Remote sensing of volcanic edifices and products has provided large quantities of data from ground, aerial and satellite-based missions (Tralli et al., 2005). Satellite based remote sensing of volcanic activity primarily uses a suite of ultraviolet (UV) and thermal infrared (TIR) sensors that can detect both large and small-scale features (e.g. Ramsey and Dehn, 2004; Campion et al., 2010; Murphy et al., 2013). The TIR data used that a range of spectral, spatial, and temporal resolutions. Even though these are powerful tools for global volcano monitoring, it is also vitally important to obtain ground-based information from the volcano (Wadge et al., 2005), particularly if high frequency activity is detected. Various different types of sensor can be deployed to better understand the movement of magma beneath the volcano, the styles of eruption produced, and volcanic products that are erupted.

Ground based methods of monitoring volcanic activity range from seismic and GPS surveys to monitor magma transport beneath the volcano, to sub-aerial studies using sensors that detect energy in the UV, visible and TIR portions of the electromagnetic (EM) spectrum. UV methods are used to quantify the emission of volcanic gases (e.g. Galle et al., 2003; Bluth et al., 2007), whereas visible light detecting webcams provide a low-cost tool for monitoring volcanic events (Orr et al., 2013). TIR methods have involved using broadband TIR cameras and spot radiometers (Harris et al., 1997; Spampinato et al., 2011) to characterize thermally anomalous

pixels, measure temperature changes on active lava flows, domes and lakes (Carter et al., 2007; Calkins et al., 2008; Ramsey et al., 2012), lava effusion rates over a period of time (Calvari et al., 2005), to monitor the number of eruptive events occurring (Calvari et al., 2010), and to analyze the structure of volcanic plumes (Patrick et al., 2007; Prata and Bernardo, 2009; Harris et al., 2013). Many commercially available thermal cameras collect broadband data in the wavelength region ~ 7 – 14 μm (Prata and Bernardo, 2009). The information contained with these images is used to map temperature changes, which although incredibly useful in monitoring and modelling volcanic processes, have limited diagnostic information on parameters such as composition and particle size. However, it is possible to adapt these cameras to collect multispectral data, if an appropriate bandpass filter set is created. These datasets would then allow the collection of emission spectra in the TIR, by filtering out incoming radiance except for what is found at the wavelength region of the bandpass. The use of TIR emissivity spectra allows for the collection of information on both composition, particle size and texture (e.g. Ramsey and Fink, 1999; Christensen et al., 2000), by analyzing the unique emission and absorption features that are controlled by the composition of the material being studied, and how the spectral contrast of these features changes as particle size decreases (Ramsey and Christensen, 1997). The potential exists to create a multispectral sensor with an off the shelf camera that provides a lower cost alternative to obtain both broadband and multispectral image data near simultaneously.

The work here describes the methods used to create this system. By building an apparatus that can attach to the exterior of a thermal camera, a functioning multispectral system was developed. This chapter describes both the creation of this system, and gives an overview of the corrections needed to process such data. Examples are given, where laboratory standard samples

have been analyzed using this camera, to derive emissivity spectra. Furthermore, data from field campaigns to Guatemala (2015, 2016 and 2018) and Japan (2016) are discussed.

4.2 THE MULTISPECTRAL CAMERA ASSEMBLY

4.2.1 Optical Filters

During this work, two sets of optical filters are utilized, described here as 1st and 2nd generation. Plots of the spectral band passes are shown in Figure 4-1. The filters were produced by Andover Optics. Each has a full width half-maximum (FWHM) of ~ 0.5 μm. These band positions were chosen to observe the primary absorption features of silicate minerals, which are found at these wavelengths. The filters allow a spectral resolution close to that of ASTER and MODIS for ground comparison studies to these data. Each filter is 51 mm in diameter, identical to the FLIR camera lens, in order to fill the cameras field of view and thus avoid any additional erroneous optical effects that can affect data acquisition.

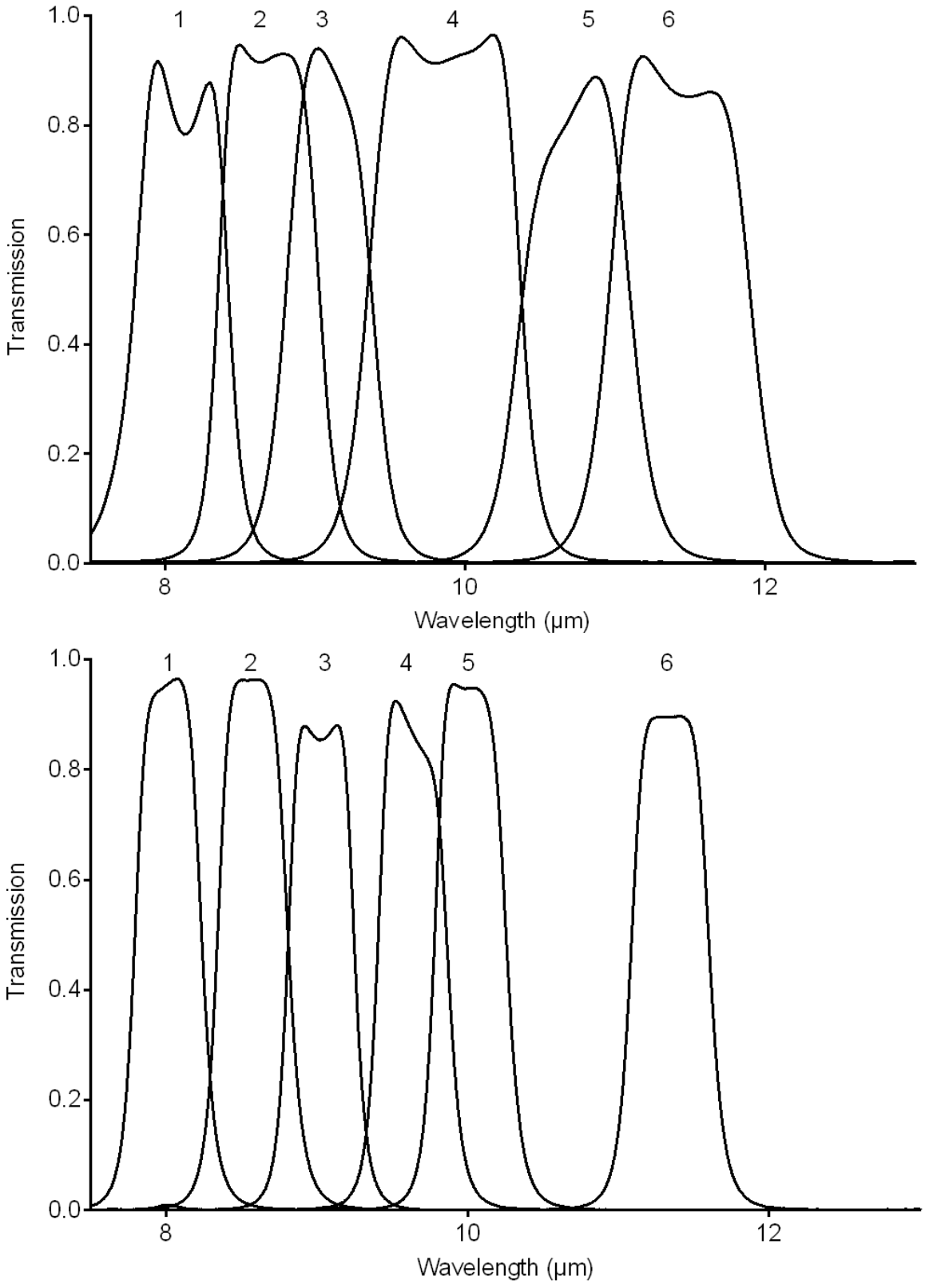

Figure 4-1 Transmission profiles for the 1st (upper panel) and 2nd generation (lower panel) filter sets.

Table 4-1 Specifications of the band pass filters used for the 1st and 2nd generation filter sets

1st Generation

Band Number	FWHM Position	Band Width at 50% (µm)	Band Center (µm)	Peak Transmission (%)
1	7.820 – 8.470	0.650	8.050	91.82
2	8.336 – 9.010	0.675	8.600	94.96
3	8.789 – 9.364	0.575	9.050	94.04
4	9.346 – 10.371	1.025	9.800	96.46
5	10.384 – 11.134	0.750	10.710	88.87
6	10.954 - 11.904	0.950	11.300	92.54

2st Generation

Band Number	FWHM Position	Band Width at 50% (µm)	Band Center (µm)	Peak Transmission (%)
1	7.830 – 8.280	0.450	8.058	96.86
2	8.329 – 8.803	0.474	8.566	96.12
3	8.803 – 9.253	0.450	9.028	89.59
4	9.348 – 9.810	0.462	9.579	93.21
5	9.804 – 10.289	0.485	10.047	94.69
6	11.103 – 11.633	0.530	11.368	89.96

4.2.2 Thermal Camera Mount Design

The multispectral thermal camera system went through several iterations in the design to find the best mechanism to collect image data. The initial proof of concept of this work (Ramsey and Harris, 2012) had the optical filters placed in casings that were then affixed to the camera individually. This works for stationary targets, but is ineffectual where attempting to obtain near-coincident image sets from dynamic volcanic flows and plumes. This promoted the creation of two different systems that could hold all six filters in place. The filters then pass in front of the camera lens mechanically, so near-coincident image data is collected. The camera used for this system has remained the same, a FLIR S40, the specifications for which can be found in Table 4-2.

Table 4-2 Specifications of the FLIR S40 camera (after Carter, 2008)

Specification	Value
Field of view/minimum focus distance	24˚ x 18˚/0.3
Spatial Resolution/IFOV	1.3 mrad
Image Frequency	Max 60 Hz
Thermal Sensitivity @50/60 Hz	0.08˚C at 30 ˚C
Detector Type	Focal plane array FPA uncooled microbolometer, 320x240 pixels
Spectral Range (µm)	7.5 to 13
Gain Settings	-40 – 120 ˚C 0 – 500 ˚C 350 – 1500 ˚C

4.2.2.1 Slider Mechanism

The first design of this system is seen in Figure 4-2. This system is simplistic, but effective, with the camera placed in contact with an aluminum plate with a port in front. A second plate which houses the filters passes in front of the filters, with a handle controlled by the user allowing which slides each filter in front. The lack of a power supply for this system makes it easily portable. Teflon tape affixed to the upper and lower portions of the filter plate allow it to glide back and forth. The system can be quickly assembled and dismantled so it can be taken to more remote regions, where larger equipment would be difficult, maybe impossible, to transport.

The drawback of this system however is the dependence on the user acquiring data. The slider mechanism is not a completely frictionless surface, and as the user moved the plate back and forth, camera stability became an issue. The images acquired were not necessarily co-located for each filter and correcting this was a time-consuming process. Furthermore, over time, after days to weeks collecting data in the field, particularly in areas with an abundance of windblown dust, this would accumulate in the slider rail. Finally, with no control over the speed of acquisition, data had to be acquired at the maximum possible speed to ensure that images obtained had each filter directly in front of the lens. With these points in mind, a new approach was taken.

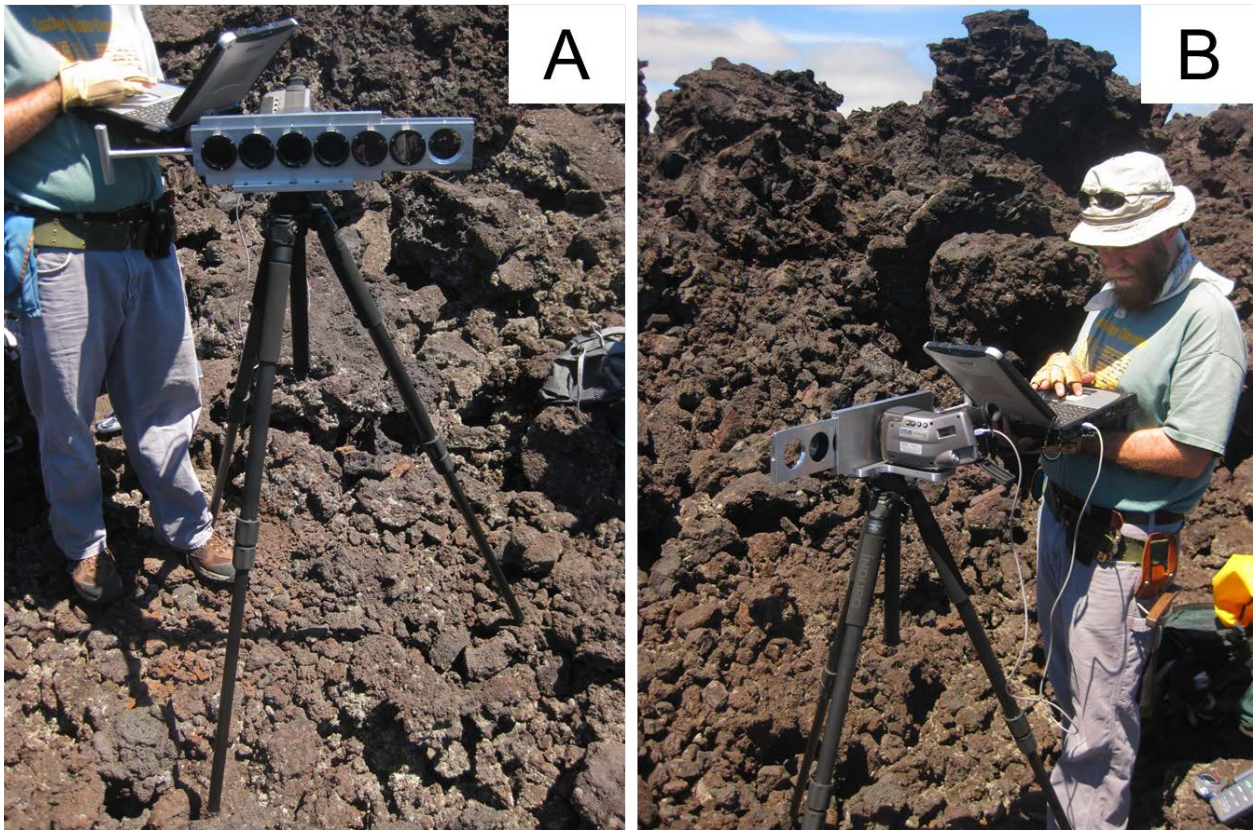

Figure 4-2 Photographs of the slider filter system (courtesy of R. Lee, SUNY Oswego).

4.2.2.2 Motorized Wheel

The updated filter system uses motorized component that makes the operation of the system easier for the user (Figure 4-3). The camera is mounted on an aluminum plate, behind a motorized wheel, which rotates in front of the camera lens. This mechanism is still portable, as each component can be separated with ease for transport to and from field sites. In order to collect as many scenes as possible as the filter passes over the lens, the camera is set to acquire data at 30 Hz. In addition to this, the motor has adjustable speed to allow for more rapid acquisition for faster moving targets, or for a greater number of images per filter by reducing the speed, if a stationary target is to be examined. The wheel is powered by one rechargeable 12-volt battery, which allows ~20 hours of continuous use. Seven ports in the wheel are designed for filter placement. One remains open so that broadband temperature measurements are acquired. Each filter is placed in an anodized aluminum casing, which are then mounted in the wheel.

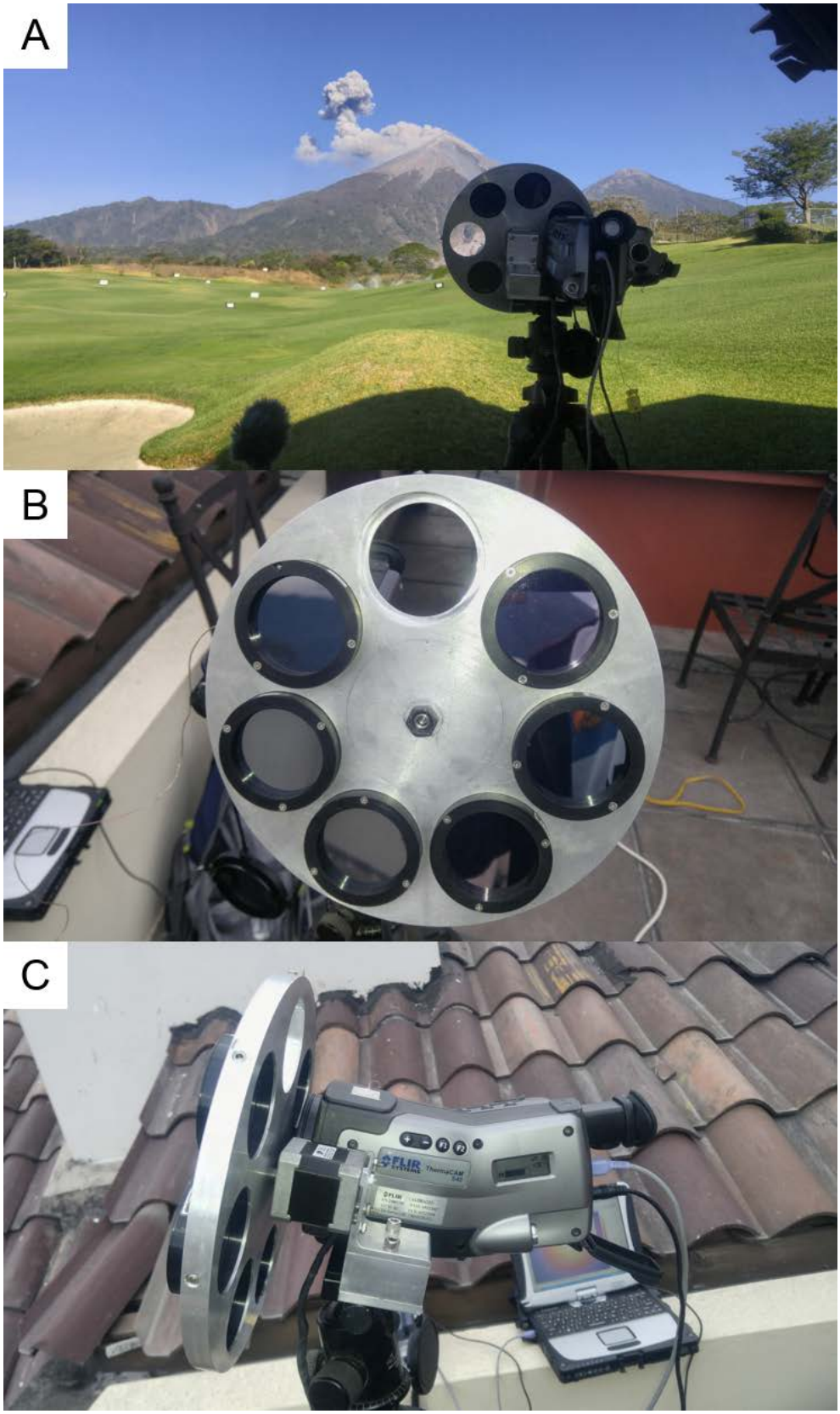

Figure 4-3 Filter wheel system deployed at Fuego, Guatemala in February 2018.

4.2.3 Calibration and Image Correction

As within any remote sensing system, a calibration regime must be applied to the data collected. The calibration for this system is outlined in detail in Thompson et al. (2018). Because the camera continuously collects data, even as the filter wheel is in front of the lens, an image extraction program is first implemented to obtain only those images where filter and lens are aligned, allowing them to be treated as 6 band image data, as satellite data are.

The optical filters have the same reflective coating on both the outward and inward facing sides. Therefore, where one passes in front of the camera, radiance produced by the camera's interior components is reflected back to the detector. This manifests itself as an optical aberration in the image data. This radiance is always present in the data but is visually less obvious where the temperature of the target is greater, due to the contrast between the detector and target temperatures. To correct for this, the camera was placed in front of an environmentally controlled microgroove blackbody at Aerospace Corporation, Los Angeles, CA. The blackbody covered the camera's field of view (FOV). Data were acquired with the multispectral apparatus, with the blackbody emitting at temperatures ranging from 10 – 120 ºC. From this, the per-pixel radiance at each temperature was compared to expected radiance with the filter in front and with the broadband port open, calculated from the Planck function. A correction was then developed for each pixel, using an exponential curve fit to estimate the blackbody radiance emitted between the temperatures collected. The correction can then be applied to temperature data that falls outside of the data range collected, particularly useful if temperatures less than 10˚C or more than 120 ˚C are found within the image data.

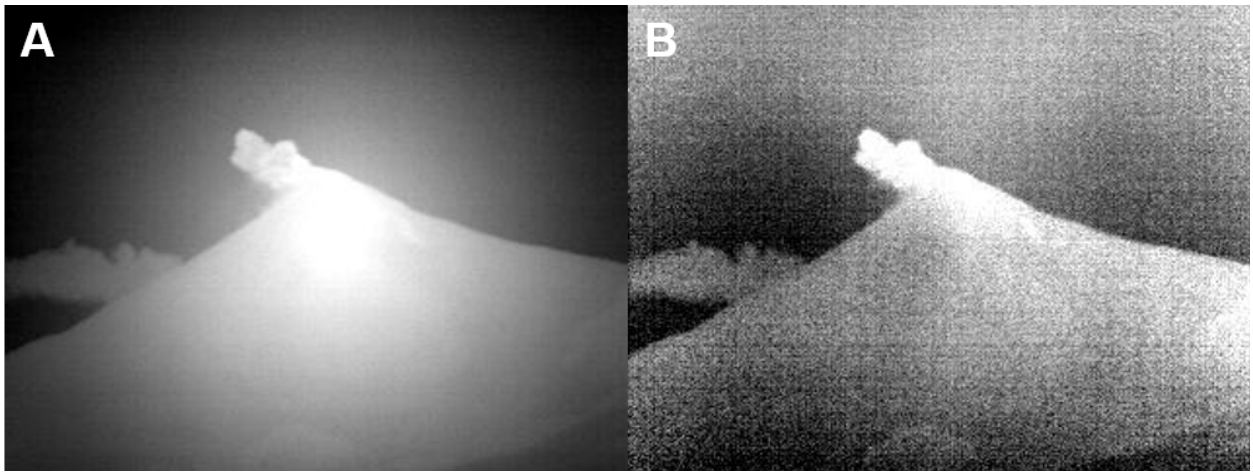

Figure 4-4 Data collected on February 23rd 2018 using the 2nd generation filters of Volcán De Fuego. Band 3 is shown here pre- (A) and post-correction (B). The optical aberration in A is a very distinct feature and appears more prominently where the camera is looking at "cooler" targets, due to the apparent temperature contrast.

This was performed at two atmospheric temperatures, 21 and 31ºC and two correction algorithms created for each temperature. Where image data are collected with the multispectral camera system, the atmospheric temperature is monitored so that the appropriate correction algorithm is applied to those data.

4.2.4 Laboratory Derived Spectra

A series of laboratory tests are required to test the accuracy. This was done here using both filter sets, with the calibration applied to the new filter data, as time constraints at the Aerospace facility denied the chance to create a calibration for both. Both filter sets were tested by imaging the laboratory standard quartz and/or obsidian used to calibrate the FTIR spectrometer. Each sample was left in the drying oven at 80˚C, removed, and placed in front of the camera. Several image sets were then taken; for the old filters with no correction, these were simply converted to emissivity using the inverted Planck function, whereas the new filter data was corrected using the exponential curve fitting algorithm to remove the optical aberration.

4.2.4.1 Old Filter Set

Testing of the old filter set began in March – May 2016 after a field campaign to Guatemala. Unfortunately, band 4 was carelessly destroyed by the author, so the work here was performed using the remaining 5 bands. Data from the laboratory obsidian standard were taken using the wheel mechanism, the results for which can be seen in Figure 4-5.

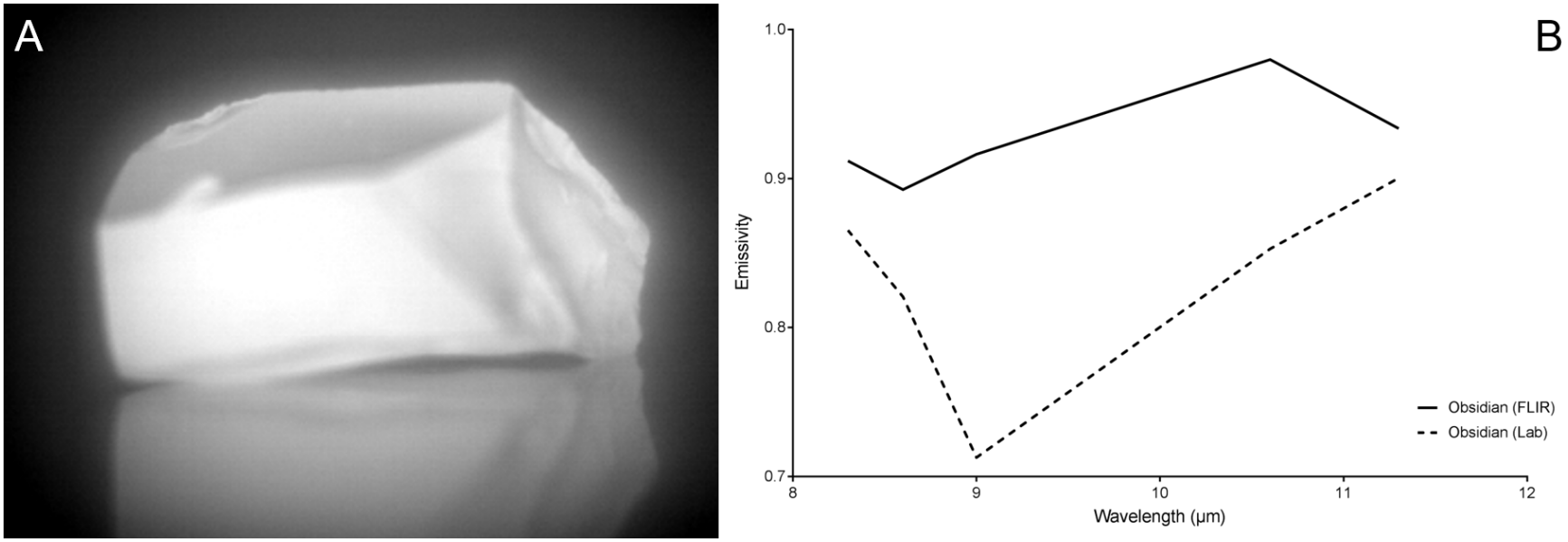

Figure 4-5 Laboratory standard obsidian measured by the 1st generation filter set. (A) Band 3 radiance image demonstrates that where the target being viewed is hot, the aberration is not as visible in the image due to the contrast. It is still present however. B) Mean emissivity spectrum for region of interest that encompassed the obsidian target, compared with the laboratory standard resolved to the FLIR multispectral wavelengths.

The data here are not calibrated with any blackbody measurements, and this clearly causes the major disparity seen between the filter derived and laboratory spectra. A full calibration of this filter set would be a great asset, particularly given the quantity of data that has been collected with this system.

4.2.4.2 New Filter Set

With the acquisition of the new filters, the obsidian target sample was again imaged with the system, as well as the microcrystalline quartz laboratory standard. These data are presented in Figure 4-6. These data were calibrated with the correction algorithm. The two corrected spectra presented here appear to contain the diagnostic spectral features of the two samples, where compared to the laboratory spectra resolved to the filter wavelengths. This represents a significant improvement on the data collected with the 1st generation filters, and therefore warranted the application of this correction routine to data collected from field sites.

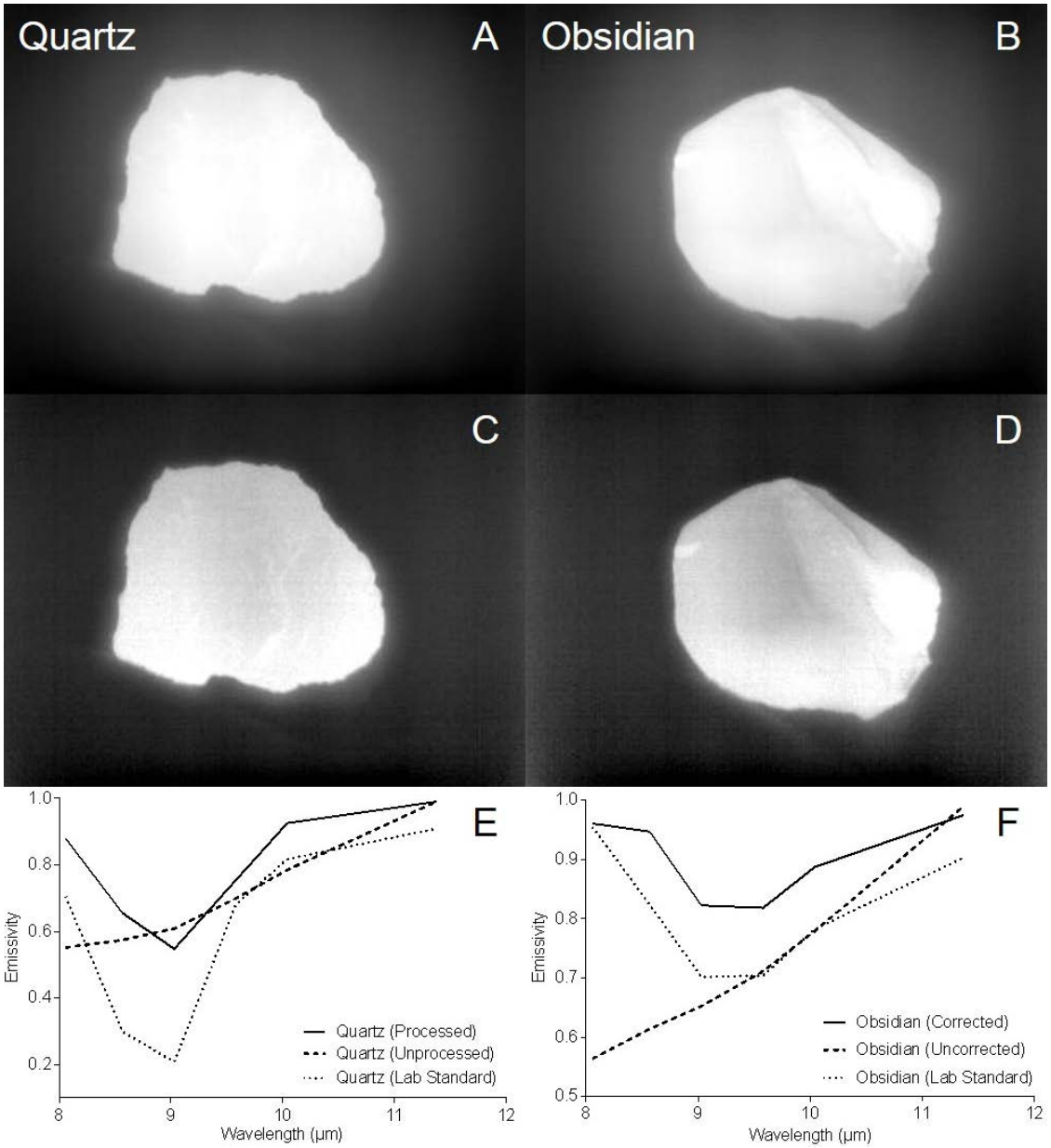

Figure 4-6 A) and B): Pre-correction image data for multispectral band 5 for the quartz and obsidian standards. The two samples are kept in a drying oven at 80 ˚C and were scanned using the system for 30 seconds immediately after being removed and were situated 20 cm from the camera. C) and D): Post-correction image data of both samples. E) and F): Emissivity spectra averaged over a region of interest on both samples. Data were processed from radiance to emissivity using the emissivity normalization technique (Realmuto, 1990), using an assumed emissivity of 0.99. Examples of emissivity spectra both pre- and post-processing are presented, as well as a laboratory spectrum of the same sample, resolved to the 6 band spectral resolution.

4.3 APPLICATIONS TO VOLCANIC PLUMES – A CASE STUDY FROM VOLCÁN DE FUEGO, GUATEMALA

The laboratory data shows promise for using the camera to extract the spectral emissivity of geologic features. The real test of the camera however obtaining data from the field. In order to build from the work described in chapters 2 and 3, it was questioned whether or not it would be possible to extract data on the composition and particle size of a volcanic ash column as it is being erupted. Obtaining an estimate of particle size distribution would better inform tephra dispersal models (e.g. Tephra2; Courtland et al., 2012). Furthermore, these data could be used to determine the composition of the initially erupted material, and how it compares to the drifting ash component, such as the proportion of glass to crystal fragments. The volcanic ash spectral libraries already exist at hyperspectral resolution and can be resampled to reflect the wavelengths covered by both the old and new sets of filters. During an ash rich eruption, it is assumed that the column at the vent will be optically and thermally opaque and will represent the solid emitting surface in the same way that the nascent portion of the plume did in ASTER data. Therefore, the camera data can, in theory, be processed using the linear deconvolution technique described in chapter 3. Data were collected during 4 field campaigns; Guatemala in 2015, 2016 (old filter set) and 2018 (new filter set), and Japan in 2016 (new filter set). Data were collected from two of the volcanoes that were simultaneously sampled for AVAL; Volcán De Fuego (Guatemala), and Sakurajima (Japan). These were chosen as test sites due to their frequent ash producing activity, as well as the multiple vantage points that were accessible around the volcano. Unfortunately, Sakurajima went through a prolonged repose period during fieldwork in November 2016, and so no ash plume data was collected. Therefore, this section focuses on the eruptions observed of Volcán de Fuego.

Volcán De Fuego erupted during each of the three campaigns, and was the most frequently active of the volcanoes, with strombolian activity recorded ~ every 5 – 30 minutes. A paroxysmal eruption of Fuego was also observed between 28 February and 2 March 2016, which included volcanic ash emission and lava fountaining from the summit vent. Data were acquired at several locations with varying degrees of success. The best locales chosen were the Fuego Volcano Observatory (OVFGO) which is operated by the Instituto Nacional de Sismología, Vulcanología, Meteorología e Hidrología (INSIVUMEH), and La Réunion Golf Resort, 25 km southwest of the city of Antigua Guatemala. Between the 2018 field campaign and the time of writing, a large eruption of Fuego in June has destroyed this second observation point.. Data acquisition would take place typically between 8 pm – 10 am, as cloud cover obscured the volcano during the day. During the field campaign of 2018, strombolian activity was once again recorded, but it appeared much stronger in comparison to the 2015 eruptions, with larger ash plumes generated from the summit that were erupted over a longer duration (minutes compared with seconds in 2015).

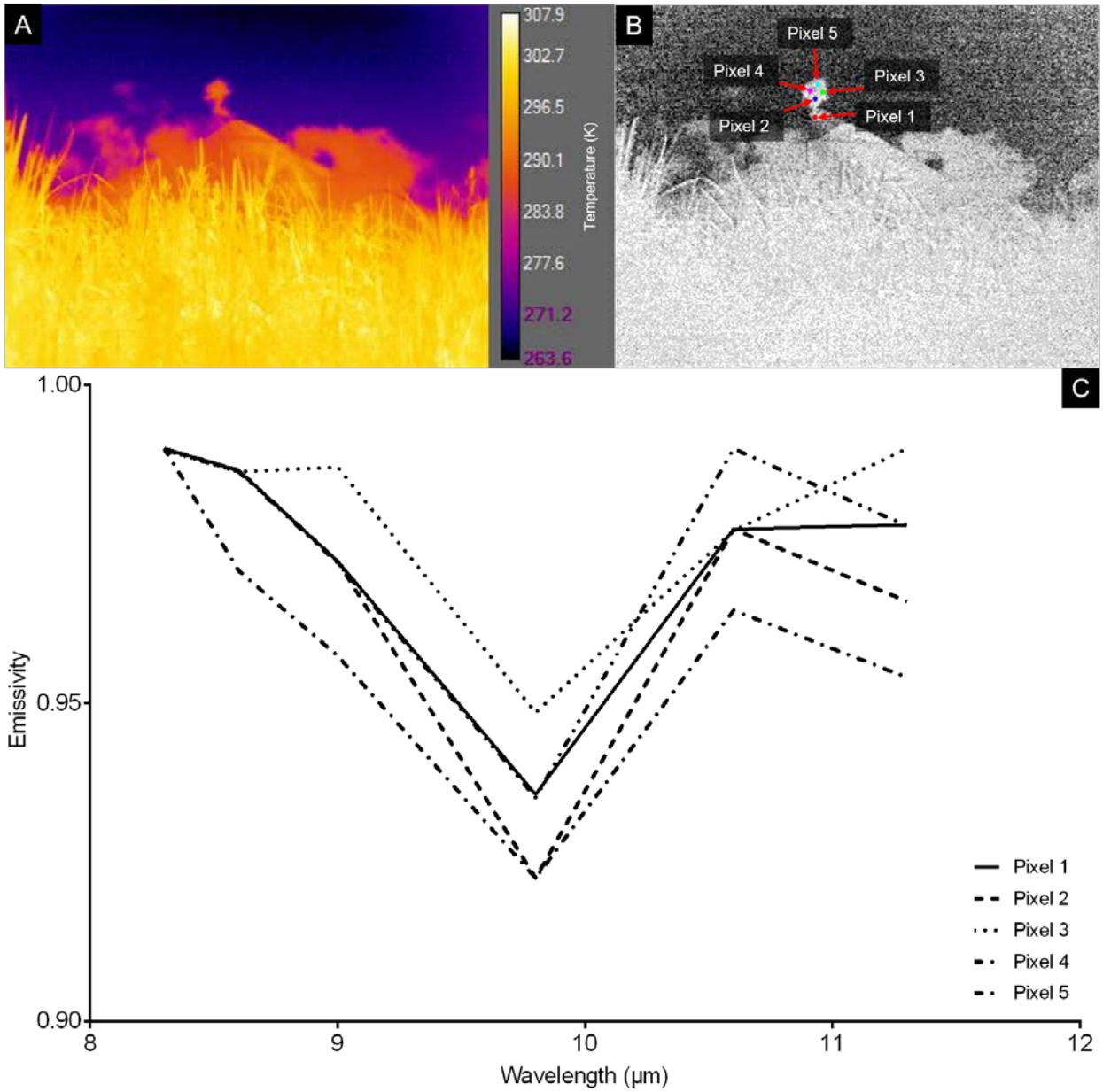

Figure 4-7 FLIR data from 2015 collected using the multispectral system with the 1st generation filters installed. This dataset was obtained during night time activity, so no visible images are provided for comparison. A) Broadband temperature image; B) Band 3 image converted to emissivity. Pixels that are selected are shown and labelled, with the corresponding spectra for each found in C).

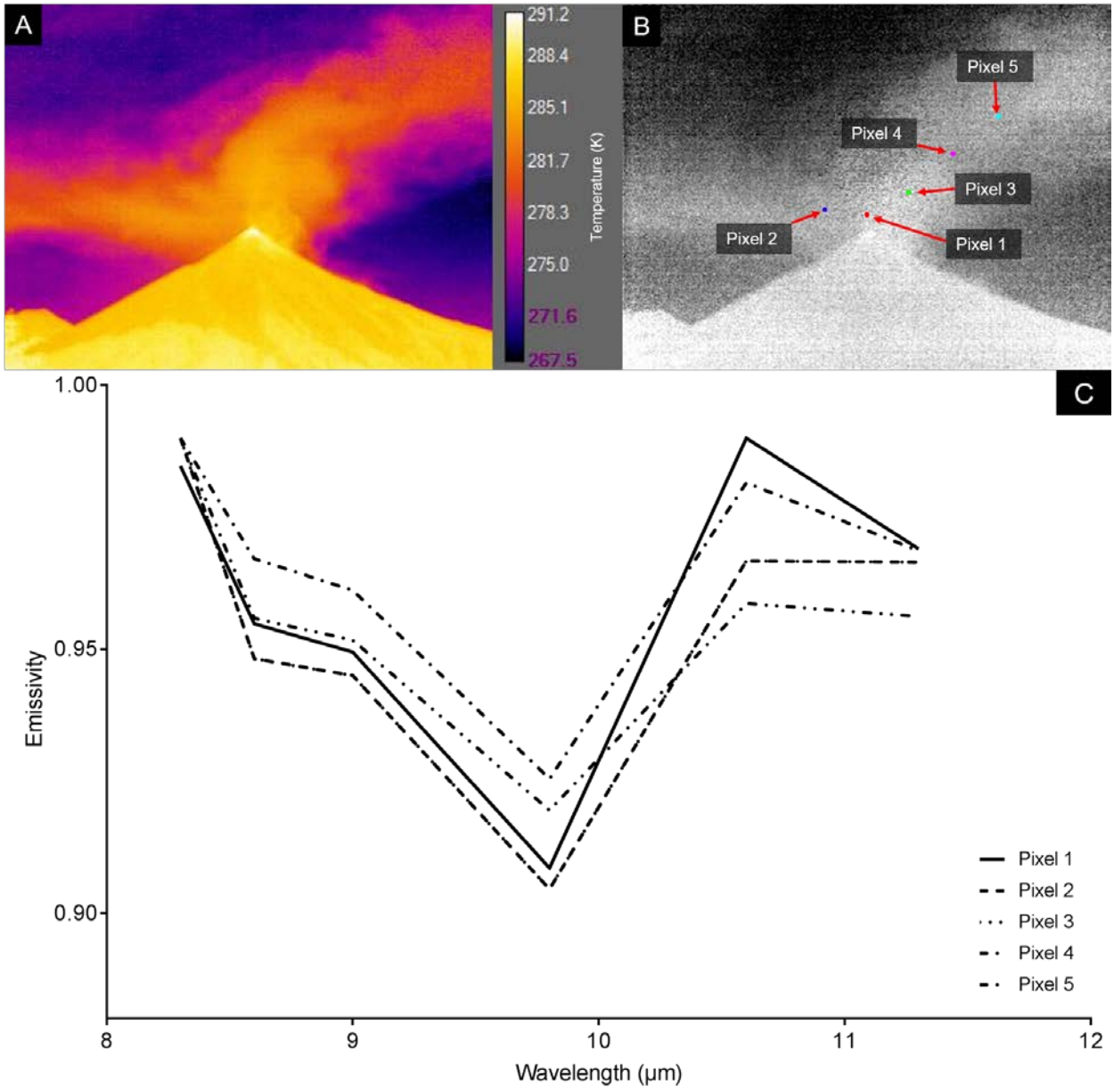

Figure 4-8 Data from the 2016 paroxysmal eruption of Fuego, collected using the multispectral system with the 1st generation filters installed. This dataset was obtained during night time activity, so no visible images are provided for comparison. A) Broadband temperature image; B) Band 3 image converted to emissivity. Pixels that are selected are shown and labelled, with the corresponding spectra for each found in C).

Image sets obtained from these eruptions are shown in Figures 4-7 and 4-8. Emissivity was extracted using the emissivity normalization method, using an assumed emissivity maximum of 0.99 (Realmuto, 1990). The datasets, despite being collected one year apart and documenting two different eruption styles, do have spectral similarities. The main absorption feature in each spectrum is found in the 9.8 μm band (band 4). This distinct emissivity low does appear abnormal in relation to the rest of the spectrum. Because these are uncalibrated data, it is not currently possible to quantify the ash emissions per pixel, and the band 4 feature does preclude these data from comparison to laboratory spectra to see if composition can be identified.

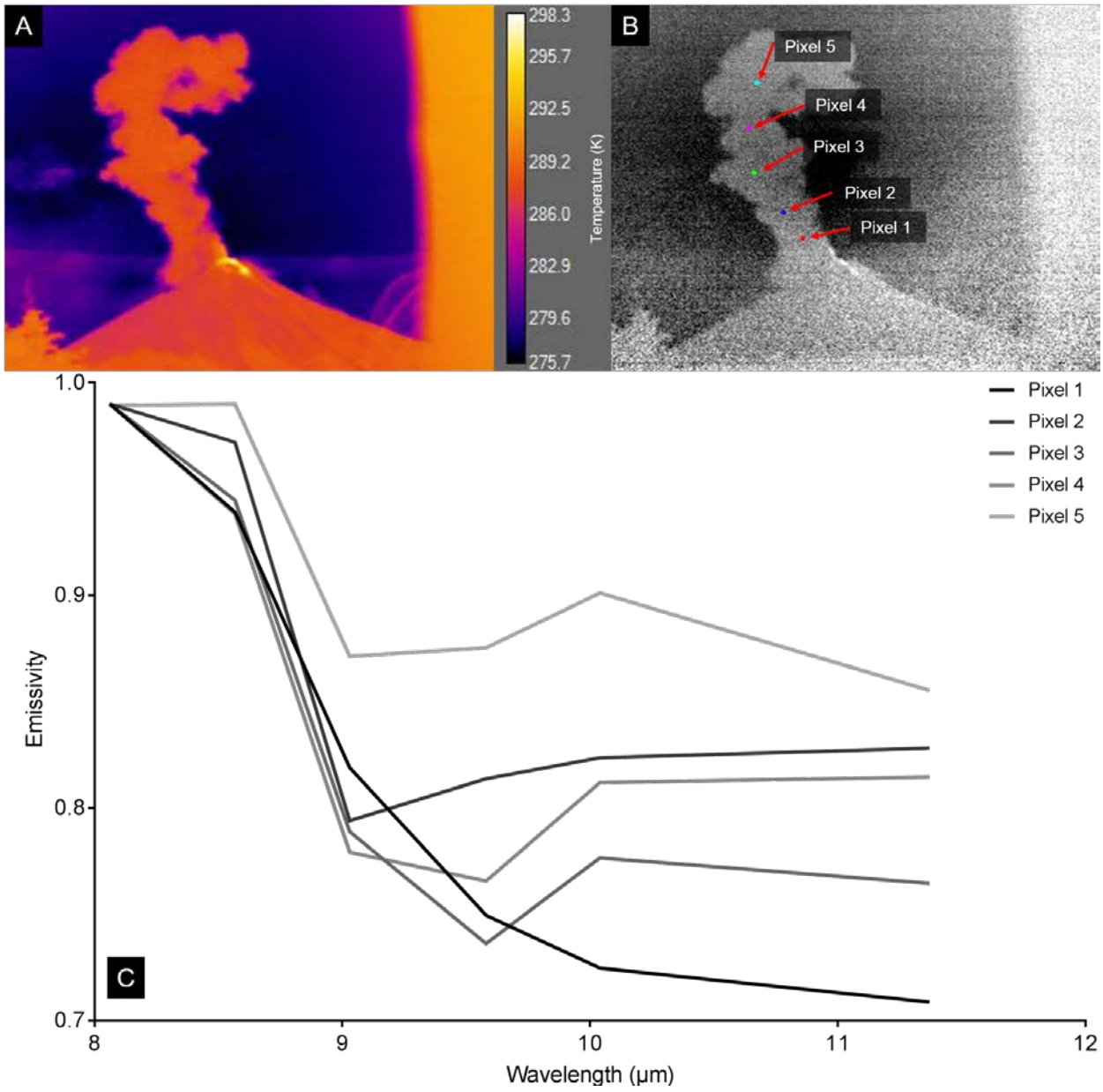

Figure 4-9 FLIR data from 2018 collected using the multispectral system with the 2nd generation filters installed. These data were collected from OFVGO 21 February 2018. A) Broadband temperature image; B) is a band 3 converted to emissivity after application of the correction routine. Pixels selected are shown and labelled, with the corresponding spectra for each found in C).

The data from 2018 are corrected for the optical aberration in the data (Figures 4-9 and 4-10). The band positions for these new filters have changed slightly, so a true comparison between the datasets is not as straightforward. The noticeable effect of the calibration here however is the depth to which emissivity is calculated, with emissivity lows of 0.7. This starkly contrasts with the emissivity lows found within the AVAL library shown in chapter 2. These datasets have all produced a spectral feature similar to the location of the feature of a silicate glass ~ 9 μm. Additionally, the spectra appear to have a negative slope imparted to them, in particular in the spectra seen in figure 4-10. This causes emissivity lows at longer wavelengths. This may be due to sub-pixel temperature mixing (Rose et al., 2014), which will be discussed further in section 4.4.

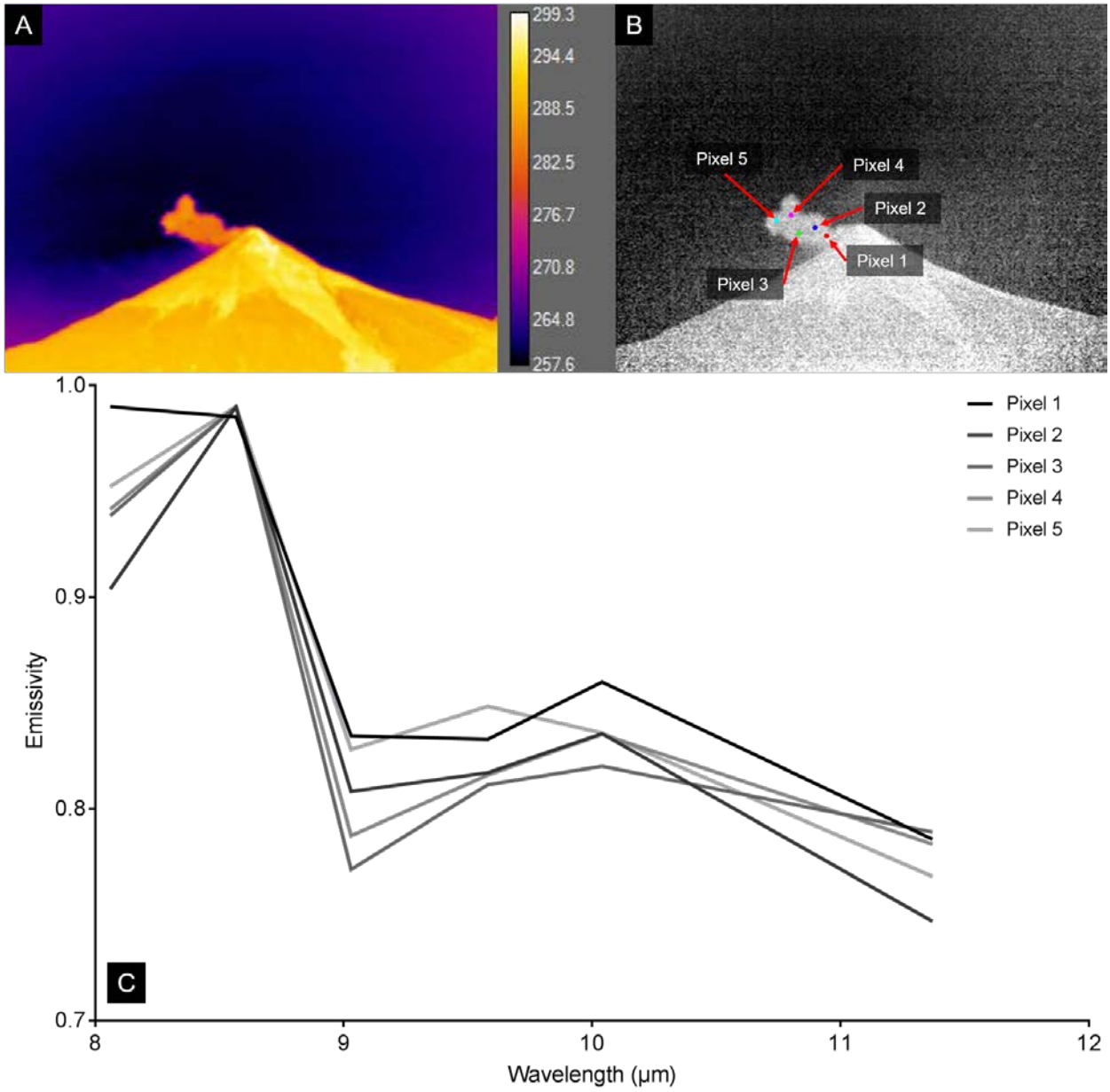

Figure 4-10 FLIR data from 2018 collected using the multispectral system with the 2nd generation filters installed. These data were collected from La Réunion golf course 23 February 2018. A) Broadband temperature image; B) is a band 3 image converted to emissivity after application of the correction routine. Pixels that are selected are shown and labelled, with the corresponding spectra for each found in C).

4.4 DISCUSSION

The spectra presented in Section 4.3 warrant further discussion due to the features seen. The system does record variable radiance and thus emissivity from a target with the filters in place, but are several issues that must be discussed that limit the collection of quantitative data that could be used with an end-member unmixing model. The 1st generation filter data still requires the development of a calibration routine, therefore this section focuses on the image data obtained with the 2nd generation filters in 2018. These data are firstly plot as relative emissivity (Figures 4-11). In this image the spectra were normalized relative to the laboratory spectrum of > 150 µm Volcán de Fuego ash using a blackbody. Spectra 1 and 3 listed appear distinct from the laboratory spectrum and do not match the shape. Spectrum 2 however does have a similar bowl, however what is consistent is that each of the spectra has an emissivity low in band 6. At first it was thought that this may be another calibration issue, however another hypothesis is that this is a result of sub-pixel temperature mixing. In chapters 2 and 3, the spectra obtained do not have a slope as the surface being observed by the detector is near-isothermal. However, it was shown in image data that where a pixel contains multiple different temperatures, a significant slope is imparted onto the derived emissivity spectrum (e.g. Gillespie et al., 1998). When a volcanic ash plumes is generated, the material cools very rapidly as it enters the atmosphere. Given the distance from the plume the camera, it is plausible that thermal mixing is occurring within these pixels.

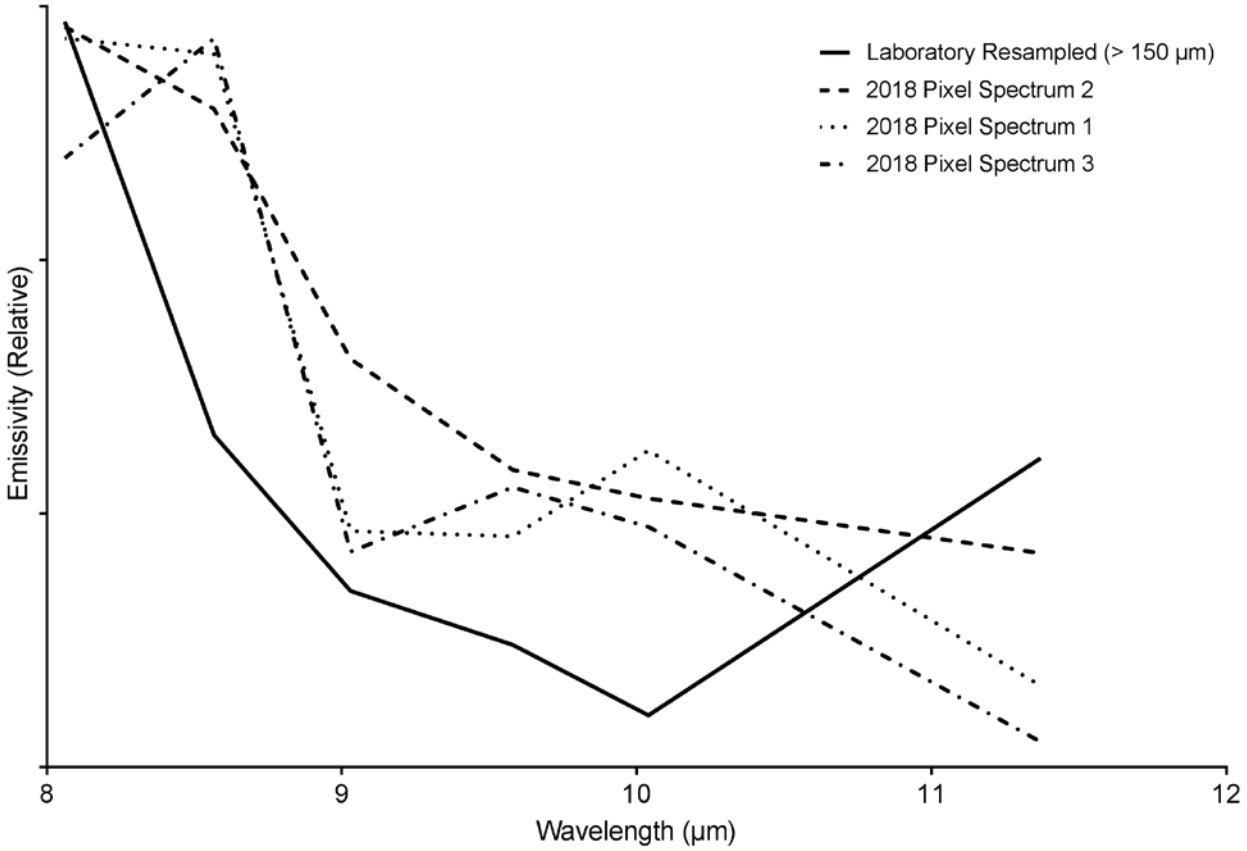

Figure 4-11 Three spectra derived from pixels from data obtained at Volcán De Fuego 21 February 2018, using the new filter sets and the aberration calibration model, compared with the laboratory spectrum of > 150 µm Fuego ash, resolved to the 2nd generation filter wavelengths. These three spectra were chosen as they represent the range of spectral shapes seen in these data. The image pixels have been normalized to the laboratory spectrum using a blackbody for better comparison.

Rose et al., (2014) developed a method of correcting for these effects, termed thermal deconvolution. In this method, ASTER data are examined, and emissivity spectra derived. These spectra are tested to see if a slope is present in the data. A value of < - 0.015 is the threshold value for algorithm application. If thermal mixing is occurring, then the algorithm uses ASTER SWIR (30 m resolution) data to determine the hot and cool temperatures within each TIR pixel and the areal percentage. From this a mixed Planck curve is produced, which is used to derive the mixed radiance value for each ASTER TIR channel. The ratio of mixed to original radiance equals the corrected emissivity for each pixel. This method is restricted by using the ASTER SWIR subsystem, which could derive sub TIR pixel temperatures from it when the system was active. In this instance, maximum and minimum temperatures per pixel of the plume could not be estimated as there was no method of acquiring these data. However, the effect of thermal mixing could be removed by calculating the slope of each spectrum in Figures 4-9 and 4-10. This was done to determine if the slope value was over the threshold set by Rose et al. (2014). These are presented in Table 4-3. Each of the 10 values calculated shows that the slope on these emissivity spectra is below the threshold value set. To demonstrate how these spectra might look if thermal deconvolution were applied, each spectrum was scaled to a line with a slope of 0. These results are shown in Figure 4-12. After these data are scaled, the spectra appear similar to the emissivity spectra measured from silicate materials. Nine of these pixels have an emissivity low centered arounds band 3 and 4 (8.57 and 9.03 μm). This is spectrally similar to the glass rich samples from the AVAL library where resolved to the 6 band resolution. Pixel 1 from the 21 February 2018 dataset is the only spectrum that produces a broad emissivity feature, indicative of less silicic material. Furthermore, of interest is the position of this pixel at the base of the ash column, whereas the assumed more glass rich spectra occur higher in the column.

Table 4-3 Slope values calculated from the 10 image pixels shown in Figures 4-9 and 4-10, collected from plume bearing pixels detected at Volcán De Fuego.

Date	Pixel Number	Slope
21-Feb-18	1	-0.08501
	2	-0.04891
	3	-0.06811
	4	-0.05302
	5	-0.04805
23-Feb-18	1	-0.06174
	2	-0.08675
	3	-0.07171
	4	-0.07373
	5	-0.07921

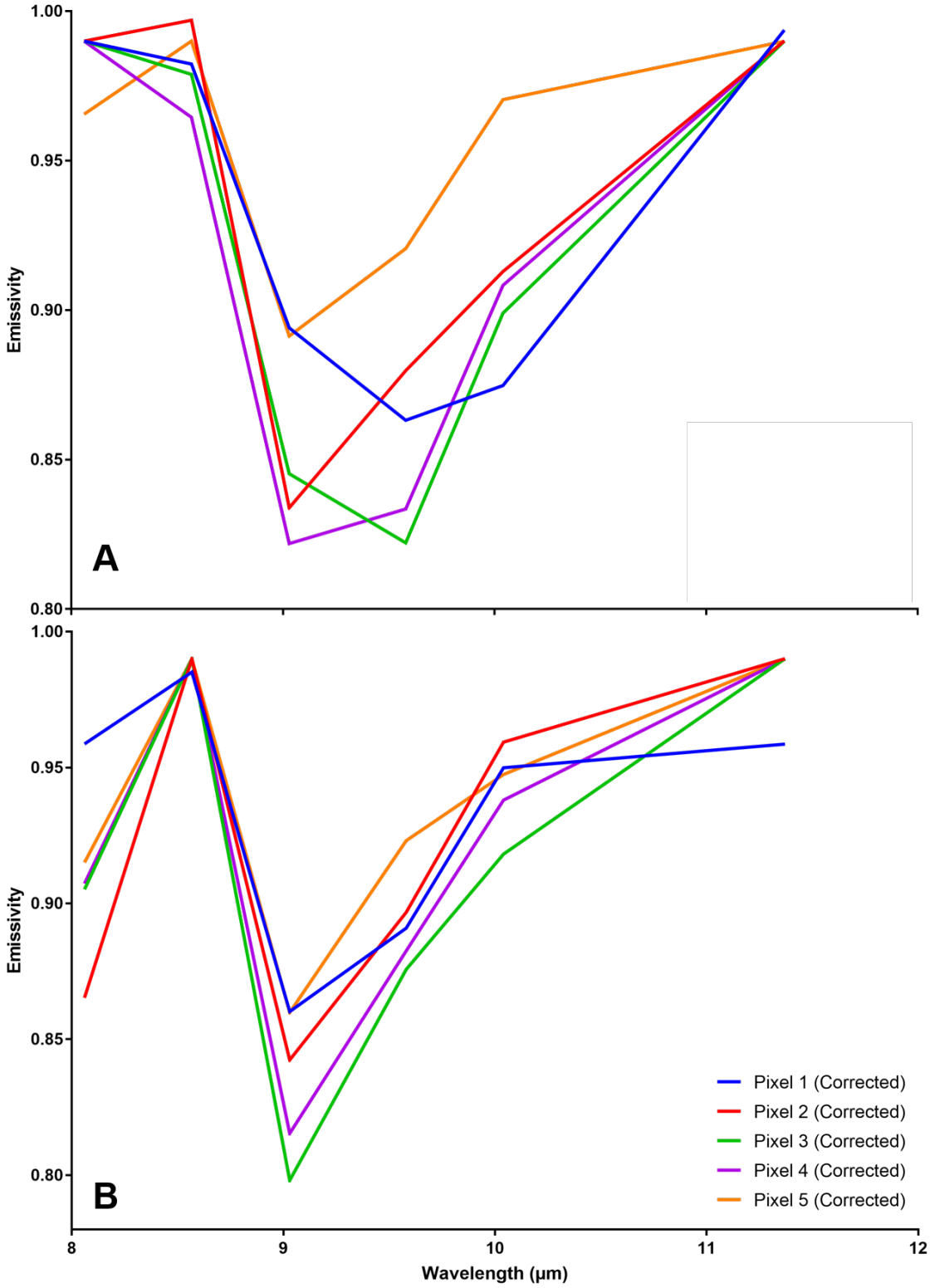

Figure 4-12 Image spectra corrected for sub-pixel temperature effects from (A) 21 February 2018 and (B) 23 February 2018.

The location of this pixel is intriguing considering the shape, and it may be indicative of silica-poor lithics that have been erupted from the vent. These larger clasts and blocks do not remain suspended for long and fall out of the column quickly after the eruption. This would leave more finer grained material suspended that is then lofted into the atmosphere. Owing to its lower density than mineral and lithic fragments, a higher proportion of glass remains suspended, and it is possible this is what is observed here. The absorption band depth of these spectra however is still low relative to what is seen in these laboratory data. A comparison of these image to laboratory resolved spectra is shown in Figure 4-13. This winnowing behavior not seen in the image data from 23 February 2018. However in this image the plume has already disconnected from the vent and is drifting as the eruption has ended. Therefore, the larger fragments will have already fallen out of suspension, leaving only the finer grained portion, of which there may, based upon these spectra, be a significant glass component.

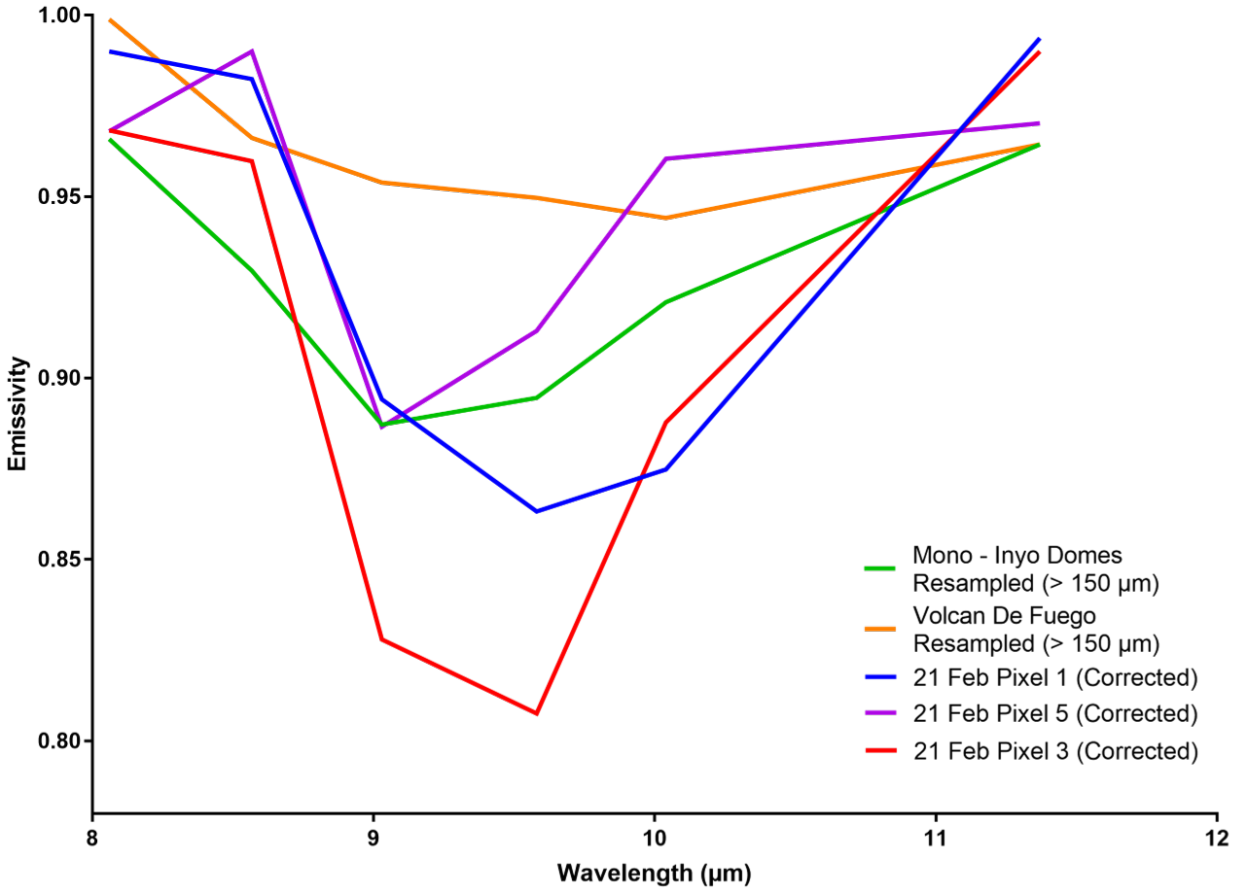

Figure 4-13 Comparison of the spectra shown in Figure 4-12 after having been corrected for the slope caused by sub-pixel temperature mixing with two > 150 µm laboratory end-members (Volcán de Fuego and Mono-Inyo obsidian). After correction, these spectra much more closely resemble those emitted by silicate minerals/glasses.

The correction of the optical aberration from the data does appear to have had a degree of success, and where the spectra have the slope accounted for and normalized, it would appear as though plume components can be identified. However, one of the major influencers on this data is the transmission of the atmosphere, and this must be the next factor to be corrected for. Figure 4-14 demonstrates this fact. These plots were created using the HITRAN2012 atmospheric model from the G & A Technical Software (GATS) Spectral Calculator (www.spectralcalc.com/atmospheric_paths/paths.php). These were calculated based on a tropical atmosphere with a starting elevation of 1128 m, looking up at an angle of 45˚ to a height of 3745 m. These parameters were chosen as they are difference in altitude between the OFVGO and the summit of Volcán de Fuego, with the hope being that these transmission profiles would simulate the atmosphere between the camera and plume. Where plotted with the transmission profiles of the two filter sets, it is obvious that certain absorption features must be accounted for and corrected.

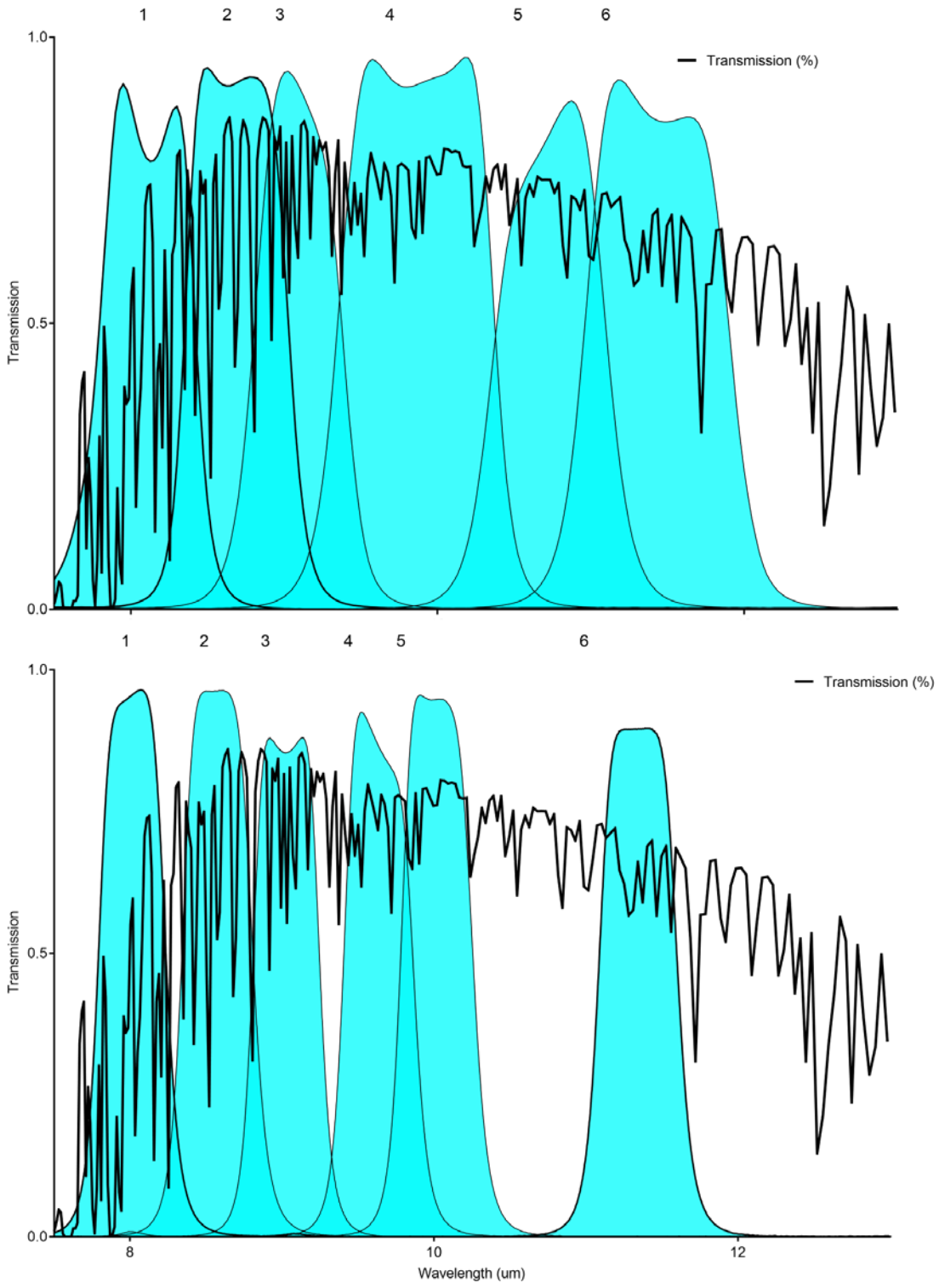

Figure 4-14 1st (upper panel) and 2nd (lower panel) filter sets (highlighted in cyan for clarity) compared with a model tropical atmosphere developed from the HITRAN model. Particularly of note are the absorptions found in band 1 (water vapor), 4 (O_3 and CO_2) and band 6 (water vapor).

Despite this, if the atmosphere can be corrected for, the aberration removal on these data can be properly quantified. If this achieved, then the same methods applied in chapter 3 can then be applied to this data. The position of bands 5 and 6 of the FLIR system would allow for the classification of opaque vs transparent pixels using the BTD method (Prata 1989 a,b; Prata and Bernardo, 2009). A spectral library for use with the FLIR has also been created, with similar diagnostic features of different samples present as they are in AVAL. It is therefore hoped that with continuing development of this system, the camera will become an invaluable tool in the quantification of the products of volcanic ash plumes.

4.5 CONCLUSIONS AND FUTURE WORK

A new apparatus for generating multispectral image data using a broadband thermal camera is described. The updated wheel version of the system is demonstrated to be more effective at obtaining these data, and images where the filter is over the lens can be picked from the dataset. These uncalibrated data do contain an optical aberration due to reflected radiance originally emitted by the camera detector. This is removed by calibrating these data using a blackbody to create a per pixel correction for this effect. Tests within a laboratory environment with obsidian and microcrystalline quartz have produced emissivity spectra that closely fit laboratory spectra that have been resolved to the filter wavelengths. Volcanic plumes erupted by Fuego were imaged during three field campaigns, and although there is a significant variation between laboratory and multispectral FLIR derived emissivity spectra, this may be in part due to sub-pixel temperature mixing. Where a slope correction was applied to these data, they more closely resemble a silicate glass spectra. However, a full atmospheric correction is also required

to obtain more accurate diagnostic information on composition and particle size from these datasets. Furthermore, fully calibrated datasets would then allow the use of the linear deconvolution algorithm which would produce a retrieval of particle size and composition, as was shown in chapter 3 with the ASTER sensor.

The compositional information contained within a volcanic ash plume can be useful in determining the processes behind an eruption. Where observed from a satellite sensor, many larger particles will have fallen out of suspension, which may leave behind a finer grained, glass rich assemblage, as was seen in chapter 3. Field data here from Volcán de Fuego showed evidence of more basaltic/basaltic andesite material at the base of the column, that was then lacking at the plume top. This may be as a result of larger lithic blocks and mineral fragments that erupted but then fall out of suspension soon after ejection. A future aim is to simultaneously collect image data from both the ground and from the ASTER sensor to compare the compositional retrieval, so that evidence of this winnowing effect could be seen. This system could also be used to retrieve particle size and composition of the material that is deposited on the tephra apron, which would provide further evidence of this compositional separation.

5.0 IDENTIFYING ERUPTIVE SOURCES OF DRIFTING VOLCANIC ASH CLOUDS USING BACK-TRAJECTORY MODELLING OF ORBITAL DATA

5.1 INTRODUCTION

Volcanic systems are complex and controlled by an array of different processes. Monitoring these systems provides insight into the potential for future eruptions and assessing their hazards. Various precursory signals, from seismic and deformation to temperature and gas flux, have been used to interpret the movement of magma beneath a volcano and to forecast future activity (Sparks et al. 2012). As satellite systems have improved, those data have also become a reliable tool for eruption monitoring. Many volcanoes worldwide are not permanently monitored from the ground, either due to cost or accessibility, and satellite sensors are now routinely employed to provide a unique perspective of global volcanic activity (Harris et al. 1997; Wright et al. 2002). Despite the orbital data availability, many volcanoes can produce large eruption plumes with little to no precursory warning (Alfano et al. 2011). Ash plumes from these eruptions can easily reach heights that affect the operation of commercial aircraft and impact local to regional populations (Casadevall 1994). Furthermore, upon injection into the upper atmosphere, these plumes are transported over a large area and in multiple directions, dependent on wind shear and speed, which can be ~ 100 m s^{-1} in the jet stream (Prata 2009).

The damage caused to aircraft by volcanic ash is well documented (Prata and Grant 2001). Many commercial aircraft flight paths lie directly over active volcanic regions. In particular, flight paths in remote areas of the world, such as the North Pacific (NOPAC) region, are at the greatest risk with the more than 100 potentially-active volcanoes present across Alaska, the Aleutian Islands and the Kamchatka Peninsula (Webley 2011). The large volume of air traffic as well as lack of alternate airports for emergency landings make this route particularly dangerous (Neal et al. 2009).

Satellite remote sensing has provided one of the most temporally and spatially practical tools for the detection and monitoring of volcanic eruptions, and is used routinely to monitor global volcanic activity (Harris et al. 2001; Rose et al. 2000; Wright et al. 2002). No particular sensor exists solely for the purpose of volcanic emissions detection, yet owing to the unique absorption spectrum of volcanic ash and sulfur dioxide (SO2) in the TIR and SO2 in the ultraviolet (UV) (e.g., Thomas and Watson, 2010), a suite of geostationary (e.g. GOES) and polar orbiting (e.g. MODIS, AIRS, OMI) satellite sensors can be used to operationally detect and track volcanic ash clouds. However, omnipresent global coverage of all volcanoes still does not completely exist, and it is feasible that during shorter onset events, such as during sub-vulcanian to vulcanian activity (such as was observed at Volcán De Fuego, described in chapter 4), these plumes may disconnect and drift before being detected by these sensors. In addition, smaller volcanic events may occur beyond the spatial resolution of the more temporarily available datasets of geostationary platforms such as GOES and the new Himawari-8 sensor, meaning detection is only possible by a handful of sensors, which may only record the cloud once it has drifted from its source location. Therefore, methods to accurately track back these plumes to a possible source should be considered.

It has been shown earlier in this work, that volcanic ash quantification using the ASTER sensor is possible, and that there is information contained within this nascent portion that can be used to determine both composition and particle size. However, ASTERs temporal resolution does not lend itself to routine ash plume monitoring. The ASTER sensor is programmed by the Urgent Request Protocol (URP) system to point off-axis and record any activity in the event that thermal anomalies are detected by lower spatial resolution sensors (Duda et al., 2009). If this were to be expanded to also include ash detection by these same sensors where no thermal anomaly is present, then a larger quantity of data that would possibly include volcanic ash plumes would then be recorded. If ash was, however first detected in an image where the volcano was not present, then this would also require some form of backward trajectory model to be used, in order to determine the region where the ASTER sensor should be pointed.

The backward trajectory modeling approach has a long history over the past several decades for studies of anthropogenic pollution (Stohl 1996; Han et al. 2007). Pollutant concentrations are collected from receptor sites and a Concentration Weighted Trajectory (CWT) is applied to identify the responsible source. Application to volcanic ash plumes has been used simply to confirm satellite-based derivations of plume height (e.g. Winker et al., 2012; Mortier et al., 2013; Prata et al., 2015). However, the approach has not been applied to determine the source location, particularly if there is limited to no data on the plume top height. To do this, it is necessary to examine multiple backward trajectories statistically in order to determine a probable source location. Modeling packages such as Trajstat (Wang et al. 2009) have been developed Graphical User Interface (GUI) tools to aid in this approach. These applications are designed, however, to observe local versus regional sources of anthropogenic pollution in cities, on the timescales of days to years, where the pollutant is measured at a fixed receptor site (Cheng et al.

2013; Pietruczuk 2013). For a temporally short event from a single point source location (i.e., a volcanic eruption) producing an ash cloud at an unknown height, these methods must be modified.

The objective of this study, therefore, is to present a method to track these disconnected volcanic clouds back to their source region. This is done using a combination of TIR satellite remote sensing data from to detect the drifting ash and assess its relative concentration, backward trajectory modelling using the HYSPLIT atmospheric model (Draxler and Hess 1998) to determine the regional location, and a geostatistical analysis within a Geographic Information Systems (GIS) framework to refine the probable volcanic source and assess the accuracy.

5.2 METHODS

One of the issues with finding "genuine" cases of plume disconnection the satellite archive is simply that a vast amount of data of the Earth's atmosphere has been collected. In addition to this, it was also considered that to test the applicability of any backward trajectory model, surely it would be more prudent to test a model where the source was known, by isolating a region that can be treated as "disconnected" and then use it as the input for any backward trajectory model. Therefore, a series of known eruptions from different volcanoes were assessed to test the methodological accuracy of the modeling approach. Ash plumes generated by the eruptions of Etna (Italy) in 2002, Kliuchevskoi (Russia) in 2007, Chaitén (Chile) in 2008, Eyjafjallajökull (Iceland) in 2010, Puyehue-Cordón Caulle (Chile) in 2008, Sangeang Api (Indonesia) in 2014, and Raung (Indonesia) in 2015 are used. The primary aim was to find ash plumes that had not drifted too far from the vent (ideally within 500 km) so as to best simulate

the style of eruption that is to be assessed with this method. However, it also did seem pertinent to see if there was a maximum distance that the method would break down, and so Puyehue was used as an extreme end-member example, with plumes that had drifted in excess of 4000 km from the volcano.

Data from the MODIS sensor is used for this analysis to detect the drifting cloud. Whereas this is one of many satellite sensors that is used to detect ash, MODIS is simply used due to user experience with these datasets, their extensive global coverage of the world's volcanoes, and the availability of the retrieval model for use with it (provided here by Dr. Helen Thomas, Nicarnica Aviation). There are two identical MODIS sensors on board the NASA Terra and Aqua satellites, each with a spatial resolution of 1 km in the TIR region (Justice et al. 1998). MODIS was chosen because of its relatively high temporal resolution, providing images of all global volcanoes (Watson et al. 2004) and multiple TIR channels, which allow the discrimination of ash from those meteorological clouds. The MODIS data archive (https://ladsweb.nascom.nasa.gov/data/search.html) was accessed to find appropriate data in proximity to the chosen volcanoes following the noted eruption. For each eruption, several images of the ash cloud were obtained. The Level 1B radiance product was used and images processed to detect the presence of ash using a simple spectral ratio based upon the Brightness Temperature Difference (BTD) approach (Prata 1989a; Prata 1989b), which returns the spatial location, concentration, and effective radius of the ash particles in each pixel cell of the image. Concentration is important as it serves as the input for the geostatistical methods used later in this study. This method is outlined extensively in chapter 3 (section 3.2). A full list of the MODIS scenes used for this study can be found in Appendix C.

These ash-rich pixels were spatially subset to exclude any portions of the plume that may have still been connected to the volcano where the image was acquired. This simulates a disconnected cloud for this analysis (Figure 5-1). Regions towards the furthest distal edge of the cloud were subset further to provide several testing scenarios for our approach. A cell grid was placed over this spatially subset section and a point located in the center of each cell. The average ash concentration of each cell is assigned to that point. This point served as the coordinate from which the backward trajectory model is initiated. This ensured that no bias was imparted in assigning trajectory run points and allowed the density of the starting grid cell coordinate to be attached to each back trajectory model run. These points seeded the HYSPLIT model, which then created backward trajectories for each.

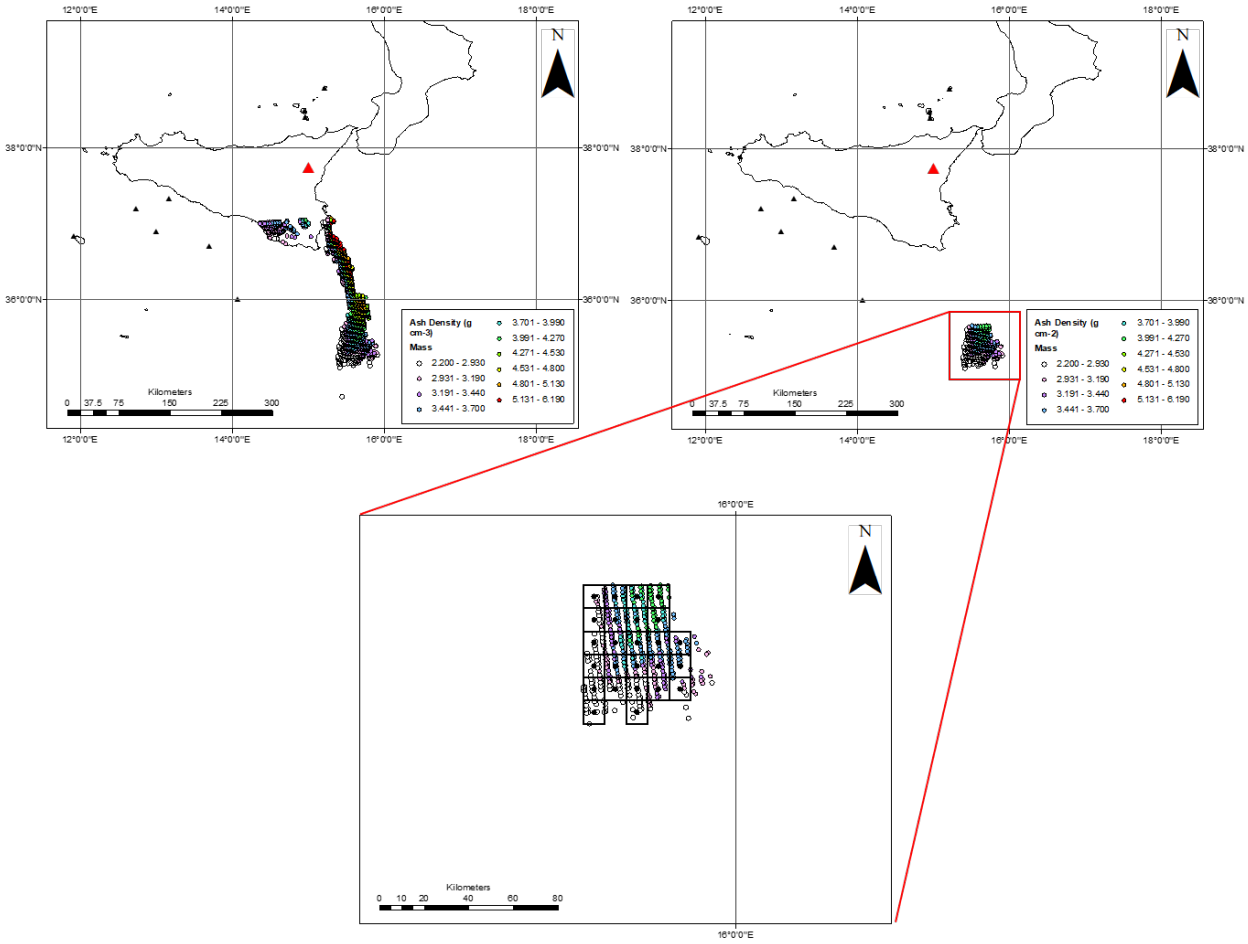

Figure 5-1 Method for creating the simulated "disconnected" ash cloud, demonstrated using a retrieval from an ash plume generation by Mt. Etna, Italy on October 28th 2002. The BTD retrieval model is first used (upper left), and then a smaller region of this plume is then identified (upper right). From this, the grid can be overlain, and coordinate points created from which the HYSPLIT backward trajectory model will be initiated (bottom).

HYSPLIT is a Lagrangian dispersal model that independently calculates the advection and diffusion components of a plume. It was chosen for this study because Lagrangian models are commonly favored where analyzing a single point source for emissions as well as allowing the emission points to be defined at any scale required (Draxler and Hess 1998). Furthermore, HYSPLIT allows multiple input heights and can output data into both shapefile and Google Earth compatible format (e.g., KML), allowing easy integration into a GIS visualization framework. One restriction of this work was that only the Graphical User Interface (GUI) download version of the model was available to the user. This restricts the user to the three height inputs. However this was also considered a possible benefit, as this produced a smaller dataset that was more manageable in a 'real world' hazard simulation. The height of the ash cloud was first estimated by comparing the 11 μm brightness temperature (BT) of pixels containing ash with radiosonde (available at https://weather.uwyo.edu/upperair/sounding) measured air temperature (Sawada 2002). However, errors associated with this approach are possible and include under- or over-cooling of the volcanic cloud as it is injected into the atmosphere, higher cloud temperatures recorded as it becomes transparent allowing upwelling radiance from the ground to be detected (Oppenheimer 1998; Webley and Mastin 2009), and distance between the cloud and radiosonde locations increases (Guffanti et al. 2005). More distal, diffuse plumes led us to assume that radiosonde data will underestimate the plume height, and so the second height level tested was set at 3000 m above the first measurement (hereby referred to as BT+). This elevation is selected so that it would lie in the middle troposphere (depending on the latitude) ensuring that the three heights spanned the lower, middle and upper troposphere. The final height chosen is the local tropopause derived from Atmospheric Infrared Sounder (AIRS) data, using the Giovanni online data system, developed and maintained by the NASA

GES DISC (Acker and Leptoukh 2007). This maximum height is used because previous testing of levels higher than the tropopause demonstrated a significant decorrelation of the plume's travel direction (Williams et al. 2013). Simulations in other studies have also shown that distal ash transport is dominated by atmospheric processes occurring near or at the regional tropopause (Fero et al. 2009).

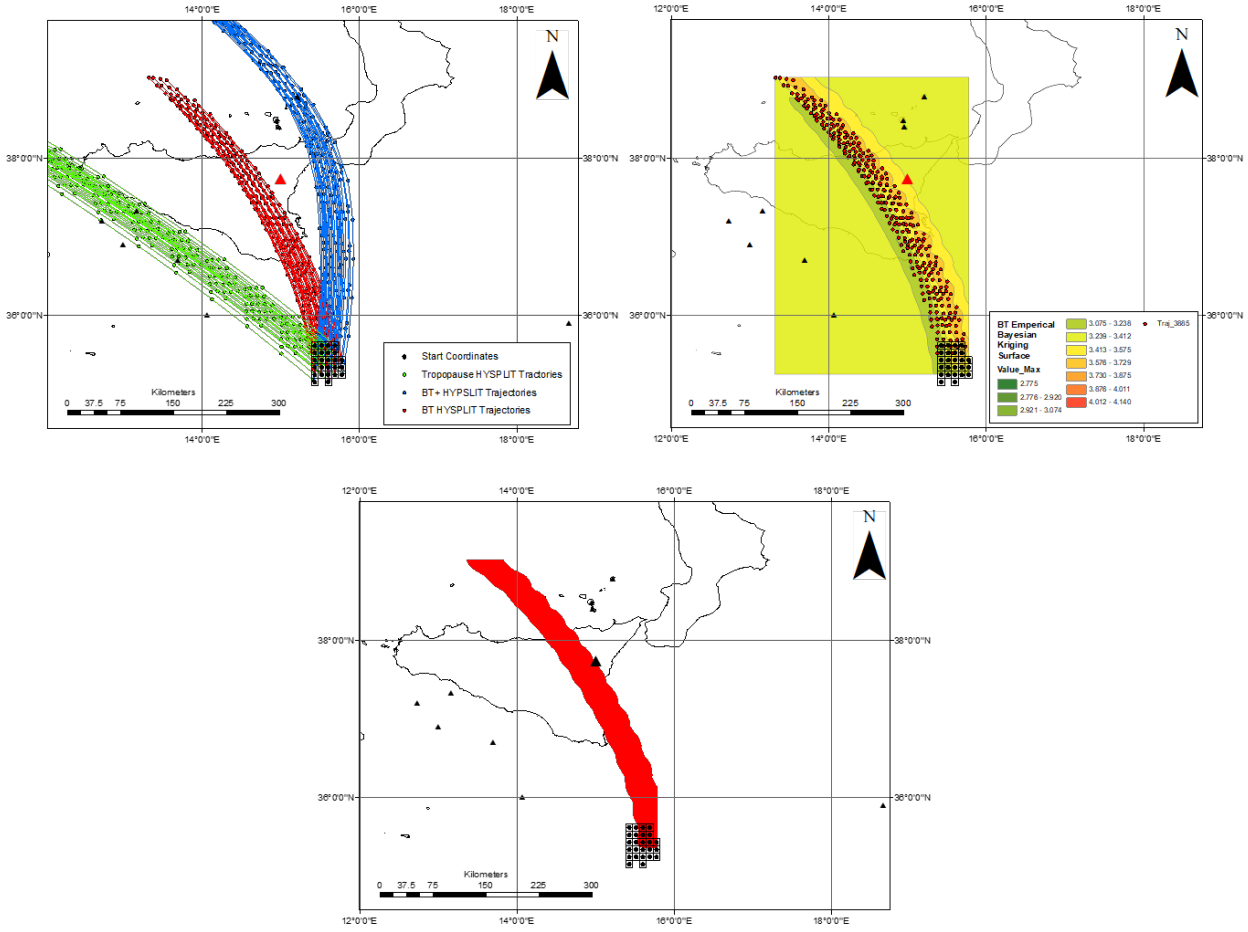

Figure 5-2 Method for creating the final trajectory for each height level. The HYSPLIT backward trajectories are plot (upper left). An interpolated surface is then calculated based on the density of the plume (upper right). The highest density region is the area chosen as most likely represented the plume path, and so from this, interpolated polygons are extracted from this dataset until a trend pathway can be extracted and presented as the assumed overall backward trajectory (bottom).

The final stage of this modeling approach involved processing the trajectories using geostatistical methods. This allowed us to create a predictive surface for the highest density regions at different times. This high-density region was considered the most reliable indicator of overall ash cloud movement. Peripheral regions of the cloud may experience atmospheric turbulence and directional changes, which are beyond the resolution of the HYSPLIT model. The ash predictive surface is created using an Empirical Bayesian Kriging (EBK) approach to interpolate the prediction surface (Figure 5-2). EBK is a probabilistic method chosen because of the lower errors associated with its predicted values, which are the result of inclusion of the semivariogram uncertainty, something not included by other Kriging methods (Krivoruchko 2012). The model is also different in the way it constructs the data semivariogram. Kriging normally uses a weighted least squares approach, whereas EBK estimates the semivariogram parameters using Restricted Maximum Likelihood (REML). This creates an interpolated surface of values that we can analyze, where the surface represents maximum likelihoods and not traditional averages or least squares. Trends within the data are located, and once a trend direction for the highest ash density regions is found, the polygons are isolated to create the final backwards trajectory pathway. Volcanoes that lie within this high-density polygon pathway are selected as potential sources. If the known source falls outside this range, then the distance to it is measured, informing our model error analysis.

5.3 RESULTS

The model was applied to fifty different scenarios, which were derived from 23 individual MODIS scenes. The results are categorized into three different distance ranges (near-,

mid- and far-range) from the volcano. The ranges are based upon the swath widths of current satellite sensors, representing the maximum distance that a volcanic plume could travel and still being in the same sensor image as the source volcano. The near-range scenarios are based upon the swath of a Landsat image (≤ 185 km), the mid-range is defined as the width of a MODIS image (185 – 2330 km) and the extreme far-range being anything greater than the MODIS swath. Whereas it is not expected that such a mode would even need to be used on these more distal ash plumes, it was simply done as a test to see if there is a break down in model effectiveness with distance.

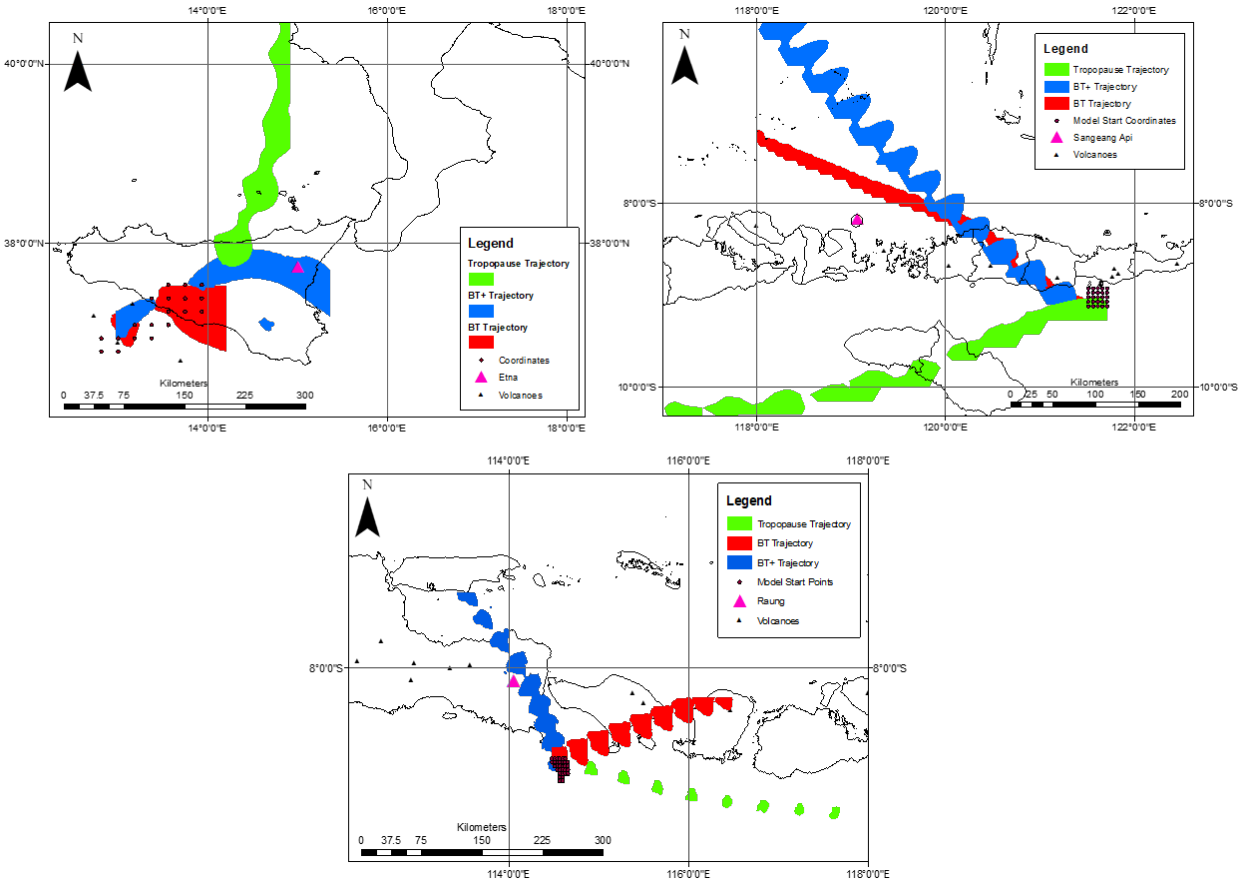

Figure 5-3 Examples of the "near- and mid-range" scenarios created using this method; Clockwise from top left – Mt. Etna, Italy, 28 October 2002 1453 UTC; Sangeang Api, Indonesia, 31 May 2014 0525 UTC; Raung, Indonesia, 12 July 2015 0240 UTC.

5.3.1 Near-Range

As one would expect, the near-range model trajectories proved the most accurate, with all but three individual trajectories across all height levels found within 200 km of the edifice. Of these results, the BT + 3000 m height level was the most accurate, with all 8 backward trajectories tracing the cloud back to within an average distance of 6.5 km of the known source. The Tropopause height level was the least accurate for the near-range scenarios. Only 2 out of 8 results traced accurately back to within 50 km. The BT derived height level had the greatest range of results, with an average distance of 58.5 km calculated. This inconsistency appears to be directly related to the assumption of volcanic ash cloud height. However, this does put all of the BT+ backward trajectories within the ASTER sensor swath, meaning that if these data were used to point the ASTER sensor at the region identified, the target volcano would be in the image, thus possible additional activity could be recorded.

Table 5-1 Results of the model using the short range scenario. The average distance to the source was found to be less than 100 km for all assumed cloud heights, although the accuracy of the BT and BT+ levels was much greater than that of the tropopause height.

Actual distance from cloud to source volcano (km)	Modelled distance to source volcano (km) using BT height	Distance from BT+ trajectory to source volcano (km)	Distance from tropopause trajectory to source volcano (km)
49.5	26.6	0	49.6
96.6	73.0	0	48.6
97.8	89.3	10.7	99.2
121.9	0	2.8	99.9
131.0	149.8	38.4	147.0
133.0	113.6	0	137.7
142.0	13.9	0.3	104.5
165.8	2.1	0	131.6

5.3.2 Mid-Range

Results in this range showed a lower level of accuracy than those in the near-range, but also had the largest number of model scenarios (36 in total). The most accurate height level was the tropopause height level, with an average distance of the back trajectory to the known source volcano of 105.5 km. The overall accuracy of each height level decreased significantly where compared to the near range trajectory models, with all height levels averaging over 100 km from their trajectories to the source volcano. This inaccuracy is further highlighted considering that the BT and BT+ levels only had 14 out of 36 clouds that were tracked back to within 50 km, and for the tropopause height level this was even lower (12 of 36). However, upon further examination of the results, this greater average distance appears to be the result of one group of model results from the Kliuchevskoi volcano. Eleven scenarios were tested for the June/July 2007 eruption. If these are removed, the mid-range results change, with the BT and BT+ height level averages improving from 135.7 and 115.3 km, to 83.7 and 77.8 respectively. Removing the Kliuchevskoi results, clearly highlights an error in the method used for this particular eruption, which is examined in the Section 5.4.3. Results from the tropopause height level maintained similar average trajectory accuracy, with or without the Kliuchevskoi results, at 105.5 and 103.8 km respectively.

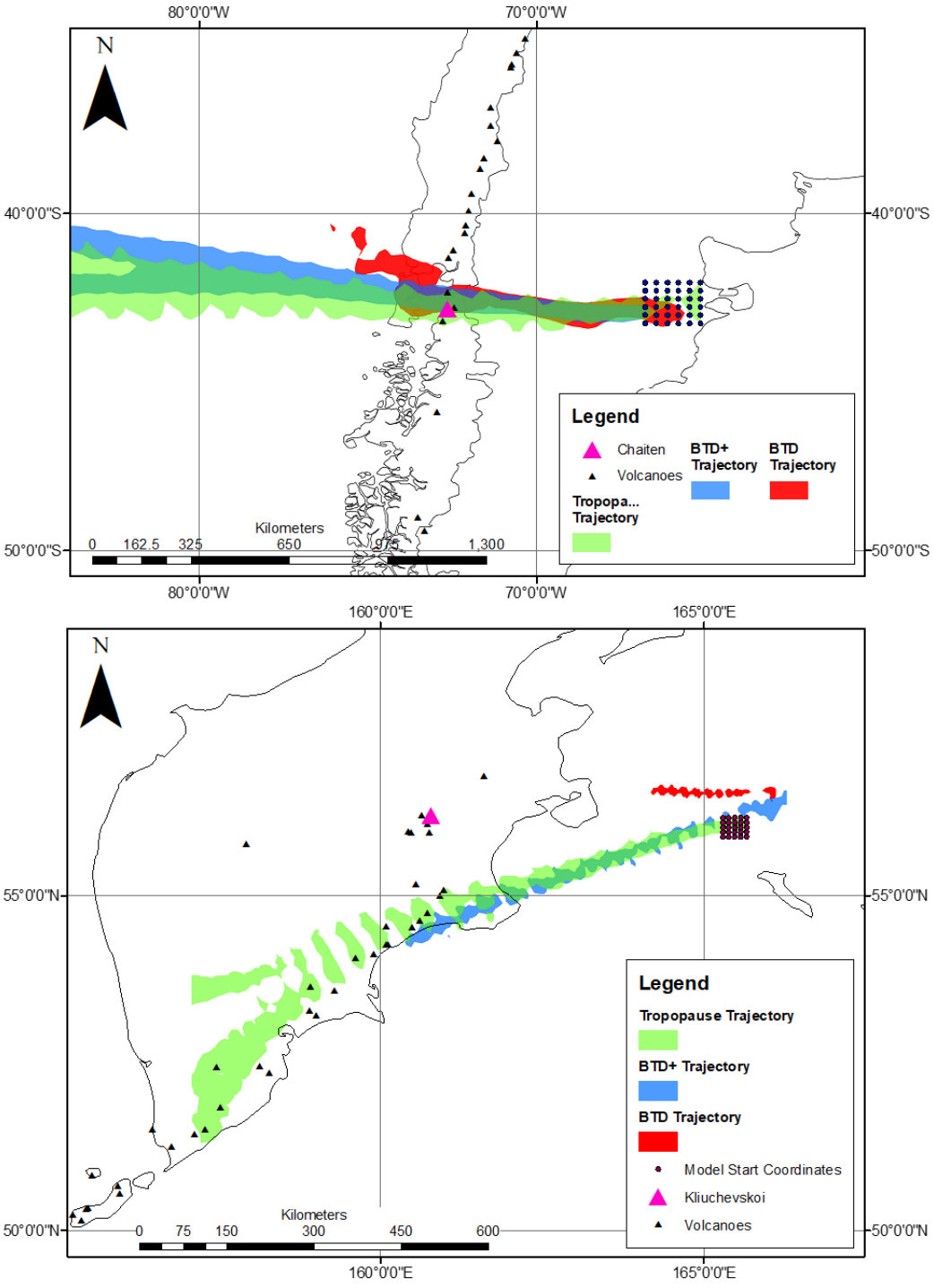

Figure 5-4 More distal end-members of the "mid-range" scenarios showed varying degrees of success. The upper scenario from Chaitén volcano (5 May 2009 1435 UTC) was accurate for all three height levels, however Kliuchevskoi (bottom; 29 June 2007 2340 UTC) was much more inaccurate.

Table 5-2 Results of the model using the mid-range scenario. The average distance was much larger than the short-range results, however this average decreases if the results from Kliuchevskoi are eliminated.

Distance from cloud to source volcano (km)	Distance from BT trajectory to source volcano (km)	Distance from BT+ trajectory to source volcano (km)	Distance from Tropopause trajectory to source volcano (km)
195.2	0	5.8	39.8
204.8	63.8	11	142.7
214.3	163.6	202.9	60.7
215.2	163.8	192.2	0
237.9	1.80	48.9	109.4
240.3	203.5	127.5	3.8
247.2	0	84.2	53.0
257.8	15.2	49.1	0
279.8	213.7	130.4	115.1
281.3	31.6	68.6	181.4
295.8	0	5.5	197.2
336.8	106.6	28.9	201.8
357.8	376.1	226.2	170.7
377.2	361.8	394.2	146.0
377.6	9.7	125.5	3.02
381.4	0	16.5	81.1
385.5	381.7	282.8	95.2
397.9	274.7	192.9	167.3
413.3	187.0	65.4	74.7
433.6	88.1	80.0	305.84
479.5	0	0	0
483.0	174.7	38.9	40.2
509.1	83.6	0	287.8
510.0	368.5	319.5	13.0
520.9	5.1	11.1	22.0
545.5	0	235.9	144.5
557.4	144.0	74.9	338.0
626.7	223.2	10.3	265.0
662.8	24.7	240.6	135.0
1350.8	645.3	172.3	115.7
2303.6	0.8	125.5	0

5.3.3 Far-Range

The far-range model results had, as was expected, the lowest overall accuracy for the BT and BT+ height levels. For clouds that had travelled further than 7000 km, the BT and BT+ height levels produced trajectories that were either more than 500 km from the known source or produced no discernable trend and making a result map impossible to create. The tropopause height level trajectories did produce results that were still within 200 km of the source volcano, with an average distance of 154.7 km. This improves significantly to 104.3 km if the most inaccurate result is removed.

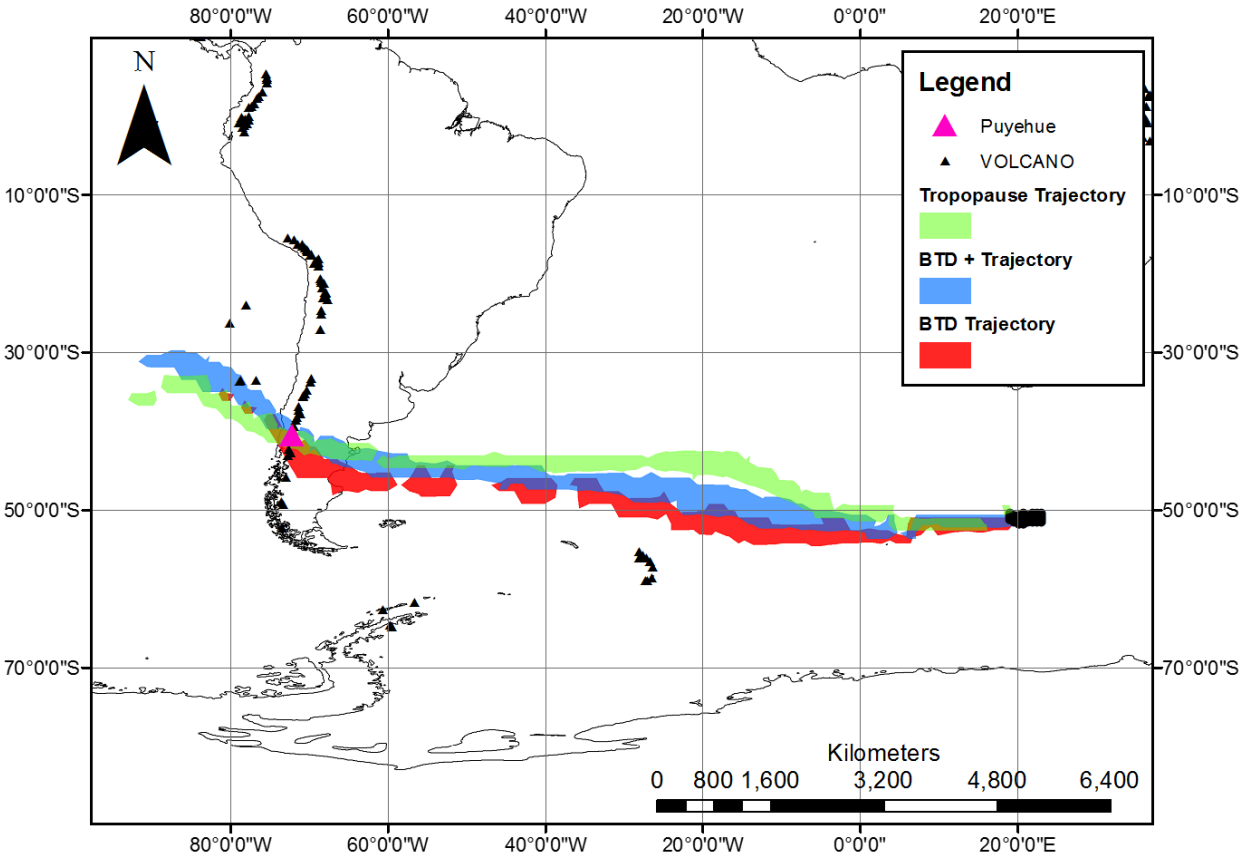

Figure 5-5 Model results from the ash cloud produced by Puyehue-Cordón Caulle, Chile, 8 June 2011 0920 UTC. Despite many of the extreme tests of the model effectiveness showing that it becomes more inaccurate with distance, this example curiously ended with all three height levels tracking back the cloud to within 60 km of the source volcano, thus within the ASTER swath width.

Table 5-3 Results of the model using the long range scenario. These results proved to be the most inaccurate, with many of the BT and BT+ trajectories not processed, as the interpolated map showed no trend from which to even create a high density trajectory. These results are marked with N/A in the Table.

Distance from cloud to source volcano (km)	Distance from BT trajectory to source volcano (km)	Distance from BT+ trajectory to source volcano (km)	Distance from tropopause trajectory to source volcano (km)
4385.0	1,875.5	0	137.8
5057.9	N/A	N/A	123.2
6109.2	N/A	N/A	408.06
6751.8	0	53.4	0
14635.8	N/A	N/A	77.2

5.4 DISCUSSION

Overall, the model produces reasonable success using the described approach to track volcanic ash clouds back to their probable source. However, as with any modeling approach, a detailed error analysis of the results is warranted.

5.4.1 Height Assignment

Determining the height of a volcanic plume is critical to understand the propagation of a cloud from its source, the magnitude of the eruption, and the down-wind hazard impacts to populations on the ground and in the air. Plume top height is commonly determined using the TIR derived temperature assuming that the cloud is in thermal equilibrium with the surrounding atmosphere. Therefore, if the atmospheric vertical temperature profile is known, the cloud height can be extracted from the temperature data. The atmospheric temperature profile is normally determined using radiosonde data, which is ineffective in certain situations. For example, because the more distal portions of the plume become optically thin, emitted radiance from the ground may also be present in the cloud data. This leads to derived temperatures that underestimate the actual cloud height for clouds within the lowest 1000 km of the atmosphere. Although some BT results show relatively high accuracy (within 50 km of the edifice), this height assignment resulted in the widest distribution of back trajectory model results. The average overall distance for all model runs was 159.8 km, with the largest being 1875.5 km.

In order to mitigate this effect, the “BT+” height was used to create a proxy for heights midway between the derived BT and tropopause height. Because the error in BT height will

depend on a variety of factors (e.g., ash cloud over/under cooling, amount of ground radiance upwelling, distance of radiosonde measurement to the location of the cloud; e.g., Oppenheimer, 1998) it becomes difficult to quantify a precise BT+ height. A height of 3000 m above the BT-derived height was chosen, as it is approximately the midway point between the average derived BT height and that of the tropopause for all example locations. Furthermore, this additional height proved to be the most accurate for the back-trajectory model, with an overall average error of 96.8 km between the model and the actual source. However, removing the results for Kliuchevskoi, which recorded the highest inaccuracy for the BT+ level, the average distance error improved to 49.5 km. One can therefore assume that most of the clouds examined in this study were drifting at heights very close to this assumed BT+ height.

The tropopause height was the easiest to determine using data from NASA's Giovanni system. The back-trajectory model results using this height improved in accuracy as vent to cloud distance increased. For example, using this height for modeling the back trajectory of the cloud produced by Puyehue Cordón-Caulle eruption resulted in locations within 500 km of the actual vent, far better than the other two heights. This improvement is due to greater distal transport of plumes that are within the upper troposphere/lower stratosphere and the relatively straight-forward wind regime at these heights. In other words, larger eruptions that produce larger ash clouds are most likely emplacing them at heights equal to or greater than the tropopause. The tropopause height assumption allowed relatively-accurate trajectories for more than 1000 km. The only exception to this came once again from the Kliuchevskoi eruption, where the tropopause height level produced the greatest accuracy for eruption clouds between 215 and 736 km from the source, with an average of 84.2 km.

Overall, correct height assignment is important to successfully locating the source volcano, which is an important not only for identifying remote unmonitored volcanoes but also to enable triggering of ground-based warning systems and data acquisition from other orbital assets (e.g., Ramsey, 2016). It is not uncommon with the current orbital satellite suite to detect a drifting ash cloud before detecting a thermal anomaly that would indicate the eruption in progress. Determination of the cloud height is not always straight-forward, however, as these estimates can be made by multiple sources, such as simultaneous LiDAR or RADAR data (if available), forward modeling (if the source is known) and ground based observations (if it occurs in a populated region). Therefore, with the assumption that a drifting ash-rich cloud is first detected by MODIS (or another high-temporal, low-spatial resolution thermal IR satellite) determining the appropriate cloud height for back trajectory modeling is critical to the final accuracy, but can be estimated with acceptable results if enough model runs are performed.

5.4.2 Model Uncertainty and Geostatistical Methods

The HYSPLIT model has proven to be a useful and relatively quick tool, which is essential for rapid response to hazards, but there are limitations that affect the results. The main source of error is model resolution. After 2006, the input wind field data for the HYSPLIT model is provided by the Global Data Assimilation System (GDAS). These data have a resolution of 0.5 or 1 degree depending on the time period that was observed, meaning any atmospheric turbulence or changing wind vectors that occur below this resolution are not resolved and used by the model. Therefore, this directly affects the lateral ash cloud distribution and its vertical profile, neither of which are measurable and therefore produce errors in the modelled trajectories. If the ash plume is more linear (e.g., Etna) or closer to the edifice (e.g., Sangeang

Api), these effects are not as pronounced. For distal and more diffuse plumes (e.g., Chaitén and Puyehue-Cordón Caulle), however, the effects of smaller scale turbulence may have more pronounced effects on the modelled ash transport trajectory.

The effects of the back-trajectory model uncertainty will also affect the subsequent geostatistical methods. If an obvious trend is present in the data, a more accurate final trajectory is created and confidence in the predicted location is improved. Where model results produce trajectories with no obvious trend, the area covered by the highest density polygons becomes larger and therefore more volcanoes are included in the final analysis. This is especially notable for volcanic arcs with closely-spaced (and recently active) volcanoes. Because the goal of this approach is to identify a geographic region, the broad-scale results appear promising but are limited to the data availability and model assumptions.

5.4.3 Kliuchevskoi Results

Results obtained from creating backward trajectories from the 2007 eruption of Kliuchevskoi volcano produced results that had much lower accuracy than the other volcanoes. In fact, where these results are not included, the average distance from the final trajectory polygon to the source volcano across all model runs decreases significantly. A prime example of this is seen in the near-range scenarios, where the average distance for the BT derived height decreased from 69.7 to 46.5 km upon removal of the Kliuchevskoi results. Because there were so many outliers in this dataset, these results were further analyzed and found to have been affected by small scale atmospheric perturbations beyond the resolution of the archive meteorological data grid. These small scale systems would be able to change the trajectory of the ash plume without the archived meteorological data able to resolve such an occurrence.

However, whereas this presents a challenge, there is also a potential solution. Given that the approach presented here is designed to be a rapid response tool to a future drifting volcanic ash cloud, higher-resolution forecast model atmospheric data would be available. The current data input for these models is available at a much higher spatial resolution than that of archive data, which is 0.25 degrees for the Global Forecast System (GFS) model data and therefore may be capable of modelling the effects of smaller-scale atmospheric disturbances.

5.4.4 Further Testing and Operational Capability

The main focus of this work is to use known volcanic eruptions as tests for a series of backward trajectory model results combined with a new geospatial analysis approach to identify the eruption source region. A drawback to this methodology is the a priori knowledge about each eruption, which influenced the back-trajectory model run time. In an actual situation where a drifting ash cloud is detected, there likely will be no knowledge of how long the cloud has been present. Therefore, the next stage in testing is to either obtain data containing disconnected clouds, or prepare a series of blind tests, whereby data are subset ahead of time and the model run with no knowledge of the eruption location. This would simulate the best practices for this modeling approach if it were to be used in a future eruption scenario.

The intention of this work is also to describe how the model could work in an operational setting. The work flow was designed to imitate how an actual fugitive cloud would be detected, tracked and assessed. The workflow for the model if used in real time would follow the same routine. First, the cloud would be detected by the satellite sensor, the ash-bearing pixels and the ash concentration next identified and then the coordinate grid overlain. Three heights could be assumed and their trajectories calculated in order to determine the potential errors in those height

assumptions. However, one important difference would be the availability of forecast model data from a source such as the GFS model, which is now at a much higher grid cell resolution. From this the geostatistical results would then be used to identify the a potential source region. These then could be automatically used as triggers for new data acquisitions, such as the ASTER Urgent Request Protocol (URP) system or ground-based systems. ASTER URP data at much higher spatial and spectral resolutions could then be examined in detail for thermal and compositional changes and assess the potential for future activity.

5.5 CONCLUSIONS

A model combining the BTD approach in TIR satellite data for ash detection, a new geostatistical treatment of the BTD results and the HYSPLIT model for back-trajectory tracing has been developed and presented. The results are used to statistically predict the backward trajectory of a drifting ash cloud to its most likely source region, with the aim to have this fall within the ASTER swath width of 60 km. This model is tested and shown to be accurate to within 100 km of the known source volcano if properly constrained with accurate input parameters such as cloud height.

Being able to constrain the specific geographic region and perhaps even the exact volcanic source of an unknown eruption is vital to allow quick satellite response of orbital and ground-based assets as well as to direct emergency response to the affected area. Furthermore, knowing the source volcano and magnitude of the eruption that produced the cloud would allow further analysis and monitoring using additional orbital assets over time to infer and predict future activity. As we continue to develop more accurate methods to both quantify volcanic ash

emissions and improve estimates of the height of volcanic ash clouds, the approach outlined here will further improve.

6.0 CONCLUSIONS AND FURTHER WORK

The work presented here has provided a new insight into the observation of volcanic ash clouds. Where previous methods sought to determine the location and density of volcanic ash clouds, and mitigate the effects to aircraft, this work has focused in on a smaller area, but in much finer detail. The use of ASTER data coupled with spectral emissivity end-member libraries have shown that the opaque plume can be treated as a solid emitting surface and unmixed linearly using these laboratory data. In turn, the laboratory data produced have shown the spectral variations in volcanic ash from different compositions, and that these have the potential to be used as a routine identifier of volcanic ash composition. The ASTER sensor has the potential to become a very powerful tool in the determination of particle size and composition of opaque volcanic plumes, providing that the input library can be expanded to include a greater variety of compositions that are produced by volcanoes. These data can also be complemented with those from the multispectral thermal camera. Whereas there are distinct issues with attempting to obtain meaningful data at the present, if the calibration and atmospheric corrections can be calculated, then this will allow the opaque rising ash column to be analyzed. In the case of drifting, transparent ash, it is hoped that the methods developed with backward trajectory modelling could be used as a resource for point higher resolution sensors towards volcanic targets. This would increase the quantity of URP data available to us, and allow further validation of this critical program.

Beyond the current datasets, it is important to determine the directions that this project can go in. Some interesting challenges have been determined from these data, what the exact emissivity spectrum of an opaque ash bearing plume is. One of the issues that also arises is the fact that ash particles are in suspension, with grains not necessarily in contact with each other. The effects on emission and scattering therefore may not be so clear. One solution to this would be to develop a chamber that could take spectral measurements of volcanic ash as the ash is in suspension, to determine if there are any differences than if the ash particles are stationary within a sample cup.

For this project to continue to seek information on volcanic ash plumes however, new multispectral, high spatial resolution satellite sensor missions need to be selected for launch into Earth orbit. The ASTER sensor, as with all satellite platforms, is a finite mission, and whereas it continues to collect and transmit data, this will not continue forever. It is hoped that work such as this, along with other aspects of the TIR remote sensing of volcanoes, will show the importance of using high spatial and spectral resolution datasets to better understand the products and processes of volcanic eruptions.

APPENDIX A

REPORT FROM R.J. LEE GROUP

This section contains the full report produced by R.J. Lee group upon examination of the volcanic ash samples used in this study. 2.5 g of each sample was placed in a glass vial and sent to the Monroeville laboratory for analysis. Results and samples were returned to the University of Pittsburgh within 15 days of receipt.

RJ LEE GROUP
DELIVERING SCIENTIFIC RESOLUTION

May 15, 2018

Daniel Williams
Department of Geology and Environmental Science
4107 O'Hara Street
Pittsburgh, PA 15260

RE: RJ Lee Group Project Number: AOH1049421-0

Dear Daniel Williams,

RJ Lee Group (RJLG) received 7 volcanic ash samples for characterization. The samples were received on April 30, 2018 in good condition and assigned the RJ Lee work order number AOH1049421-0. Estimated modal percent of phases for each sample are shown in Table 1 along with a color designation from the Munsell rock color chart.

Polarized Light Microscopy (PLM) Results

All 7 samples were analyzed by PLM to identify phases as well as visually estimated concentration of those phases as shown in Table 1. All 7 samples had varying degrees of volcanic glass, plagioclase, and olivine. Stereoscopic overviews are shown in Figures 1-7 and PLM photomicrographs were taken of all 7 samples immersed in a refractive index oil of 1.550 displayed in Figures 8-14.

These results are submitted pursuant to RJ Lee Group's current terms and conditions of sale, including the company's standard warranty and limitation of liability provisions. No responsibility or liability is assumed for the manner in which the results are used or interpreted. Unless notified to return the samples covered in this report, RJ Lee Group will store them for a period of ninety (90) days before discarding.

Should you have any questions regarding this information, please do not hesitate to contact me.

Sincerely,

Logan Solotky
Geologist
LSolotky@rjleegroup.com
724 387-1867

Table 1: Visual estimation and Munsell rock color designation.

RJLG Sample #	Client Sample #	Modal %	Color of Sample
10435942	Fuego 2015	76% Plagioclase, 20% Volcanic Glass, 2% Olivine 2%, and <1% Monoclinic Amphibole, Organics, Miscellaneous	5Y 6/1 Light Olive Gray
10435943	Fuego 2016	83% Volcanic Glass, 15% Plagioclase, Olivine 1%, and 1% Miscellaneous	5YR 2/1 Brownish Red
10435944	Sakurajima 2013	64% Volacanic Glass, 20% Plagioclase, 15% Olivine, 1% Pyroxene and <1% Miscellaneous	N3 Dark Gray
10435945	Sakurajima 2016	80% Volcanic Glass, 18% Plagioclase, 1% Olivine, 1% pyroxene, and <1% Miscellaneous	5YR 4/1 Brownish Gray
10435946	Santiaguito 2011	75% Volcanic Glass, 25% Plagioclase, and <1% Olivine, Pyroxene, Organics	5YR 6/1 Light Brownish Gray
10435947	Santiaguito 2016	64% Volcanic Glass, 35% Plagioclase, 1% Olivine, and <1% Pyroxene, Miscellaneous	5YR 4/1 Brownish Gray
10435948	SHV 2010	76% Volcanic Glass, 20% Plagioclase, 2% Olivine, 2% Monoclinic Amphibole, <1% Miscellaneous	N6 Medium Light Gray

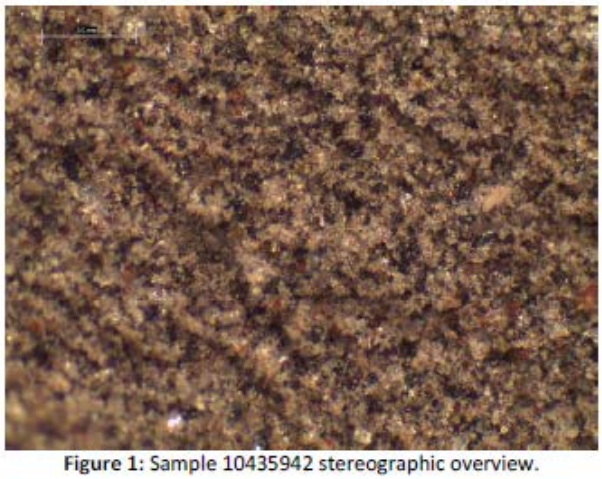

Figure 1: Sample 10435942 stereographic overview.

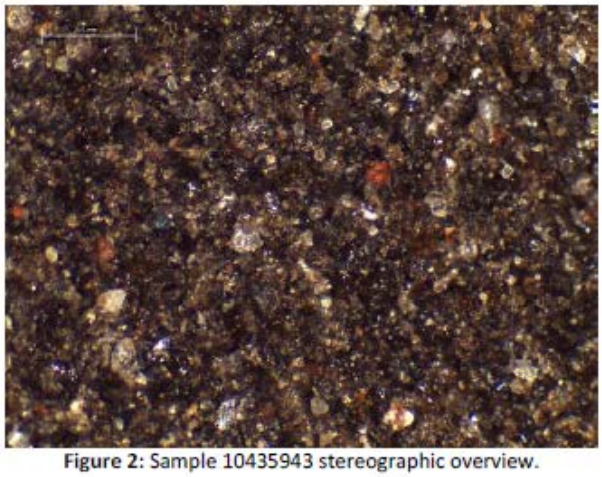

Figure 2: Sample 10435943 stereographic overview.

Figure 3: Sample 10435944 stereographic overview.

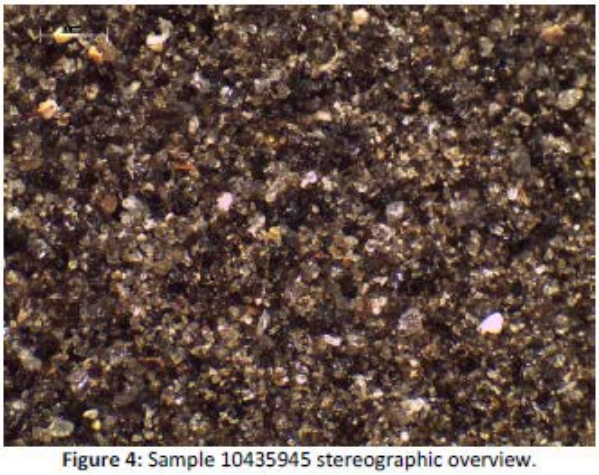

Figure 4: Sample 10435945 stereographic overview.

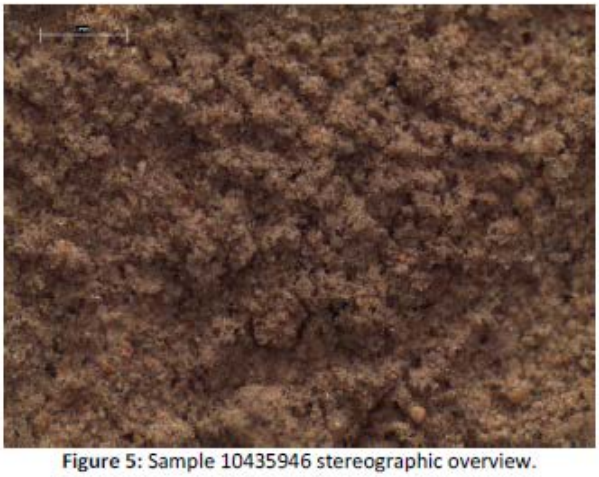

Figure 5: Sample 10435946 stereographic overview.

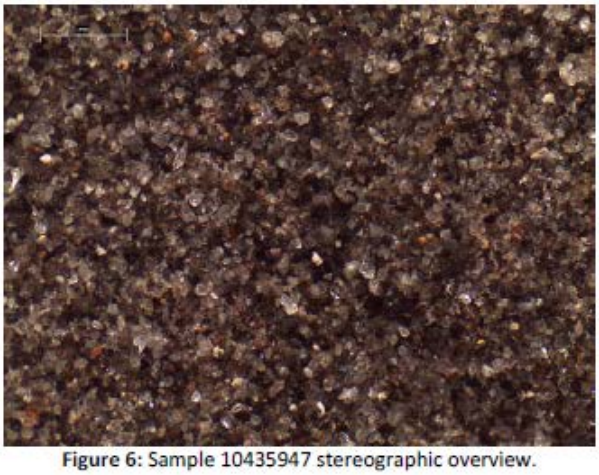

Figure 6: Sample 10435947 stereographic overview.

Figure 7: Sample 10435948 stereographic overview.

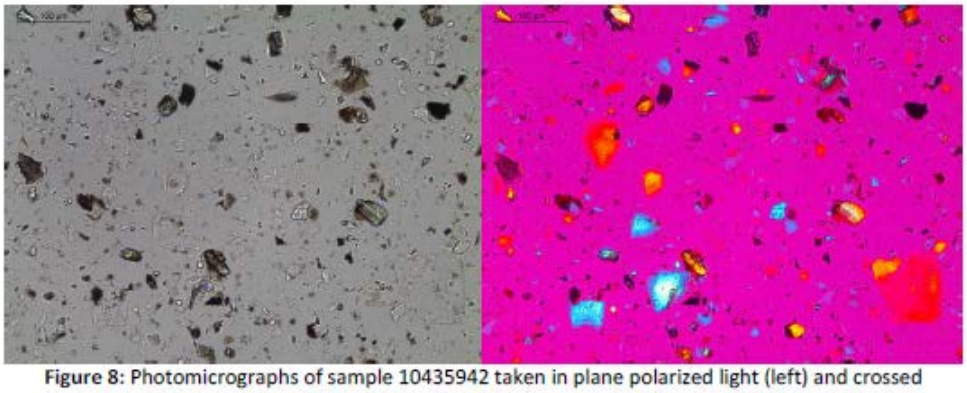

Figure 8: Photomicrographs of sample 10435942 taken in plane polarized light (left) and crossed polarized light with gypsum analyzer (right).

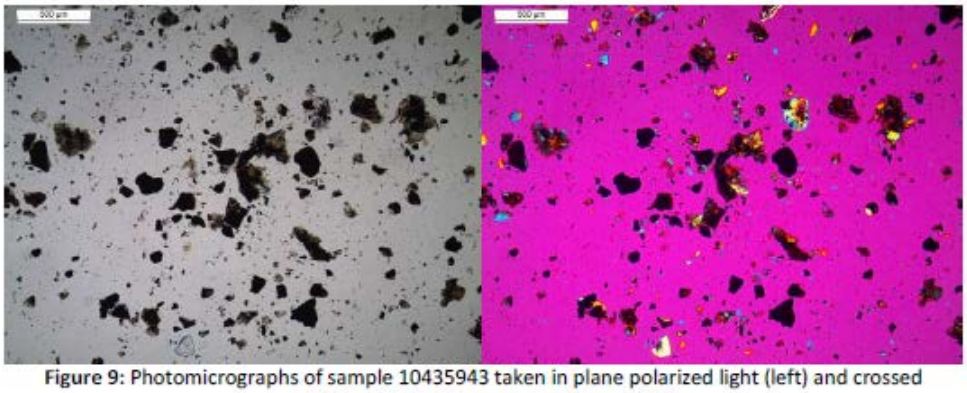

Figure 9: Photomicrographs of sample 10435943 taken in plane polarized light (left) and crossed polarized light with gypsum analyzer (right).

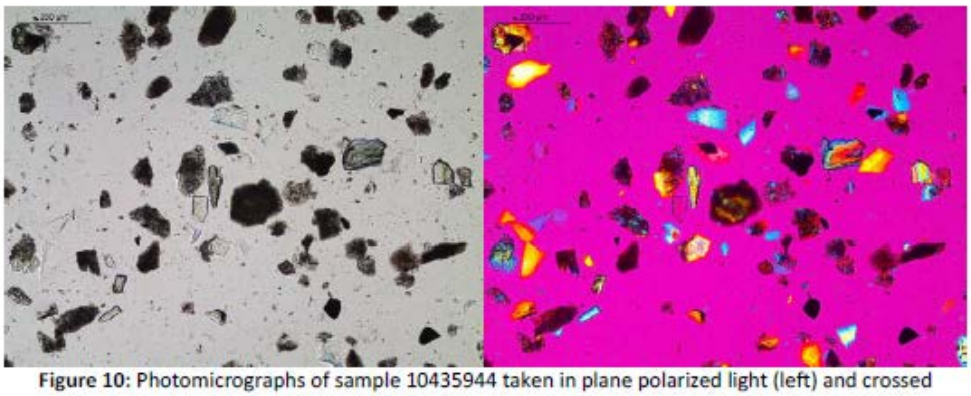

Figure 10: Photomicrographs of sample 10435944 taken in plane polarized light (left) and crossed polarized light with gypsum analyzer (right).

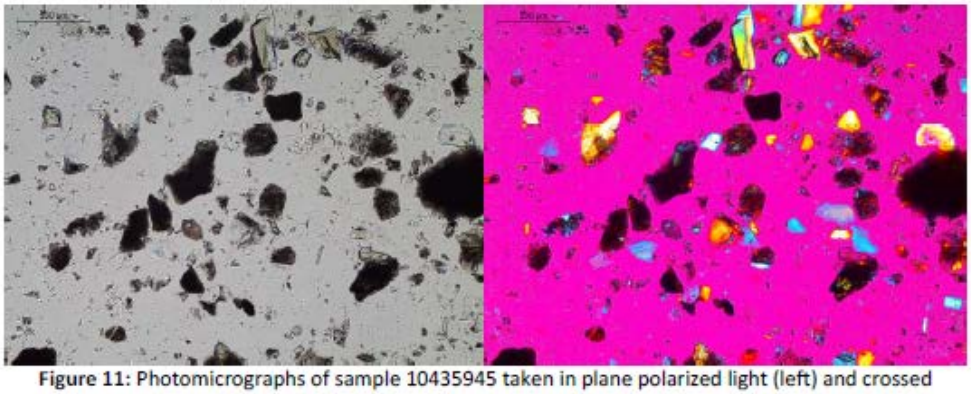

Figure 11: Photomicrographs of sample 10435945 taken in plane polarized light (left) and crossed polarized light with gypsum analyzer (right).

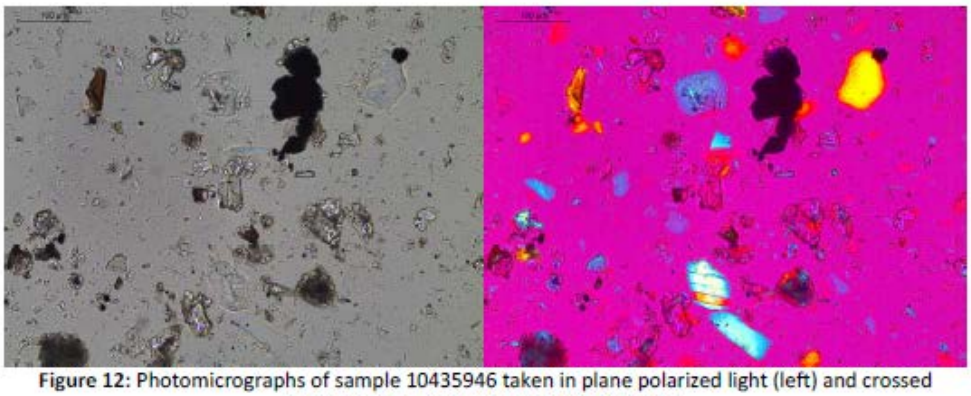

Figure 12: Photomicrographs of sample 10435946 taken in plane polarized light (left) and crossed polarized light with gypsum analyzer (right).

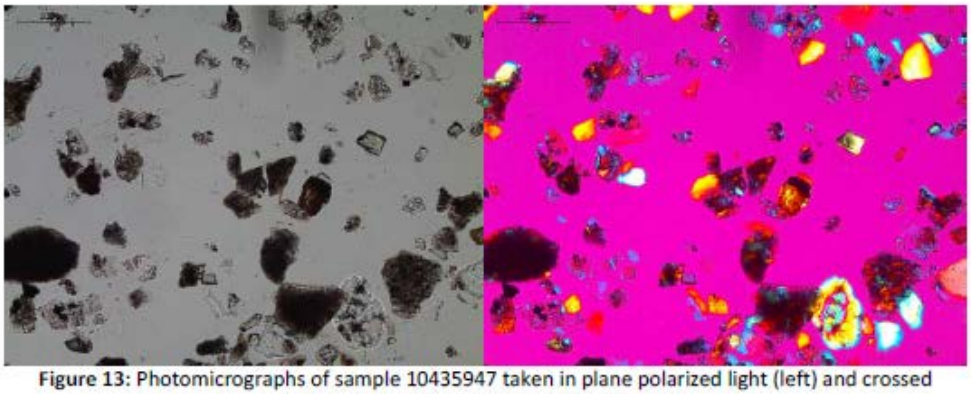

Figure 13: Photomicrographs of sample 10435947 taken in plane polarized light (left) and crossed polarized light with gypsum analyzer (right).

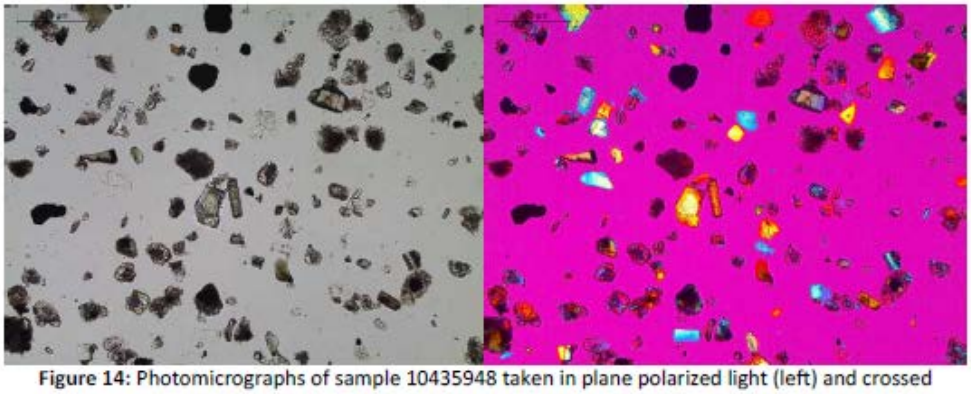

Figure 14: Photomicrographs of sample 10435948 taken in plane polarized light (left) and crossed polarized light with gypsum analyzer (right).

APPENDIX B

ASTER AND MODIS DATA SCENES

This appendix is divided into two sections, each for the full list of ASTER and MODIS scenes that were used in the creation of this work. Both the Aqua and Terra MODIS instruments were used for this work, with the Terra MODIS file names beginning MOD, and the Aqua MODIS files MYD.

B.1 ASTER DATA SCENE LIST

ASTER Scene ID	Volcano Targeted
AST_09T_00304262015034811	Calbuco
AST_09T_00301192009145437	Chaitén
AST_09T_00303312009035431	Chaitén
AST_09T_00305312008035351	Chaitén
AST_09T_00306182008144807	Chaitén
AST_09T_00308192008035349	Chaitén
AST_09T_00304172010224304	Eyjafjallajökull
AST_09T_00304172010224313	Eyjafjallajökull
AST_09T_00304192010125131	Eyjafjallajökull
AST_09T_00304192010125140	Eyjafjallajökull
AST_09T_00304192010125149	Eyjafjallajökull
AST_09T_00304192010125158	Eyjafjallajökull
AST_09T_00304262010125729	Eyjafjallajökull
AST_09T_00305032010130341	Eyjafjallajökull
AST_09T_00305052010223049	Eyjafjallajökull
AST_09T_00305052010223057	Eyjafjallajökull
AST_09T_00305072010123918	Eyjafjallajökull
AST_09T_00305102010224915	Eyjafjallajökull
AST_09T_00305122010125734	Eyjafjallajökull
AST_09T_00305122010223702	Eyjafjallajökull
AST_09T_00305192010224316	Eyjafjallajökull
AST_09T_00302132012145257	Puyehue-Cordón Caulle
AST_09T_00306112011034127	Puyehue-Cordón Caulle
AST_09T_00306112011144634	Puyehue-Cordón Caulle
AST_09T_00306272011034130	Puyehue-Cordón Caulle
AST_09T_00306272011144638	Puyehue-Cordón Caulle
AST_09T_00310242011034733	Puyehue-Cordón Caulle
AST_09T_00312272011145305	Puyehue-Cordón Caulle
AST_09T_00301292012020503	Sakurajima
AST_09T_00302162013020520	Sakurajima
AST_09T_00303042011132356	Sakurajima
AST_09T_00303172015021147	Sakurajima
AST_09T_00303172015021155	Sakurajima
AST_09T_00303192001021604	Sakurajima
AST_09T_00303222015133046	Sakurajima
AST_09T_00304272015020544	Sakurajima
AST_09T_00304292010020519	Sakurajima
AST_09T_00305042012020521	Sakurajima
AST_09T_00305072013020537	Sakurajima
AST_09T_00306102012132350	Sakurajima

AST_09T_00307102013020531	Sakurajima
AST_09T_00308112013020538	Sakurajima
AST_09T_00308272013020542	Sakurajima
AST_09T_00309122013020540	Sakurajima
AST_09T_00309242013133030	Sakurajima
AST_09T_00309282013020530	Sakurajima
AST_09T_00312122011020513	Sakurajima
AST_09T_00312172011132403	Sakurajima
AST_09T_00312192012132359	Sakurajima
AST_09T_00301192016164206	Santiaguito
AST_09T_00301132010023110	Soufrière Hills Volcano
AST_09T_00302122006022348	Soufrière Hills Volcano
AST_09T_00302122006022356	Soufrière Hills Volcano
AST_09T_00302192006023005	Soufrière Hills Volcano
AST_09T_00304172006022425	Soufrière Hills Volcano
AST_09T_00305102006023032	Soufrière Hills Volcano
AST_09T_00306112006023039	Soufrière Hills Volcano
AST_09T_00312122009023120	Soufrière Hills Volcano
AST_09T_00312182008022537	Soufrière Hills Volcano

B.2 MODIS DATA SCENE LIST

MODIS Scene	Terra/Aqua	Volcano Targeted
MOD021KM.A2008170.1445	Terra	Chaitén
MOD021KM.A2008124.1435	Terra	Chaitén
MOD021KM.A2008126.1420	Terra	Chaitén
MOD021KM.A2008129.1450	Terra	Chaitén
MOD021KM.A2010105.1135	Terra	Eyjafjallajökull
MOD021KM.A2010106.1040	Terra	Eyjafjallajökull
MOD021KM.A2010126.1155	Terra	Eyjafjallajökull
MOD021KM.A2002305.2120	Terra	Etna
MOD021KM.A2002306.2025	Terra	Etna
MOD021KM.A2002301.2145	Terra	Etna
MOD021KM.A2002302.2050	Terra	Etna
MOD021KM.A2007182.0025	Terra	Kliuchevskoi
MOD021KM.A2007180.1010	Terra	Kliuchevskoi
MOD021KM.A2007180.2340	Terra	Kliuchevskoi
MOD021KM.A2007181.1055	Terra	Kliuchevskoi
MOD021KM.A2011158.1015	Terra	Puyehue-Cordón Caulle
MOD021KM.A2011159.0920	Terra	Puyehue-Cordón Caulle
MYD021KM.A2011162.0405	Aqua	Puyehue-Cordón Caulle
MYD021KM.A2011163.0310	Aqua	Puyehue-Cordón Caulle
MOD021KM.A2015193.0240	Terra	Raung
MOD021KM.A2015193.1455	Terra	Raung
MOD021KM.A2014151.0235	Aqua	Sangeang Api
MYD021KM.A2014151.0525	Aqua	Sangeang Api

BIBLIOGRAPHY

Abrams M (2000), The Advanced Spaceborne Thermal Emission and Reflection Radiometer (ASTER): Data products for the high spatial resolution imager on NASA's Terra platform, Int. J. Rem. Sens., 21(5):847-859

Acker JG, Leptoukh G (2007) Online analysis enhances use of NASA earth science data. Eos Trans. Am. Geophys. Union 88:14-17

Ackerman SA (1997) Remote sensing of aerosols using satellite infrared observations. J. Geophys. Res. Atmos. 102(D14):17069-17079

Alidibirov M, Dingwell DB (1996) Magma fragmentation by rapid decompression, Nature, 380:146-148

Alfano F, et al (2011) Tephra stratigraphy and eruptive volume of the May, 2008, Chaitén eruption, Chile. Bull. Volc. 73:613-630

Arai K, Tonooka, H (2005). Radiometric performance evaluation of ASTER VNIR, SWIR, and TIR. IEEE Trans. Geo. Rem. Sens., 43(12):2725-2732.

Bailey RA (1989) Geologic map of Long Valley caldera. Mono-Inyo Craters volcanic chain, and vicinity, eastern California: US Geological Survey Miscellaneous Investigations Map I-1933, pp. 11

Bailey RA, Hill DP (1990) Magmatic unrest at Long Valley Caldera, California, 1980-1990. Geosci. Can. 17(3):175-179

Baldridge AM, Hook SJ, Grove CI and Rivera G (2009) The ASTER Spectral library version 2.0, Rem. Sens. Env. 113(4):711 – 715

Bandfield JL, Hamilton VE, Christensen, PR, (2000) A global view of Martian surface compositions from MGS-TES, Sci. 287(5458):1626-1630

Barsotti S, et al (2010) Quantitative assessment of volcanic ash hazards for health and infrastructure at Mt. Etna (Italy) by numerical simulation, J. Volc. Geotherm. Res., 192(1-2):85-96

Baxter PJ et al. (1999) Cristobalite in volcanic ash of the Soufriere Hills Volcano, Montserrat, British West Indies. 283(5405):1142-1145

Bebbington M, et al (2008) Quantifying volcanic ash fall hazard to electricity infrastructure, J. Volc. Geotherm. Res., 177(4):1055-1062

Berk A, Berstein SL, Roberston DC (1989) MODTRAN: a moderate resolution model for LOWTRAN-7. Air Force Geophys. Lab Tech. Rept. GL-TR-89-0122, Hanscom AFB, MA.

Bessho K et al. (2016) An introduction to Himawari-8/9 – Japan's new-generation geostationary meterological satellites. J. Meteorol. Soc. Jpn. 94(2):151-183

Biass S et al. (2017) Potential impacts of tephra fallout from a large-scale explosive eruption at Sakurajima volcano, Japan. Bull. Volc. 79:73

Bignami C et al. (2014) Multisensor satellite monitoring of the 2011 Puyehue-Cordon Caulle eruption, IEEE J. Select. Top. App. Earth Obs. Rem. Sens. 7:2786-2796

Bluth GJS, Rose WI (2004) Observations of eruptive activity at Santiaguito volcano, Guatemala. J. Volc. Geotherm. Res. 136:297-302

Bonadonna C, Phillips JC (2003) Sedimentation from strong volcanic plumes, J. Geophys. Res. Sol. Earth, 108:B7

Bonadonna C et al. (2012) Future developments in modelling and monitoring of volcanic ash clouds: outcomes from the first IAVCEI-WMO workshop on Ash Dispersal Forecast and Civil Aviation, Bull. Volc., 74(1):1-10

Bonis S, Salazar O (1973) The 1971 and 1973 eruptions of Volcan De Fuego, Guatemala, and some socio-economic considerations for the volcanologist. Bull. Volc. 37(3) 394-400

Bray B, Stix J, Cousens B (2017) Mafic replenishment of multiple felsic reservoirs at the Mono domes and Mono Lake islands, California. Bull. Volc. 79:54

Brown RJ, Bonadonna C, Durant AJ (2011) A review of volcanic ash aggregation, Phys. Chem. Earth, Parts A/B/C, 45-46:65-88

Buckland HM, Eychenne J, Rust AC, Cashman KV (2018) Relating the physical properties of volcanic rocks to the characteristics of ash generated by experimental abrasion. J. Volc. Geotherm. Res. 349:335-350

Bulgin CE, Mittaz JPD, Embury O, Eastwood S, Merchant CJ (2018) Bayesian Cloud Detection for 37 years of Advanced Very High Resolution Radiometer (AVHRR) Global Area Coverage (GAC) data. Rem. Sens. 10(1):97

Bursik MI, Carey SN, Sparks RSJ (1992) A gravity current model for the May 18, 1980 Mount St. Helens plume, Geophys. Res. Lett. 19(16):1663-1666

Byrnes JM, Ramsey MS, King PL, Lee RJ (2007) Thermal infrared reflectance and emission spectroscopy of quartzofeldspathic glasses, J. Geophys. Res., 34:L01306

Cashman KV, Scheu B (2015) Magmatic fragmentation, In Sigurdsson H (ed.) Encyc. Volc. 2nd Ed. 473-484

Cashman KV, Rust AC (2015) Volcanic Ash: Generation and Spatial Variations, In Mackie S, Cashman KV, Rickets H, Rust AC and Watson IM (eds) Volc. Ash: Haz. Obs. 1st Ed. 5:24

Casadevall TJ (1994) The 1989–1990 eruption of Redoubt Volcano, Alaska: impacts on aircraft operations. J. Volc. Geotherm. Res. 62:301-316

Casadevall TJ, Delos Reyes P, Schneider DJ (1996) The 1991 Pinatubo eruptions and their effects on aircraft operations. In: Newhall CG and Punongbayan RS (eds.) Fire and Mud: eruptions and lahars of Mount Pinatubo, Philippines, University of Washington Press, Seattle, pp 625-636

Castro JM, Dingwell DB (2009) Rapid ascent of rhyolitic magma at Chaitén volcano, Chile, Nature. 461:780-783

Castruccio A et al. (2016) Eruptive parameters and dynamics of the April 2015 sub-Plinian eruptions of the Calbuco volcano (southern Chile) Bull. Volc. 78:62

Chahine MT et al. (2006) AIRS: Improving weather forecasting and providing new data on greehouse gases. Bull. Am. Meteorol. Soc. 87(7): 911 - 926

Cheng I et al. (2013) Concentration-weighted trajectory approach to identifying potential sources of speciated atmospheric mercury at an urban coastal site in Nova Scotia, Canada. Atmos. Chem Phys. 13:6031-6048

Chesner CA, Rose WI (1984) Geochemistry and avolution of the Fuego volcanic complex, Guatemala. J. Volc. Geotherm. Res. 21:25-44

Christopher TC et al. (2014) Petrological and geochemical variation during the Soufriere Hills eruption, 1995 to 2010. Geol. Soc. Lon. Mem. 39(1):317-342

Christensen PR, Harrison ST (1993) Thermal infrared emission spectroscopy of natural surfaces: Application to desert varnish coatings on rocks, J. Geophys Res. 98(B11);19819-19834

Christensen PR et al. (2000) Identification of a basltic component on the Martian surface from Thermal Emission Spectrometer data, J. Geophys. Res., 105(E4):9609 – 9621

Christensen PR et al. (2000) A thermal emission spectral library of rock-forming minerals, J. Geophys. Res. Plan. 105(E4):9735-9739

Clark RN et al. (2007) USGS digital spectral library splib06a, USGS Digital Data Series 231

Clerbaux C et al. (2009) Monitoring of atmospheric composition using the thermal infrared IASI/MetOp sounder. Atmos. Chem. Phys. 9:6041-6054

Cole PD et al. (2014) Vulcanian explosions at Soufriere Hills Volcano, Montserrat between 2008 and 2010. Geol. Soc. Lon. Mem. 39:93-111

Corradini S et al. (2008) Mt. Etna tropospheric ash retrieval and sensitivity analysis using Moderate Resolution Imaginge Spectroradiometer measurements. J. Appl. Rem. Sens. 2(1):023550

Cronin SJ et al (1998) Agronomic impact of tephra fallout from 1995 and 1996 Ruapehu Volcano eruptions, New Zealand, Env. Geo., 34(1):21-30

Courtland LM et al. (2012) Introducing Geoscience Students to Numerical Modeling of Volcanic Hazards: The example of Tephra2 on VHub.org, Numeracy, 5(2):6

Dingwell DB, Lavallée Y, Kueppers U (2012) Volcanic ash: A primary agent in the Earth system, Phys. Chem. Earth, Parts A/B/C, 45:2-4

Draxler RR, Hess G (1998) An overview of the HYSPLIT_4 modelling system for trajectories. Aust. Meteorol. Mag. 47:295-308

Duda K et al (2009) Optical satellite volcano monitoring: A multi-sensor rapid response system, In: Ho PG (ed.) Geoscience and Remote sensing, 473 – 496

Durant AJ, Rose WI (2009) Sedimentological constraints on hydrometeor-endhanced particle deposition: 1992 eruptions of Crater Peak, Alaska, J. Volc. Geotherm. Res., 186(1-2):40-59

Edwards CE et al (2011) Mosaicking of global planetary image datasets: 1. Techniques and data processing for Thermal Emission Imaging System (THEMIS) multi-spectral data, J. Geophys. Res., 116(E10008)

Fero J, Carey SN, Merrill JT (2009) Simulating the dispersal of tephra from the 1991 Pinatubo eruption: implications for the formation of widespread ash layers. J. Volc. Geotherm. Res. 186:120-131

Fink JH (1985) Geometry of Silicic Dukes beneath the Inyo Domes, California. J. Geophys. Res. 90(B13):11127-11133

Folch A, Sulpizio R (2010) Evaluating long-range volcanic ash hazard using supercomputing facilities: application to Somma-Vesuvius (Italy), and consequences for civil aviation over the Central Mediterranean Area, Bull. Volc., 72(9):1039-1059

Fubini B, Arean CO (1999) Chemical aspects of the toxicity of inhaled mineral dusts. Chem. Soc. Rev., 28(6):373-381

Gangale G, Prata AJ, Clarisse L (2010) The infrared spectral signature of volcanic ash determined from high-spectral resolution satellite measurements, Rem. Sens. Env., 114(2):414-425

Gillespie A et al. (1998) A tempreature and emissivity separation algorithm for Advanced Spaceborne Thermal Emission and Reflection Radiometer (ASTER) images . IEEE Trans. Geosci. Rem. Sens. 36(4):1113 - 1126

Guehenneux Y, Gouhier H, Labazuy P (2015) Improved spaceborne detection of volcanic ash for real-time monitoring using 3-Band method. J. Volc. Goetherm. Res. 293:25-45

Guffanti M et al. (2005) Volcanic-ash hazard to aviation during the 2003–2004 eruptive activity of Anatahan volcano, Commonwealth of the Northern Mariana Islands. J. Volc. Geotherm. Res. 146:241-255

Gudmundsson MT et al (2010) Eruptions of Eyjafjallajökull Volcano, Iceland, Eos Trans. AGU, 91(21):190-191

Gudmundsson MT et al. (2012) As generation and distribution from the April-May 2010 eruption of Eyjafjallajökull, Iceland, Nat. Sci. Rep. 2:572

Hamilton VW, Christensen PR, McSween HY (1997) Determination of martian meteorite lithologies and mineralogies using vibrational spectroscopy, J. Geophys. Res. 102(E11):25593-25603

Hamilton VW et al. (2001) Analysis of Terrestrial and Martian volcanic compositions using thermal emission spectroscopy 2: Application to Martian surface spectra from the Mars Global Surveyor Thermal Emission Spectrometer, J. Geophys Res., 106(7): 14733 - 14746

Han Y-J, Holsen TM, Hopke PK (2007) Estimation of source locations of total gaseous mercury measured in New York State using trajectory-based models. Atmos. Environ. 41:6033-6047

Harris AJL et al. (1997) Low-cost volcano surveillance from space: case studies from Etna, Krafla, Cerro Negro, Fogo, Lascar and Erebus. Bull. Volc. 59:49-64

Harris AJL et al., (1997) A chronology of the 1991 to 1993 Mount Etna eruption using advanced very high resolution radiometer data: Implications for real-time thermal volcano monitoring, J. Geophys. Res. Sol. Earth, 102(B4): 7985-8003

Harris AJL et al. (2001) Automated, high temporal resolution, thermal analysis of Kilauea volcano, Hawai'i, using GOES satellite data. Int. J. Remote Sens. 22:945-967

Harris AJL, Rose WI, Flynn LP (2003) Temporal trends in alva dome extrusion at Santiaguito 1922-2000. Bull. Volc. 65:77-89

Heiken G, Wohletz K, (1991) Fragmentation processes in explosive volcanic eruptions. In: Fisher RV, Smith GA (Eds.) Sedimentation in Volcanic Settings: SEPM Spec. Pub., 45:19-26

Henney LA (2012) Remote Sensing of Volcanic Plumes using the Advanced Spaceborne Thermal Emission and Reflection Radiometer (ASTER). Michigan Technological University, Houghton, Michigan, 297 pp

Henney LA, Rodriquez LA, Watson IM (2012) A comparison of SO_2 retrieval techniques using mini-UV spectrometers and ASTER imagery at Lascar volcano, Chile. Bull. Volc. 74:589-594

Hirabayashi J, Ossaka J, Ozawa T (1982) Relationship between volcanic activity and chemical composition of the volcanic gases – A case study on the Sakurajima Volcano. Geochem. J. 16:11-21

Holland ASP et al. (2011) Degassing processes during lava dome growth: Insights from Santiaguito lava dome, Guatemala. J. Volc. Geotherm. Res. 202:153-166

Horwell CJ et al. (2003) Surface reactivity of volcanic ash from the eruption of Soufriere Hills volcano, Montserrat, West Indies with implications for health hazards. Environ. Res. 93:202-215.

Horwell, CJ, Baxter, PJ (2006) The respiratory health hazards of volcanic ash: a review for volcanic risk mitigation. Bull. Volc., 69(1):1-24

Hulley G et al. (2017) ECOSTRESS, a NASA Earth-ventures instrument for studying links between the water cycle and plant health over the diurnal cycle, 2017 IEEE Int. Geosci. Rem. Sens. Symp. 5494-5496

Iguchi M et al. (2013) Characteristics of volcanic activity at Sakurajima Volcano's Showa crater during the period 2006 to 2011. Bull. Volc. Soc. Jpn. 58(1):115-135

Iwasaki A, Fujisada H (2005) ASTER geometric performance. IEEE Trans. Geo. Rem. Sens. 43(12):2700-2706

Jaupart C, Allègre CJ (1991) Gas content, eruption rate and instabilities of eruption regime in silicic volcanoes, E. Plan. Sci. Lett., 102:413-429

Jensen JR (2005) Introductory Digital image processing: A remote sensing perspective. Third Edition. Prentice Hall

Jones MT, Gislason SR (2008) Rapid releases of metal salts and nutrients following the deposition of volcanic ash into aqueous environments. Geochim. Cosmo. Acta 72:3661-3680

Justice CO et al. (1998) The Moderate Resolution Imaging Spectroradiometer (MODIS): Land remote sensing for global change research. IEEE Trans. Geo. Remote Sens. 36:1228-1249

Kahle AB et al (1991), The advanced spaceborne thermal emission and reflectance radiometer (ASTER), Int. J. Imaging Syst. Technol., 3:144–156

Kempfert KD et al. (2001) Detectors for Fouriere Transform Spectroscopy, Thermo Nicolet Application Note, AN-00125

Klüser L, Erbertseder T, Meyer-Arnek J (2013) Observation of volcanic ash from Puyehue-Cordón Caulle with IASI, Atmos. Meas. Tech. 6:35-46

Krivoruchko K (2012) Empirical bayesian kriging Esri: Redlands, CA, USA. http://www. esri. com/news/arcuser/1012/empirical-byesian-kriging. Accessed August 2nd 2016

Kurniawan WA, Sakakibara M, Suparka E (2016) Petrological monitoring of the AD 2011-2012 volcanic ash from Sakurajma Volcano, southern Kyushu, Japan. Geosci. 6:12

Langmann B et al (2012) Volcanic ash over Europe during the eruption of Ejyafjallajökull on Iceland, April – May 2010, Atmos. Env., 48:1-8

Lyon RJP (1965) Analysis of rocks by spectral infrared emission (8 – 25 microns), Econ. Geol. 60:715-736

Lyons JJ, et al (2010) Patterns in open vent, strombolian behavior at Fuego volcano, Guatemala, 2005-2007. Bull. Volc. 72:1-15

Mackie S, Millington S, Watson IM (2014) How assumed composition affects the interpretation of satellite observations of volcanic ash, Met. App., 21(1):20-29

Mangan TP et al. (2017) Heterogeneous ice nucleation by Soufriere Hills volcanic ash immersed in water droplets. Plos One. 12(1):e0169720

Marple VA, Rubow KL, Behm SM (1991) A microorifice uniform deposit impactor (MOUDI): Description, calibration, and use, Aero. Sci. Tech., 14(4):434-446

Martin DP, Rose WI (1981) Behavioral patterns of Fuego volcano, Guatemala. J. Volc. Goetherm. Res. 10:67-81

Mastin LG et al (2009) A multidisciplinary effort to assign realistic source parameters to models of volcanic ash-cloud transport and dispersion during eruptions, J. Volc. Geotherm. Res., 186(1-2):10-21

Matsumoto A et al (2013) Temporal variations of the petrological features of the juvenile materials during 2006 to 2010 from Showa crater, Sakurajima volcano, Kyushu, Japan, Bull. Volc. Soc. Jap. 58(1):191-212

Maturilli A, Helbert J, Moroz L (2008) The Berlin emissivity database (BED), Plan. Space. Sci. 56:420-425

Miller CD (1985) Holocene Eruptions at the Inyo Volcanic Chain, California: Implications for Possible Eruptions in Long Valley Caldera. Geology 13(1):14-17

Miller TP, Casadevall TJ (2000) Volcanic ash hazards to aviation, In: Sigurdsson H (Ed.) Encyc. Volc., Academic Press, San Diego

Minitti ME and Hamilton VE (2010) A search of basaltic-to-intermediate glasses on Mars: Accessing martian crustal mineralogy. Icarus 210(1):135-149

Miwa T et al. (2009) Correlations of volcanic ash texture with explosion earthquakes from vulcanian eruptions at Sakurajima volcano, Japan. J. Volc. Geotherm. Res. 184:473-486

Moersch JE, Christensen PR (1995) Thermal emission from particulate surfaces, J. Geophys. Res. 100(E4), 7465-7477

Mortier A. et al. (2013) Detection and characterization of volcanic ash plumes over Lille during the Eyjafjallajökull eruption. Atmos. Chem. Phys. 13: 3075-3720.

Mueller SB et al. (2016) Experimental volcanic ash aggregation: Internal structuring of accretionary lapilli and the role of liquid bonding, Earth Plan. Sci. Lett. 433:232-240

Murphy MD et al. (2000) Rembolization of andesite magma by intrusion of mafic magma at the Soufriere Hills Volcano, Montserrat, West Indies. J. Petro. 31(1):21-42

Murray BJ, O'Sullivan D, Atkinson JD, Webb ME (2012) Ice nucleation by particles immersed in supercooled cloud droplets. Chem. Soc. Rev. 41:6519-6554

Mustard JF, JE Hays (1997) Effects of hyperfine particleson on reflectance spectra from 0.3 – 25 μm, Icarus, 125:145-163

Nash DB et al. (1993) Evaluation of infrared emission spectroscopy for mapping the moon's surface composition from lunary orbit, J. Geophys. Res., 98(E12):23,535-23552

Neal C, Girina O, Senyukov S, Rybin A, Osiensky J, Izbekov P, Ferguson G (2009) Russian eruption warning systems for aviation. Nat. Hazards 51:245-262

Oishi M et al. (2018) Distribution of mass of terphra-fall deposits from volcanic eruptions of Sakurajima Volcano based on posteruption surveys. Bull. Volc. 80:42

Oppenheimer C (1998) Review article: Volcanological applications of meteorological satellites Int. J. Remote Sens. 19:2829-2864

Pavolonis MJ, Feltz WF, Heidinger AK, Gallina GM (2006) A daytime complement to the reverse absorption technique for improved automate detection of volcanic ash. J. Atmos. Ocean. Tech. 23:1422 – 1444

Pergola NV et al. (2004) Improving volcanic ash cloud detection by a robust satellite technique, Rem. Sens. Env. 90(1):1-22R

Pieri D, Abrams M (2004) ASTER watches the world's volcanoes: a new paradigm for volcanological observations from orbit. J. Volc. Geotherm. Res. 135:13 – 28

Pietruczuk A (2013) Short term variability of aerosol optical thickness at Belsk for the period 2002–2010. Atmos. Environ. 79:744-750

Piscini A et al (2011) Volcanic ash cloud detection from space: a comparison between the RST_{ASH} technique and the water vapour corrected BTD procedure, Geomat. Nat. Haz. Risk, 2(3):263-277

Plumlee GS, Morman SA, Cook A, (2012) Environmental and Medical Geochemistry in Urban Disaster Response and Preparedness. Elem. 8(6):451-457

Pollack JB, Toon OB, Khare BN (1973) Optical properties of some terrestrial rocks and glases, Icarus, 19:372-389

Poulidis AP et al. (2018) Statistical analysis of dispersal and deposition patterns of volcanic emissions from Mt. Sakurajima, Japan. Atmos. Env. 179:305-320

Prata AJ (1989a) Infrared radiative transfer calculations for volcanic ash clouds. Geophys. Res. Lett. 16:1293-1296

Prata AJ (1989b) Observations of volcanic ash clouds in the 10-12 μm window using AVHRR/2 data. Int. J. Remote Sens. 10:751-761

Prata AJ (2009) Satellite detection of hazardous volcanic clouds and the risk to global air traffic Nat. Hazards 51:303-324

Prata AJ, Grant I (2001) Retrieval of microphysical and morphological properties of volcanic ash plumes from satellite data: Application to Mt Ruapehu, New Zealand. Q. J. Royal Meteorol. Soc. 127:2153-2179

Prata AJ et al. (2001) Comments on “Failures in detecting volcanic ash from a satellite-based technique”. Remote. Sens. Environ. 78:341-346

Prata AJ, Kerkmann J (2007) Simultaneous retrieval of volcanic ash and SO_2 using MSG-SEVIRI measurements. Geophys. Res. Lett. 35(4):L05813

Prata AT, Siems ST, Manton MJ (2015) Quantification of volcanic cloud top heights and thicknesses using A-train observations for the 2008 Chaitén eruption. J. Geophys. Res.: Atmos. 120:2928-2950.

Price MA, Ramsey MS, Crown DA (2016) Satellite-based thermophysical analysis of volcaniclastic deposits: A terrestrial analog for mantled lava flows on Mars. Rem. Sens. 8:152

Ramsey MS (2002) Ejecta distribution patterns at Meteor Crater, Arizona: On the applicability of lithologic end-member deconvolution for spaceborne thermal infrared data of Earth and Mars, J. Geophys. Res., 107(E8)

Ramsey MS (2016) Synergistic use of satellite thermal detection and science: a decadal perspective using ASTER. Geol. Soc. Lond. Spec. Publ. 426:115-136

Ramsey MS, Christensen PR (1998) Mineral abundance determination: Quantitative deconvolution of thermal emission spectra. J. Geophys. Res. Sol. Earth. 103(B1): 577-596

Ramsey MS, Fink JH (1999) Estimating silicic lava vesicularity with thermal infrared remote sensing: A new technique for volcanic mapping and monitoring, Bull. Volc. 61:32-39

Ramsey MS et al. (1999) Identification of sand sources and transport pathways at the Kelso Dunes, California, using thermal infrared remote sensing, Geo. Soc. Am. Bull., 111(5):646-662

Ramsey MS, Dehn J (2004) Spaceborne observations of the 2000 Bezymianny, Kamchatka eruption: the integration of high-resolution ASTER data into near real-time monitoring using AVHRR, J. Volc. Geotherm. Res., 135(1):127-146

Ramsey MS, Wessels RL, Anderson SW (2012) Surface textures and dynamics of the 2005 lava dome at Shiveluch Volcano, Kamchatka. GSA Bull. 124(5-6): 678-689

Ramsey MS, Harris AJL (2013) Volcanology 2020: How will thermal remote sensing of volcanic surface activity evolve over the next decade? J. Volc. Geotherm. Res. 249: 217-233

Ramsey MS et al (2017) A new orbital concept for measuring passive volcanic degassing and small plumes, IAVCEI Scientific Assembly, Portland, OR

Realmuto VJ (1990) Separating the effects of temperature and emissivity: emissivity spectrum normalization. Proc. Second TIMS Workshop. JPL Pub. 90-55:31-35

Realmuto VJ, Abrams MJ, Buongiorno MF, Pieri DC (1994) The use of multispectral thermal infrared image data to estimate the slufr dioxide flux from volcanoes: a case study from Mount Etna, Sicily, Jul 29th, 1986. J. Geophys. Res. 102(B7): 15057-15072

Realmuto VJ, Worden HK (2000) Impact of atmospheric water vapor on the thermal infrared remote sensing of volcanic sulfur dioxide emissions: A case study from the Pu'u 'O'o ventof Kilauea Volcano, Hawaii. J. Geophys. Res. 105(B9):21497-21508

Realmuto VJ, Berk A (2016) Plume Tracker: Interactive mapping of volcanic sulfur dioxide emissions with high-performance radiative transfer modeling. J. Volc. Geotherm. Res. 327:55-69

Reath KA, Ramsey MS, Dehn J, Webley PW (2016) Predicting eruptions from precursory activity using remote sensing data hybridization. J. Volc. Geotherm. Res. 321:18-30

Rose SR, Ramsey MS (2009) The 2005 eruption of Kliuchevskoi volcano: Chronology and processes derived from ASTER spaceborne and field-based data. J. Volc. Geotherm. Res. 184:367-380

Rose SR et al. (2014) Thermal deconvolution: Accurate retrieval of multispectral infrared emissivity from thermally-mixed volcanic surfaces, Rem. Sens. Env., 140:690-703

Romero JE et al. (2016) Eruption dynamics of the 22-23 April 2015 Calbuco Volcano (Southern Chile): Analyses of tephra fall deposits. J. Volc. Geotherm. Res. 317:15-29

Rose WI (1972) Santiaguito volcanic dome, Guatemala. GSA. Bull. 83:1413-1434

Rose WI et al. (1978) The October 1974 basaltic tephra from Fuego volcano: Description and history of the magma body. J. Volc. Geotherm. Res. 4:3-53

Rose WI, Bluth G, Ernst G (2000) Integrating retrievals of volcanic cloud characteristics from satellite remote sensors: a summary. Philos. Trans. R. Soc. Lond. A: Math. Phys. Eng. Sci. 358:1585-1606

Rose WI et al. (2001) Observations of volcanic clouds in their first few days of atmospheric residence: The 1992 eruptions of Crater Peak, Mount Spurr Volcano, Alaska. J. Geo. 109:677-694

Rose WI, Durant AJ (2009) Fine ash content of explosive eruptions, J. Volc. Geotherm. Res. 186:32-39

Rose WI, Durant AJ (2011) Fate of volcanic ash: Aggregation and fallout. Geol. 39:895-896

Rowan LC et al. (1991) Evaluation of visible and near-infrared and thermal-infrared reflectance spectra for studying thermal alteration of Piere Shale, Wolcott, Colorado, J. Geophys Res. 96(B11):18047-18057

Ruff SW et al. (1997) Quantitative thermal emission spectroscopy of minerals: A laboratory technique for measurement and calibration. J. Geophys. Res.: Sol. Earth. 102(B7):14899-14913

Ruff SW, Christensen PR (2002) Bright and dark regions on Mars: Particle size and mineralgoical characteristics based on Thermal Emission Spectrometer data, J. Geophys. Res. 107(E12):5127

Sahetapy-Engel ST, Harris AJL, Marchetti E (2008) Thermal, seismic and infrasound observations of persistent explosive activity and conudit dynamics at Santiguito lava dome, Guatemala. J. Volc. Geotherm. Res. 173:1-14

Salisbury JW, D'Aria DM (1992) Emissivity of terrestrial materials in the 8 – 14 μm atmospheric window, Rem. Sens. Env. 42:83-106

Salisbury JW, Wald AE (1992) The role of volume scattering in reducing spectral contrast of restrahlen bands in spectra of powdered minerals, Icarus, 96:121-128

Salisbury JW, Wald A, D'Aria DM (1994) Thermal-infrared remote sensing and Kirchhoff's law 1. Laboratory measurements, J. Geophys. Res. 99(B6):11897-11911

Sawada Y (1987) Study on analysis of volcanic eruptions based on eruption cloud image data obtained by the Geostationary Meteorological Satellite (GMS) Tech. Rep. Meteorol. Res. Inst. 22:335pp

Sawada Y (2002) Analysis of eruption cloud with geostationary meteorological satellite imagery (Himawari). J. Geogr. Tokyo 111:374-394

Schmit T et al. (2017) A closer look at the ABI on the GOES-R series. Bull. Am. Meteorol. Soc. 98(4): 681 – 698

Scott JAJ (2013) The Santiaguito volcanic dome complex, Guatemala. University of Oxford, Oxford, UK, 59 pp

Scott JAJ et al. (2012) The magmatic plumbing system beneath Santiaguito Volcano, Guatemala. J. Volc. Geotherm. Res. 237:54-68

Sigmundsson F et al. (2010) Intrusion triggering of the 2010 Eyjafjallajökull explosive eruption, Nature. 7322:426

Simpson JJ, Hufford G, Pieri D, Berg J (2000) Failures in detecting volcanic ash from a satellite-based technique. Remote Sens. Environ. 72:191-217

Simpson JJ, Hufford G, Pieri D, Berg J (2001) Response to "Comments on 'Failures in detecting volcanic ash from a satellite-based technique. Rem. Sens. Env. 78(3): 347-357

Smith CM et al. (2018) Correlating the electricification of volcanic plumes with ashfall textures at Sakurajima Volcano, Japan, Earth. Plan. Sci. Lett. 492:47-58

Sparks RSJ (2003) Forecasting volcanic eruptions. Earth Planet. Sci. Lett. 210:1-15

Sparks RSJ (1998) The dimensions and dynamics of volcanic eruption columns, Bull. Volc. 48:3-15

Sparks RSJ et al. (1998) Magma production and growth of the lava dome of the Soufriere Hills Volcano, Montserrat, West Indies: November 1995 to December 1997. Geophys. Res. Lett. 25(18):3421 - 3424

Sparks RSJ, Young SR (2002) The eruption of Soufriere Hills Volcano, Montserrat (1995 – 1999): Overview of scientific results. Geol. Soc. Lon. Mem. 21:45-69

Sparks RSJ, Biggs J, Neuberg J (2012) Monitoring volcanoes. Science 335:1310-1311

Stevenson JA et al. (2015) Big grains go far: understanding the discrepancy between tephrochronology and satellite ingrared measurements of volcanic ash. Atmos Meas. Tech. 8:2069-2091

Stohl A (1996) Trajectory statistics-a new method to establish source-receptor relationships of air pollutants and its application to the transport of particulate sulfate in Europe. Atmos. Environ. 30:579-587

Stohl A et al. (2011) Determination of time- and height resolved volcanic ash emissions and their use for quantitative ash dispersion modeling: the 2010 Eyjafjallajökull eruption, Atmos. Chem. Phys. 11:4333-4351

Thomas HE, Watson IM (2010) Observations of volcanic emissions from space: current and future perspectives. Nat. Hazards, 54:323-354.

Tonooka H (2001) An atmopshierc correction algorithm for the thermal infrared multispectral data over land- a water-vapor scaling method, IEEE Trans. Geosci. Rem. Sens., 39(3):682-692

Tonooka H (2005) Accurate atmospheric correction of ASTER thermal infrared imagery using the WVS method, IEEE Trans. Geosci. Rem. Sens., 43(12):2778 – 2792

Tonooka, H, Palluconi, FD (2005) Validation of ASTER/TIR standard atmospheric correction using water surfaces. IEEE Trans. Geo. Rem. Sens., 43(12):2769-2777

Tuffen H et al. (2013) Exceptional mobility of an advancing rhyolitic obsidian flow at Cordón Caulle volcano in Chile, Nat. Comm. 4:2709

Tupper A et al. (2009) Tall clouds from small eruptions: the sensitivity of eruption height and fine ash content to tropospheric instability. Nat. Hazards 51:375-401

Vallance JW et al. (2001) Volcano hazards at Fuego and Acatenango, Guatemala. USGS Open-File Rep. 01-431:24pp

Van Eaton AR et al (2015) Hail formation triggers rapid ash aggregation in volcanic plumes, Nat. Comm., 6:1-7

Van Manen SM, Dehn J (2009) Satellite remote sensing of thermal activity at Bezymianny and Kliuchevskoi from 1993 to 1998, Geo. 37(11):983-986

Varga RJ, Bailey RA, Suemnicht GA (1990) Evidence for 600 year-old basalt and magma mixing and Inyo Craters Volcanic Chain, Long Valley Caldera, California, J. Geophys. Res., 95(B13):21441-21450

Vogel A et al. (2017) Reference data set of volcanic ash physiochemical and optical properties, J. Geophys. Res. Atmos., 122:9485-9514

Voight B et al. (1999) Magma flow instability and cyclic activity at Soufrière Hills Volcano, Montserrat, British West Indies. Science 283:1138-1142

Wadge G et al. (2014) An overview of the eruption of the Soufrière Hills Volcano, Montserrat from 2000 to 2010. Geol. Soc. Lon. Mem. 39:1-40

Wald AE, Salisbury JW (1995) Thermal infrared directional emissivity of powdered quartz, J. Geophys. Res. Sol. Earth. 100(B12):24665-24675

Walter LS, Salisbury JW (1989) Spectral characterization of igneous rocks in the 8-to 12-μm region, J. Geophys. Res. Sol. Earth. 94(B7):9203-9213

Wang Y, Zhang X, Draxler RR (2009) TrajStat: GIS-based software that uses various trajectory statistical analysis methods to identify potential sources from long-term air pollution measurement data. Environ. Model. Softw. 24:938-939

Watson IM et al. (2004) Thermal infrared remote sensing of volcanic emissions using the moderate resolution imaging spectroradiometer. J. Volc. Geotherm. Res. 135:75-89

Waythomas CF et al. (2014) The 2013 eruption of Pavlof Volcano, Alaska: a spatter eruption at an ice- and snow-clad volcano, Bull. Volc. 76:862

Webley PW, Mastin L (2009) Improved prediction and tracking of volcanic ash clouds. J Volc. Geotherm Res. 186:1-9

Webley PW et al. (2009) Near-real-time volcanic ash cloud detection: Experiences from the Alaska Volcano Observatory, J. Volc. Geotherm. Res. 186:79-90

Webley PW (2011) Virtual Globe visualization of ash–aviation encounters, with the special case of the 1989 Redoubt–KLM incident. Comput. Geosci. 37:25-37

Weinzierl B et al. (2012) The Eyjafjallajökull Eruption in 2010 and the Volcanic Impact on Aviation, In: Schumann U (Ed.) Atmos. Phys., Springer, Heidelberg, 625-644

Wen S, Rose WI (1994) Retrieval of sizes and total masses of particles in volcanic clouds using AVHRR bands 4 and 5. J. Geophys. Res. 99(D3):5421-5431

Wenrich ML, Christensen PR (1996) Optical constants of minerals derived from emission spectroscopy: Application to quartz, J. Geophys. Res. 101(B7):15921-15931

White J, Houghton B (2006) Primary volcaniclastic rocks. Geol. 34:677-680

Williams DB, Thomas HE (2011) An assessment of volcanic hazards to aviation – a case study from the 2009 Sarychev Peak eruption. Geo. Nat. Haz. Risk. 2(3):233-246

Williams DB, Ramsey MS, Karimi B (2013) Identifying the Volcanic Source of Disconnected Ash Clouds using the HYSPLIT Dispersion Model. In: AGU Fall Meet. Abstr. p 1538

Wilson L, Sparks RSJ, Walker GPL (1980) Explosive volcanic eruptions – IV. The control of magma properties and conduit geometry on eruption column behavior, Geophys. J. Int. 63:117-148

Wilson TM et al, (2012) Volcanic ash impacts on critical infrastructure, Phys. Chem. Earth. Int. A/B/C. 45:5-23

Winker DM et al. (2012) CALIOP observations of the transport of ash from the Eyjafjallajökull volcano in April 2010. J. Geophys. Res. Atmos. 117(D20)

Wohletz KH (1983) Mechanisms of hydrovolcanic pyroclast formation: grain-size scanning electron microscopy, and experimental studies, J Volc. Geotherm. Res. 17(1):31-63

Woods AW, Self S (1992) Thermal disequilibrium at the top of volcanic clouds and its effect on estimates of the column height, Nature, 355:628-630

Woods AW, Kienle J (1994) The dynamics and thermodynamics of volcanic clouds: Theory and observations from the April 15 and April 21, 1990 eruptions of Redoubt Volcano, Alaska, J. Volc. Geotherm. Res., 62:273-299

Wright R, Flynn L, Garbeil H, Harris A, Pilger E (2002) Automated volcanic eruption detection using MODIS. Remote Sens. Environ. 82:135-155

Xiong X et al. (2013) VIIRS on-orbit calibration methodology and performance. J. Geophys. Res. 119(9):5065 - 5078

Yamaguchi Y et al (1998) Overview of Advanced Spaceborne Thermal Emission and Reflection Radiometer (ASTER), IEEE Trans. Geosci. Rem. Sens. 36:1062-1071

Yamamoto H, Watson IM, Phillips JC, Bluth GJ (2008) Rise dynamics and relative ash distribution in vulcanicn eruption plumes at Santiaguito Volcano, Guatemala, revealed using an ultraviolet imaging camera. Geophys. Res. Lett. 35:L08314

Young SJ, Johnson R, Hackwell JA (2002) An in-scene method for atmospheric compensation of thermal hyperspectral data, J. Geophys, Res., 107(D24)

Young SR et al. (1998) Overview of the eruption of Soufrière Hills Volcano, Montserrat, 18 July 1995 to December 1997. Geophys. Res. Lett. 25(18):3389-3392

Zimanowski B, Wohletz K, Pierfrancesco D, Büttner R (2003) The volcanic ash problem. J. Volc. Geotherm. Res. 122:1-5

Zimanowski B et al (2015) Magma-water interaction and phreatomagmatic fragmentation, In Sigurdsson H (ed.) Encycl. Volc. 473-484